CYCLOPARAPHENYLENES AS BUILDING BLOCKS FOR SELF-ASSEMBLED NANOTUBE-LIKE STRUCTURES

by

ERIK JAMES LEONHARDT

A DISSERTATION

Presented to the Department of Chemistry and Biochemistry
and the Graduate School of the University of Oregon
in partial fulfillment of the requirements
for the degree of
Doctor of Philosophy

June 2020

DISSERTATION APPROVAL PAGE

Student: Erik James Leonhardt

Title: Cycloparaphenylenes as Building-Blocks for Self-Assembled Nanotube-Like Structures

This dissertation has been accepted and approved in partial fulfillment of the requirements for the Doctor of Philosophy degree in the Department of Chemistry and Biochemistry by:

Mark Lonergan	Chairperson
Ramesh Jasti	Advisor
Michael Haley	Core Member
Hailin Wang	Institutional Representative

and

Kate Mondloch	Interim Vice Provost and Dean of the Graduate School

Original approval signatures are on file with the University of Oregon Graduate School.

Degree Awarded June 2020

© 2020 Erik James Leonhardt

DISSERTATION ABSTRACT

Erik James Leonhardt
Doctor of Philosophy
Department of Chemistry and Biochemistry
June 2020
Title: Cycloparaphenylenes as Building Blocks for Self-Assembled Nanotube-Like Systems

Since its first synthesis in 2008, the cycloparaphenylene (CPP), or “carbon nanohoop”, has quickly evolved from a synthetic novelty to a readily accessible and highly tunable molecular scaffold. With accessibility no longer an issue, many researchers have begun exploring how the unique properties of CPPs can be practically utilized. Chapter **I** provides an overview of the emerging applications of CPPs in a variety of fields, ranging from chemical biology to organic electronics.

Inspired by the long-standing challenge of synthesizing carbon nanotubes (CNTs) in a precise, size-selective fashion, we aimed to develop methods to use CPPs (which themselves represent fragments of CNTs) as supramolecular synthons to produce highly tunable CNT mimics. Chapter **II** discloses our initial effort toward this, showing how fluorination of the [12]CPP backbone results in CNT-like nanohoop self-assembly via organofluorine interactions. In Chapter **III**, we present the synthesis of two additional fluorinated nanohoops, one of lesser diameter and one bearing a lower degree of fluorination, and show that both molecules exhibit tubular self-assembly in the solid-state. These materials were found capable of a variety of functions, such as linear solid-state guest alignment and appreciable N_2 uptake. Additionally, in Chapter **IV**, we show that fluorination of the nanohoop backbone may provide a means of improving π-π interactions between nanohoops in order to improve solid-state charge transfer. Preliminary data is provided showing that thin-films of a fluorinated [10]CPP analog exhibit an average conductivity ten-times higher than those of the non-fluorinated analog.

Having established a reliable strategy for constructing CPP-based non-covalent CNT mimics, we began pursuing a perhaps loftier goal of producing fully covalent CNT-

like systems using nanohoops. In Chapter **V**, we present our initial foray towards this goal via the synthesis of a catechol containing nanohoop that, via proton NMR experiments, is shown to be readily capable of undergoing condensation reactions with boronic acids to form structures with boronic ester linkages. These results suggest that more complex boronic ester-linked nanohoop systems such as nanotubes and cages are indeed accessible.

This dissertation includes previously published and unpublished co-authored material.

CURRICULUM VITAE

NAME OF AUTHOR: Erik James Leonhardt

GRADUATE AND UNDERGRADUATE SCHOOLS ATTENDED

Ramapo College of New Jersey, Mahwah
University of Oregon, Eugene

DEGREES AWARDED

Doctor of Philosophy, Chemistry, 2020, University of Oregon
Bachelor of Arts, Psychology, 2014, Ramapo College of New Jersey

AREAS OF SPECIAL INTEREST:

Synthetic Organic Chemistry
Materials Chemistry

PROFESSIONAL EXPERIENCE

Teaching Fellow, University of Oregon, 2015-2020

GRANTS, AWARDS, AND HONORS:

ACS Undergraduate Award in Inorganic Chemistry, Ramapo College of New Jersey, Department of Chemistry, 2014

PUBLICATIONS:

Leonhardt, E. J.; Van Raden, J. M.; Miller, D.; Zakharov, L. N.; Alemán, B.; Jasti, R. A Bottom Up Approach to Solution-Processed, Atomically Precise Graphitic Cylinders on Graphite. *Nano Lett.* **2018**, *18*, 7991–7997.

Leonhardt, E. J.; Jasti, R. Emerging Applications of Carbon Nanohoops. *Nat. Rev. Chem.* **2019**, *3*, 672–686.

Van Raden, J. M.; Leonhardt, E. J.; Zakharov, L. N.; Pérez-Guardiola, A.; Pérez-Jiménez, A. J.; Marshall, C. R.; Brozek, C. K.; Sancho-García, J.-C.; Jasti, R. Precision Nanotube Mimics via Self-Assembly of Programmed Carbon Nanohoops. *J. Org. Chem.* **2020**, *85*, 129–141.

Schaub, T. A.; Prantl, E.; Kohn, J.; Bursch, M.; Marshall, C. R.; Leonhardt, E. J.; Lovell, T. C.; Zakharov, L. N.; Brozek, C. B.; Waldvogel, S. R.; Grimme, S.; Jasti, R. Exploration of the Solid-State Sorption Properties of Shape-persistent Macrocyclic Nanocarbons as Bulk Materials and Small Aggregates. *J. Am. Chem. Soc.* **2020**, *Available Online*.

ACKNOWLEDGEMENTS

I would like to begin by thanking my advisor, Professor Ramesh Jasti, for taking me on as a graduate student in his lab. Having had no prior experience in synthetic organic chemistry, I am immensely grateful for his patience and encouragement throughout my graduate studies. He has fostered a lab environment that, in my opinion, encourages creativity, curiosity, and personal growth above all else, and I am forever thankful for the opportunity to have been a part of it.

I would also like to thank all of the Jasti lab members who have helped me along the way. Dr. Evan Darzi, in particular, was an incredible mentor and friend whose infectious enthusiasm heavily inspired the research I went on to do in the Jasti Lab. Dr. Brittany White was also a great friend and endlessly supportive throughout my time working with her. A special thanks goes out to Dr. Jeff Van Raden, who was not only a good friend but a great coworker who was integral in molding the way I approach chemistry.

I would also like to thank current Jasti lab members Terri Lovell, Curtis Colwell, Ruth Maust, Claire Otteson, James May, Julia Fehr, and Tavis Price, as well as undergraduate students Brian Sun and Zach Garrison, for all having been a pleasure to work with every day. Additionally, I would like to extend a special thanks to my undergraduate student, Eli Jaffe, for his never-ending curiosity and genuine love of science. My appreciation also goes out to previous Jasti lab members Dr. Penghao Li, Dr. Tobias Schaub, and Dr. Evan Jackson, as well as the members of the Haley lab for the help they provided me throughout the years. Finally, I would like to thank Justin Dressler, who has been my “partner-in-crime” since my first days at the University of Oregon.

I would also like to thank my graduate committee. Thanks to Professor Mark Lonergan for his wisdom and guidance, which has inspired me to be more thoughtful in the way I approach both science and everyday life. Thank you to Professor Michael Haley for, among other things, instilling in me an attention to scientific detail that has bled into and improved other areas of my life as well. Thanks as well to Professor Hailin Wang for being an excellent out-of-department committee member who has shown genuine interest not only in my scientific work but in my growth as a researcher.

Thank you to all of my childhood friends, namely Keith Gotta, Daniel Gotta, Tom Monteiro, Christopher Godowski, Dean Zonkowski, Alex Kielmanski, Brian Howarth, and Charles Gorman, for always being there for me. Thank you to the Polanskys and the Garneys for always treating me like family during my time in Eugene. Thank you as well to the Pfieffers for their hospitality and friendship.

Nothing that I have accomplished would have been possible without the help of my family. Thank you to my mother, Linda Diem, for the unconditional love and support she has provided throughout my life. My appreciation for her encouragement in all of my endeavors cannot be put into words. Thank you to my father, Erik Leonhardt, for passing on his sense of adventure and for always encouraging my creativity. Thank you to my stepfather, Michael Diem, for being an amazing father figure and for treating me as your own son from the moment you entered our family. Thank you to my sister, Cheyanne Diem, for your love and encouragement. I'm incredibly proud of everything you have accomplished and I know you will do great things in the future. A huge thank you to Jorge Arias, Blanca Deleg, Nicole Arias, Andres Arias, Ana Arias, Israel Caimayo, Isabella Caimayo, and Victoria Caimayo, for welcoming me into their families as if I had always been there. Additionally, I would like to thank my dog, Freyja, for always challenging me and for serving as a living reminder that progress doesn't happen overnight but is rather the result of a million little steps.

I am forever indebted to the love and support that my grandmother, Dorothy Lyons, provided me during her time on Earth. She was a caregiver, a cheerleader, and a best friend. She not only encouraged my interests but would actively dedicate her time to helping me push the boundaries of what I was capable of. She was perhaps the most generous person I have ever known and passed on to me the true joy that can be found in giving selflessly.

Finally, I would like to thank my wife, Andrea Arias, for her love and her unconditional support of all my dreams. Thank you for being there every step of the way on this crazy journey. Thank you for pulling my head out of the clouds when I need it. Thank you for thinking I am capable of anything even when I do not believe it myself. I cannot express how excited I am to see what the future holds for us.

Dedicated to Andrea Arias, my wife and best friend

TABLE OF CONTENTS

Chapter Page

I. EMERGING APPLICATIONS OF CARBON NANOHOOPS 1

I.1. Introduction 2

I.2. CPPs as Versatile Fluorophores 3

I.3. CPP Rotaxanes as Fluorescent Sensors 6

I.4. CPPs as Biological Fluorophores 7

I.5. CPPs as Solid-State Emitters 9

I.6. CPPs in Electronic Applications 11

I.7. Fullerene@CPP Systems 15

I.8. CPPs as Building Blocks for Carbon Nanomaterials 19

I.9. Conclusions and Outlook 23

I.10. Bridge to Chapter II 23

II. A BOTTOM-UP APPROACH TO SOLUTION-PROCESSED, ATOMICALLY PRECISE GRAPHITIC CYLINDERS ON GRAPHITE 25

II.1. Introduction 25

II.2. Results and Discussion 27

I.2.1. Synthesis and Solid-State Analysis 27

I.2.2. Construction and Characterization of Vertically Aligned Nanohoop “Forests” 31

II.3. Conclusion 36

II.4. Experimental Section 37

II.4.1. Materials and Methods 37

II.4.2. X-Ray Crystallographic Data 38

II.4.3. General Sample Preparation for Surface Studies 39

II.4.4. SEM Images of Various Pillar Sizes and Morphologies 41

II.4.5. SEM Images of **II.2** and [12]CPP on Multi-Layer Graphene 42

II.4.6. EDS Analysis 42

II.4.7. Photophysical Characterization of **II.1** and [12]CPP in Solution 43

II.4.8. Synthetic Schemes for Intermediates **II.2** and **II.3** 43

II.4.9. Synthetic Prodedures 44

II.4.10. ^{1}H NMR Spectra 53

II.4.11. ^{13}C NMR Spectra 57

II.4.12. ^{19}F NMR Spectra 61

II.5. Bridge to Chapter III 66

III. PRECISION NANOTUBE MIMICS VIA SELF-ASSEMBLY OF PROGRAMMED CARBON NANOHOOPS 67

III.1. Introduction 68

III.2. Synthesis and X-ray Crystal Structure Analysis 70

III.3. Solid- and Solution-State Analysis of the C_{60}@III.2 Host—Guest Complex 75

III.4. N_2 Uptake Studies on Nanohoop **III.1** 76

III.5. Computational Analysis 79

III.6. Conclusion and Outlook 82

III.7. Experimental Section 83

III.7.1. General Information 83

Chapter Page

III.7.2. Synthetic Schemes 84

III.7.3. Synthetic Procedures 84

III.7.4. ^{1}H NMR Spectra 91

III.7.5. ^{13}C NMR Spectra 96

III.7.6. ^{19}F NMR Spectra 100

III.7.7. Photophysical Data 105

III.7.8. Binding Constant (K_a) Determination 106

III.7.9. Crystallographic Data 107

III.7.10. Thermogravimetric (TGA) Analysis of Nanohoop **III.1** 114

III.7.11. N_2 Uptake Studies 115

III.7.12. Powder X-ray Diffraction (PXRD) Analysis 116

III.7.13. Estimation of Cohesive Energies of **III.2**, **III.2S**, and **III.1** 117

III.7.14. Additional Computational Data 117

III.7.15. Bridge to Chapter IV 118

IV. CHAPTER IV IMPROVING THE SOLID-STATE CONDUCTIVITY OF NANOHOOPS VIA ARENE-PERFLUOROARENE-INDUCED FACE-TO-FACE PACKING 120

IV.1. Introduction 121

IV.2. Results and Discussion 124

IV.3. Conclusion and Outlook 125

IV.4. Device Fabrication and Measurements 126

IV.5. Thin-Film Characterization via Optical Microscopy 127

IV.6. Computational Data 128

Chapter Page

IV.7. Cyclic Voltammetry Data 132

IV.8. Bridge to Chapter V 133

V. SYNTHESIS OF HYDROXY FUNCTIONALIZED NANOHOOPS TOWARDS THE CONSTRUCTION OF COVALENT NANOTUBE MIMICS AND RELATED STRUCTURES 134

V.1. Introduction 134

V.2. Results and Discussion 137

V.3. Conclusion and Outlook 141

V.4. Experimental Section 142

V.4.1. General Information 142

V.4.2. Synthetic Schemes 142

V.4.3. Synthetic Procedures 143

V.4.4. ^{1}H NMR Spectra 150

VI. CONCLUDING REMARKS 155

REFERENCES CITED 156

LIST OF FIGURES

Figure Page

I.1. **Cycloparaphenylenes are the smallest cross-sectional fragments of armchair carbon nanotubes.** A cycloparaphenylene [*n*]CPP consists of *n para*-phenylene moieties linked together to form a hoop. [5]CPP resembles the armchair edge of the carbon nanotube [5,5]CNT (a). [*n*]CPPs feature a strained structure with a radially oriented *π*-electron system and an electron-rich central cavity similar to that in carbon nanotubes (b). Three common synthetic routes to cycloparaphenylenes are shown (c). Two routes make use of cyclohexadiene and cyclohexane as "masked" benzene rings. These sp^3-C-containing precursors have the appropriate curvature and are Subjected to a strain-building aromatization step to afford the desired cycloparaphenylene ([12]CPP in this case). An alternative route employs a Pt molecular square with 4,4'-biphenylene sides, reductive elimination of which affords a [4*n*]CPP, such as [8]CPP 4

I.2. **The electronic structures of cycloparaphenylenes are size-dependent.** (a) The energies of the highest occupied molecular orbital (HOMO) and the lowest unoccupied molecular orbital (LUMO) in a [*n*]CPP (n = 5-12) lead to an energy gap $E_g = E_{HOMO} – E_{LUMO}$ that decreases with decreasing n. (b) Ultraviolet-visible absorption and emission spectra (solid and dashed traces, respectively) of [5-12]CPP. (c) The photophysical properties of [5-12]CPP and average dihedral angles between phenylenes in optimized geometries. (d) Orbitals in electronic ground and excited states of [12]CPP, [5]CPP, and *m*[5]CPP. (e) Generic structure of *m*[*n*]CPP. (f) Photophysical data for *m*[*n*]CPP (n = 5-8, 10, 12) 5

I.3. **Applications of cycloparaphenylenes in biological imaging.** (a) Pyridyl-*m*[6]CPP rings can bind a catalytic Cu^I ion and serve as the active template in the synthesis of rotaxanes **I.1** and **I.1S**, which bear a triazole-containing thread. (b) The pyridyl-*m*[6]CPP ring, in conjunction with Cu^I, can also mediate alkyne-alkyne coupling to give diyne rotaxane **I.2**, the X-ray crystal structure of which is also presented. (c) Fluorescence turn-on of **I.2** on treatment with ^{n}Bu$_4$NF. (d) Desilylation of **I.2** with F$^-$ leads to dethreading and liberation of the emissive pyridyl-*m*[6]CPP ring. (e). Structure of a bis(sulfonate) derivative of [8]CPP (**I.3**). (f) Fluorescence intensity from **I.3** is pH-independent, while the fluorescence intensity of fluorescein is pH-dependent. (g) Photophysical data of **I.3**, [8]CPP, and fluorescein 9

Figure Page

I.4. **Electrical and optical stimulation of cycloparaphenylenes.** (a) Electrical stimulation of [10]CPP•2I_2 affords polyiodide chains and a change from blue To white emission. (b) Emission broadening of [10]CPP•2I_2 as the electrical stimulus is maintained over 250 min. (c) Raman spectra of [10]CPP•2I_2 before (blue) and after (red) the stimulus (d) X-ray absorption near-edge spectroscopy data of [10]CPP•2I_2 before (blue) and after (red) stimulus. (e) Emission from luminescent solar concentrators containing [8]CPP at two concentrations, as well as the standard dye Lumogen, as a function of optical distance *d*. (f) The same experiment as in part e carried out using [10]CPP................................ 12

I.5. **Electronic properties of cycloparaphenylenes.** (a) Highest occupied molecular orbital (HOMO) and lowest unoccupied molecular orbital (LUMO) energies and energy gaps $E_g = E_{HOMO} - E_{LUMO}$ for cycloparaphenylenes (from left to right) [8]CPP, aza[8]CPP, 1,15 diaza[8]CPP, *N*-methylaza[8]CPP triflate and *N*,*N*-dimethyl-1,15-diaza[8]CPP ditriflate. (b) X-ray crystal structures of and calculated charge mobilities in [n]CPP (n = 5–12). (c) Structures of dimers of C_{60}, [5]CPP and [10]CPP, along with intermolecular distances, calculated energetic disorders σ, reorganization energies λ and mobilities μ. (d) Chemical structure of tetrabutoxy-functionalized [10]CPP **I.4**. (e) The generic device architecture used for space-charge-limited current (SCLC).. 16

I.6. **Electron transfer involving cycloparaphenylenes.** (a) The porphyrin-appended [10]CPP host **I.5** can bind C_{60} to form a charge-transfer complex. (b) Differential absorption spectra of C_{60}@**I.5** in PhCN acquired in pump-probe experiments (430 nm, 500 nJ). (c) Time-absorption profiles and fits of the absorption fingerprints of the C_{60} radical cation at 670 nm (red). (d) Lifetimes of charge-separated states of $(C_{60})_2$@**I.5** and **I.5**@$(C_{60})_2$@**I.5**. (e) Highest occupied molecular orbital (HOMO) and lowest unoccupied molecular orbital (LUMO) energies (relative to vacuum) of [10]CPP, nanohoop **I.6**, nanohoop **I.7**, and C_{60}. (f) Photocurrent response of spin-coated films of C_{60}@**I.7** (black), **I.7** (red), C_{60}@**I.6** (dark blue), **I.6** (light blue), [10]CPP@C_{60} (pink) and [10]CPP (purple). (g) *I-V* profiles of C_{60}@**I.7** before (blue) and during (red) photoirradiation... 20

Figure Page

I.7. **Cycloparaphenylenes can serve as building blocks for nanomaterials.** (a) Crystals of the cycloparaphenylene [12]CPP feature pores that are available to guest molecules. (b) Adsorption (filled circles) and desorption (open circles) isotherms for MeOH and [12]CPP. (c) In situ powder X-ray diffraction measurements of [12]CPP during MeOH uptake. The letters correspond to points in the isotherms in (b). (d) Schematic of the proposed structure of a vesicle formed by self-assembly of [10]CPP in THF–H_2O or Me_2SO–H_2O solvent mixtures. (e) Cryo-transmission electron micrograph of [10]CPP vesicles. (f) Fluorescence microscope images of [10]CPP vesicles within A549 and CT26 cells at 4 °C and 37 °C 21

II.1. (a) Cartoon representation of a [12,12] armchair CNT and an X-ray crystal structure of its smallest cross-sectional fragment, [12]CPP (crystal structure data from ref 36). (b) (Left) schematic depiction of hexagonal circle packing, in which the central circle in the lattice is symmetrically surrounded by six other circles. CPPs can be seen as geometrically equivalent to perfect circles. (Right) stacking sheets of hexagonally packed hollow circles resulting in the formation of channels with diameters defined by the constituent circles................. 28

II.2. (a) Coupling of intermediates **II.2** and **II.3** via Suzuki−Miyaura conditions affords macrocycle **II.4**, which is then deprotected with TBAF and subsequently aromatized under mild tin-mediated conditions to provide fluorinated nanohoop **II.1**. (b) X-ray crystal structure of nanohoop **II.1**, showing that the compound self-assembles into noncovalent nanotubes in the solid state. (c) Cross-section of a nanotube of **II.1**, highlighting the 1.63 nm diameter. (d) Aryl C−H···F interactions (dotted lines) that guide the vertical assembly of **II.1**, which range in distance from 2.53 to 2.62 Å. (e) Top-down view showing the hexagonal circle packing of **II.1**, which is guided by six arene−perfluoroarene interactions that measure at 3.69 Å (purple dotted lines) (chloroform solvent molecules omitted for clarity).. 30

II.3. (a) Optical microscopy of hexagonal pillars and needle-like structures on HOPG surface. (b) Angled-SEM of an array of hexagonal pillars. Dense forests of hexagonal pillars are scattered across the sample with heights ranging from a few hundred nanometers to several microns. (c) Angled focused ion beam (FIB) microscopy of isolated hexagonal pillars. The flat hexagonal faces and top are readily apparent. (d) (Left) segment of a larger (25 μm × 16 μm) SEM image of short pillars showing growth templated by the substrate. The pillars are preferentially aligned in one of two angles, separated by ~23.5°. (Right) histogram of orientation angles in the full 25 μm × 16 μm image. A total of 290 hexagons are identified in the full image and nearly all of them are oriented in one of two angles. (e) FIB image of needle-like structures formed by **II.1**, which preferentially orient at 60 relative to one another on the HOPG surface.. 33

II.4. (a) Raman spectrum of a single hexagonal pillar of **II.1**, with peaks observed at 1201, 1278, 1401, 1604, and 1634 cm^{-1}. (b) (Top) PeakForce AFM image of two hexagonal pillars and several needle-like structures. (Bottom) cross-sectional cut of the AFM image (indicated by the dashed white line) showing both the height of the hexagonal pillars (blue) and the elastic modulus (orange) 34

II.5. (a) False-colored but visually accurate wide-field fluorescence image of hexagonal pillars and large needle-like structures under UV excitation. The image brightness is enhanced in the boxed region due to the lower fluorescence intensity of the smaller structures within. (b) Emission spectrum at excitation wavelengths ranging from 380 to 420 nm for the single-pillar shown in the inset. Two emission peaks at 440 and 480 nm are apparent for every excitation wavelength. (c) Maximum photoluminescence (PL) intensity from (b) for both the 440 and 480 nm emission maxima peaks as a function of excitation wavelength. The fluorescence efficiency begins to saturate around 380 nm, which is at the limit of our measurement range 35

II.6. X-ray crystal structure of **II.1** with three resolved $CHCl_3$ solvent molecules (F atoms in green, Cl atoms in yellow, H atoms in white) 39

II.7. Experimental set up used for sample preparation of **II.1** and [12]CPP on graphite/graphene substrates 40

II.8. Images showing different sizes and morphologies of grown pillars. All dimension values are approximate and representative of specific regions. a) SEM image showing vertical pillars grown at the edge of a solvent drying ring: **1.** Pillars at the edge of the drying ring become quite large and start to aggregate. **2.** Pillars inside the drying ring have smaller diameters and are isolated from one another. b) SEM image showing several types of pillars: **3.** Dense pillars with width of 3-5 μm and height of 1-3 μm. **4.** Sparse pillars with width of 0.5-1 μm and height of 5-10 μm. **5.** Dense pillars with height ~10 μm that have been knocked over, presumably during solvent evaporation. **6.** Sparse pillars with width of 0.2-0.5 μm and height of 5-10 μm. **7.** Region of small pillars at their initial stage of growth. c) FIB image of pillars near a drying ring: **8.** Very short pillars with width 1-2 μm and height 200-500 nm. **9.** Pillars with height of 5-10 μm and width 200-500 nm 41

II.9. a) **II.1** and b) [12]CPP deposited onto multi-layer graphene grown on copper foil (Graphenen). Both samples were produced using the procedure in Section II.4.3 42

Figure Page

II.10. EDS was used to characterize the elemental composition both on and off the hexagonal pillars composed of **II.1**, deposited on HOPG. Three representative spectra are shown with their locations marked in the SEM image above. Spectrum 1 shows well defined x-ray lines for carbon, oxygen, fluorine, and silicon. Fluorine and carbon content is expected for solid state structures formed from **II.1** while the silicon likely arises from contamination introduced during the deposition process. Spectrum 5 shows the spectrum of bare HOPG, which lacks any peaks other than carbon, as expected. Spectrum 7 shows the EDS spectrum from another pillar, which lacks the silicon peak observed in spectrum **II.1**. This indicates the silicon is a surface contaminant rather than a structural part of the vertical pillars. The presence of fluorine in all spectra taken of the pillars on the HOPG suggests that that is an integral component of the pillars, consistent with structures formed from **II.1** 42

II.11. Absorbance and emission spectra of **II.1** and [12]CPP in solution 43

III.1. CNT fragment [12]CPP exhibits a herringbone-like packing in the solid state, while nanohoop **III.1**, a fluorinated CNT fragment, self-assembles into nanotube-like columns. These columns can be fabricated in vertical “forests” on graphite substrates via mild solution casting, taking the form of hexagonal pillars 71

III.2. Columnar packing, arene-perfluoroarene interactions (highlighted in purple), and C−H—F distances (dotted lines, C−F distances shown in parentheses) observed in the crystal packings of nanohoops **III.1** (a-c), **III.2** (d-f), and **III.3** (g-i) 74

III.3. a) Observed emission response of nanohoop **III.2** to increasing quantities of C_{60}. b) Peapod-like crystal packing of the C_{60}@**III.2** complex (top) and views of a single host−guest complex (bottom); c) X-ray crystal structure of the C_{60}@[10]CPP complex in the solid state. Fluorine atoms are colored in green, hydrogens are colored in white, carbons are colored in gray, and C_{60} has been colored purple 76

III.4. Comparison of N_2 uptake isotherms of **III.1** (black), [12]CPP (blue), and **III.3** (gray) collected at 77 K 78

III.5. Set of lateral-like dimers extracted from the crystal structure of nanohoop **III.2** along with their respective interaction energies 80

Figure Page

III.6. a) Calculated interaction energy for the vertical dimer extracted from the crystal structure of nanohoop 2, along with the structures and respective interaction energies for this dimer upon the removal of fluorine atoms (b-e) 82

III.7. Absorbance (black) and emission (blue) spectra for nanohoop **III.2**........ 105

III.8. Absorbance (black) and emission (blue) spectra for nanohoop **III.3**........ 105

III.9. Change in emission intensity fluorinated nanohoop **III.2** with increasing concentration of C_{60}. The initial concentration of **III.2** was 5.00×10^{-7} mol L^{-1}, while the concentration of C_{60} was varied from $0.00 - 2.88 \times 10^{-7}$ mol L^{-1}........ 106

III.10. Correlation of [C_{60}] on the fluorescence intensity of fluorinated nanohoop **III.2** in toluene. The change in fluorescence at 460 nm (obtained from Figure III.9) was fit to eq III.1 to obtain the K_a........ 107

III.11. C—H---F interactions (dotted lines) observed in the crystal packing of C_{60}@**III.2.** C---F distances measure from 3.20-3.81 Å........ 111

III.12. (a-d) Observed solid-state packing of fluorinated nanohoop **III.2S**, with fluorine atoms disordered across six phenylene moieties........ 111

III.13. Molecular structure of nanohoop **III.1**, with ellipsoids drawn at the 50% probability level. Crystals were grown via slow evaporation from $CHCl_3$........ 112

III.14. Molecular structure of nanohoop **III.2**, with ellipsoids drawn at the 50% probability level. Crystals were grown via layering of pentane onto a solution of **III.2** in THF........ 112

III.15. Molecular structure of nanohoop **III.3**, with thermal ellipsoids drawn at the 50% probability level. Crystals were grown via slow evaporation from CH_2Cl_2........ 113

III.16. Molecular structure of C_{60}@**III.2**, with thermal ellipsoids drawn at the 50% probability level. Crystals were grown via vapor diffusion of diethyl ether into a dilute THF/1,2-dichlorobenzene/toluene (1:1:1) solution of fluorinated nanohoop **III.2** and C_{60} (1:1)........ 113

Figure Page

III.17. Molecular structure of **III.2S**, with thermal ellipsoids drawn at the 50% probability level. Fluorine atoms were found to be disordered throughout the structure. Crystals were grown via layering pentane onto a solution of **III.2S** in THF 114

III.18. TGA analysis of nanohoop **III.1**. The sharp mass loss at ~210 °C is attributed to a physical loss of material from the sample pan 114

III.19. N_2 uptake isotherm of nanohoop **III.1** shown at low relative pressures (P/P_0) in semi-log scale 115

III.20. Brunauer-Emmett-Teller (BET) plot of nanohoop **III.1**. Analysis was based on a linear fit (shown in red) to N_2 isotherm data at relative pressures between $10^{-5} – 10^{-1}$ P/P_0........ 116

III.21. Powder X-ray diffraction (PXRD) data for nanohoop **III.1** before (bottom) and after (top) evacuation to 2 μtorr at 125 °C. Calculated PXRD pattern for **III.1** based on the provided crystal structure is shown in red (calculated using Mercury visualization software) 116

III.22. Powder X-ray diffraction (PXRD) data for nanohoop **III.3** before (bottom) and after (top) evacuation to 2 μtorr at 125 °C........ 117

III.23. Offset-tubular dimer extracted from the herringbone-like crystal structure of [10]CPP 117

III.24. Tubular-like dimer extracted from the crystalline structure of nanohoop **III.1**........ 118

III.25. Set of lateral-like dimers extracted from the crystalline structure of nanohoop **III.1**........ 118

IV.1. Examples of linear conjugated organic electronic materials and their respective thin-film charge mobilities (references 8-10, from left to right) 122

IV.2. ORTEP representations (50% probability) of (a) **IV.1**, (b) [10]CPP and observed solid-state packing of (c) **IV.1** and (d) [10]CPP (carbon atoms in gray, hydrogen atoms in white, fluorine atoms in yellow)........ 123

IV.3. (a) Schematic of two-contact devices used; (b) I-V curves of **IV.1** (green) and [10]CPP (red) 124

Figure Page

IV.4. Optical microscope images of thin-films of **IV.1** (left) and [10]CPP, both prepared as described in Chapter **IV.4** 127

IV.5. DFT calculated frontier molecular orbitals (FMO) and their respective energy levels for [10]CPP (left) and **IV.1** (right). The energy level between each FMO is colored in purple 128

IV.6. Minimized structure of **IV.1** 128

IV.7. Reduction curve of **IV.1** 132

IV.8. Oxidation curve of **IV.1** 132

V.1. a) Example of a covalent organic framework synthesized using dynamic covalent bond formation (reference 8); b) Examples of organic cage compounds synthesized using dynamic processes (references 12 and 13) 136

V.2. a) Proposed synthesis of a CPP-based nanotube via a condensation reaction between a hydroxy-functionalized nanohoop and 1,4-benzenediboronic acid; b) Synthesis of a CPP-based cage using proposed nanohoop **V.2** as a synthon 138

V.3. (top) Synthetic scheme to access **V.7**; (bottom) Proton NMR spectrum of **V.7** showing proton assignments (black "X" marks represent excess 4-*tert*-butylphenylboronic acid) 140

V.4. (top) Synthetic scheme to access **V.8**; (bottom) Proton NMR spectrum of **V.8** showing proton assignments (residual toluene is clearly highlighted) 141

LIST OF SCHEMES

Scheme Page

II.1. Synthesis of intermediate **II.2** 43

II.2. Synthesis of intermediate **II.3** 43

III.1. Synthetic routes toward nanohoops **III.2**, **III.3**, and **III.**1 72

III.2. Synthetic route towards intermediate **III.7** 84

III.3. Synthetic route towards nanohoop **III.2S** 84

V.1. Synthetic route used to access nanohoop **V.1** 139

V.2. Synthetic route used to access intermediate **V.4** 142

V.3. Synthetic scheme used to access intermediate **V.5** 143

CHAPTER I

EMERGING APPLICATIONS OF CARBON NANOHOOPS

This chapter is based on a review published in *Nature Reviews Chemistry* in 2019. Writing and editing duties were shared by myself and Professor Ramesh Jasti. The review appears herein as it was originally published with minor alterations.

Chapter **II** is based on work published in the journal *Nano Letters* in 2018. I am the primary author on this work and the overall concept was created by myself and Professor Ramesh Jasti. Dr. Jeff Van Raden developed a major portion of the synthetic route and aided in writing and editing. David Miller carried out the necessary materials characterization and contributed to relevant text and figures within the manuscript. Dr. Lev N. Zakharov provided the X-ray crystallography data described in the manuscript. Professor Benjamín Alemán contributed conceptually and to relevant written discussions within the manuscript.

Chapter **III** is based primarily on work published in the *Journal of Organic Chemistry* in 2020. I am co-first author on this work along with Dr. Jeff M.Van Raden. Dr. Van Raden and I both contributed equally to the design, synthesis, and characterization of the molecules described in the manuscript and shared writing and editing duties along with Professor Ramesh Jasti. Dr. Lev N. Zakharov provided the X-ray crystallography data described in the manuscript. Andrés Pérez-Guardiola, Angel Jose Pérez-Jiménez, and Juan-Carlos Sancho-García carried out the computational work included in the manuscript and provided relevant written discussion. Checkers R. Marshall and Professor Carl K. Brozek acquired and analyzed the N_2 uptake data described in the manuscript as well as providing relevant figures and written discussion. N_2 uptake data for one molecule discussed in this chapter is not included in the above manuscript and instead will be part of an as-of-now unpublished manuscript written by Dr. Tobias A. Schaub. I synthesized the necessary compound and Checkers R. Marshall and Professor Carl K. Brozek acquired and analyzed the N_2 uptake data.

Chapter **IV** is based on unpublished work, the concept of which was designed by myself, Dr. Jeff Van Raden, Dr. Evan Darzi, Professor Mark Lonergan, and Professor Ramesh Jasti. Dr. Jeff Van Raden carried out the synthesis of the fluorinated [10]CPP analog used in these studies and provided all cyclic voltammetry (CV) data and computational results. I fabricated the nanohoop-based organic field-effect transistors (OFETs) used in these studies and measured their conductivities. Professors Mark Lonergan and Ramesh Jasti contributed conceptually and to experimental design in regard to device measurements.

Chapter **V** is based on unpublished work, the concept of which was designed by myself and Professor Ramesh Jasti. I carried out the synthesis and characterization of the compounds described in this chapter.

A cycloparaphenylene can be thought of as the shortest possible cross-section of an armchair carbon nanotube. Although envisioned decades ago, these molecules — also referred to as carbon nanohoops — can be highly strained and, thus, eluded chemical synthesis. However, the past decade has seen the development of methods to access carbon nanohoops of varying size and composition. In contrast to many carbon-rich materials, the nanohoops are atom-precise and structurally tunable because they are prepared by stepwise organic synthesis. Accordingly, a variety of unique size-dependent optoelectronic and host–guest properties have been uncovered. In this Review, we highlight recent research that aims to leverage the unique physical properties of nanohoops in applications and emphasize the connection between structure and properties.

I.1. Introduction.

The pursuit of unusual and synthetically challenging molecular entities often results in unpredictable developments in terms of applications. This is perhaps unsurprising given that unique molecular architectures often give rise to novel chemical properties. Possessing strikingly distorted phenylene moieties and radially-oriented π-systems, the cycloparaphenylenes (CPPs) — often referred to as carbon nanohoops — exemplify how a unique molecular form can afford equally unique functions (Fig. I.1.).[1] Initially envisioned as seeds from which to begin the size-selective growth of carbon nanotubes (CNTs), CPPs have, since their first synthesis in 2008 by Jasti and Bertozzi, quickly established themselves as interesting molecules in their own right. This is in no small part due to the bent cyclic geometries of CPPs exhibiting a wealth of unexpected unique photophysical and electronic properties.[5-10] In parallel with these studies, our synthetic methodologies have advanced to allow access to CPPs on the gram scale[11-13] —

a roughly three-orders-of-magnitude increase over the first synthesis.[1] Likewise, a variety of synthetic strategies have been developed that allow bottom-up functionalization of CPPs to further fine-tune their properties.[14-20] With ready access to tunable CPPs, many chemists have sought to explore their practical utility.

In this Review, we focus primarily on the applications of CPPs that have begun to surface in the literature throughout the last 5 years. These applications include the implementation of CPPs as novel solution- and solid-state fluorophores,[21-24] organic electronic components,[13, 25-26] and synthons for the construction of bulk supramolecular carbon-rich nanomaterials.[27-29] We also describe how these properties are intimately connected to the strained, cyclic nature of the nanohoop structures. The development of CPP syntheses has been covered thoroughly in numerous reviews,[30-34] and we thus choose not to focus on synthetic developments; a brief summary of general synthetic approaches towards CPPs can be found in Figure I.1. Likewise, non-applied synthetic landmarks in the field of nanohoop chemistry will not be covered, although we acknowledge recent advancements in the syntheses of both aromatic belts and interlocked CPP-based structures.[35-37] We speculate here on potential CPP applications, proposing CPPs as potential imaging agents for the study of complex biological phenomena, electronic materials that are tunable by functionalization or guest uptake, and building blocks for self-assembled solid-state materials.

I.2. CPPs as Versatile Fluorophores.

The structures of CPPs are strained and non-planar and afford size-dependent photophysical phenomena.[5-10] Specifically, the energy gap between the highest occupied molecular orbital (HOMO) and the lowest unoccupied molecular orbital (LUMO) of a CPP decreases with decreasing numbers of phenylenes n in the hoop (Fig. I.2a.). This trend is opposite to that observed for linear oligo(para-phenylene) species, the HOMO–LUMO gaps of which decrease with increasing n due to extended conjugation.[38] Although decreasing the number of phenylene moieties in a [*n*]CPP lowers the potential extent of conjugation, it also leads to radial planarity of the π-system (a lowering of torsional angles) due to increased strain (Fig. I.2b, c.). The average dihedral angle θ between phenylenes in odd-numbered CPPs is typically lower than the trend would imply due to greater angular variance.[39-40]

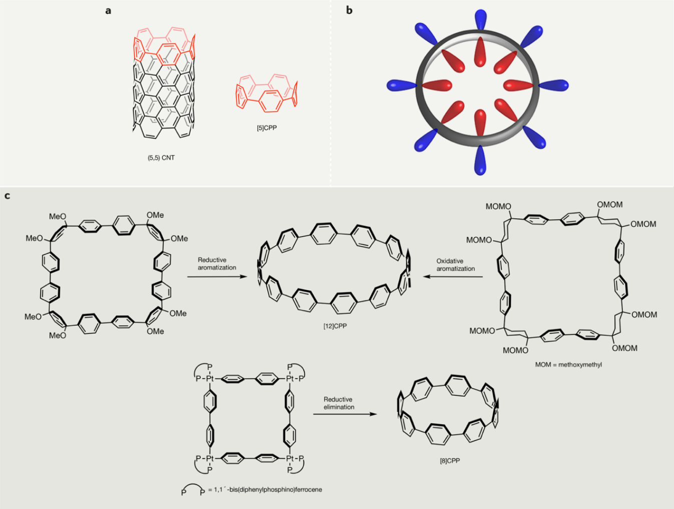
a
(5,5) CNT
[5]CPP
b
c
MeO
MeO
OMe
OMe
MeO
MeO
OMe
OMe
Reductive aromatization
[12]CPP
Oxidative aromatization
MOMO
OMOM
OMOM
MOMO
MOMO
MOMO
OMOM
OMOM
MOM = methoxymethyl
P
P-Pt
Pt-P
Reductive elimination
[8]CPP
= 1,1´-bis(diphenylphosphino)ferrocene

Figure I.1. Cycloparaphenylenes are the smallest cross-sectional fragments of armchair carbon nanotubes. A cycloparaphenylene [*n*]CPP consists of *n para*-phenylene moieties linked together to form a hoop[1]. [5]CPP resembles the armchair edge of the carbon nanotube [5,5]CNT (a). [*n*]CPPs feature a strained structure with a radially oriented π-electron system and an electron-rich central cavity similar to that in carbon nanotubes[139] (b). Three common synthetic routes to cycloparaphenylenes are shown (c). Two routes make use of cyclohexadiene[1] and cyclohexane[99] as "masked" benzene rings. These sp^3-C-containing precursors have the appropriate curvature and are subjected to a strain-building aromatization step to afford the desired cycloparaphenylene ([12]CPP in this case). An alternative route employs a Pt molecular square with 4,4'-biphenylene sides, reductive elimination of which affords a [4*n*]CPP, such as [8]CPP[99].

Despite the different energies of their frontier molecular orbitals, all CPPs share a common absorbance maximum at ~340 nm (Fig. I.2b, c.) assigned to a symmetry-forbidden (on account of centrosymmetry) HOMO→LUMO electronic transition.[6] Because of this, the absorptions observed for CPPs of all sizes are the result of energetically similar transitions, such as HOMO→LUMO+1/LUMO+2 and HOMO−1/HOMO−2→LUMO. In contrast, CPP emission red-shifts with decreasing n (Fig. I.2b, c.), which follows the HOMO–LUMO trend. A theoretical study[41] indicates that CPP emission is dependent on the breaking of orbital symmetry in the excited state, which results from partial planarization of the nanohoop backbone (Fig. I.2d.). Therefore, by simply changing n we can access emission maxima in the range 450–587 nm (in the *n* = 7–12 series) without functionalization of the nanohoop backbone.

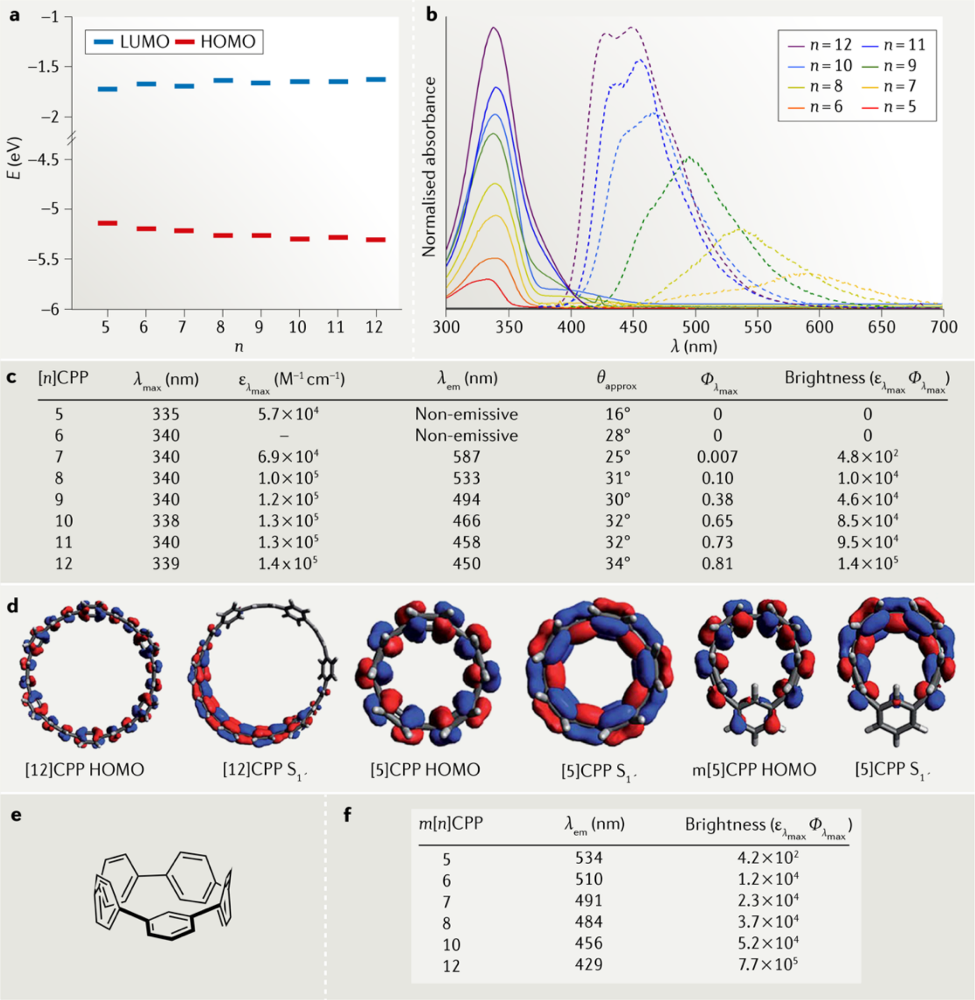

[*n*]CPP	λ_{max} (nm)	$\varepsilon_{\lambda_{max}}$ ($M^{-1} cm^{-1}$)	λ_{em} (nm)	θ_{approx}	$\Phi_{\lambda_{max}}$	Brightness ($\varepsilon_{\lambda_{max}} \Phi_{\lambda_{max}}$)
5	335	5.7×10^4	Non-emissive	16°	0	0
6	340	–	Non-emissive	28°	0	0
7	340	6.9×10^4	587	25°	0.007	4.8×10^2
8	340	1.0×10^5	533	31°	0.10	1.0×10^4
9	340	1.2×10^5	494	30°	0.38	4.6×10^4
10	338	1.3×10^5	466	32°	0.65	8.5×10^4
11	340	1.3×10^5	458	32°	0.73	9.5×10^4
12	339	1.4×10^5	450	34°	0.81	1.4×10^5

m[*n*]CPP	λ_{em} (nm)	Brightness ($\varepsilon_{\lambda_{max}} \Phi_{\lambda_{max}}$)
5	534	4.2×10^2
6	510	1.2×10^4
7	491	2.3×10^4
8	484	3.7×10^4
10	456	5.2×10^4
12	429	7.7×10^5

Figure I.2. The electronic structures of cycloparaphenylenes are size-dependent. (a) The energies of the highest occupied molecular orbital (HOMO) and the lowest unoccupied molecular orbital (LUMO) in a [*n*]CPP (*n* = 5-12) lead to an energy gap $E_g = E_{HOMO} - E_{LUMO}$ that decreases with decreasing *n*. (b) Ultraviolet-visible absorption and emission spectra (solid and dashed traces, respectively) of [5-12]CPP. (c) The photophysical properties of [5-12]CPP and average dihedral angles between phenylenes in optimized geometries[37]. (d) Orbitals in electronic ground and excited states of [12]CPP, [5]CPP, and *m*[5]CPP. (e) Generic structure of *m*[*n*]CPP. (f) Photophysical data for *m*[*n*]CPP (*n* = 5-8, 10, 12).

The strain-induced planarization that gives rise to the unique photophysical properties of CPPs also prevents emission from smaller nanohoops (*n* = 5, 6).[41-43] Thus, the substantial strain present in [5]CPP and [6]CPP (119 kcal mol^{-1} and 97 kcal mol^{-1}, respectively)[42-43] inhibits partial planarization and the breaking of orbital symmetry in their respective excited states,[41] such that fluorescence emission is Laporte-forbidden (Fig. I.2d.). However, the emission window accessible using nanohoop structures can be expanded by breaking molecular symmetry, as can be achieved by introducing a single meta connectivity.[44] For example, a series of [*n*]CPPs (*n* = 5–8, 10, 12) in which a single phenylene is meta substituted (denoted *m*[*n*]CPPs, Fig. I.2e.) exhibits size-dependent emission almost identical in nature to that observed for the all-para-linked CPPs. The incorporation of a meta-linked phenylene allows for excited-state orbital symmetry breaking in each of the studied *m*[*n*]CPP species, with even *m*[5]CPP displaying moderately bright emission ($\varepsilon_{\text{Amax}} \times \Phi_{\text{Amax}} = 4.2 \times 10^2$). Importantly, the brightness of the *m*[*n*]CPPs was found to be comparable to or even greater than that of their respective all-para-linked counterparts (Fig. II.2f),[1, 4, 42-43, 45-47] thus providing a viable alternative strategy for accessing the unique size-dependent emissive properties of CPPs. Additionally, as with CPPs, the *m*[*n*]CPPs all share a common absorbance, here at ~328 nm. As will be discussed below, both [*n*]CPPs and the more recently developed *m*[*n*]CPPs are quickly proving themselves to be effective scaffolds for fluorophore development.

I.3. CPP Rotaxanes as Fluorescent Sensors.

Interlocked architectures such as rotaxanes and catenanes[48] have garnered a great deal of attention, not least serving as the basis of the 2016 Nobel Prize in Chemistry[49]. A variety of applications of these systems are beginning to take shape,[50-54] notable among which are sensors comprising interlocked systems in which the thread component exhibits a photophysical response to a particular analyte.[51-52] With CPPs being rare examples of highly emissive macrocycles, we were curious to investigate whether one could invert this paradigm and have the macrocycle serve as the responsive component of a rotaxane sensor. For example, an interlocked *m*[*n*]CPP scaffold, where the meta-substitution takes the form of a 2,6-substituted pyridine, has been incorporated into small-molecule sensing platforms (Fig. I.3a,b.).21 A key design feature of pyridyl-m[n]CPPs is the position of the N atom — directed towards the inside of the nanohoop. This atom can bind a metal such as Cu^I, which can mediate an azide–alkyne cycloaddition or a Cadiot-Chodkiewicz alkyne cross-coupling within the nanohoop cavity. This approach, in which the nanohoops act as ligands to promote coordinate coupling reactions within the macrocyclic pore, is often referred to as an active template strategy[54-56]. The fluorescence from **I.1**, a pyridyl-*m*[6]CPP-based rotaxane with dimethylisophthalate stoppers (Fig. I.3a.), could be almost entirely quenched by adding equimolar $[Pd(MeCN)_4](BF_4)$. This effect, presumably due to coordination of Pd^{II} to the triazole in the thread and the pyridyl in the nanohoop, is reversible — demetallating the complex with one molar equivalent of ethylenediaminetetraacetate resulted in a 30-fold increase in emission intensity. Hydrolysis of the ester groups in rotaxane **I.1** affords the H_2O-soluble carboxylic acid derivative **I.1S** (Fig. I.3a.), which exhibited the same turn-on sensor behavior with a 10-fold increase in fluorescence upon demetallation. These responsive nanohoop rotaxanes inspired the design of unsymmetric rotaxanes such as **I.2**, which bears a pyridyl-*m*[6]CPP around a butadiyne thread with bulky Si^iPr_3 and 3,5-dinitrobenzene stopper groups on either end (Fig. I.3b.). Emission from the nanohoop is completely quenched when it exists as part of the rotaxane, and density functional theory calculations suggest this is a result of charge transfer from the nanohoop to the dinitrobenzene stopper group. Adding $^nBu_4NF$ cleaves off the Si^iPr_3 stopper, leading to dethreading and a striking 123-fold increase in fluorescence intensity (Fig. I.3c,d.). Nanohoop-containing interlocked structures are thus predicted to afford tunable platforms from which to develop small molecule sensors. Additionally, one can imagine that the Si^iPr_3 group of nanohoop rotaxane **I.2** could be replaced with a variety of cleavable functional groups, allowing this scaffold to be engineered to sense a myriad of small molecules beyond F^-. Indeed, pyridyl-*m*[6]CPP is relatively small, such that its dethreading can be prevented by a wide variety of stoppers, even relatively small groups.

I.4. CPPs as Biological Fluorophores.

Imaging techniques that rely on small-molecule fluorescent dyes are becoming increasingly important tools for studying biological phenomena at the cellular level.[57-59] Despite this, there is a surprising dearth of structural diversity among biologically-relevant fluorophores.[60-63] The inherent brightness and tunable emission of CPPs makes them excellent potential scaffolds for new biological probes. Additionally, the common absorption shared by all CPPs has been predicted to enable multiplexed imaging,[64] whereby multiple CPP fluorophores could, in principle, be excited simultaneously by a single laser to more closely study complex biological phenomena. Inspired by this, we reported the synthesis of a bis(sulfonate) [8]CPP analog[22] **I.3** (Fig. I.3e.) which, unlike its parent [8]CPP, is soluble in aqueous media and exhibits cellular uptake. The photophysical properties of **I.3** in both Me2SO and phosphate-buffered saline (PBS) were found to be almost identical to those of [8]CPP (Fig. I.3f,g.). Compared to commercially available fluorescein,[65] **I.3** exhibits moderately lower brightness, albeit with a substantially larger effective Stokes shift (41 nm for fluorescein versus 180 nm for **I.3**). Additionally, the emission intensity from **I.3** is unaffected by pH over a wide range (pH 3–11), whereas that from fluorescein drops off dramatically when the probe exists in acidic solution.

Nanohoop **I.3**, and most likely a range of nanohoop derivatives, are biologically compatible. Indeed, treating live HeLa cells with up to 25 μM of **I.3** revealed the latter not to be cytotoxic according to the WST-8 formazan reduction and CCK-8 cell assay65 (Fig. I.3h.). To test the utility of **I.3** as a biological probe, HeLa cells were incubated with **I.3** (10 μM in fetal-bovine-serum-free free Dulbecco's Modified Eagle Medium with 0.5% Me_2SO) and the nuclear stain NucRed 647 for 1 h. After washing the cells, they exhibited clear permeation, with moderate colocalization in the cytosol and lower colocalization in the mitochondria and endoplasmic reticulum but no colocalization[66] with the nuclear dye (Fig. I.3i–l.). Building on this, an azide-functionalized [8]CPP was synthesized and 'clicked' to an alkyne-functionalized folic acid group, such groups having been proven to be effective in targeting cancer cells.[67-68] This folic-acid-functionalized [8]CPP is taken up in HeLa cells, suggesting that azide-functionalized nanohoops could provide a versatile scaffold for targeted cell imaging. The ultimate realization of such work would be the incorporation of azide groups into CPPs of various sizes, where one could 'click' distinct targeting groups to each one. This could potentially allow for simultaneous imaging of various targeted cellular structures by multiplexed imaging.

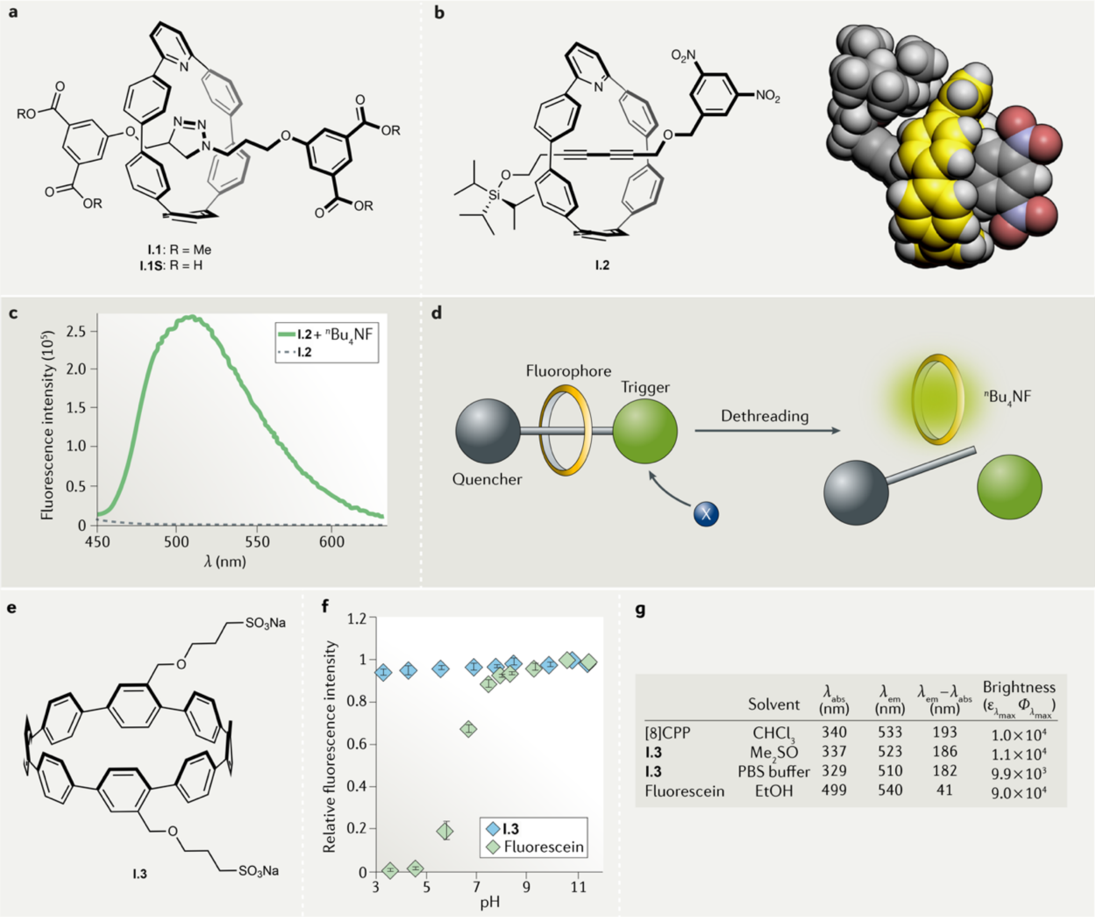
a
I.1: R = Me
I.1S: R = H
b
I.2
c
Fluorescence intensity (10⁵)
λ (nm)
I.2 + ⁿBu₄NF
I.2
d
Fluorophore
Trigger
Quencher
Dethreading
ⁿBu₄NF
X
e
I.3
f
Relative fluorescence intensity
pH
I.3
Fluorescein
g

	Solvent	λ_{abs} (nm)	λ_{em} (nm)	$\lambda_{em} - \lambda_{abs}$ (nm)	Brightness ($\varepsilon_{\lambda_{max}} \Phi_{\lambda_{max}}$)
[8]CPP	$CHCl_3$	340	533	193	1.0×10^4
I.3	Me_2SO	337	523	186	1.1×10^4
I.3	PBS buffer	329	510	182	9.9×10^3
Fluorescein	EtOH	499	540	41	9.0×10^4

Figure I.3. Applications of cycloparaphenylenes in biological imaging. (a) Pyridyl-*m*[6]CPP rings can bind a catalytic Cu^I ion and serve as the active template in the synthesis of rotaxanes **I.1** and **I.1S**, which bear a triazole-containing thread. (b) The pyridyl-*m*[6]CPP ring, in conjunction with Cu^I, can also mediate alkyne-alkyne coupling to give diyne rotaxane **I.2**, the X-ray crystal structure of which is also presented. (c) Fluorescence turn-on of **I.2** on treatment with ^{n}Bu$_4$NF. (d) Desilylation of **I.2** with F^- leads to dethreading and liberation of the emissive pyridyl-*m*[6]CPP ring. (e). Structure of a bis(sulfonate) derivative of [8]CPP (**I.3**). (f) Fluorescence intensity from **I.3** is pH-independent, while the fluorescence intensity of fluorescein is pH-dependent. (g) Photophysical data of **I.3**, [8]CPP, and fluorescein.

I.5. CPPs as Solid-State Emitters.

Organic small-molecule fluorophores are of great interest as solid-state emitters due to their synthetic tunability, solution processability, and potential to be implemented into flexible devices.[69-71] However, the luminescence of many organic fluorophores is severely quenched on aggregation in the solid-state.[70] In contrast, the bright emission of CPPs in solution is retained in the solid state[23-24, 29] and, as discussed above, enables highly tunable emission. Additionally, the central pores of CPPs — not a feature found in traditional fluorophore scaffolds — offer a handle by which to tune emission[23]. A prime example of the exploitation of these properties in a functional capacity is [10]CPP·2I_2,[23] an I_2 inclusion complex that is responsive to electrical stimuli[72-75] (Fig. I.4a.). Simply evaporating solvent from a solution of [10]CPP and I_2 affords crystalline [10]CPP·2I_2, which assumes a herringbone-like packing arrangement of [10]CPP molecules, each of which hosts two I_2 molecules. Application of a 500 mV stimulus to solid [10]CPP·2I_2 resulted not only in decreased electrical resistivity but also a broadened white-light emission profile that contrasts the green–blue emission prior to the stimulus (Fig. I.4b.). The underlying mechanisms of these phenomena are not yet understood but are most likely the result of structural changes in I_2 guest molecules — a effect that has been reported in numerous studies.[76-78] In support of this, the formation of anionic iodine chains within the nanohoop pores after the stimulus was identified using Raman spectroscopy and X-ray absorption near-edge spectroscopy (XANES). Raman spectra feature a stretching mode for I_2 (Fig. I.4c.) that is after electrical shifted from 207 cm^{-1} to 205 cm^{-1} upon stimulating, and the new bands at 112 cm^{-1} and 165 cm^{-1} have been ascribed to polyiodide chains.[79] Likewise, XANES data for [10]CPP·2I_2 (Fig. I.4d.) suggest that the antibonding orbitals in I_2 become populated after electrical stimulation, as evidenced by a decrease in a peak at 5187 eV (representing the transition from the 2s to 5p antibonding orbital of I) and the emergence of a peak at 5194 eV that has been previously observed for polyidodide chains.[80] A small change in a C–C breathing mode of [10]CPP from 1587 cm^{-1} to 1589 cm^{-1} is also suggested as evidence of a small amount of CPP being oxidized and thus balancing the negative charge of the polyiodide chains. Regardless of the mechanism behind the aforementioned emission broadening, achieving white-light emission is typically difficult,[81-82] and doing so with a single-component system is relatively rare.[81-82] Perhaps more important than the results themselves, however, is the proof-of-concept that the uptake of guest molecules into a nanohoop can dramatically affect the system's photophysics. As we describe below, it turns out to be relatively common to observe fluorescence quenching in CPPs upon guest uptake.[11, 83] This study shows that CPPs can be incorporated into complex host–guest systems with photophysical properties that can be tuned in a reversible, non-covalent fashion by the stimulus-induced response of a guest.

A more recent report describes the incorporation of CPPs into luminescent solar concentrator (LSC) devices,[24] which are of interest due to their ability to efficiently convert optical power to electrical power.[84-88] CPPs are considered attractive for this purpose due to their large effective Stokes shifts (193 nm for [8]CPP and 128 nm for [10]CPP), which render photon reabsorption highly unlikely and thus improve LSC device efficiencies. Photoluminescence (PL) spectra were acquired for rectangular polymethylmethacrylate (PMMA) slabs doped with either [8]CPP or [10]CPP, revealing unique behaviour of the nanohoop fluorophores within this device geometry. The CPPs did indeed behave as effective LSC fluorophores, with solid-state emission very obviously concentrating at the edges of the PMMA slabs upon UV irradiation (365 nm) (Fig. I.4e,f. and insets). Additionally, photon reabsorption was found to be very minor (~10% loss) over a wide range of optical distances (0–18 cm, the length between the point of UV laser excitation and the point of emission detection) for both [8]CPP (Fig. I.4e.) and [10]CPP (Fig. I.4f.). In terms of efficiency, the nanohoop-based LSCs far outperform devices constructed using Lumogen R 30589 (Fig. I.4e,f.), a commercial perylene diimide marketed for the purposes of concentrating emitted light in devices such as LSCs. Along with the promising LSC performance, this study revealed important fundamental details regarding the solid-state emission of CPPs. The first and arguably most important detail is that nanohoop photophysics remain almost completely unchanged when incorporated into a solid-state matrix such as PMMA, such that future CPP-based optical devices can be predictably designed. Additionally, embedding CPPs within a solid slab of PMMA was found to moderately increase PL decay time, implying that immobilizing CPPs in solid media could provide a viable means to improve the efficiency of their solid-state PL devices.

I.6. CPPs in Electronic Applications.

Recent studies indicated that fully-conjugated macrocyclic systems can outperform their linear analogs as active components in organic electronics.[90]

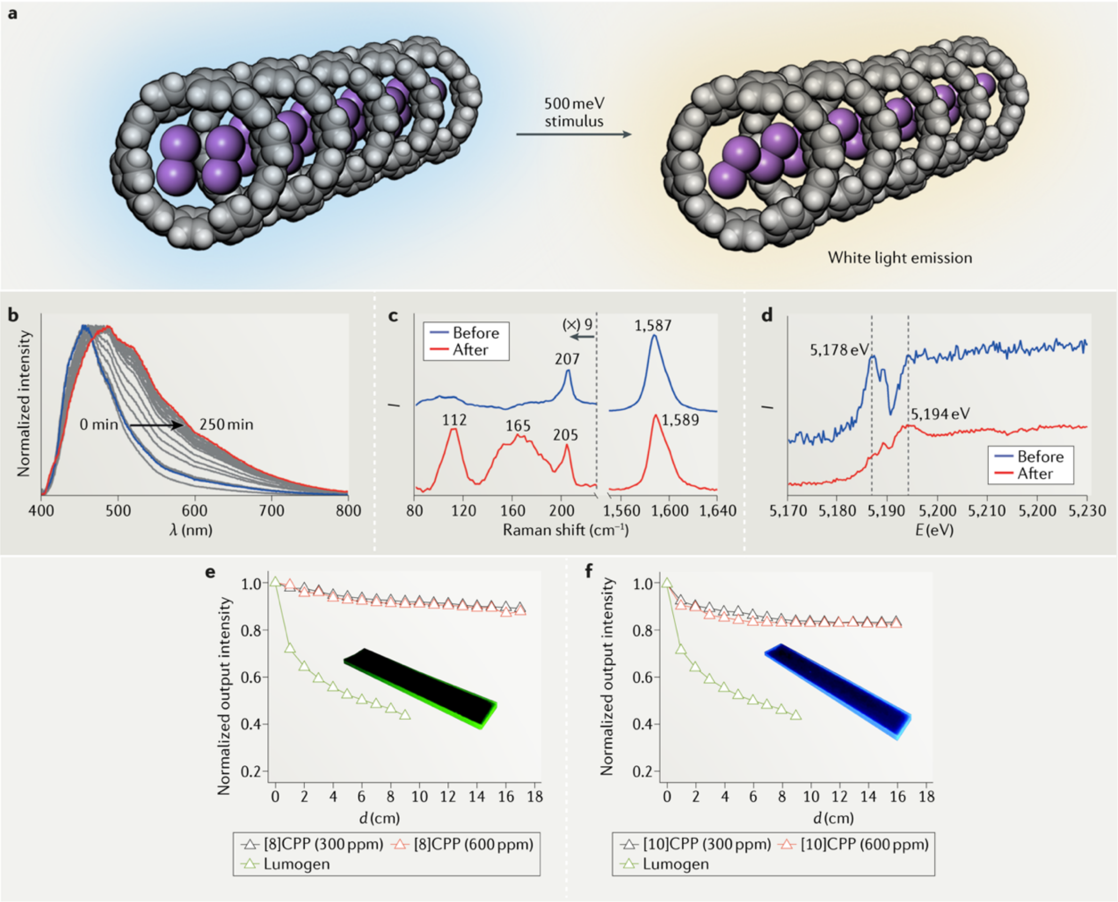

Figure I.4. Electrical and optical stimulation of cycloparaphenylenes. (a) Electrical stimulation of [10]CPP•2I$_2$ affords polyiodide chains and a change from blue to white emission. (b) Emission broadening of [10]CPP•2I$_2$ as the electrical stimulus is maintained over 250 min. (c) Raman spectra of [10]CPP•2I$_2$ before (blue) and after (red) the stimulus (d) X-ray absorption near-edge spectroscopy data of [10]CPP•2I$_2$ before (blue) and after (red) stimulus. (e) Emission from luminescent solar concentrators containing [8]CPP at two concentrations, as well as the standard dye Lumogen, as a function of optical distance *d*. (f) The same experiment as in part **e** carried out using [10]CPP.

This phenomenon is largely attributed to the radial geometries exhibited by certain conjugated macrocycles, which, like the 3D shape of fullerenes, allows for more intermolecular contacts than a comparable linear system.[90] Thus, the radially oriented π-systems of CPPs are expected to make them a potentially attractive scaffold for small-molecule-based electronics. Additionally, as discussed above, nanohoops offer an inherently tunable electronic scaffold in that their HOMO–LUMO gaps decrease with decreasing n (Fig. I.2a.).[5-10] Furthermore, numerous reports have established that the frontier molecular orbital energies of CPPs can be further tuned by functionalization reactions, such as the protonation or alkylation of pyridine-containing nanohoops, which afford charged donor–acceptor systems.[91-93] Although incorporating either one or two pyridine moieties into the [8]CPP backbone has little impact on frontier molecular orbital levels, methylating these systems to afford the analogous mono- or dicationic *N*-methylpyridinium species results in a striking decrease in HOMO–LUMO gaps (Fig. I.5a.).[93] Approaches such as fluorination[20] and the inclusion of a tetracyanoanthraquinodimethane (TCAQ) moiety into the nanohoop backbone[94] have also proven successful for tuning the electronic structures of CPP. In this way, CPPs are fascinating frameworks with predictably tunable frontier molecular orbitals, a highly sought-after property in the field of organic electronics.

Although experiments interrogating the electronic capabilities of CPPs have been limited, interest in nanohoop-based electronics has been heightened by a number of theoretical reports probing their potential utility.[95-98] For example, the charge mobilities μ of crystalline CPP assemblies can be estimated (Fig. I.5b.)[99] using kinetic Monte Carlo simulations on solid-state assemblies of [5–12]CPP (extracted from their respective crystal structures).[3-4, 11, 42, 100-103] While the smaller nanohoops (n = 5–9) are predicted to exhibit low-to-moderate mobilities, [10–12]CPP exhibit mobilities >1 and thus could offer formidable performance in organic semiconductors (Fig. I.5c.). Additionally, the theoretical charge transport properties of both [5]CPP and [10]CPP can be compared to those of C_{60}[104] in an effort to gauge where the bulk electronic properties of CPPs lie with respect to other curved carbon-rich systems (Fig. I.5d.). The curved π–π contacts in all three systems are comparable, suggesting that they might have similar charge transport capabilities. The calculations indicate that energetic disorder σ and reorganization energy λ dominate the mobilities. For [5]CPP, both energetic disorder ($\sigma = 66$ meV) and reorganization energy ($\lambda = 261$ meV) were predicted to be substantially higher than those of C_{60} ($\sigma = 4$ meV, $\lambda = 135$ meV), providing theoretical grounds for the two-orders-of-magnitude difference in mobility between [5]CPP ($\mu = 0.05$ cm^2 V^{-1} s^{-1}) and C_{60} ($\mu = 3.1$ cm^2 V^{-1} s^{-1}). Although the calculated reorganization energy of [10]CPP ($\lambda = 98$ meV) is markedly lower than that of C_{60}, its higher energetic disorder (σ = 66 meV) allows us to rationalize its moderately low charge mobility (μ = 0.83 $cm^2 V^{-1} s^{-1}$). While experimental verification is still necessary, these results serve as excellent theoretical groundwork from which CPP-based electronic systems can be designed.

Numerous reports describe the redox properties of CPPs, which appear to be good electron acceptors. We have reported the isolation of $[8]CPP^{4-}$,[105] $[6]CPP^{-}$, and $[6]CPP^{2-}$ [106] as salts of ether-ligated Na^+ or K^+. These reduced nanohoop structures exhibit enhanced quinoidal character, which is evidenced by a shortening of the C–C bonds between phenylene moieties, and, in the case of $[8]CPP^{4-}$, considerable structural perturbations resulting in an oval-like geometry. It should also be noted that both the tri- and tetraanions of [6]CPP were detected using UV–visible spectroscopy but have so far eluded isolation.[106] CPPs can also be readily oxidized,[107-111] with the mono- and dications of [*n*]CPP (n = 5, 6, 8, 10, 12) all being accessible by oxidizing the neutral species with $[NO]SbF_6$ or SbF_5.[110] A wealth of fundamental information regarding these oxidized states has been reported, including the full charge delocalization in both $[n]CPP^{\bullet+}$ and $[n]CPP^{2+}$ species and even the emergence of biradical character in $[10]CPP^{2+}$ and $[12]CPP^{2+}$.[110] The weak near-infrared emission from $[6–9]CPP^{2+}$ implies a drastic alteration in electronic structure upon oxidation,[111] which has been attributed to in-plane aromaticity relevant to the oxidized CPP structures.[109, 111] The strategy of altering CPP properties by reduction or oxidation is no doubt a fascinating prospect worthy of lengthier discussion, but the studies described above are also vital in furthering our understanding of nanohoops in the context of organic electronics. The ability of CPPs to readily accept or donate electrons bodes well for their use as potential bulk charge-transport materials. Additionally, the fundamental characterization of oxidized and reduced CPP structures that has been carried out thus far provides us with an approximate picture of how CPPs will behave on the molecular level when incorporated into electronics, allowing for better practical design of future CPP-based devices.

Despite numerous computational studies on the electronic applications of CPPs, only one experimental report describing properties of a CPP-based device exists. This is possibly a result of both the general difficulty in preparing these materials and the, until recently, relatively small number of researchers working in this area. A 2018 report described a streamlined synthesis of [10]CPP that enables access to a variety of tetraalkoxy[10]CPP derivatives.[13] Although the addition of alkoxy substituents to the [10]CPP backbone perturbed photophysics/electronics only to a small extent, the new [10]CPP derivatives exhibit substantially improved solubility in $CHCl_3$, making them amenable to solution-processing techniques,[112] such as spin-casting, for the preparation of thin films. Of the [10]CPP derivatives synthesized, only tetrabutoxy[10]CPP (**I.4**, Fig. I.5e.) could be implemented into a vertical device architecture (Fig. I.5f.) that can allow for the space charge limited current (SCLC) to be measured.[113] Analysis of the current–voltage behavior of the device revealed an electron mobility of 4.5×10^{-6} cm^2 V^{-1} s^{-1} (Fig. I.5g.), which, while a relatively low value, provides a baseline for future studies of CPP electronics. The HOMO and LUMO energy levels of [10]CPP and **I.4** are comparable, so the massive six-orders-of-magnitude discrepancy between the observed mobility for **I.4** and the theoretical mobility for the parent compound [10]CPP is instead rationalized in terms of differences in bulk morphology between the two systems. The theoretical study relied on the experimental X-ray crystal structure of [10]CPP, and **I.4** presumably assumes a less-ordered solid-state structure on account of the conformationally flexible butoxy groups[114] (further characterization of these thin films would be required to confirm this). Single-crystal device measurements[115] on the [*n*]CPP (n = 5–12) series would therefore be intriguing, because such measurements could be directly compared to established theoretical work to produce a more complete picture of the fundamental bulk electronic properties of CPPs.

I.7. Fullerene@CPP Systems.

Fullerenes are ubiquitous in organic electronics because their anomalously low LUMO levels mean that their anions are relatively stable. This useful n-type behaviour is complemented by their ability to be readily incorporated into device architectures.[116-117] However, tuning fullerene properties by functionalization is a non-trivial task. As a result, supramolecular approaches to altering fullerene behavior are attractive methods to prepare novel fullerene-based systems.[118] A particularly notable example of this is the linear encapsulation of C_{60} by CNTs to give ‘CNT peapods’,[119-120] in which there is enhanced electronic communication between the fullerene guest molecules.[121]

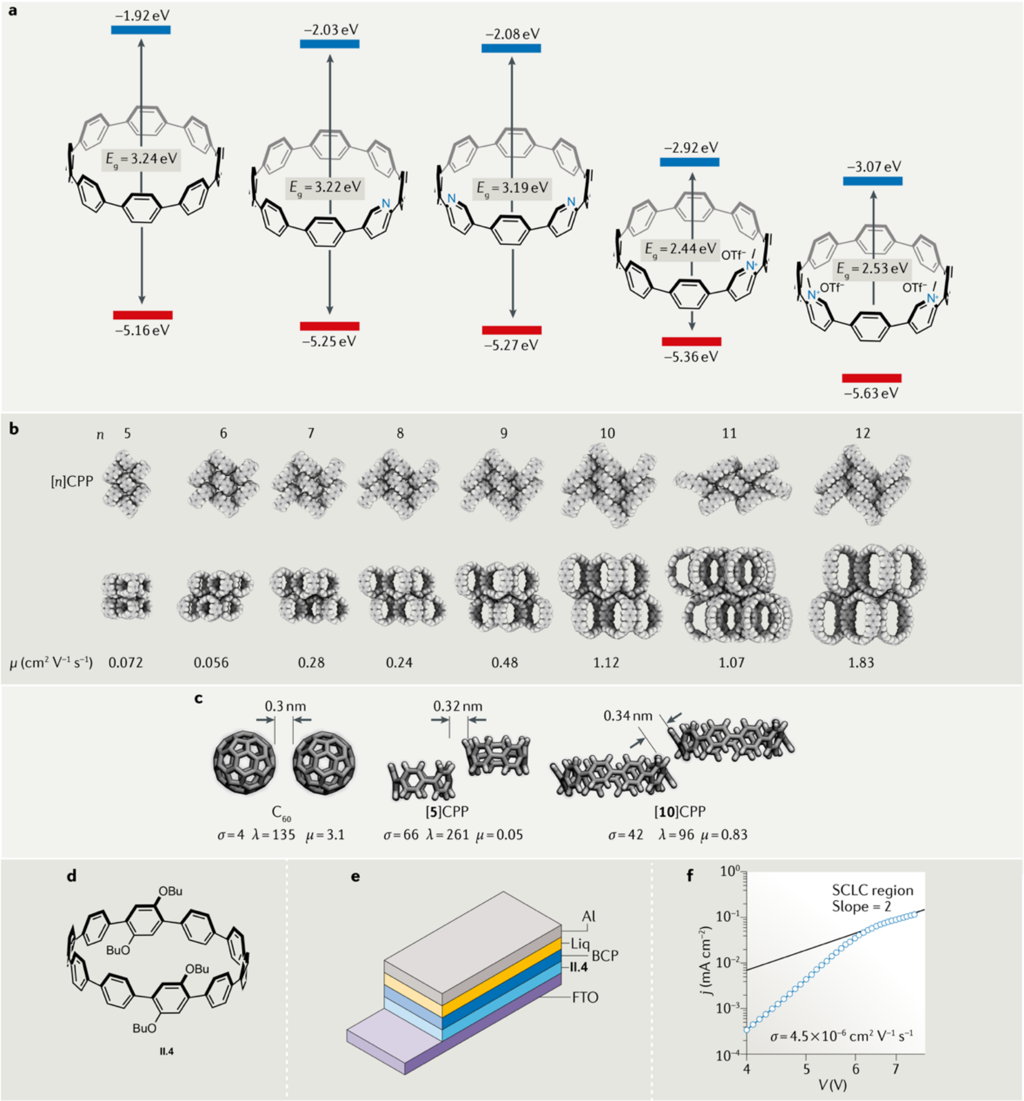
a
−1.92 eV
E_g = 3.24 eV
−5.16 eV
−2.03 eV
E_g = 3.22 eV
N
−5.25 eV
−2.08 eV
E_g = 3.19 eV
N
N
−5.27 eV
−2.92 eV
E_g = 2.44 eV
OTf⁻
N⁺
−5.36 eV
−3.07 eV
E_g = 2.53 eV
OTf⁻
OTf⁻
N⁺
N⁺
−5.63 eV
b
n 5 6 7 8 9 10 11 12
[n]CPP
μ (cm² V⁻¹ s⁻¹) 0.072 0.056 0.28 0.24 0.48 1.12 1.07 1.83
c
0.3 nm
0.32 nm
0.34 nm
C60
σ = 4 λ = 135 μ = 3.1
[5]CPP
σ = 66 λ = 261 μ = 0.05
[10]CPP
σ = 42 λ = 96 μ = 0.83
d
OBu
BuO
OBu
BuO
II.4
e
Al
Liq
BCP
II.4
FTO
f
SCLC region
Slope = 2
10⁰
10⁻¹
10⁻²
10⁻³
10⁻⁴
j (mA cm⁻²)
σ = 4.5×10⁻⁶ cm² V⁻¹ s⁻¹
4
5
6
7
V (V)

Figure I.5. Electronic properties of cycloparaphenylenes. (a) Highest occupied molecular orbital (HOMO) and lowest unoccupied molecular orbital (LUMO) energies and energy gaps $E_g = E_{HOMO} - E_{LUMO}$ for cycloparaphenylenes (from left to right) [8]CPP, aza[8]CPP, 1,15 diaza[8]CPP, *N*-methylaza[8]CPP triflate and *N*,*N*-dimethyl-1,15-diaza[8]CPP ditriflate. (b) X-ray crystal structures of and calculated charge mobilities in [n]CPP (n = 5–12). (c) Structures of dimers of C_{60}, [5]CPP, and [10]CPP, along with intermolecular distances, calculated energetic disorders σ, reorganization energies λ and mobilities μ. (d) Chemical structure of tetrabutoxy-functionalized [10]CPP **I.4**. (e) The generic device architecture used for space-charge-limited current (SCLC). measurements. f | Acquiring SCLC data for devices constructed using **I.4** enables one to calculate the mobility.

Similarly, the linear encapsulation of C_{60} within $ExBox_2^{4+}$ (an extended-bipyridinium-containing cyclophane) affords $C_{60} \subset ExBox_2^{4+}$, which has the desirable electrical conductivity of C_{60} without the air- and moisture-sensitivity of bulk C_{60} anions.[122] The CNT-like inner pores of CPPs offer a unique electron-rich environment and their ready encapsulation of fullerenes[11, 83] making CPPs an ideal platform to tune fullerene behavior. The first evidence of a fullerene@CPP system came in 2012 with the reported of a C_{60}@[10]CPP complex,[83] which is stable on account of the remarkably high binding constant (2.79×10^6 M^{-1}). Shortly after this, we reported the first crystal structure of C_{60}@[10]CPP, which reflects the beautiful π–π complementarity of the two components.[11] The formation of C_{60}@[10]CPP is accompanied by a dramatic quenching of [10]CPP emission, suggesting photophysical and electronic consequences of binding. In 2013, C_{70} was shown to be captured by both [10]CPP and [11]CPP, expanding the scope of fullerene@CPP host–guest chemistry.[123] Furthermore, inspired by the unique electronic and magnetic properties of metallofullerenes,[124-127] came syntheses of (La@C_{82})@[11]CPP[128] and (Li^+@C_{60})@[10]CPP,[129] respectively. Interestingly, both systems exhibit varying degrees of charge-transfer behaviour, a property not observed for the analogous all-hydrocarbon fullerene@CPP complexes. Although outside of the scope of this Review, we note that fullerenes exhibit unique frictionless rotation within nanohoop pores,[130-132] and these nanoscale ‘bearings’ might one day be used as components of nanoscale machinery.

The propensity of fullerenes to accept electrons has made them popular for implementation into small-molecule charge-transfer systems. Among the most studied of these are fullerene–porphyrin dyads, in which an excited porphyrin moiety can transfer an electron to an appended fullerene.[133-135] The syntheses of these systems are typically non-trivial as they require a covalent linkage between the porphyrin and fullerene components. Instead, a clever use of CPP@fullerene host–guest chemistry has afforded porphyrin-functionalized [10]CPP (**I.5**, Fig. I.6a.), which, upon binding of C_{60} within the appended [10]CPP, allowed for through–space charge transfer between the porphyrin and fullerene without the need for fullerene functionalization.[25] Transient absorption spectra of C_{60}@**I.5** have features at ~670 nm and 1090 nm (Fig. I.6b,c.) assigned to the singly-oxidized porphyrin[136] and singly-reduced C_{60},[137] respectively, that are part of a metastable charge-separated state C60$^{\bullet-}$@**I.5**$^{\bullet+}$ that has a lifetime of 4.3 ns. This contrasts the behavior of uncomplexed **I.5**, in which the porphyrin excited state eventually undergoes intersystem crossing to afford an excited triplet state. Charge-separation has also been observed for several other fullerene derivatives, which exhibit comparable lifetimes when irradiated. The study also explored the use of a fullerene dimer $(C_{60})_2$ in this system. It was found that, by varying stoichiometry and concentration, either a 1:1 complex $(C_{60})_2$@**I.5** or a 2:1 complex **I.5**@$(C_{60})_2$@**I.5** could be formed (Fig. I.6d.). For the 1:1 complex, the formation of two distinct fullerene monoanions was observed, one with a lifetime of ~2.5 ns and another with a greatly extended lifetime of ~13.4 ns (Fig. I.6d.). The longer-lived anion is thought to be have the negative charge on the non-complexed fullerene, which is situated farther away from the porphyrin moiety of **I.5**. Particularly surprising was the discovery of a ~541 ns lifetime for the charge-separated state of the 2:1 complex **I.5**@$(C_{60})_2$@**I.5**, which was attributed to charge delocalization in the system (Fig. I.6d.). Overall, this study suggests that altering the relative spatial arrangement of donor and acceptor in this [10]CPP-based supramolecular system, perhaps by lengthening of the phenylene linker of **I.5**, might allow for unprecedented control over charge-separated state lifetimes in fullerene–porphyrin charge-transfer systems.

One of the more popular uses of fullerenes is as the n-type component (electron acceptor) in photovoltaic systems.[116] Thus, a CPP derivative with appropriately tuned frontier molecular orbital levels could be used as an electron donor component in conjunction with a fullerene to afford a unique supramolecular photovoltaic system. Despite this prospect, electronic applications of fullerene@CPP systems have been relatively unexplored from a practical viewpoint. An exception to this is a very recent report describing the first implementation of fullerene@CPP complexes into functional device architectures.[26] Two new [10]CPP derivatives were prepared: one containing a tribenzo[fj,ij,rst]pentaphene (TBP) group (**I.6**, Fig. I.6e.) and another with a hexa-peri-hexabenzocoronene (HBC) moiety embedded in the nanohoop backbone (**I.7**, Fig. I.6e.). The LUMO energies of both **I.6** and **I.7** are lower than that of the parent [10]CPP, suggesting that C_{60} may engage in faster electron transfer when complexed to **I.6** or **I.7** than if complexed to [10]CPP (Fig. I.6e.). The binding constants of C_{60} to nanohoops **I.6** and **I.7** ($K_a = 3.34 \times 10^6$ L^{-1} mol for **I.6**; 2.33×10^7 L^{-1} mol for **I.7**) are higher than that of C_{60} to [10]CPP due to the smaller π-conjugated surface area of the latter (Fig. I.6f.). One can probe the electronic properties of these host–guest systems by spin-coating them as films onto fluorine-doped tin oxide (FTO) working electrodes. These electrodes can then be irradiated and it is possible to measure photocurrent that may arise from excited state charge-transfer from the nanohoop to the fullerene. Notably, photocurrent was observed for C_{60}@**I.6**, C_{60}@**I.7**, and C_{60}@[10]CPP as well as the free nanohoops **I.6** and **I.7**, with no photocurrent observed for free [10]CPP (Fig. I.6g.). Of these systems, **I.7** was found to have the greatest photocurrent response, presumably due to the lower LUMO energy of **I.7** and thus greater ease with which it can transfer electrons to the LUMO of C_{60}. Further analysis of the current–voltage response of C_{60}@**I.7** revealed a 1000-fold increase in current upon photoirradiation (Fig. I.6h.). Similar to fullerene@**I.5** systems,[25] time-resolved transient absorption spectroscopy revealed that both C_{60}@**I.6** and C_{60}@**I.7** form metastable charge-separated states upon excitation and thus represent supramolecular donor–acceptor charge-transfer systems. Overall, the superior performance of the C_{60}@**I.7** complex in the generation of photocurrent implies that nanohoops can indeed be precisely tuned to afford ideal hosts for the construction of high-performance photovoltaics.

I.8. CPPs as Building Blocks for Carbon Nanomaterials.

CPPs were originally envisioned as potential templates for the growth of homochiral CNTs, a prospect that has yet to be realized, despite promising preliminary results.[138] As an alternative to using CPPs as precursors to carbon nanomaterials, research is rapidly emerging regarding the use of bulk CPP systems as novel materials in their own right. One of the first such studies reported that [12]CPP behaves as a soft, porous, molecular solid.[24] The pores of bulk [12]CPP are inaccessible to N_2 and CO_2 gas at 77 K and 87 K, respectively, presumably due to the material's dense, herringbone-like packing[99] (Fig. I.7a.). Although no N_2 was adsorbed at 195 K, this higher temperature allowed for CO_2 uptake corresponding to a Brunauer–Emmett–Teller surface area of 503 m^2 g^{-1} — a relatively high value for bulk assemblies of intrinsically porous macrocycles.[140,141]

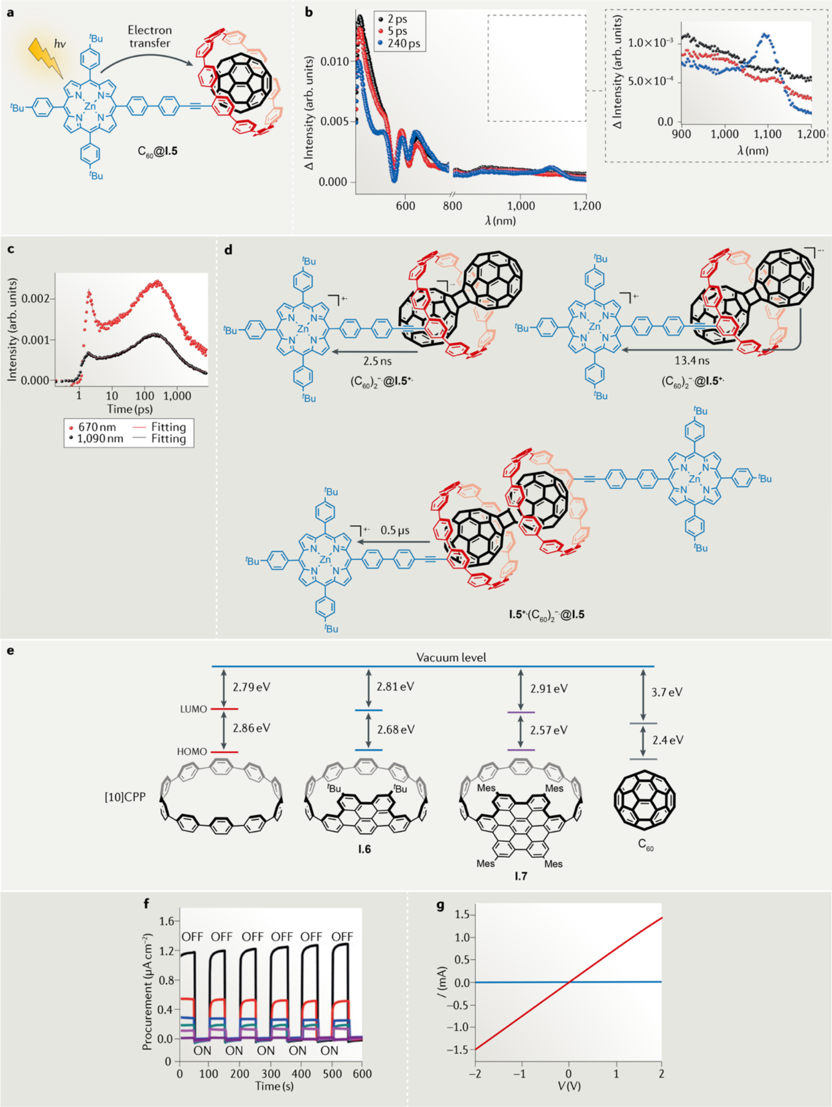

Figure I.6. Electron transfer involving cycloparaphenylenes. (a) The porphyrin-appended [10]CPP host **I.5** can bind C$_{60}$ to form a charge-transfer complex. (b) Differential absorption spectra of C$_{60}$@**I.5** in PhCN acquired in pump-probe experiments (430 nm, 500 nJ). (c) Time-absorption profiles and fits of the absorption fingerprints of the C$_{60}$ radical cation at 670 nm (red). (d) Lifetimes of charge-separated states of (C$_{60}$)$_2$@**I.5** and **I.5**@(C$_{60}$)$_2$@**I.5**. (e) Highest occupied molecular orbital (HOMO) and lowest unoccupied molecular orbital (LUMO) energies (relative to vacuum) of [10]CPP, nanohoop **I.6**, nanohoop **I.7**, and C$_{60}$. (f) Photocurrent response of spin-coated films of C$_{60}$@**I.7** (black), **I.7** (red), C$_{60}$@**I.6** (dark blue), **I.6** (light blue), [10]CPP@C$_{60}$ (pink) and [10]CPP (purple). (g) *I*-*V* profiles of C$_{60}$@**I.7** before (blue) and during (red) photoirradiation.

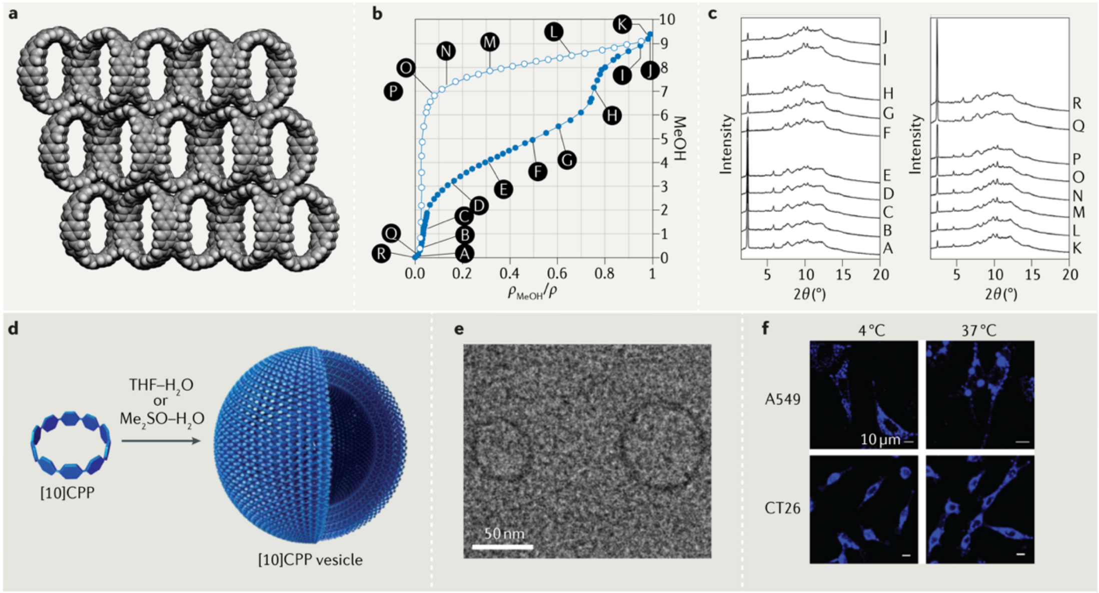

Figure I.7. Cycloparaphenylenes can serve as building blocks for nanomaterials. (a) Crystals of the cycloparaphenylene [12]CPP feature pores that are available to guest molecules. (b) Adsorption (filled circles) and desorption (open circles) isotherms for MeOH and [12]CPP. (c) In situ powder X-ray diffraction measurements of [12]CPP during MeOH uptake. The letters correspond to points in the isotherms in (b). (d) Schematic of the proposed structure of a vesicle formed by self-assembly of [10]CPP in THF–H_2O or Me_2SO–H_2O solvent mixtures. (e) Cryo-transmission electron micrograph of [10]CPP vesicles. (f) Fluorescence microscope images of [10]CPP vesicles within A549 and CT26 cells at 4 °C and 37 °C.

The increased molecular motion at elevated temperatures increases the average pore size of bulk [12]CPP, which, apparently, is selective for CO_2 at this temperature.[142] The material also adsorbs MeOH, EtOH, cyclohexane and *n*-hexane vapour, although it does not take up H_2O because H_2O forms stable, hydrogen-bonded aggregates that were thought to be too large for the small [12]CPP pores. The bulk [12]CPP material was also found to be soft in the sense that its solid-state morphology could change to accommodate guests. For example, powder X-ray diffraction (XRD) measurements during MeOH uptake revealed clear changes in peak pattern and intensity upon increasing MeOH uptake (Fig. I.7b,c.). Importantly, this process was found to be reversible, with the [12]CPP diffraction pattern returning to its initial state upon desorption. These XRD data served as the basis for a stepwise mechanistic proposal, in which MeOH uptake involves multiple distinct structural deformations, ultimately resulting in the uptake of ~9 molecules per nanohoop. The ability of bulk CPP samples to adsorb various analytes opens the door to myriad potential studies. For example, because guests can alter the emissive properties of CPPs, bulk CPP samples could be used as dynamic sensors that exhibit altered fluorescence upon analyte uptake.

Self-assembled carbon nanomaterials have begun to see use as novel materials to target specific cellular sites.[143–145] However, the design of these materials is difficult because most biomaterials enter cells by endocytosis and localize in endosomes before undergoing degradation in lysosomes.[146,147] Therefore, it remains a challenge to find supramolecular synthons from which biomaterials can be self-assembled. Due to their low cytotoxicity[18] and bright emission, CPPs represent excellent candidates for the fabrication of new functional biomaterials. This is further supported by a recent observation, using cryo-transmission electron microscopy, of vesicle-like [10]CPP aggregates in THF or Me_2SO upon the addition of H_2O[25] (Fig. I.7d,e.). The size of these vesicles could be loosely controlled by varying the cosolvent:H_2O ratios at [10]CPP constant concentration. To explore the uptake of the [10]CPP vesicles in cells, vesicles of 78 nm in mean diameter were co-incubated with human alveolar basal epithelial cells (A549) and mouse colon cancer cells (CT26) in Me_2SO–PBS (1:99). [10]CPP vesicle uptake was observed in both cell lines, with bright-blue emission from [10]CPP appearing primarily in the cytoplasm, with none coming from the nucleus (Fig. I.7f.). Interestingly, vesicle uptake was observed at both 4 °C and 37 °C, implying that the uptake mechanism is independent of both energy and temperature. Likewise, cellular uptake of [10]CPP vesicles was found to be unaffected by a variety of endocytosis inhibitors, suggesting that cellular permeation by the vesicles does not occur through an endocytosis-dependent mechanism. Cell-viability experiments revealed IC_{50} values of 7.2 $\mu g\ ml^{-1}$ and 4.9 $\mu g\ ml^{-1}$ for the A549 and CT26 cell lines, respectively. These preliminary results, which implicate a non-endocytotic uptake mechanism, encourage the further exploration of nanohoops as building blocks for functional self-assembled biomaterials.

The above CPP vesicles represent a unique case of CPP self-assembly induced by an external stimulus (the presence of H_2O). We have taken a different approach and chosen to focus on the programmed self-assembly of functionalized nanohoops. Inspired by the idea of using CPPs in the size-selective construction of CNTs, we hypothesized that it would be possible to construct non-covalent CNT mimics from appropriately functionalized CPPs. The realization of this idea will be discussed in detail in Chapter **II**.

I.9 Conclusions and Outlook.

In just a decade, CPPs have gone from being synthetic curiosities to readily accessible materials with highly tunable properties. The syntheses of CPPS are motivated by a broad scope of exciting applications ranging from solid-state nanomaterials to biological imaging. The bright, tunable emission from CPPs in solution and in the solid state is expected to be useful in next-generation display technologies and new biologically-relevant fluorophores and sensors, among other applications. Likewise, the ability to tune the electronic structure of CPPs by covalent functionalization or complexation with guest molecules such as fullerenes is predicted to be advantageous in areas such as organic photovoltaics. Finally, the self-assembly of CPPs, which has attracted little attention until recently, has already proved to be useful to form microporous materials, biologically-relevant nanomaterials, and atomically-precise CNT mimics. With such a wide breadth of potential uses already beginning to emerge, we foresee carbon nanohoops and their derivatives evolving into ubiquitous atom-precise scaffolds in carbon-based nanomaterials.

I.10. Bridge to Chapter II.

Among the emerging applications for CPPs describe in Chapter **I** was their use as building blocks in the construction of novel self-assembled nanomaterials. In Chapter **II**, we will explore in more detail the design, synthesis, and materials properties of a nanohoop-based CNT-mimic, which was briefly discussed in Chapter **I**. It was discovered that judicious fluorination of the CPP backbone resulted in tubular self-assembly of the nanohoops in the solid state, resulting in arrays of CNT-like channels with precisely defined diameters. Moreover, dropcasting of this material on a highly-ordered pyrolytic graphite (HOPG) surface resulted in the almost instantaneous formation of relatively large (~1-2 μm in height and width on average) hexagonal pillars comprised entirely of self-assembled, vertically aligned nanohoops. These pillars formed relatively dense “forests” on the HOPG surface and were found to exhibit high flexibility and bright blue emission.

CHAPTER II

A BOTTOM-UP APPROACH TO SOLUTION-PROCESSED, ATOMICALLY PRECISE GRAPHITIC CYLINDERS ON GRAPHITE

Chapter **II** is based on work published in the journal *Nano Letters* in 2018. I am the primary author on this work and the overall concept was created by myself, Dr. Jeff Van Raden, and Professor Ramesh Jasti. Dr. Jeff Van Raden developed a major portion of the synthetic route and aided in writing and editing. David Miller carried out the necessary materials characterization and contributed to relevant text and figures within the manuscript. Dr. Lev N. Zakharov provided the X-ray crystallography data described in the manuscript. Professor Benjamín Alemán contributed conceptually and to relevant written discussions within the manuscript.

Extended carbon nanostructures, such as carbon nanotubes (CNTs), exhibit remarkable properties but are difficult to synthesize uniformly. Herein, we present a new class of carbon nanomaterials constructed via the bottom-up self-assembly of cylindrical, atomically precise small molecules. Guided by supramolecular design principles and circle packing theory, we have designed and synthesized a fluorinated nanohoop that, in the solid state, self-assembles into nanotube-like arrays with channel diameters of precisely 1.63 nm. A mild solution-casting technique is then used to construct vertical "forests" of these arrays on a highly ordered pyrolytic graphite (HOPG) surface through epitaxial growth. Furthermore, we show that a basic property of nanohoops, fluorescence, is readily transferred to the bulk phase, implying that the properties of these materials can be directly altered via precise functionalization of their nanohoop building blocks. The strategy presented is expected to have broader applications in the development of new graphitic nanomaterials with π-rich cavities reminiscent of CNTs.

II.1. Introduction.

Carbon nanotubes (CNTs) exhibit a wide range of unique properties depending on their precise atomic structure. The remarkable optical and electronic properties of CNTs are intimately connected to CNT chirality.[1] The scalable preparation of single-chirality CNTs, therefore, has been a longstanding goal in the field of nanoscience.[2–4] Similarly, the unique frictionless channels of CNTs exhibit fascinating mass transport behavior, but only when the channel diameters are smaller than 2 nm,[5,6] again highlighting the need for precise CNT structural control. In addition to chirality and diameter, the position and orientation of CNTs on substrates (for example, the vertical alignment of CNTs into surface-bound "forests")[7] is important for fully realizing potential applications such as membranes,[8] sensors,[9,10] and electronics.[11] While much progress has been made in the synthesis and deposition of CNTs, a completely new approach to these types of cylindrical materials may open up new opportunities. Herein, we disclose a "bottom-up" synthesis strategy based on self-assembly of short fragments of CNTs (i.e., cycloparaphenylenes or carbon nanohoops, Figure II.1.a.) to produce vertically oriented "forests" of graphitic cylinders on surfaces with precise structural control.

Inspired by the work of Smalley regarding the amplification[12] of CNTs, the synthesis of cycloparaphenylenes (CPPs) aimed to provide ideal templates or building blocks for the uniform fabrication of CNTs.[13–15] Since their initial synthesis in 2008,[16] methods have been developed to synthesize these "carbon nanohoops" in various sizes[17–20] and with numerous functionalities.[21–23] More recently, "carbon nanobelts" have been synthesized by Itami and co-workers, again in hopes of accessing effective seed molecules for CNT growth.[24,25] As a consequence of their curved geometries and cyclic conjugation, carbon nanohoops and nanobelts exhibit unique size-dependent electronic and photophysical properties.[24–27] Despite their fascinating circular geometries, CNT-like pores, and highly tunable properties, CPPs and related structures have only recently begun to be explored in the context of solid-state materials.[28–32] Seeking to expand on this, we envisioned the development of a new class of CPP-based carbon nanomaterials that would mimic the tubular structures of CNTs. Through the vertical self-assembly of CPPs, we speculated that it would be possible to construct arrays of noncovalent nanotubes with diameters that could be synthetically altered with atomic precision. Moreover, the properties of these materials could be fine-tuned via the bottom-up functionalization of nanohoop building blocks. In this work, we merge synthetic organic chemistry, supramolecular design, and fundamental circle packing theory to construct arrays of noncovalent nanotubes with uniform channel diameters of precisely 1.63 nm via the self-assembly of functionalized nanohoop building blocks. We then prepare vertically oriented "forests" of these structures on a highly ordered pyrolytic graphite (HOPG) surface through epitaxial growth using a simple solution-casting approach.

CPPs are unique among macrocyclic small molecules in that their full sp^2 hybridization and para connectivity gives rise to a circular geometry. Thus, we were curious to what extent CPPs could be treated as geometrically perfect circles, as this would allow for elementary circle packing concepts in our design.[33] Inspired by the dense arrangements found within CNT bundles,[34] we ultimately targeted a hexagonal circle packing motif, the densest arrangement for circles of identical diameters.[33] This packing requires each circle in the 2D lattice to be symmetrically surrounded by six other circles (Fig. II.1b.). Stacking these hexagonal "sheets" vertically would then afford the desired CNT-like columns (Fig. II.1b.). Translating all of this into practical molecular design necessitated a supramolecular strategy that would allow for both face-to-face (horizontal) and edge-to-edge (vertical) interactions between nanohoops. Unfunctionalized CPPs do not exhibit face-to-face arene−arene stacking, as is often observed in linear acene systems[35] and instead tend to adopt dense herringbone-like packing motifs with inaccessible pores as a result of the hoops "filling" one another.[27,36] However, arene−perfluoroarene interactions have yet to be thoroughly explored as a self-assembly strategy in CPP systems and were viewed as an attractive alternative to induce the desired face-to-face arrangement. Arene−perfluoroarene interactions, which result from the favorable electronic interaction between electron-rich aryl rings and electron-deficient perfluorinated aryl rings,[37] have proven useful in supramolecular design due to their powerful and relatively predictable self-assembly capabilities.[38,39] Conveniently, aryl C−H···F interactions are also known to be powerful guiding forces in systems containing fluorinated aryl moieties.[40] Therefore, we hypothesized that a drive to maximize C−H···F contacts would "lock" **II.1** into a vertical assembly.

II.2. Results and Discussion.

II.2.1. Synthesis and Solid-State Analysis.

Nanohoop **II.1** (Fig. II.2a.) was designed to leverage the symmetry of the [12]CPP backbone to afford six arene−perfluoroarene interactions per hoop, where every interaction represents one of the six hoop-to-hoop contacts needed for hexagonal packing.

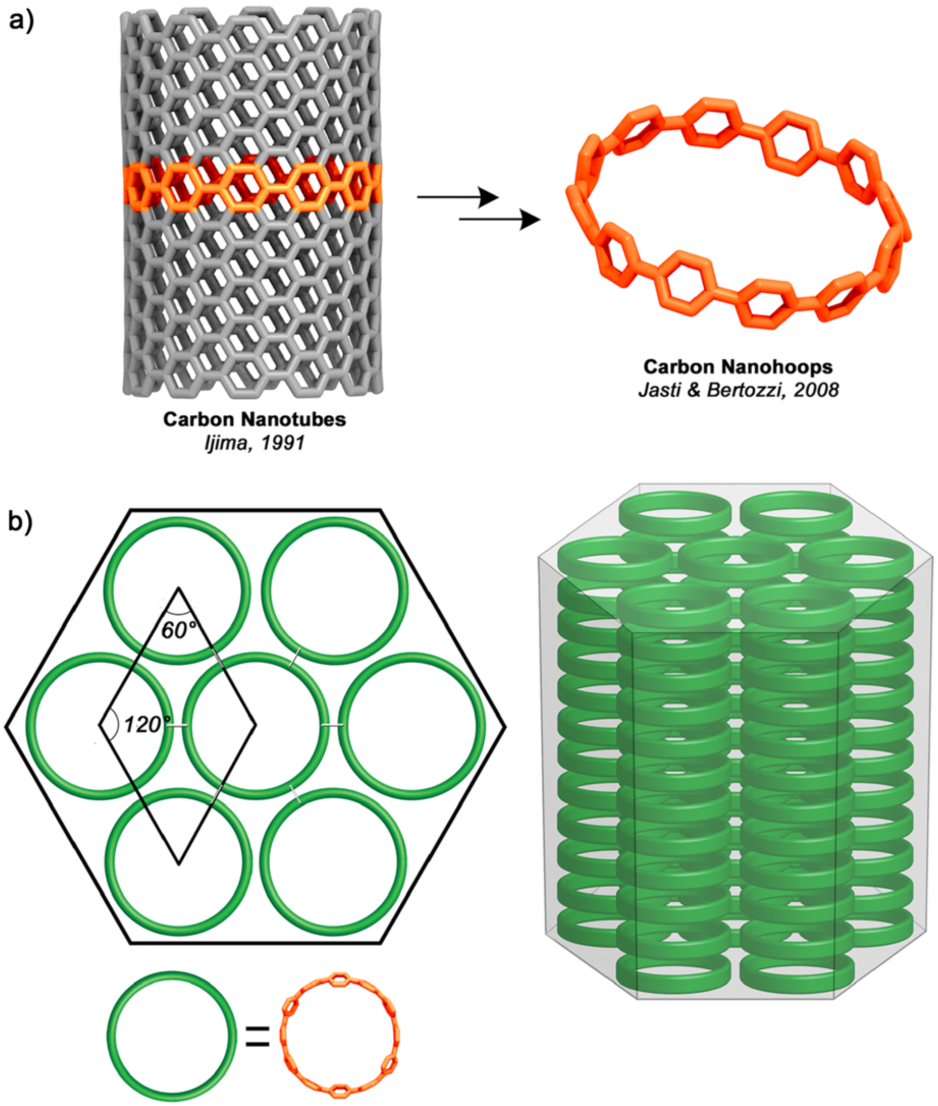
a)
Carbon Nanotubes
Ijima, 1991
Carbon Nanohoops
Jasti & Bertozzi, 2008
b)
60°
120°
=

Figure II.1. (a) Cartoon representation of a [12,12] armchair CNT and an X-ray crystal structure of its smallest cross-sectional fragment, [12]CPP (crystal structure data from ref 36). (b) (Left) schematic depiction of hexagonal circle packing, in which the central circle in the lattice is symmetrically surrounded by six other circles. CPPs can be seen as geometrically equivalent to perfect circles. (Right) stacking sheets of hexagonally packed hollow circles resulting in the formation of channels with diameters defined by the constituent circles.

Additionally, we hypothesized that C−H···F interactions would align **II.1** into nanotube-like channels. Yamago and co-workers have recently found that incorporation of fluorines into a nanohoop backbone can indeed result in tubular solid-state structures via fluorine−hydrogen interactions.[41] The synthesis of **II.1** relied on previously established synthetic routes toward the size-selective synthesis of [*n*]CPPs.[17,19] Compounds **II.2** and **II.3**, which can be easily accessed on a multigram scale (Supporting Information, Schemes II.1. and II.2.), were subjected to a dilute Suzuki−Miyaura cross-coupling reaction, a common aryl−aryl bond forming reaction,[42] to afford macrocycle **II.4** in 65% yield (Fig. II.2a.). Next, the triethylsilyl (TES) groups on the macrocycle were removed with tetrabutylammonium fluoride (TBAF) in the presence of excess acetic acid to afford an intermediate alcohol-functionalized compound. Finally, the cyclohexadiene moieties of this macrocycle were converted to benzene rings via reductive aromatization under mild tin-mediated conditions[19] to afford nanohoop **II.1** in a 4% yield over two steps as an off-white powder. We attribute this low yield to difficulty in the reductive aromatization step, a problem that also plagued Yamago and co-workers when employing the same aromatization conditions to their syntheses of fluorinated cycloparaphenylenes.[41] Halogenated cycloparaphenylenes have been calculated to have higher strain energies than their all-hydrocarbon counterparts which could be contributing to the low yields.[43]

Nanohoop **II.1** was found to readily form colorless, needle-like crystals via slow evaporation from chloroform. X-ray diffraction of these crystals revealed that **II.1** assembles into the desired nanotube-like structures, exhibiting a uniform array of 1.63 nm channels (Fig. II.2b, c.). The vertical assembly of **II.1** appeared to be guided by a multitude of aryl C−H···F interactions (Fig. II.2d.), resulting in perfectly linear columns. Thirty-six C−H···F interactions per hoop were found in the crystal packing of **II.1**, ranging from 2.53 to 2.62 Å.[41] The ability of the top and bottom "edges" of macrocycles with radially oriented π systems to take part in a large number of weak contacts has been observed previously[44] and highlights a potential advantage of using nanohoop-like structures to maximize vertical interactions in the construction of molecular crystalline systems. Upon closer inspection of this solid-state packing, we also observed six well-defined arene-perfluoroarene interactions per nanohoop with centroid-to-centroid distances of 3.69 Å (Fig. II.2e.), well within the range of approximately 3.4−3.9 Å commonly observed in other studies.[38,39] Importantly, these interactions result in an ideal 2D hexagonal circle packing motif, which is beautifully reflected in the symmetric, diamond-shaped unit cell of the lattice with vertices located at the centers of four nanohoops.

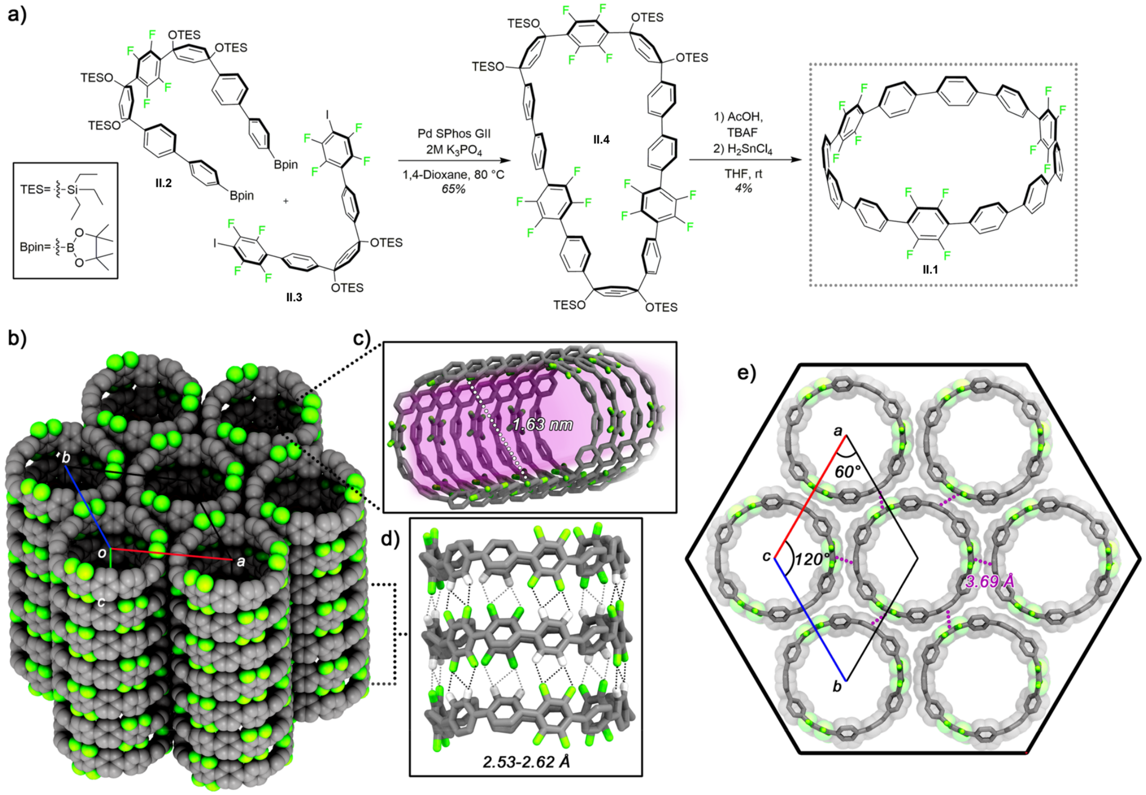
a)
TES=
Bpin=
OTES
TESO
Bpin
II.2
II.3
Pd SPhos GII
2M K3PO4
1,4-Dioxane, 80 °C
65%
II.4
1) AcOH, TBAF
2) H2SnCl4
THF, rt
4%
II.1
b)
c)
1.63 nm
d)
2.53-2.62 Å
e)
a
b
c
o
60°
120°
3.69 Å

Figure II.2. (a) Coupling of intermediates **II.2** and **II.3** via Suzuki−Miyaura conditions affords macrocycle **II.4**, which is then deprotected with TBAF and subsequently aromatized under mild tin-mediated conditions to provide fluorinated nanohoop **II.1**. (b) X-ray crystal structure of nanohoop **II.1**, showing that the compound self-assembles into noncovalent nanotubes in the solid state. (c) Cross-section of a nanotube of **II.1**, highlighting the 1.63 nm diameter. (d) Aryl C−H···F interactions (dotted lines) that guide the vertical assembly of **II.1**, which range in distance from 2.53 to 2.62 Å. (e) Top-down view showing the hexagonal circle packing of **II.1**, which is guided by six arene−perfluoroarene interactions that measure at 3.69 Å (purple dotted lines) (chloroform solvent molecules omitted for clarity).

II.2.2 Construction and Characterization of Vertically-Aligned Nanohoop “Forests”.

At the outset of this work, one of our primary goals was to mimic vertically oriented CNT “forests” through the vertical assembly of **II.1** on surfaces. Substrate-templated epitaxial growth has previously been shown to be an effective strategy for accessing well-oriented molecular assemblies.[45] Thus, we chose highly oriented pyrolytic graphite (HOPG) as a possible template, since HOPG has a lattice constant of a factor of 8 less than the horizontal lattice constants of **II.1** (a = 2.46 Å for HOPG vs a/b = 19.81 Å for **II.1**). On the basis of this idea of lattice matching, we predicted that HOPG would serve as a suitable template for epitaxial growth of vertically aligned structures of **II.1**. We found that drop-casting **II.1** from a chloroform solution onto a HOPG substrate at humid ambient conditions (Section II.4.3. and Fig. II.7.) resulted in the rapid (∼1−2 min) formation of numerous hexagonal and needle-like crystalline structures that were easily observable via optical microscopy (Fig. II.3a.). Scanning electron microscopy (SEM) revealed that the hexagonal crystals were in fact nanowire-like pillars that form dense arrays on many regions of the substrate (Fig. II.3b.). The structures displayed in Figure II.3.b. range in size from 1 to 2 μm in both height and width, although various other morphologies, such as tall and thin pillars (5−10 μm in height and 0.2− 0.5 μm in width) and short and wide structures (200−500 nm in height and 1−2 μm in width) were also found (see Fig. II.8. for additional images and analysis of the various pillar sizes and morphologies observed). The largest pillars and densest pillar populations were found along the chloroform drying rings that resulted from solution casting, an observation that could inform future optimization of this solution processing technique. Focused ion beam (FIB) microscopy of individual hexagonal pillars revealed that these structures do indeed exhibit six well-defined walls and a flat hexagonal top (Fig. II.3c.). Satisfyingly, the hexagonal geometries of these pillars directly reflected the hexagonal molecular packing observed in the crystal structure of **II.1**, supporting the notion that the pillars we observed were composed of vertically aligned columns of **II.1**. These pillars were also successfully fabricated on multilayer graphene surfaces grown on copper foil (Fig. II.9a.). It is worth noting that deposition of the nonfluorinated analog ([12]CPP) onto an identical graphene−copper substrate produced no such structures, and instead affords flat plate-like structures consistent with the morphology of solution grown crystals of [12]CPP (Fig. II.9b.).

Further inspection of the hexagonal pillars of **II.1** revealed preferential orientations on the HOPG surface, which is indicative of epitaxial growth on the graphite lattice. We used a home-built image processing algorithm to identify hexagons and quantify their angles relative to an arbitrary normal. This allowed us to map regions of high pillar density and analyze the relative orientations of grouped pillars. Two distinct orientations for a given area emerged, averaging at 26.0° rotation and 49.5° rotation from an arbitrary normal, which were observed in relatively equal quantities (Fig. II.3d.). We currently hypothesize that these populations represent two energetically favorable orientations that **II.1** can adopt on the HOPG surface. This notion is supported by a recent theoretical study implying that nanohoops should indeed exhibit energetically preferred orientations on graphene surfaces.[46] However, while our findings clearly indicate substrate-directed preferential orientation of the observed hexagonal pillars, further studies are required to elucidate the mechanisms behind the growth and orientation of nanohoop-based structures on graphite. Interestingly, we observe that the needle-like structures align to the graphite surface in multiples of 60° (Fig. II.3e.), consistent with the 3-fold symmetry of the graphite lattice. This again supports the notion that the HOPG surface exhibits a heavy influence on the growth and orientation of the structures formed by **II.1**. Importantly, this well-templated growth offers the potential for deterministic growth of hexagonal wires. For example, a graphene sheet could be patterned into hexagonal growth templates, which would likely facilitate localized growth of pillars.

We used energy-dispersive X-ray spectroscopy (EDS) and Raman spectroscopy to provide additional confirmation that the hexagonal pillars are indeed composed of fluorinated nanohoops. EDS analysis of both pillars and needles produced readily apparent fluorine peaks in addition to carbon (Fig. II.10.). Solid-state Raman spectroscopy of a single pillar yields a spectrum consistent with previous solution-based measurements of cycloparaphenylenes (Fig. II.4a.).[47] Three previously reported peaks associated with [12]CPP are observed at 1201 cm^{-1} (related to C−H bond bending), 1278 cm^{-1} (attributed to deformation of a benzene ring), and 1604 cm^{-1} (related to C−C stretching). Two additional peaks, located at 1401 and 1643 cm^{-1}, which have not been seen in CPPs of any diameter, are likely due to the incorporation of fluorine into the atomic structure but could also be due to vibrational modes of the supramolecular crystal.

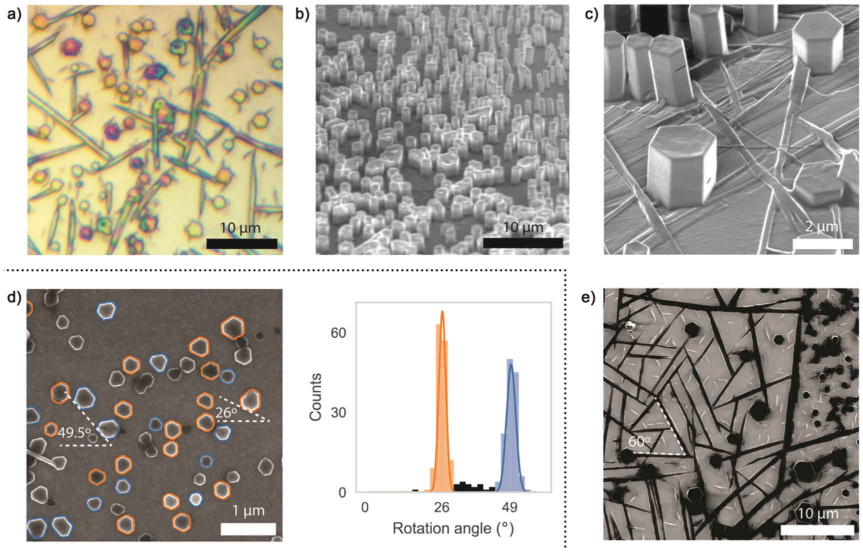

Figure II.3. (a) Optical microscopy of hexagonal pillars and needle-like structures on HOPG surface. (b) Angled-SEM of an array of hexagonal pillars. Dense forests of hexagonal pillars are scattered across the sample with heights ranging from a few hundred nanometers to several microns. (c) Angled focused ion beam (FIB) microscopy of isolated hexagonal pillars. The flat hexagonal faces and top are readily apparent. (d) (Left) segment of a larger (25 µm × 16 µm) SEM image of short pillars showing growth templated by the substrate. The pillars are preferentially aligned in one of two angles, separated by ~23.5°. (Right) histogram of orientation angles in the full 25 µm × 16 µm image. A total of 290 hexagons are identified in the full image and nearly all of them are oriented in one of two angles. (e) FIB image of needle-like structures formed by **II.1**, which preferentially orient at 60° relative to one another on the HOPG surface.

Taken together, the EDS and Raman spectra are consistent with columns of **II.1** and are in agreement with the atomic structure inferred from X-ray crystallography. The hexagonal pillars formed by **II.1** were found to be surprisingly flexible yet mechanically robust. During SEM imaging, we observed the pillars oscillating like cantilever beams, possibly because of electron-beam-induced electrostatic repulsion between neighboring pillars (see supplementary video). This flexibility is likely a result of the noncovalent assembly of these pillars, demonstrating an inherent utility of a molecular crystalline approach versus assembly methods that involve covalent bond formation.[48] The out-of-plane modulus of the hexagonal pillars, which provides a measure of material stiffness, was found to be similar to those generally observed in molecular crystalline systems.[49] We used PeakForce atomic force microscopy (AFM) to obtain topographical and quantitative nanomechanical images of the pillars (Fig. II.4b.). From this data, we determined that the pillars have an out-of-plane elastic modulus ~12 GPa, about 2/3 that of the HOPG substrate (Fig. II.4b.). The relative flexibility of the vertical nanowires composed of **II.1**, both in- and out-of-plane, suggest that this material can be potentially implemented into flexible devices.[50]

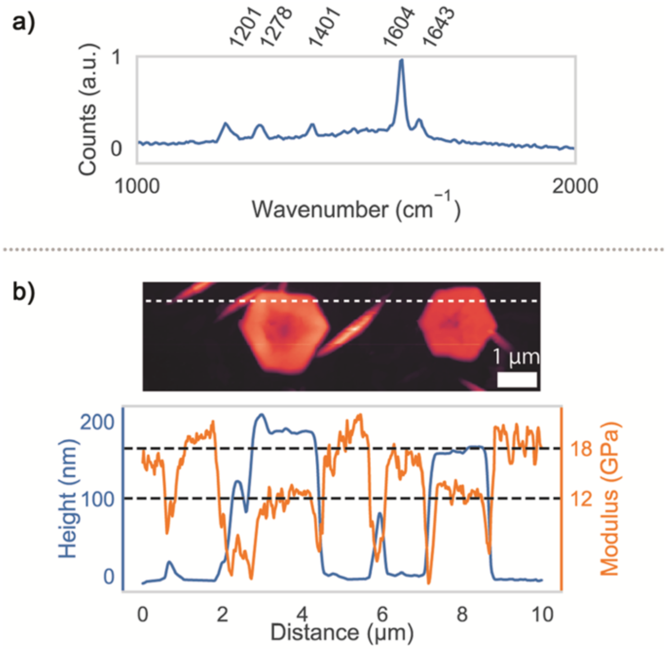

Figure II.4. (a) Raman spectrum of a single hexagonal pillar of **II.1**, with peaks observed at 1201, 1278, 1401, 1604, and 1634 cm^{-1}. (b) (Top) PeakForce AFM image of two hexagonal pillars and several needle-like structures. (Bottom) cross-sectional cut of the AFM image (indicated by the dashed white line) showing both the height of the hexagonal pillars (blue) and the elastic modulus (orange).

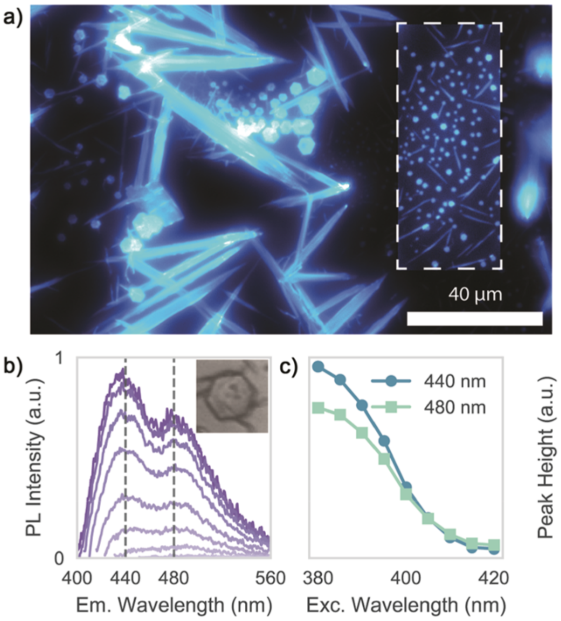

Figure II.5. (a) False-colored but visually accurate wide-field fluorescence image of hexagonal pillars and large needle-like structures under UV excitation. The image brightness is enhanced in the boxed region due to the lower fluorescence intensity of the smaller structures within. (b) Emission spectrum at excitation wavelengths ranging from 380 to 420 nm for the single-pillar shown in the inset. Two emission peaks at 440 and 480 nm are apparent for every excitation wavelength. (c) Maximum photoluminescence (PL) intensity from (b) for both the 440 and 480 nm emission maxima peaks as a function of excitation wavelength. The fluorescence efficiency begins to saturate around 380 nm, which is at the limit of our measurement range.

The bright fluorescence and emission wavelength of the nanohoop building blocks were largely adopted by the hexagonal pillars observed in the solid state. We found the incorporation of fluorine atoms into the backbone of **II.1** to have little impact on the molecule's photophysical properties in solution, in agreement with the observations of Yamago and co-workers.[41] Compared to emission profile of the parent all-hydrocarbon [12]CPP in solution,[36] the emission profile of **II.1** is blue-shifted by ~10 nm (Fig. II.11.). In the solid state, the fluorescence of **II.1** is retained and possesses a striking bright blue emission from both the hexagonal pillars and needle-like structures that form following solution deposition onto HOPG (Fig. II.5a.). The emission spectrum of a single-hexagonal pillar reveals two maxima: one at 440 nm, which is also found in solution (Fig. II.11.), and another lower intensity peak at 480 nm, which is only observed in the solid-state phase (Fig. II.5b.). The absence of the second peak at 480 nm in solution could be due to inhomogeneous broadening,[51] or might be indicative of phonon interactions unique to the solid-state packing of **II.1**. Fluorescence efficiency was found to increase as photon wavelength decreases, before beginning to saturate below 380 nm (Fig. II.5c.), which is consistent with a HOMO−LUMO gap of ~3 eV and falls within the HOMO−LUMO gap range of 2.71−3.63 eV that has been calculated for [5] -[12]CPP.[52] Given how the fluorescence of **II.1** in solution directly translates to the bulk phase, we expect that the capability to tune CPP properties via size-alteration or functionalization[26,27,53] will allow for the precise tuning of bulk properties in these nanohoop-based materials via the controlled, bottom-up functionalization of nanohoop building blocks.

II.3. Conclusion.

In conclusion, we have demonstrated the rational design and synthesis of a fluorinated nanohoop (**II.1**) that, in the solid state, self-assembles into hexagonally packed bundles of noncovalent nanotubes that bear a striking resemblance to single-walled CNT bundles. Furthermore, vertically aligned “forests” of these hexagonal bundles were constructed on a HOPG substrate via mild solution-casting conditions, which we expect will allow for easy implementation of this material in future solid-state applications. We attribute this preference for vertical growth to the close matching of the respective lattices of **II.1** and the HOPG surface, which we have supported experimentally via relative angle analysis of both the hexagonal pillars and flat-lying needles observed. The hexagonal pillars formed by **II.1** were further characterized by Raman spectroscopy, AFM imaging, and fluorescence spectroscopy, the latter of which revealed that these pillars retain the bright blue emission exhibited by **II.1** in solution. The access to precise nanometer-scale channels allowed by this material is expected to be particularly advantageous in highly selective membrane applications. Additionally, unique optical uses are foreseen due to the material’s bright emission, which we predict to be synthetically tunable to meet specific needs. More broadly, this study provides an initial blueprint toward the design of self-assembled tubular systems with the potential to mimic the channel environments found within CNTs, albeit with significantly greater control over channel diameter. We also intend to explore this strategy as a means of preorganizing molecular precursors for the precise bottom-up synthesis of CNTs and other extended carbon nanostructures.

II.4. Experimental Section.

II.4.1 Materials and Methods.

^{1}H NMR spectra were recorded at 500 MHz on Varian VNMR spectrometer, 500 MHz on a Bruker, or 600 MHz on Bruker. All ^{1}H NMR spectra are referenced to TMS (δ 0.00 ppm), CH_2Cl_2 (δ 5.32 ppm), or $(CH_3)_3CO$ (δ 2.05 ppm). All ^{13}C NMR spectra are references to a residual $CHCl_3$ (δ 77.16 ppm), CH_2Cl_2 (54.00 ppm), or $(CH_3)_3CO$ (δ 29.84 ppm).

All reagents were obtained commercially and used without further purification unless otherwise noted. All glassware was flame-dried and cooled under an inert atmosphere of nitrogen unless otherwise noted. Moisture sensitive reactions were carried out under an inert atmosphere of nitrogen using standard syringe/septa technique. Silica column chromatography was conducted with Zeochem Zeoprep 60 Eco 40-63 µM silica gel while alumina chromatography utilized Sorbent Technologies 50-200 um Basic Activity II-II Alumina. Aryl bromide **II.5** was prepared as reported in reference 54. Diboronate **II.10** was reported in reference 55.

SEM (Scanning Electron Microscopy), FIB (Focused Ion Beam), and EDS (Energy Dispersive X-Ray Spectroscopy) analysis were performed in an FEI Helios 600i FIB-SEM. The SEM images were taken with an accelerating voltage 5 kV while the Ga^+ FIB was operated at 30 kV Angled SEM and FIB was performed at an angle of 52°. EDS data was acquired with a 5 kV electron beam.

Widefield fluorescent imaging was performed on a Nikon Eclipse Ti-U epifluorescence optical microscope with a 50x objective lens using a Nikon DAPI filter set (Excitation Filter at 375 nm, Dichroic Mirror at 415 nm, and a barrier filter at 460 nm).

Quantitative nanomechanical mapping was performed with a Bruker Dimension Icon atomic force microscope with an OTESPA-R3 probe (nominal spring constant 26

N/m) in PeakForce tapping mode. The force set-point was 60 nN, which was high enough to indent both the hexagonal structures as well as the HOPG substrate. We use the known elastic modulus of HOPG (~18 GPa) to infer the modulus of the hexagons (~12 GPa).

Raman spectroscopy was performed in a WiTec alpha300 confocal Raman spectrometer with a 532 nm excitation laser and a 60x, 0.7 NA objective. Laser power was kept low to minimize damage to the hexagonal structures.

Measurements of the excitation and emission spectra were performed using a homebuilt fluorescence microscope with a 100x, 0.7 NA objective. A monochromator was used to select a 5 nm FWHM wavelength band from a Mercury/Xenon excitation source, which was then focused onto the sample with a spot-size comparable to a single hexagon. The excitation power of all bands was measured after the objective and used to normalize the emission intensity. The emitted light was separated from the incident light using a 50:50 beamsplitter and spectra were acquired using an Ocean Optics Flame Spectrometer with an integration time of 1 second.

II.4.2. X-Ray Crystallographic Data.

Diffraction intensities for **II.1** were collected at 173 K on a Bruker Apex2 CCD diffractometer using CuKα radiation, λ= 1.54178 Å. The space group was determined based on systematic absences. Absorption correction was applied by SADABS.[56] X-ray diffraction at high angles were weak and as a result R_{int} for the data collected is relatively high, R_{int} = 0.1426. The structure was solved by direct methods and Fourier techniques and refined on F^2 using full matrix least-squares procedures. All non-H atoms were refined with anisotropic thermal parameters. All H atoms were refined in calculated positions in a rigid group model. The molecules form a column in the packing. In the crystal structure there are five $CHCl_3$ solvent molecules filling out empty space inside and outside of these columns. Three of these solvent molecules have been located and refined. Two of them are located on a 3-fold axis outside the hoop and one inside the hoop. Two additional $CHCl_3$ solvent molecules located inside the hoop are highly disordered around in the center lines of the columns. Refinement revealed that these disordered positions could be also partially occupied. Attempts to find a solution for this disorder were unsuccessful. These disordered $CHCl_3$ solvent molecules were treated by

SQUEEZE.[57] The correction of the X-ray data by SQUEEZE is 498 electron/cell. All calculations were performed by the Bruker SHELXL-2014 package.[58]

*Crystallographic Data for **II.1***: $C_{77}H_{41}Cl_{15}F_{12}$, M = 1725.85, 0.13 x 0.02 x 0.02 mm, T = 173(2) K, Trigonal, space group *P*-3, *a* = 19...8149(6) Å, *b* = 19.8149(6) Å, *c* = 13.6041(6) Å, α = 90°, β = 90°, γ = 120°, *V* = 4625.8(3) $Å^3$, *Z* = 2, D_c = 1.239 Mg/m^3, μ(Cu) = 4.606 mm^{-1}, *F*(000) = 1732, $2\theta_{max}$ = 133.18°, 33778 reflections, 5443 independent reflections [R_{int} = 0.1426], R1 = 0.0829, wR2 = 0.2261 and GOF = 1.033 for 5443 reflections (313 parameters) with I>2σ(I), R1 = 0.1466, wR2 = 0.2475 and GOF = 1.033 for all reflections, max/min residual electron density +0.683/-0.594 $eÅ^{-3}$.

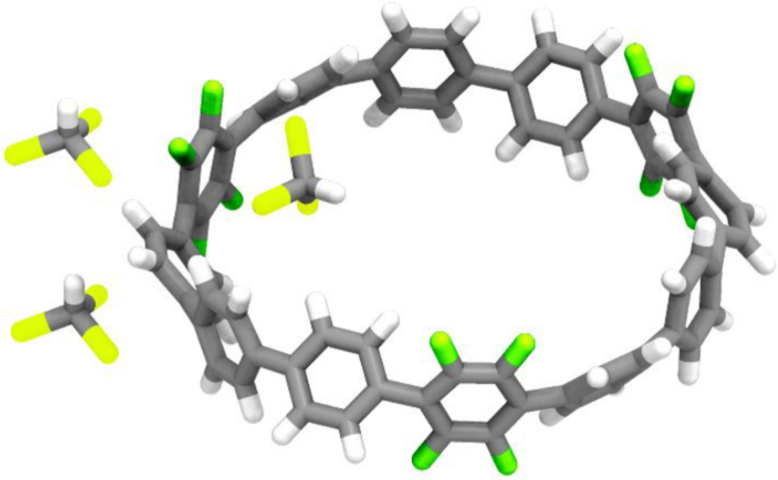

Figure II.6. X-ray crystal structure of **II.1** with three resolved $CHCl_3$ solvent molecules (F atoms in green, Cl atoms in yellow, H atoms in white).

II.4.3. General Sample Preparation for Surface Studies.

Samples were prepared on either a freshly cleaved highly-ordered pyrolytic graphite (HOPG) substrate (SPI supplies HOPG Advanced Ceramics Brand Grade ZYH and Mikromasch HOPG Grade ZYA, both 12 x 12 x 2 mm) or on multi-layer graphene grown on Cu foil (Graphenen). A 1 mg/ml solution of **II.1** in chloroform was prepared and heated to roughly 45-50 °C, causing the solution to go from cloudy to clear. A small crystallizing dish was then filled halfway with deionized water and covered with a sheet of aluminium foil with small holes cut into it. The dish was then heated 85 °C on a hotplate. Next, the chosen substrate was carefully placed on the foil covering the dish so as to be centered and level. The substrate was then flooded (approx. 0.05-0.1 mL) with the chloroform solution of **II.1** via dropcasting through a syringe filter (0.2 µm PTFE membrane). Subsequently, an appropriately-sized watch glass was quickly placed on top of the dish to induce a crude humid environment. The substrate was removed once the chloroform had completely evaporated (1-2 min.).

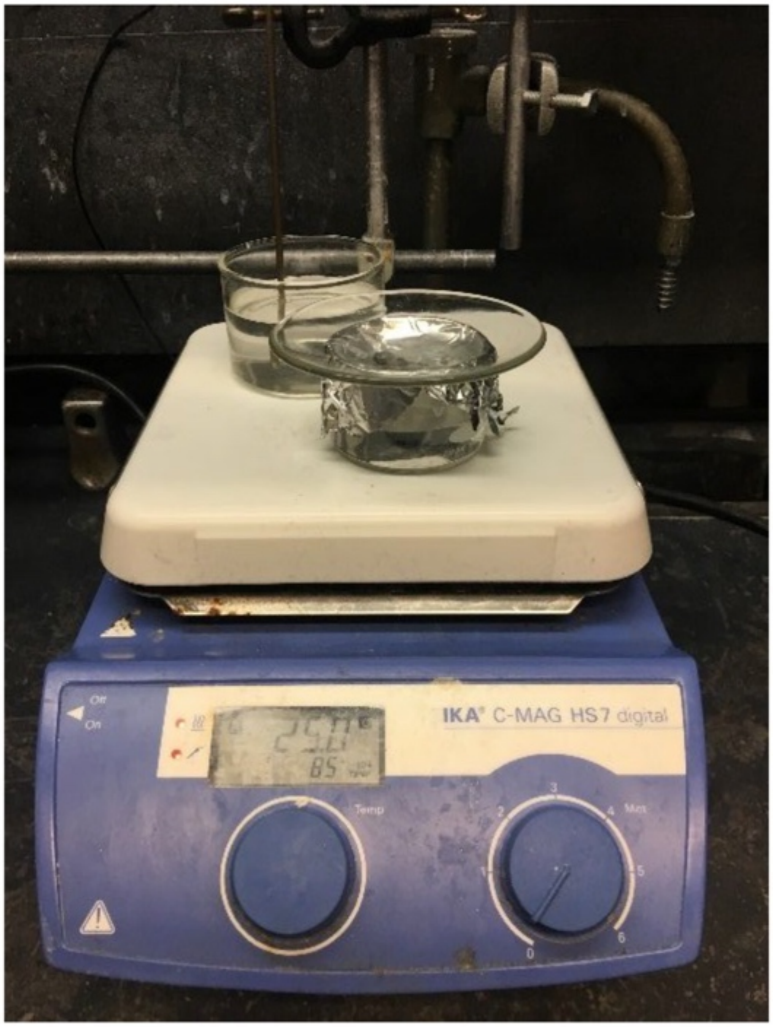

Figure II.7. Experimental set up used for sample preparation of **II.1** and [12]CPP on graphite/graphene substrates.

II.4.4. SEM Images of Various Pillar Sizes and Morphologies.

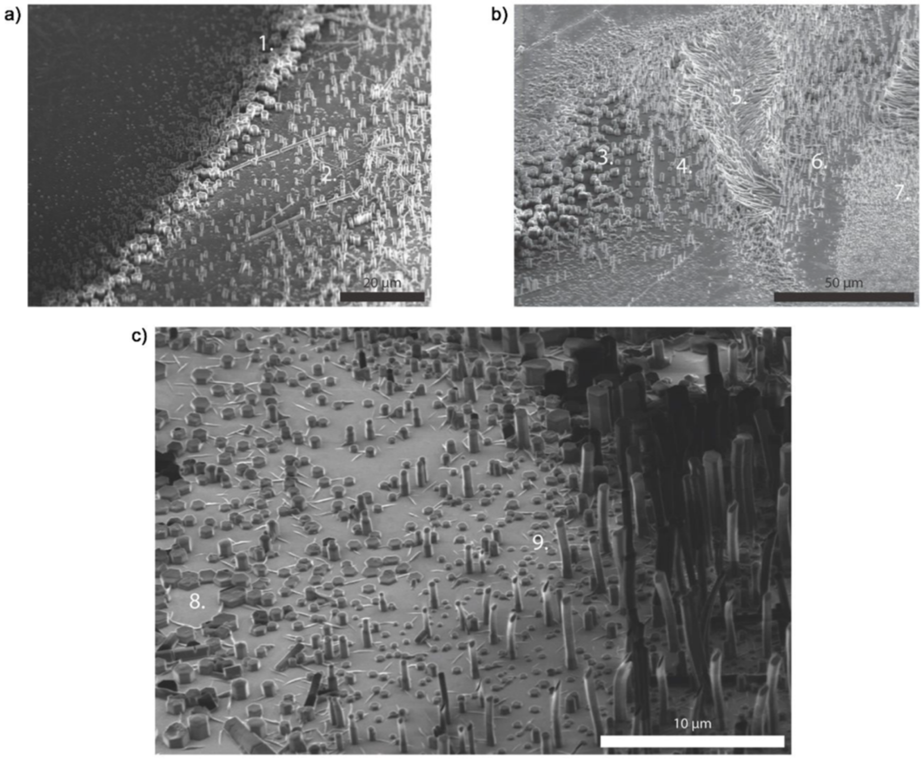

Figure II.8. Images showing different sizes and morphologies of grown pillars. All dimension values are approximate and representative of specific regions. a) SEM image showing vertical pillars grown at the edge of a solvent drying ring: **1.** Pillars at the edge of the drying ring become quite large and start to aggregate. **2.** Pillars inside the drying ring have smaller diameters and are isolated from one another. b) SEM image showing several types of pillars: **3.** Dense pillars with width of 3-5 μm and height of 1-3 μm. **4.** Sparse pillars with width of 0.5-1 μm and height of 5-10 μm. **5.** Dense pillars with height ~10 μm that have been knocked over, presumably during solvent evaporation. **6.** Sparse pillars with width of 0.2-0.5 μm and height of 5-10 μm. **7.** Region of small pillars at their initial stage of growth. c) FIB image of pillars near a drying ring: **8.** Very short pillars with width 1-2 μm and height 200-500 nm. **9.** Pillars with height of 5-10 μm and width 200-500 nm.

II.4.5. SEM Images of II.1 and [12]CPP on Multi-Layer Graphene.

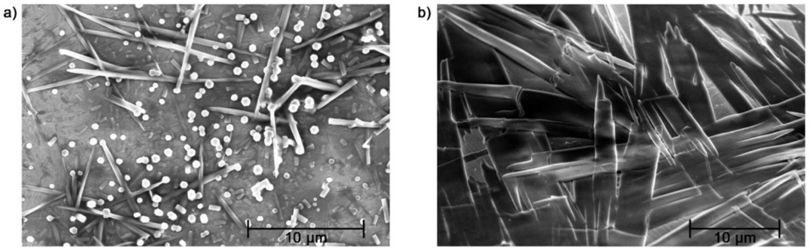

Figure II.9. a) **II.1** and b) [12]CPP deposited onto multi-layer graphene grown on copper foil (Graphenen). Both samples were produced using the procedure in Section II.4.3.

II.4.6. EDS Analysis.

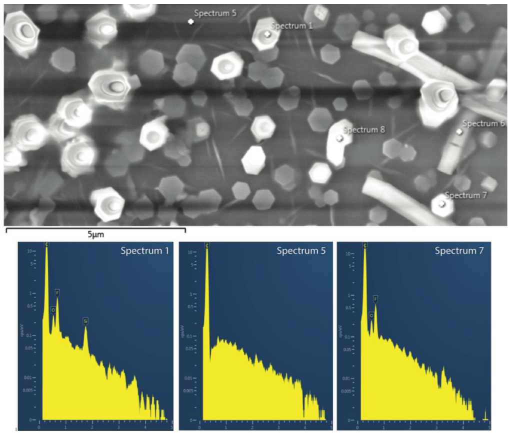

Figure II.10. EDS was used to characterize the elemental composition both on and off the hexagonal pillars composed of **II.1**, deposited on HOPG. Three representative spectra are shown with their locations marked in the SEM image above. Spectrum 1 shows well defined x-ray lines for carbon, oxygen, fluorine, and silicon. Fluorine and carbon content is expected for solid state structures formed from **II.1** while the silicon likely arises from contamination introduced during the deposition process. Spectrum 5 shows the spectrum of bare HOPG, which lacks any peaks other than carbon, as expected. Spectrum 7 shows the EDS spectrum from another pillar, which lacks the silicon peak observed in spectrum **II.1**. This indicates the silicon is a surface contaminant rather than a structural part of the vertical pillars. The presence of fluorine in all spectra taken of the pillars on the HOPG suggests that that is an integral component of the pillars, consistent with structures formed from **II.1**.

II.4.7. Photophysical Characterization of II.1 and [12]CPP in Solution.

The absorbance spectrum for **II.1** in solution was collected in dichloromethane (DCM) in a 1 cm quartz cuvette on an Agilent Cary 60 UV-Vis spectrophotometer. The emission spectrum for **II.1** in solution was collected in DCM on a Horiba Jobin Yvon Fluoromax-4 Fluorometer.

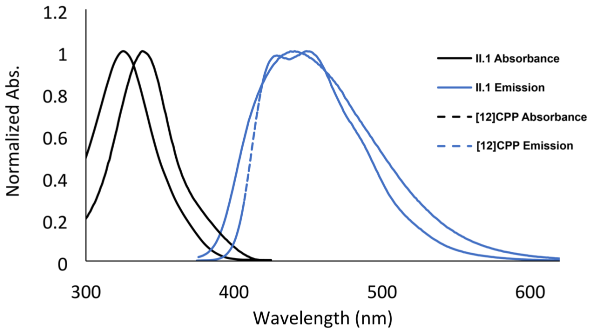

Figure II.11. Absorbance and emission spectra of **II.1** and [12]CPP in solution.

II.4.8. Synthetic Schemes for Intermediates II.2 and II.3.

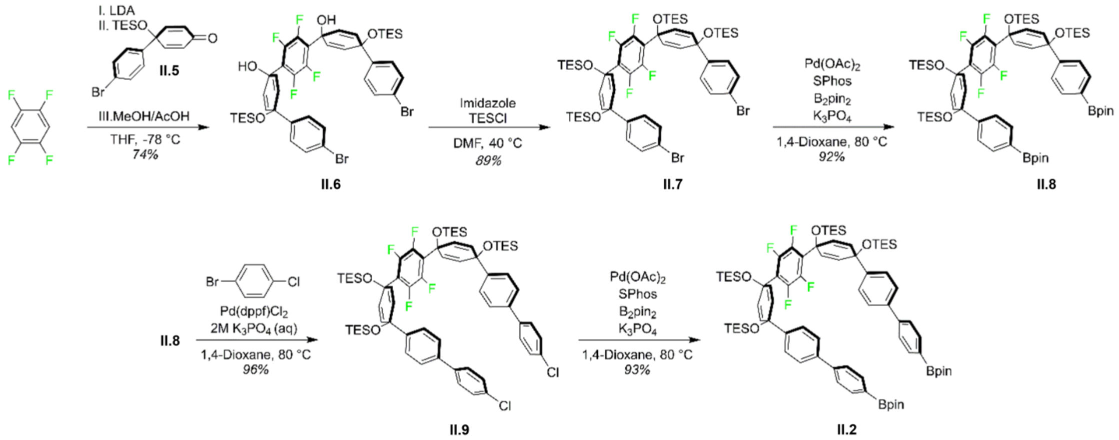
I. LDA
II. TESO
II.5
Br
III.MeOH/AcOH
THF, -78 °C
74%
F
OH
OTES
HO
TESO
Br
II.6
Imidazole
TESCl
DMF, 40 °C
89%
OTES
TESO
II.7
Pd(OAc)2
SPhos
B2pin2
K3PO4
1,4-Dioxane, 80 °C
92%
Bpin
II.8
II.8
Br
Cl
Pd(dppf)Cl2
2M K3PO4 (aq)
1,4-Dioxane, 80 °C
96%
II.9
Pd(OAc)2
SPhos
B2pin2
K3PO4
1,4-Dioxane, 80 °C
93%
II.2

Scheme II.1. Synthesis of intermediate **II.2**.

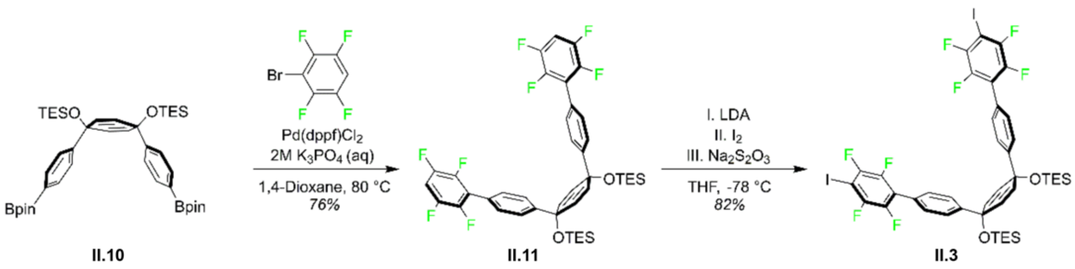
TESO
OTES
Bpin
Bpin
II.10
F
Br
Pd(dppf)Cl2
2M K3PO4 (aq)
1,4-Dioxane, 80 °C
76%
OTES
II.11
I. LDA
II. I2
III. Na2S2O3
THF, -78 °C
82%
I
II.3

Scheme II.2. Synthesis of intermediate **II.3**.

II.4.9. Synthetic Procedures.

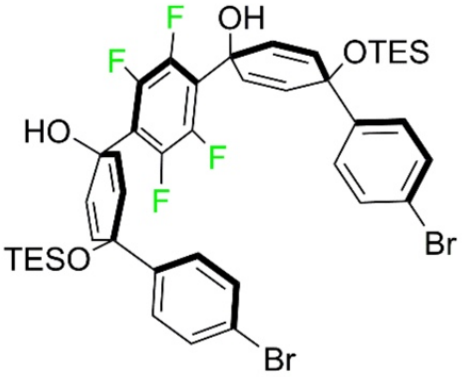

Synthesis of II.6: To a flame-dried 100 mL flask containing THF (30 mL) was added distilled diisopropylamine (0.774 mL, 5.49 mmol, 2.60 equiv). This flask was then cooled to 0 °C at which point *n*BuLi (2.5 M in hexanes, 1.94 mL, 4.85 mmol, 2.30 equiv.) was added dropwise. After stirring for 10 minutes at 0 °C, the flask was then cooled to -78 °C over 45 minutes. To this flask was then added 1,2,4,5-tetrafluorobenzene (neat) (240 uL, 2.11 mmol, 1.00 equiv) followed by **II.5** (as a solution in 3 mL THF) (2.0 g, 5.27 mmol, 2.5 equiv) resulting in a bright yellow solution that slowly became brown/orange over the course of 1 h. After 1 hour of stirring, the reaction was slowly quenched with a 20% acetic acid/methanol solution (5 mL), resulting in a colorless solution which was then brought to room temperature. The organic solvents were then removed via rotary evaporation and the remaining slightly yellow aqueous layer was extracted with ethyl acetate (3 x 75 mL). The combined organic phases were washed with H_2O (3 x 100 mL), and brine (1 x 100 mL), and dried over sodium sulfate. The solvent was removed under reduced pressure to afford a faint yellow oil. Chromatography (0 to 10% EtOAc/Hexanes) of this oil yielded **II.6** as a colorless oil (1.41 g, 74%). ^{1}H NMR (500 MHz, Chloroform-*d*) δ 7.41 (d, *J* = 8.7 Hz, 4H), 7.21 (d, *J* = 8.5 Hz, 4H), 6.30 (d, *J* = 10.2 Hz, 4H), 6.01 (d, *J* = 10.1 Hz, 4H), 2.55 (s, 2H), 0.99 (t, *J* = 7.9 Hz, 18H), 0.69 (q, *J* = 7.9 Hz, 12H). ^{13}C NMR (126 MHz, $CDCl_3$) δ 143.96, 134.16, 131.48, 127.64, 127.41, 121.43, 71.06, 68.02, 7.18, 6.58. ^{19}F NMR (471 MHz, Chloroform-*d*) δ -138.00 (s). δ HRMS (TOF, ES+) (m/z): [M+2Na]+ calculated for $C_{42}H_{47}O_4Na_2Br_2F_4Si_2$, 951.1111; found, 951.1354.

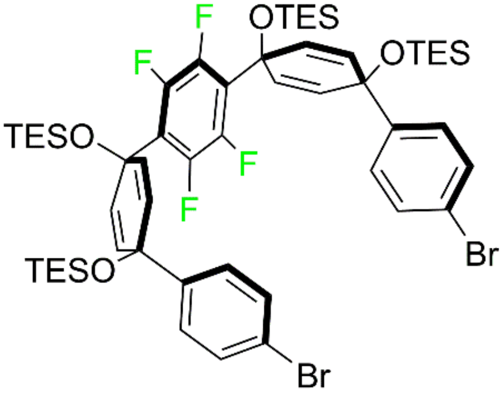

Synthesis of II.7. Imidazole (0.420 g, 6.16 mmol, 4.0 equiv), and **II.6** (1.40 g, 1.54 mmol, 1.00 equiv.) were added to a 100 mL flame-dried RBF, then dissolved in 25 mL DMF. The resulting solution was heated to 40 °C at which point chlorotriethylsilane (TESCl) (0.700 g, 4.63 mmol, 3.00 equiv.) was added dropwise. The reaction was monitored via ^{1}H NMR until all the starting material was consumed (typically 4 hours). Once complete, the reaction was neutralized with sodium bicarbonate followed by extraction of the resulting white suspension with EtOAc (3 x 75 mL). The combined organic phases were washed with 5% LiCl (5 x 100 mL), followed by H_2O (1 x 100 mL), brine (1 x 100 mL), and then placed over sodium sulfate. Removal of solvent via rotary evaporation yielded a yellow oil which was then triturated with MeOH followed by filtration and collection of the resulting white solid to give **II.7** (1.52 g, 89%). ^{1}H NMR (500 MHz, Chloroform-*d*) δ 7.32 (d, *J* = 8.7 Hz, 4H), 7.13 (d, *J* = 8.7 Hz, 4H), 6.35 (d, *J* = 9.7 Hz, 4H), 5.95 (d, *J* = 10.2 Hz, 4H), 0.99 – 0.86 (m, 36H), 0.70 – 0.53 (m, 24H). ^{13}C NMR (126 MHz, $CDCl_3$) δ 144.58, 132.84, 131.32, 129.09, 127.32, 121.29, 71.15, 69.87, 7.17, 6.92, 6.53, 6.33. ^{19}F NMR (471 MHz, $CDCl_3$) δ -136.88 (s). δ LRMS (TOF, MALDI) (m/z): [M]+ calculated for $C_{54}H_{76}O_4Br_2F_4Si_4$, 1136.315; found, 1136.425.

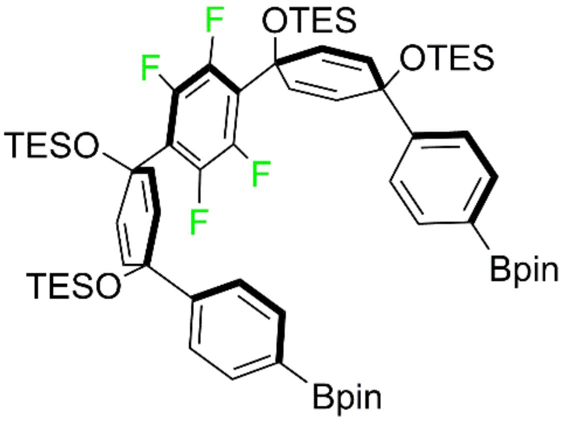

Synthesis of II.8. To a 100 mL flame-dried flask was added Pd(OAc)$_2$ (11.0 mg, 0.0484 mmol, 0.100 equiv), 2-dicyclohexylphosphino-2′,6′dimethoxybiphenyl (50.0 mg, 0.121 mmol, 0.250 equiv), bis(pinacolato)diboron (0.492 g, 1.94 mmol, 4.00 equiv.), **II.7** (0.550 g, 0.484 mmol, 1.00 equiv.), and K_3PO_4 (0.520 g, 2.45 mmol, 5.00 equiv.). After the solids were added, the flask was evacuated and backfilled with nitrogen 5 times. 1,4-dioxane (30 mL) was then added to the flask resulting in an orange solution, which was then placed into an 80 °C oil bath. After 3 h, the resulting black solution was brought to room temperature and the solvent was removed under reduced pressure. To this black solid was added H_2O (50 mL), followed by extraction with hexanes (3 x 75 mL). The combined organic phases were then washed with water (3 × 50 mL), brine (1 × 100 mL), and then dried over sodium sulfate. After removing the organic solvent via rotary evaporation, the resulting white solid was then washed with plenty of methanol, which after filtration gave **II.8** as a white solid (2.99 g, 92%). ^{1}H NMR (500 MHz, Chloroform-*d*) δ 7.66 (d, *J* = 8.4 Hz, 4H), 7.27 (d, *J* = 8.2 Hz, 4H), 6.34 (d, *J* = 10.1 Hz, 4H), 5.99 (d, *J* = 10.2 Hz, 4H), 1.30 (s, 24H), 0.98 – 0.88 (m, 36H), 0.68 – 0.56 (m, 24H). ^{13}C NMR (126 MHz, $CDCl_3$) δ 148.48, 134.84, 133.04, 128.90, 124.86, 83.78, 71.57, 69.96, 25.00, 7.19, 6.95, 6.59, 6.33. ^{19}F NMR (471 MHz, $CDCl_3$) δ -137.01 (s). δ HRMS (TOF, ES+) (m/z): [M+Na]+ calculated $C_{66}H_{100}O_8NaF_4Si_4B_2$, 1253.6515; found, 1253.6544.

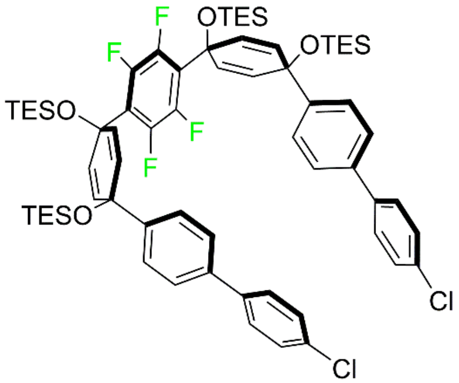

Synthesis of II.9. To a 100 mL flame-dried flask was added **II.8** (0.296 g, 0.240 mmol, 1 equiv), 1-bromo-4-chlorobenzene (0.276 g, 1.44 mmol, 6 equiv), and [1, 1'bis(diphenylphosphino)ferrocenedichloropalladium (0.018 g, 0.024 mmol, 0.100 equiv). After the solids were added, the flask was evacuated and backfilled with nitrogen 5 times. 1,4-dioxane (10.0 mL) was then added to the flask and the solution was sparged with N_2 for 10 min. before aqueous 2M K_3PO_4 (0.660 mL, 1.32 mmol, 5.5 equiv), sparged with N_2 for 1 h prior to use, was added. The solution was then placed in an 80 °C oil bath and allowed to stir for 12 h. The next day, the reddish-black solution was allowed to come to room temperature before removing the solvent under reduced pressure. Next, H_2O (50 mL) was added, followed by extraction with hexanes (3 x 50 mL). The combined organic phases were then washed with water (3 x 50 mL), brine (1 x 75 mL), and dried over sodium sulfate. After removal of solvent via rotary evaporation, the resulting yellow oil was purified via column chromatography (2-5% EtOAc/Hexanes) to afford a **II.9** as a clean, colorless oil that was pure via NMR. If desired, the oil can be washed with methanol to access the compound as a white solid (0.276 g, 96%). ^{1}H NMR (500 MHz, Chloroform-*d*) δ 7.40 – 7.35 (m, 8H), 7.31 (dd, *J* = 15.0, 8.0 Hz, 8H), 6.37 (d, *J* = 9.7 Hz, 4H), 6.01 (d, *J* = 9.7 Hz, 4H), 0.98 (t, *J* = 7.7 Hz, 19H), 0.91 (t, *J* = 8.9, 7.1 Hz, 19H), 0.67 (q, *J* = 7.9 Hz, 13H), 0.59 (q, *J* = 7.9 Hz, 13H). ^{13}C NMR (126 MHz, Chloroform-*d*) δ 144.74, 139.15, 138.72, 133.27, 133.02, 128.81, 128.77, 128.17, 126.69, 125.91, 71.21, 69.84, 7.06, 6.80, 6.44, 6.21. ^{19}F NMR (471 MHz, Chloroform-*d*) δ -136.83. δ HRMS (TOF, ES+) (m/z): [M+Na]+ calculated for $C_{66}H_{84}O_4NaF_4Si_4Cl_2$, 1221.4658; found, 1221.4629.

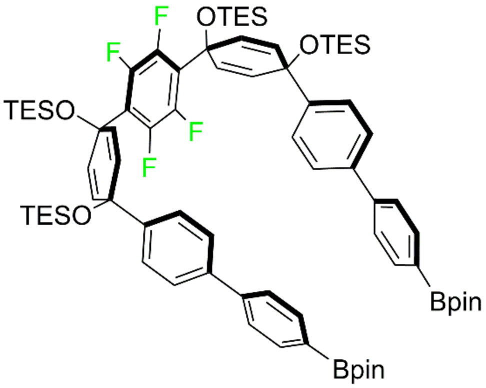

Synthesis of II.2. To a 100 mL flame-dried flask was added $Pd(OAc)_2$ (0.003 g, 0.029 mmol, 0.05 equiv), 2-dicyclohexylphosphino-2’6’dimethoxybiphenyl (0.015 g, 0.036 mmol, 0.125 equiv), bis(pinacolato)diboron (0.584 g, 2.30 mmol, 8 equiv), **II.9** (0.353 g, 0.290 mmol, 1 equiv), and K_3PO_4 (0.228 g, 2.30 mmol, 8 equiv). After the solids were added, the flask was evacuated and backfilled with nitrogen 5 times. 1,4-dioxane (8.0 mL) was then added to the flask and the solution was sparged with N_2 for 10 minutes before being placed in an 80 °C oil bath overnight. The next day, the black solution was brought to room temperature and the solvent was removed under reduced pressure. To the resulting black solid was added H_2O (50 mL), followed by extraction with DCM (3 x 50 mL). The combined organic phases were then washed with water (3 x 50 mL), brine (1 x 100 mL), and then dried over sodium sulfate. After removing the solvent via rotary evaporation, the resulting brown solid was washed with methanol, which after filtration afforded **II.2** as a white solid (0.374 g, 93%). ^{1}H NMR (500 MHz, Chloroform-*d*) δ 7.82 (d, *J* = 7.4 Hz, 4H), 7.52 (d, *J* = 7.4 Hz, 4H), 7.45 (d, *J* = 7.6 Hz, 4H), 7.33 (d, *J* = 7.9 Hz, 4H), 6.36 (d, *J* = 9.8 Hz, 4H), 6.01 (d, 8H), 1.35 (s, 24H), 0.98 (t, *J* = 7.9 Hz, 18H), 0.90 (t, *J* = 7.6 Hz, 18H), 0.67 (q, *J* = 7.9 Hz, 12H), 0.59 (q, *J* = 7.9 Hz, 12H). ^{13}C NMR (126 MHz, Chloroform-*d*) δ 144.66, 143.42, 139.71, 135.16, 133.07, 128.70, 126.93, 126.29, 125.79, 83.77, 71.25, 69.85, 24.88, 7.07, 6.80, 6.44, 6.19. ^{19}F NMR (471 MHz, Chloroform-*d*) δ -136.83 (s). δ HRMS (TOF, ES+) (m/z): [M+Na]+ calculated for $C_{78}H_{108}O_8NaB_2F_4Si_4$, 1405.7141; found, 1405.7137.

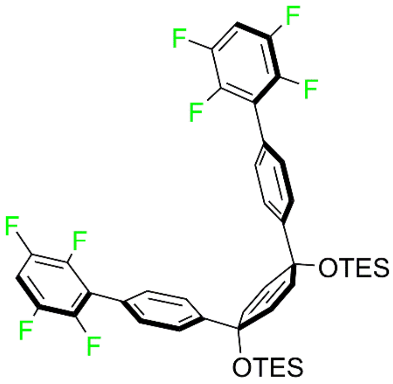

Synthesis of II.11. To a 100 mL flame-dried flask was added **II.10** (0.224 g, 0.300 mmol, 1 equiv) and [1, 1'bis(diphenylphosphino)ferrocenedichloropalladium (0.022, 0.030 mmol, 0.100 equiv). After the solids were added, the flask was evacuated and backfilled with nitrogen 5 times. 1,4-dioxane (8.0 mL) was then added to the flask, followed by 1-bromo-2,3,5,6-tetrafluorobenzene (0.412 g, 1.80 mmol, 6 equiv), and the solution was sparged with N_2 for 10 minutes before 2M K_3PO_4 (0.825 mL, 1.65 mmol, 5.5 equiv), sparged for 1 h prior to use, was added. The solution was then placed in an 80 °C oil bath and allowed to stir overnight. The next day, the black solution was allowed to come to room temperature before removing the solvent under reduced pressure. Next, H_2O (50 mL) was added, followed by extraction with hexanes (3 x 50 mL). The combined organic phases were then washed with water (3 x 50 mL), brine (1 x 75 mL), and dried over sodium sulfate. After removing the solvent via rotary evaporation, the crude, yellow-orange oil was purified via column chromatography (2-5% EtOAc/Hexanes) and **II.11** was isolated as a pale-yellow oil (0.175 g, 74%). ^{1}H NMR (500 MHz, Chloroform-*d*) δ 7.47 (d, *J* = 7.7 Hz, 2H), 7.37 (d, *J* = 7.9 Hz, 2H), 7.04 (p, *J* = 8.4 Hz, 2H), 6.07 (s, 4H), 0.96 (t, *J* = 7.9 Hz, 18H), 0.64 (q, *J* = 7.8 Hz, 12H). ^{13}C NMR (126 MHz, Chloroform-*d*) δ 146.95, 131.58, 129.94, 126.12, 71.38, 7.03, 6.46. ^{19}F NMR (471 MHz, Chloroform-*d*) δ -139.24 (m, *J* = 22.4, 11.3 Hz), -143.81 (m, *J* = 21.1, 12.7, 7.4 Hz). δ HRMS (TOF, ES+) (m/z): [M+Na]+ calculated for $C_{42}H_{44}O_2NaF_8Si_2$, 811.2650; found, 811.2651.

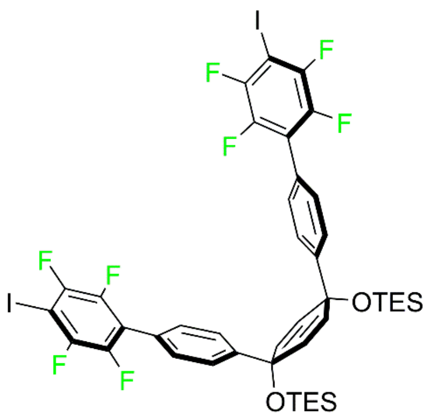

Synthesis of II.3. To a 250 mL flame-dried flask was added 20 mL THF and distilled diisopropylamine (0.093 mL, 0.666 mmol, 3 equiv). This solution was placed in a 0 °C ice bath and allowed to stir for 20 minutes before *n*-butyllithium (2.2 M in hexanes, 0.252 mL, 0.555 mmol, 2.5 equiv) was added dropwise. The solution was allowed to stir for 15 minutes before being transferred to a -78 °C dry ice bath, after which the solution was allowed to cool for 45 minutes. Next, **II.11** (0.175 g, 0.222 mmol, 1 equiv), dissolved in minimal THF (approx. 2 mL), was added dropwise and the solution was allowed to stir for 10 minutes before I_2 (0.279 g, 1.11 mmol, 5 equiv.), dissolved in minimal THF (approx. 2 mL), was added quickly, turning the solution dark orange-brown. The solution was allowed to stir for 2 h before being quenched with concentrated $Na_2S_3O_3$ (approx. 100 mL), resulting in an off-white solution. The solution was brought under reduced pressure to remove THF and 50 mL of water was added, followed by a workup in EtOAc (3 x 50 mL). The combined organic phases were washed with water (3 x 50 mL), brine (1 x 50 mL), and dried over sodium sulfate. After removing the solvent via rotary evaporation, the crude yellow-brown oil was purified via column chromatography (10-25% DCM/Hexanes), resulting in a waxy clear oil. Washing with methanol then afforded **II.3** as a white powdery solid, which was collected via vacuum filtration (0.190 g, 82%). ^{1}H NMR (500 MHz, Chloroform-*d*) δ 7.47 (d, *J* = 8.2 Hz, 2H), 7.36 (d, *J* = 8.0 Hz, 2H), 6.07 (s, 4H), 0.95 (t, *J* = 7.9 Hz, 18H), 0.64 (q, *J* = 7.9 Hz, 12H). ^{13}C NMR (126 MHz, Chloroform-*d*) δ 147.16, 131.57, 129.87, 126.18, 71.38, 7.03, 6.46. ^{19}F NMR (471 MHz, Chloroform-*d*) δ -120.77 (m), -141.47 (m). δ HRMS (TOF, ES+) (m/z): [M]+ calculated for $C_{44}H_{41}O_2F_8Si_2I_2$, 1063.0607; found, 1063.0608.

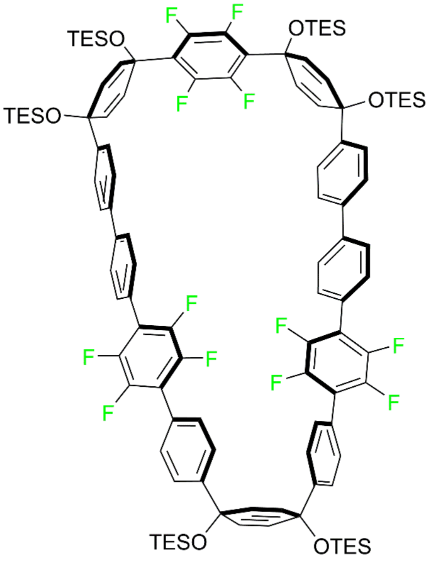

Synthesis of II.4. To a flame-dried 250 mL round bottom flask equipped with a stir bar was added **II.2** (0.183 g, 0.132 mmol, 1.00 equiv.), **II.3** (0.137 g, 0.132 mmol, 1.00 equiv.), and SPhos-Pd-G2 (0.019 g, 0.0264 mmol, 0.200 equiv.). The flask was evacuated and back-filled with N_2 5 times, followed by addition of 1,4-dioxane (44 mL). This solution was then vigorously sparged with N_2 for 1 h at which point the solution was placed into an oil bath at 80 °C. Next, an aqueous solution of 2M K_3PO_4 (4.4 mL, 2.20 mmol, 17.0 equiv), sparged with N_2 for 1 h prior to use, was added. The solution was allowed to stir for 12 hr, after which the solution was brought to room temperature and the solvent was removed under reduced pressure. Water (50 mL) was added, followed by extraction with hexanes (3 x 50 mL). The combined organic phases were washed with water (3 x 50 mL), brine (1 x 50 mL), and dried over sodium sulfate. The solvent was removed via rotary evaporation, and the resulting reddish solid was purified via gel permeation chromatography to afford **II.4** as a white crystalline solid. Alternatively, the crude material can be washed with acetone and minimal isopropyl alcohol at a slight loss of purity (0.164 g, 65%). ^{1}H NMR (500 MHz, Chloroform-*d*) δ 7.64 (d, *J* = 7.7 Hz, 4H), 7.57 – 7.45 (m, 16H), 7.38 (d, *J* = 7.8 Hz, 4H), 6.41 (d, *J* = 9.5 Hz, 4H), 6.11 (s, 4H), 6.06 (d, *J* = 9.6 Hz, 4H), 1.05 – 0.88 (m, 54H), 0.66 (dt, *J* = 28.5, 7.6 Hz, 36H). ^{13}C NMR (151 MHz, Chloroform-*d*) δ 146.95, 144.90, 141.52, 139.01, 133.05, 131.58, 130.49, 130.04, 128.80, 128.63, 127.14, 126.91, 126.14, 125.93, 71.26, 69.86, 7.06, 6.81, 6.47, 6.43, 6.20. ^{19}F NMR (471 MHz, Chloroform-*d*) δ -136.86 (s), -144.33 (m).

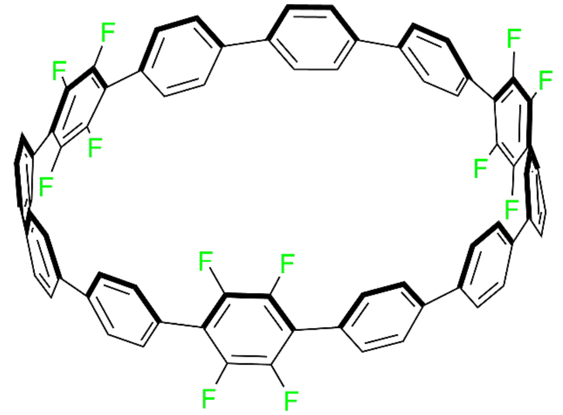

Synthesis of II.1. To a flame-dried 50 mL round bottom flask equipped with a stir bar was added **II.4** (0.174 g, 0.091 mmol, 1.00 equiv.) followed by THF (10 mL). To this solution was then added glacial acetic acid (0.261 mL, 4.54 mmol, 50.0 equiv.), followed by tetrabutylammonium fluoride (1M in THF, 2.27 mL, 2.27 mmol, 25.0 equiv.) dropwise. This solution was then stirred for 18 h at which point H_2O (10 mL) was added, followed by removal of THF via rotary evaporation. The resulting suspension was vacuum filtered, washed with water and minimal DCM, and allowed to fully dry. The resulting crude white solid was then added to an oven-dried 100 mL round bottom flask equipped with a stir bar, followed by THF (8 mL), resulting in a white suspension. Next, H_2SnCl_4 (0.04 M, 18.15 mL, 8 equiv) was added dropwise, after which the solution was allowed to stir for 3 h. Next, the THF was removed via rotary evaporation and water (50 mL) was added followed by extraction in DCM (3 x 50 mL). The combined organic phases were then washed with water (3 x 50 mL), brine (1 x 50 mL), and dried over sodium sulfate. The solvent was removed via rotary evaporation and the resulting white solid was purified via column chromatography (0-40% DCM/Hexanes) using basic alumina as the stationary phase. After the removal of solvent, **II.1** was isolated as a light beige solid (0.004 g, 4%). ^{1}H NMR (500 MHz, Chloroform-*d*) δ 7.69 (d, *J* = 6.2 Hz, 24H), 7.59 (d, *J* = 8.2 Hz, 12H). ^{19}F NMR (471 MHz, Chloroform-*d*) δ -143.82 (s). Due to insolubility, ^{13}C NMR data could not be obtained. MALDI TOF, m/z calculated for $C_{72}H_{36}F_{12}$ (M)+ 1128.2625, found 1128.0620.

II.4.10. ^{1}H NMR Spectra.

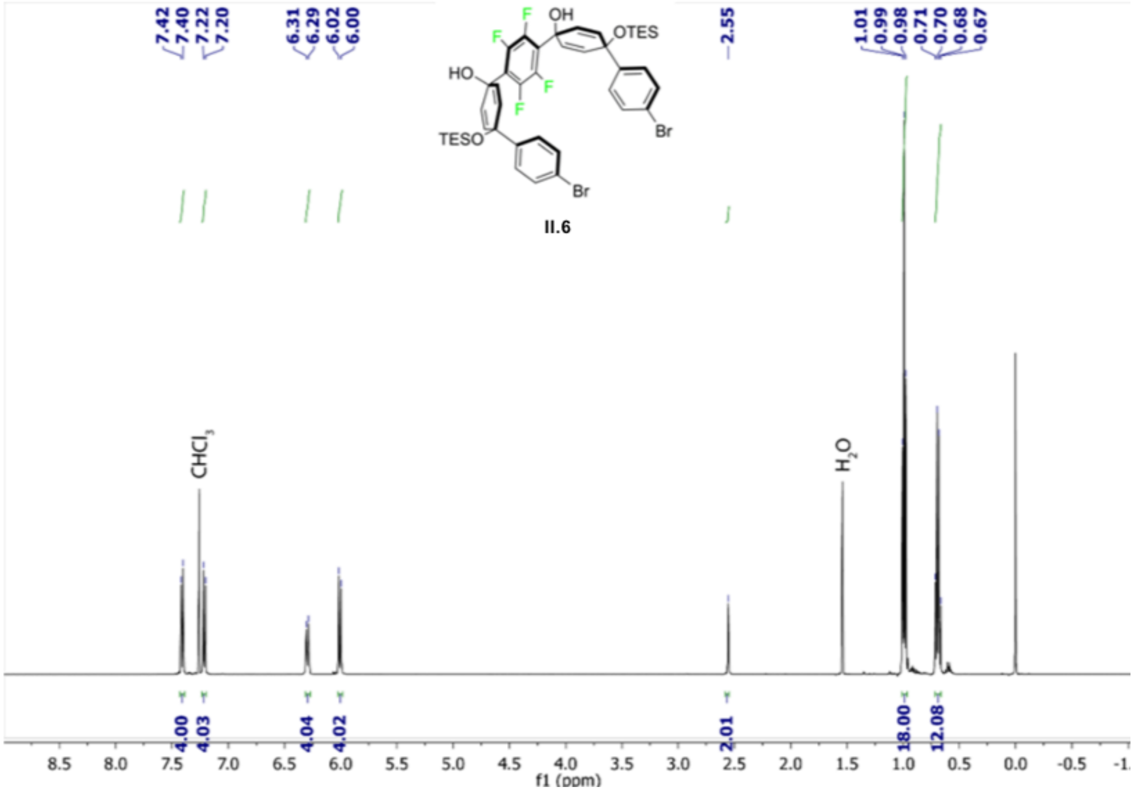

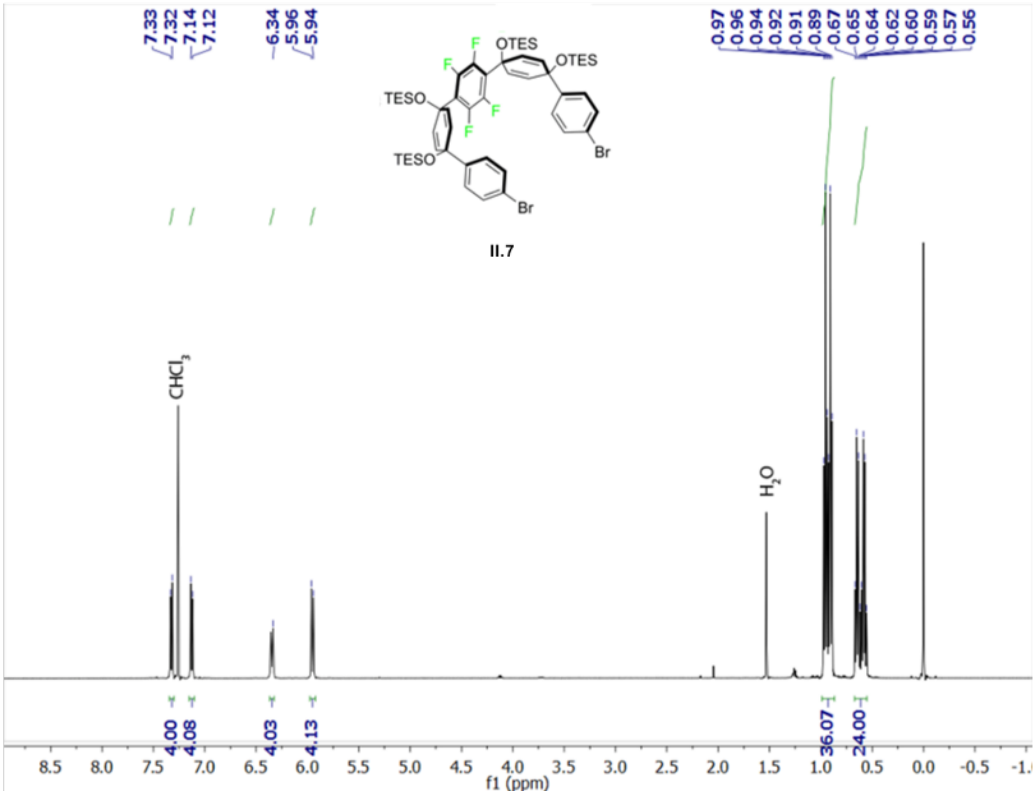

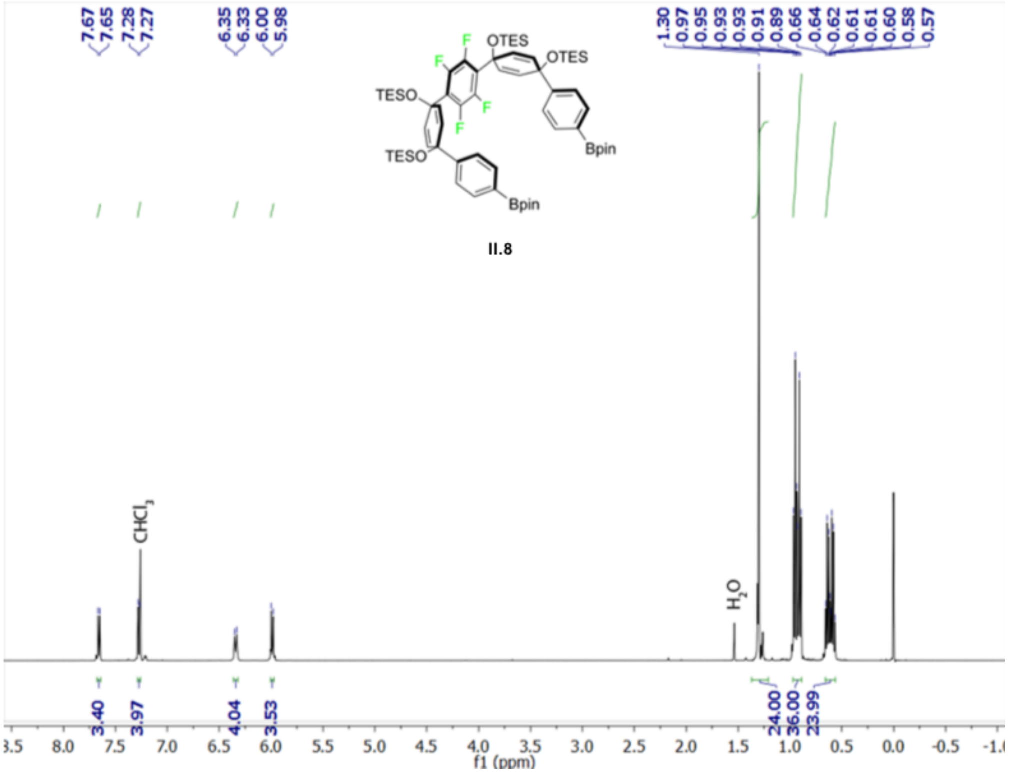

II.8

7.67
7.65
7.28
7.27
6.35
6.33
6.00
5.98
1.30
0.97
0.95
0.93
0.93
0.91
0.89
0.66
0.64
0.62
0.61
0.61
0.60
0.58
0.57
OTES
OTES
TESO
TESO
F
F
F
F
Bpin
Bpin
CHCl$_3$
H$_2$O
3.40
3.97
4.04
3.53
24.00
36.00
23.99
8.5
8.0
7.5
7.0
6.5
6.0
5.5
5.0
4.5
4.0
3.5
3.0
2.5
2.0
1.5
1.0
0.5
0.0
-0.5
-1.0
f1 (ppm)

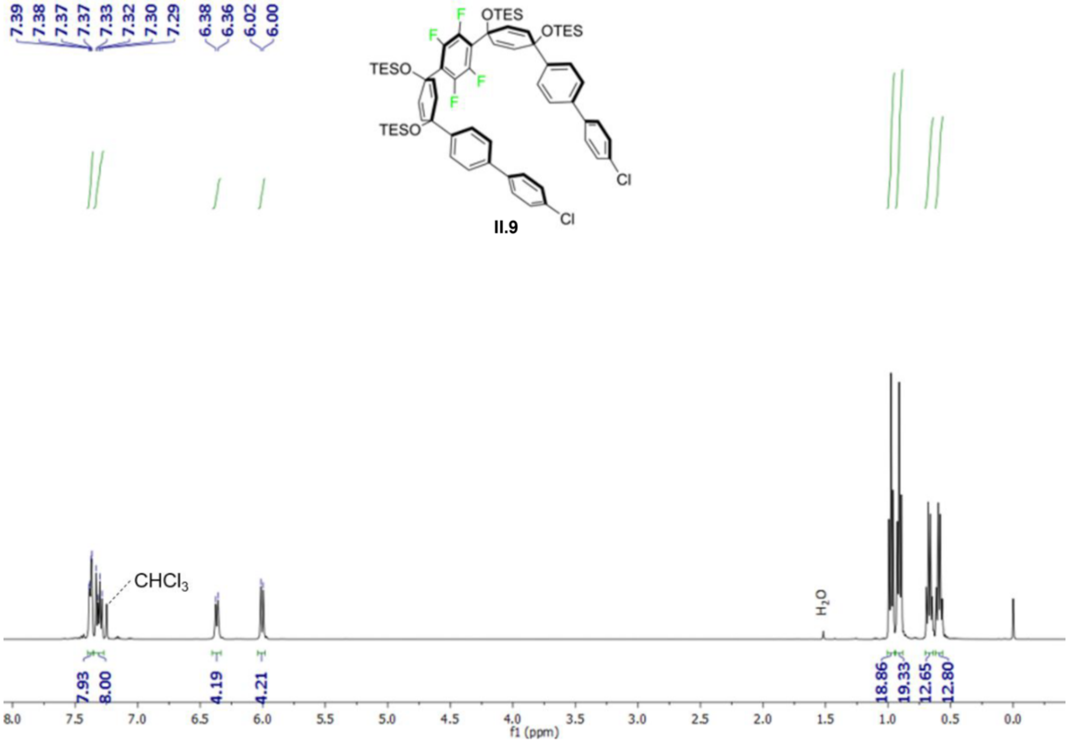

II.9

7.39
7.38
7.37
7.37
7.33
7.32
7.30
7.29
6.38
6.36
6.02
6.00
OTES
OTES
TESO
TESO
F
F
F
F
Cl
Cl
CHCl$_3$
H$_2$O
7.93
8.00
4.19
4.21
18.86
19.33
12.65
12.80
8.0
7.5
7.0
6.5
6.0
5.5
5.0
4.5
4.0
3.5
3.0
2.5
2.0
1.5
1.0
0.5
0.0
f1 (ppm)

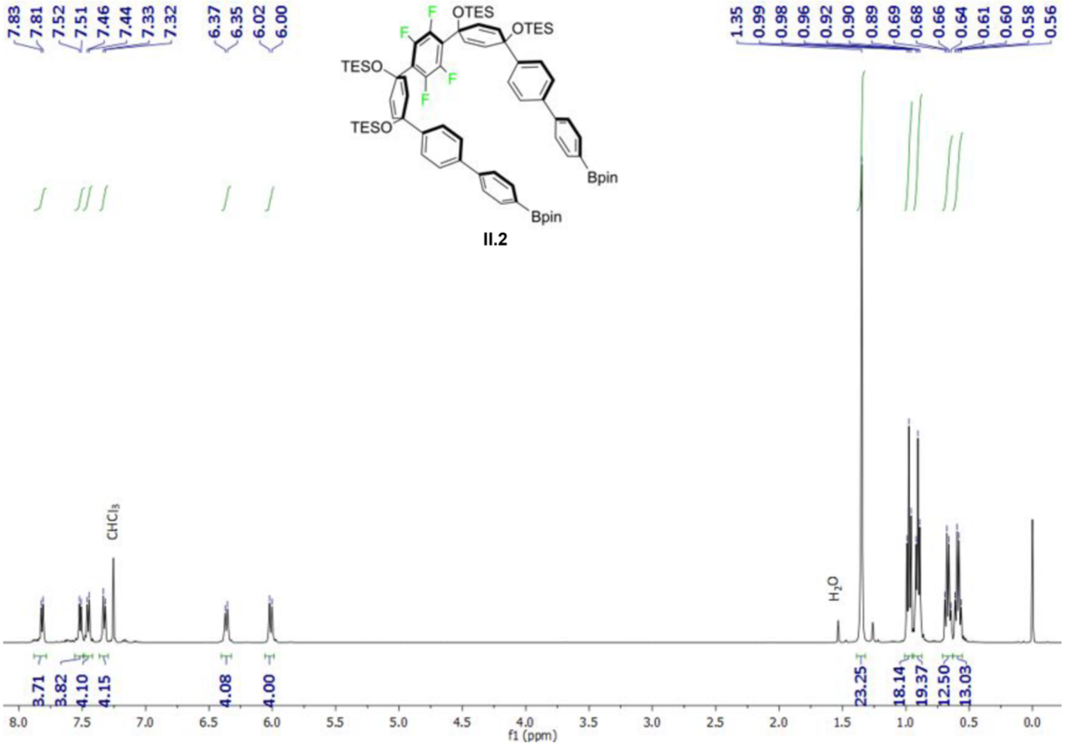
7.83
7.81
7.52
7.51
7.46
7.44
7.33
7.32
6.37
6.35
6.02
6.00
1.35
0.99
0.98
0.96
0.92
0.90
0.89
0.69
0.68
0.66
0.64
0.61
0.60
0.58
0.56
OTES
OTES
TESO
TESO
F
F
F
F
Bpin
Bpin
CHCl3
H2O
3.71
3.82
4.10
4.15
4.08
4.00
23.25
18.14
19.37
12.50
13.03
8.0
7.5
7.0
6.5
6.0
5.5
5.0
4.5
4.0
3.5
3.0
2.5
2.0
1.5
1.0
0.5
0.0
f1 (ppm)

II.2

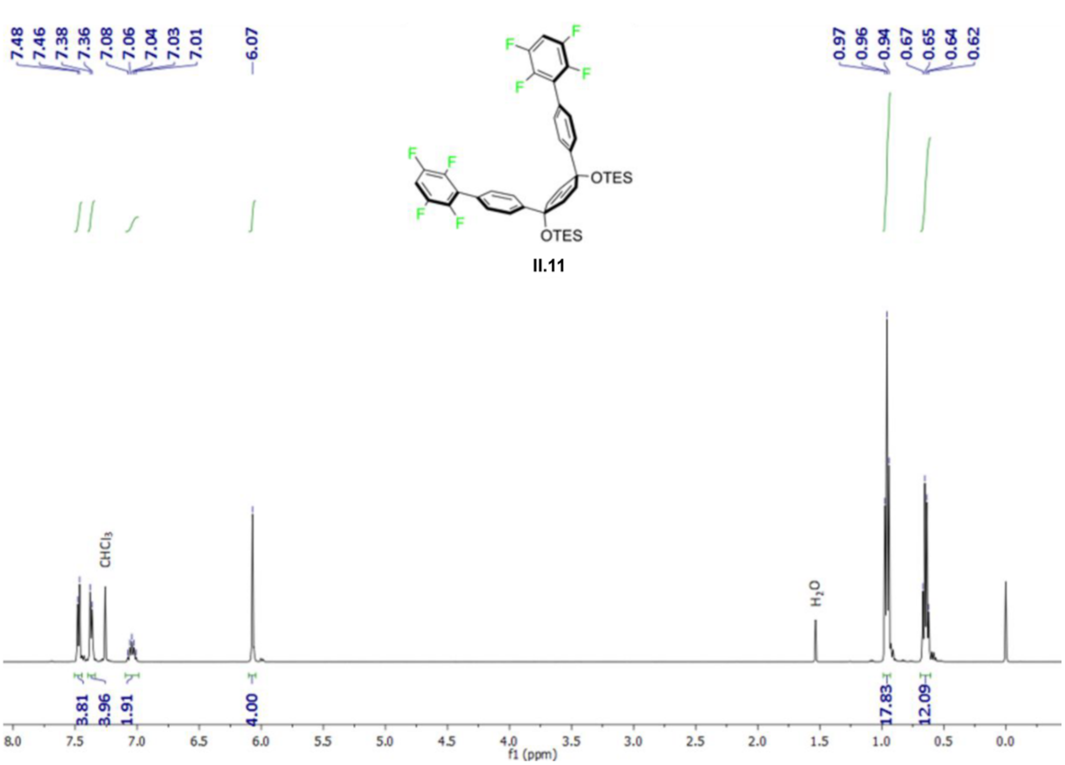
7.48
7.46
7.38
7.36
7.08
7.06
7.04
7.03
7.01
6.07
0.97
0.96
0.94
0.67
0.65
0.64
0.62
F
F
F
F
F
F
F
F
OTES
OTES
CHCl3
H2O
3.81
3.96
1.91
4.00
17.83
12.09
8.0
7.5
7.0
6.5
6.0
5.5
5.0
4.5
4.0
3.5
3.0
2.5
2.0
1.5
1.0
0.5
0.0
f1 (ppm)

II.11

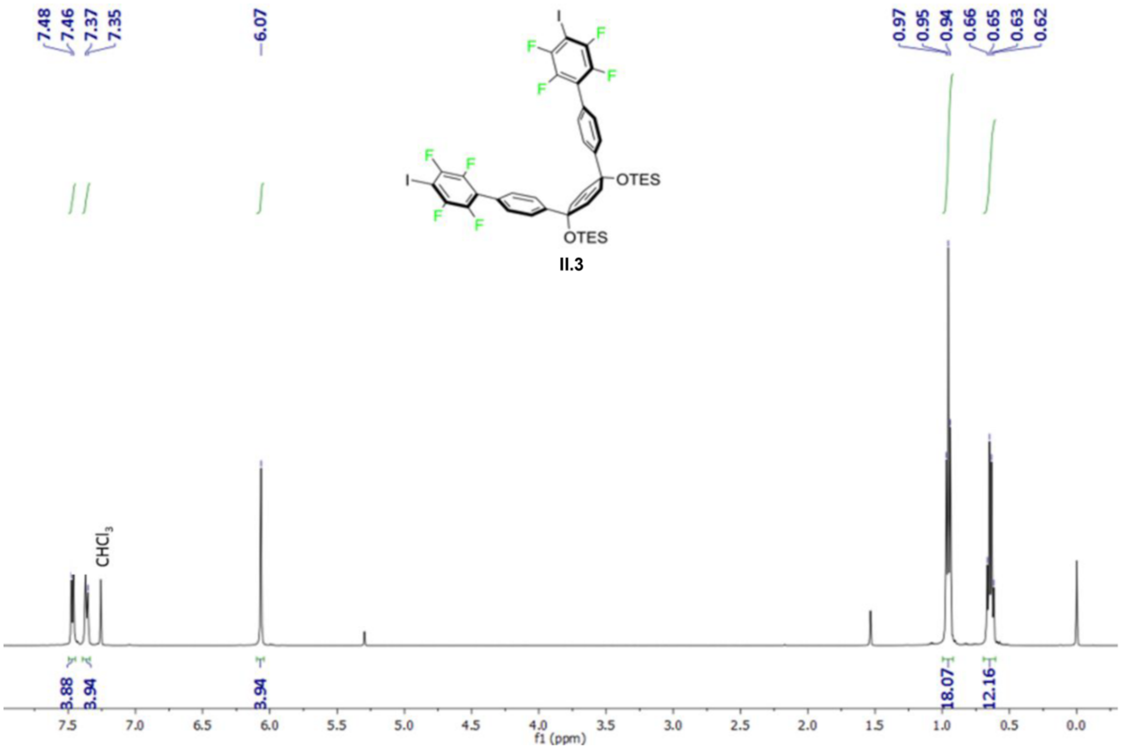
7.48
7.46
7.37
7.35
6.07
0.97
0.95
0.94
0.66
0.65
0.63
0.62
I
F
F
F
F
I
F
F
F
F
OTES
OTES
CHCl$_3$
3.88
3.94
3.94
18.07
12.16
7.5
7.0
6.5
6.0
5.5
5.0
4.5
4.0
3.5
3.0
2.5
2.0
1.5
1.0
0.5
0.0
f1 (ppm)

II.3

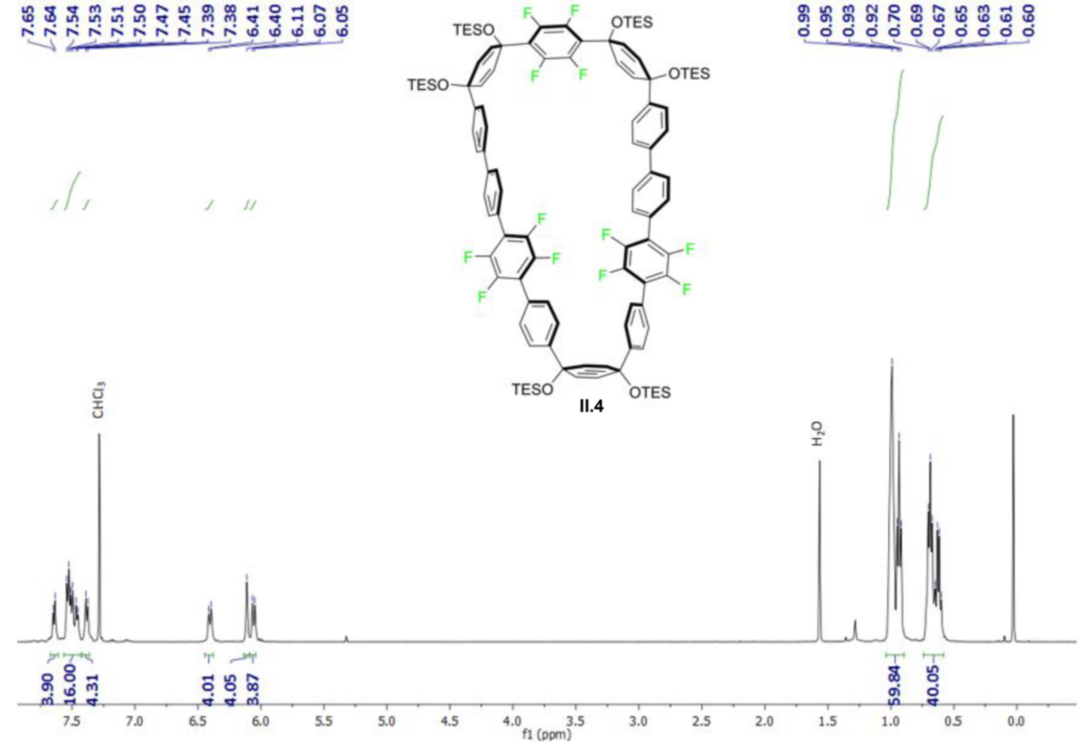
7.65
7.64
7.54
7.53
7.51
7.50
7.47
7.45
7.39
7.38
6.41
6.40
6.11
6.07
6.05
0.99
0.95
0.93
0.92
0.70
0.69
0.67
0.65
0.63
0.61
0.60
TESO
TESO
OTES
OTES
TESO
OTES
F
F
F
F
F
F
F
F
F
F
F
F
CHCl$_3$
H$_2$O
3.90
16.00
4.31
4.01
4.05
3.87
59.84
40.05
7.5
7.0
6.5
6.0
5.5
5.0
4.5
4.0
3.5
3.0
2.5
2.0
1.5
1.0
0.5
0.0
f1 (ppm)

II.4

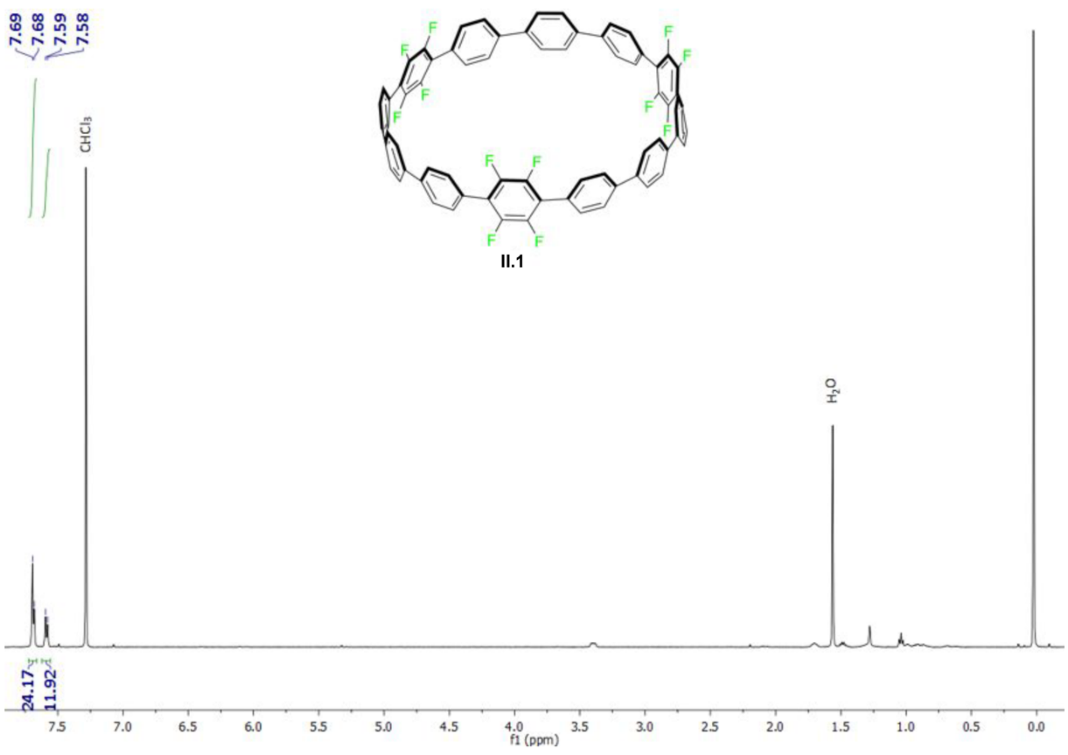

II.4.11. ^{13}C NMR Spectra.

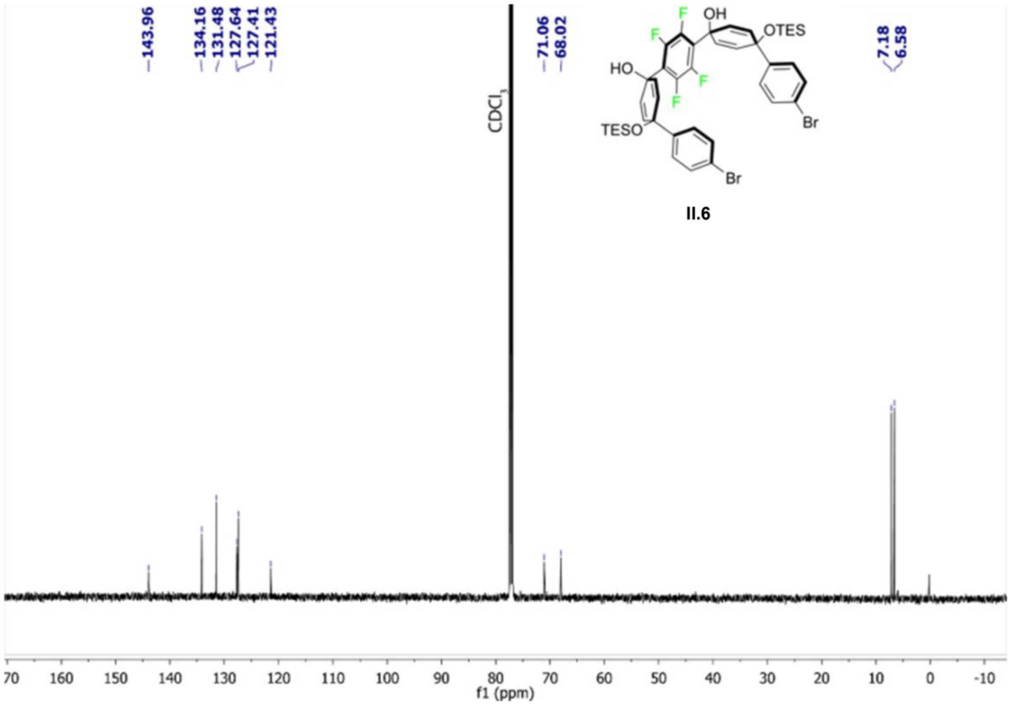

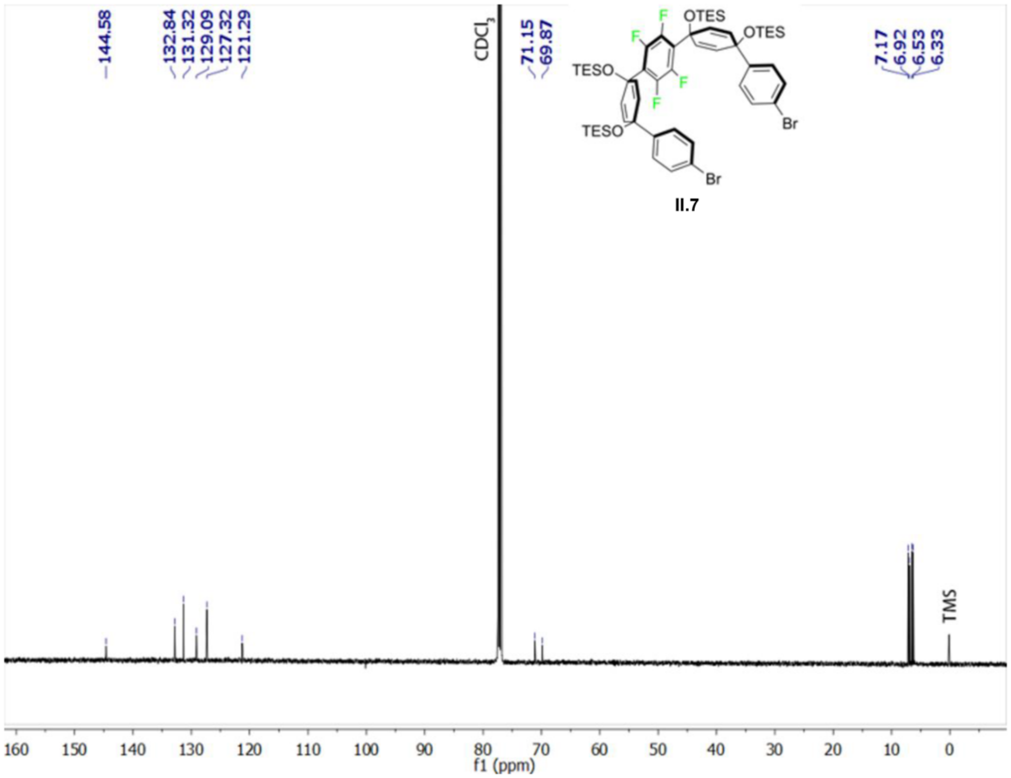
144.58
132.84
131.32
129.09
127.32
121.29
CDCl3
71.15
69.87
7.17
6.92
6.53
6.33
TMS
OTES
OTES
TESO
TESO
F
F
F
F
Br
Br
160 150 140 130 120 110 100 90 80 70 60 50 40 30 20 10 0
f1 (ppm)

II.7

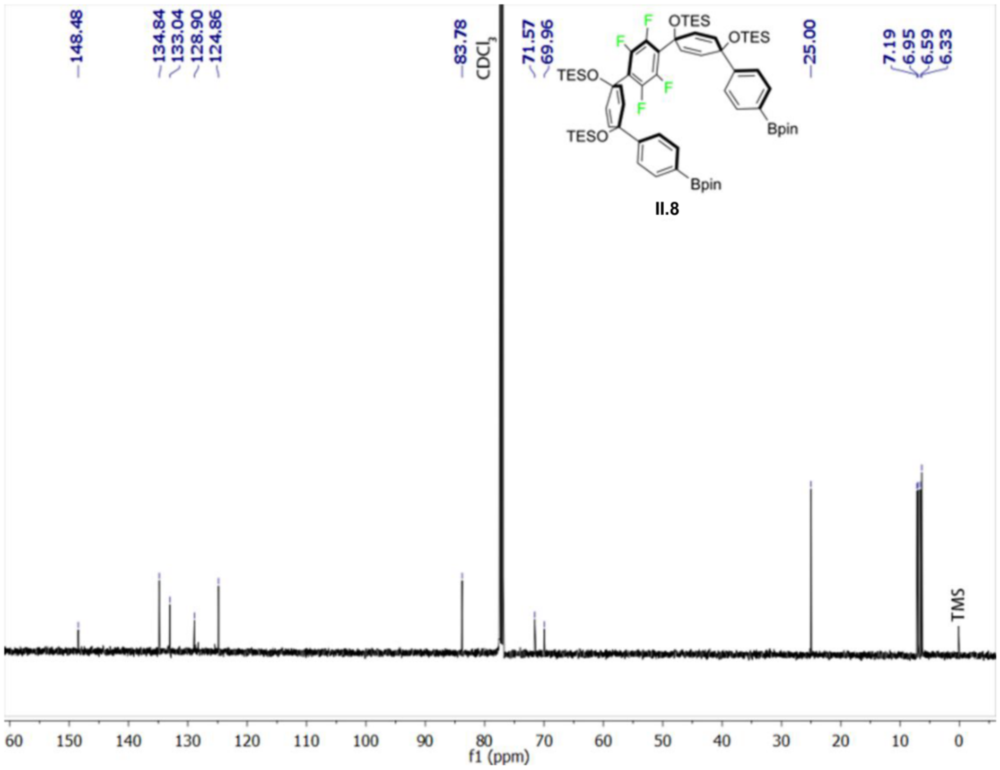
148.48
134.84
133.04
128.90
124.86
83.78
CDCl3
71.57
69.96
25.00
7.19
6.95
6.59
6.33
TMS
OTES
OTES
TESO
TESO
F
F
F
F
Bpin
Bpin
60 150 140 130 120 110 100 90 80 70 60 50 40 30 20 10 0
f1 (ppm)

II.8

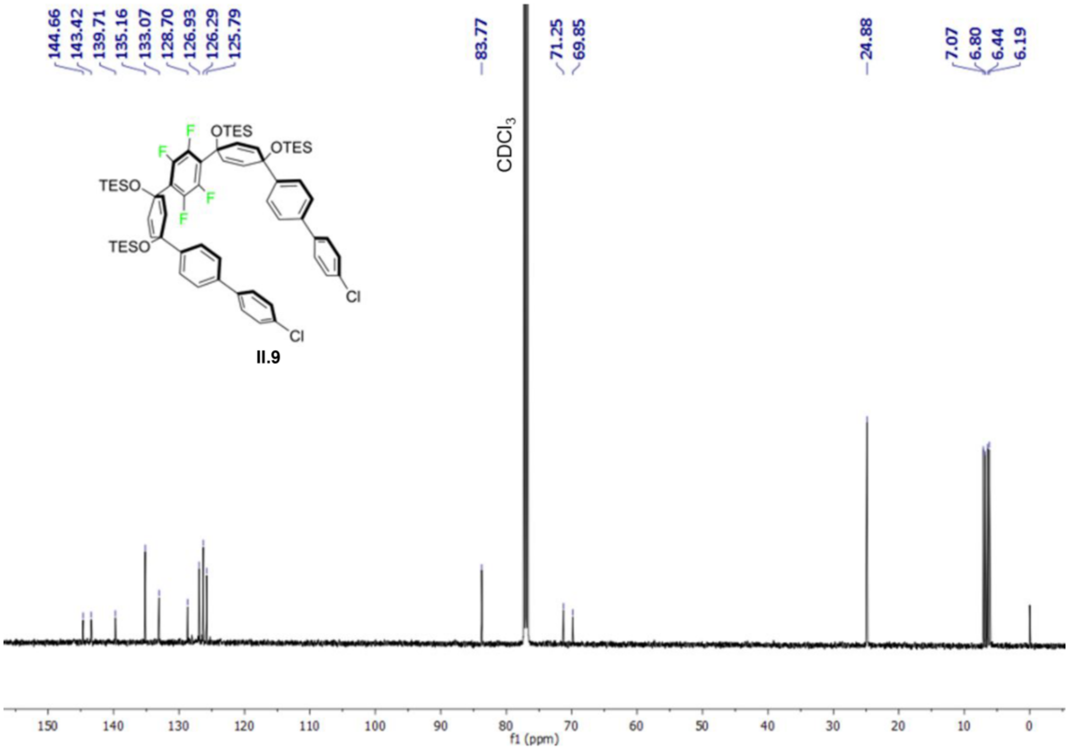
144.66
143.42
139.71
135.16
133.07
128.70
126.93
126.29
125.79
83.77
71.25
69.85
24.88
7.07
6.80
6.44
6.19
CDCl3
F
F
F
F
OTES
OTES
TESO
TESO
Cl
Cl
150 140 130 120 110 100 90 80 70 60 50 40 30 20 10 0
f1 (ppm)

II.9

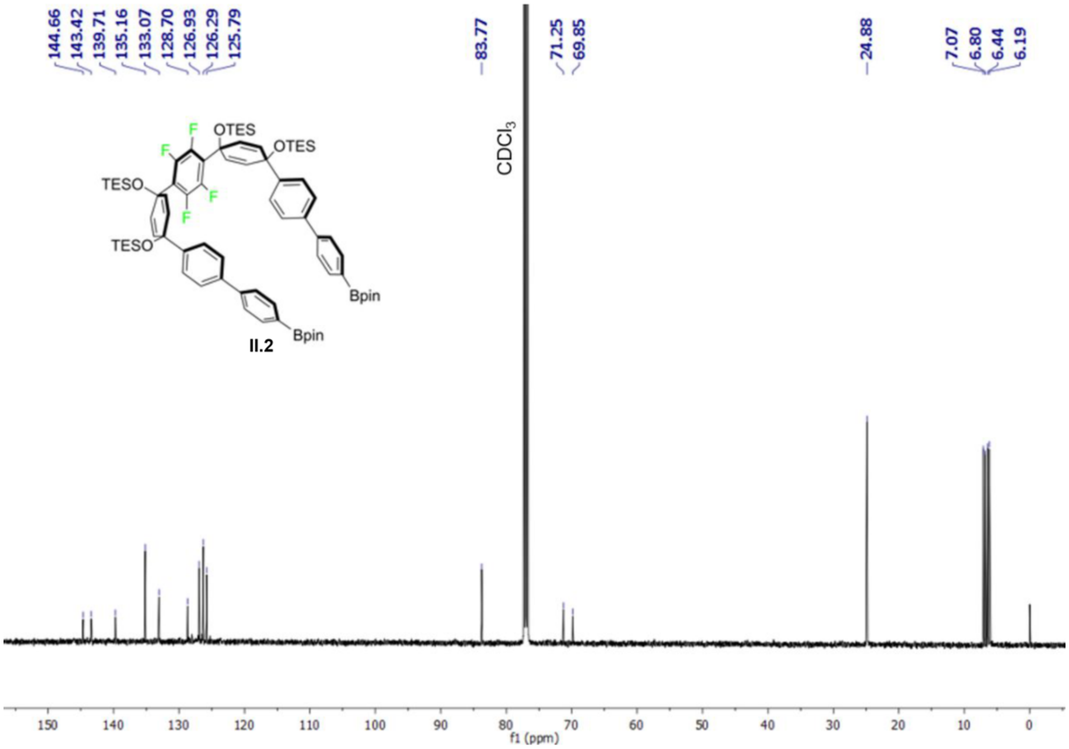
144.66
143.42
139.71
135.16
133.07
128.70
126.93
126.29
125.79
83.77
71.25
69.85
24.88
7.07
6.80
6.44
6.19
CDCl3
F
F
F
F
OTES
OTES
TESO
TESO
Bpin
Bpin
150 140 130 120 110 100 90 80 70 60 50 40 30 20 10 0
f1 (ppm)

II.2

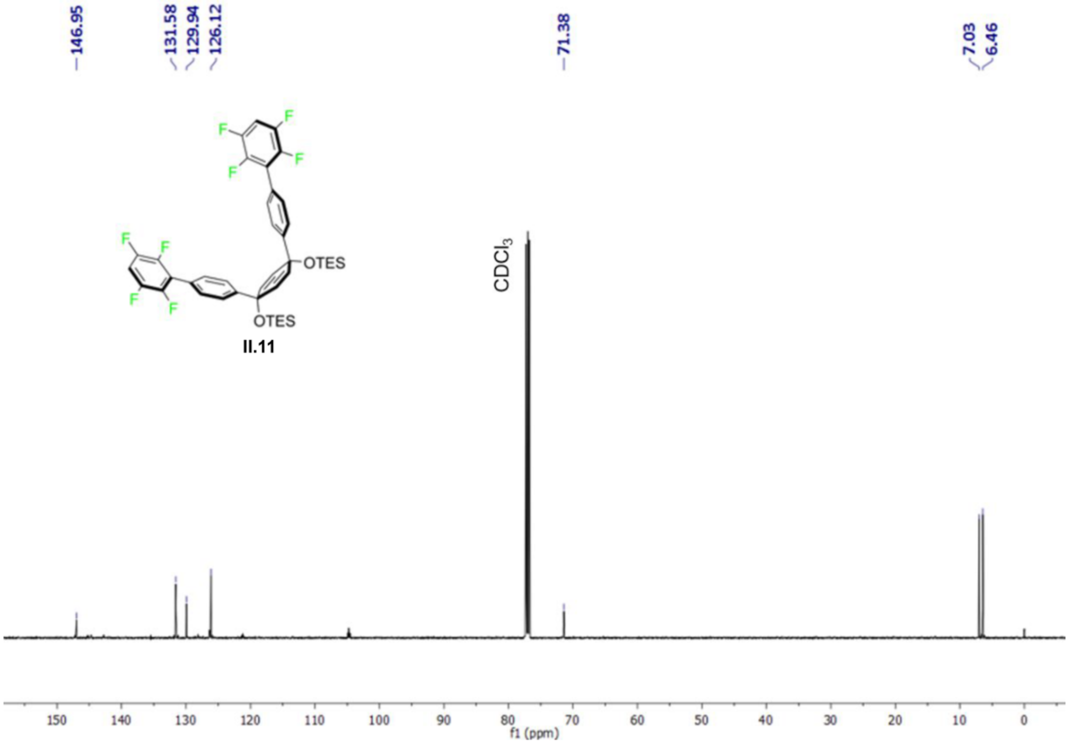
146.95
131.58
129.94
126.12
71.38
7.03
6.46
CDCl3
F
F
F
F
F
F
F
F
OTES
OTES
150
140
130
120
110
100
90
80
70
60
50
40
30
20
10
0
f1 (ppm)

II.11

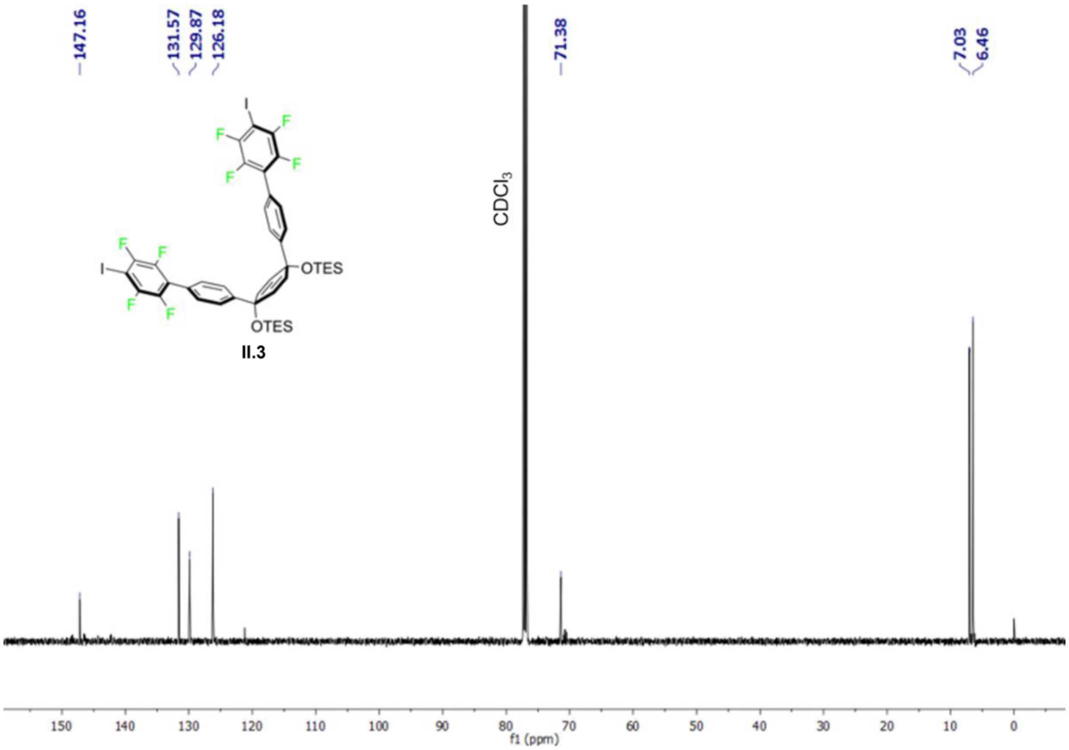
147.16
131.57
129.87
126.18
71.38
7.03
6.46
CDCl3
I
F
F
F
F
I
F
F
F
F
OTES
OTES
150
140
130
120
110
100
90
80
70
60
50
40
30
20
10
0
f1 (ppm)

II.3

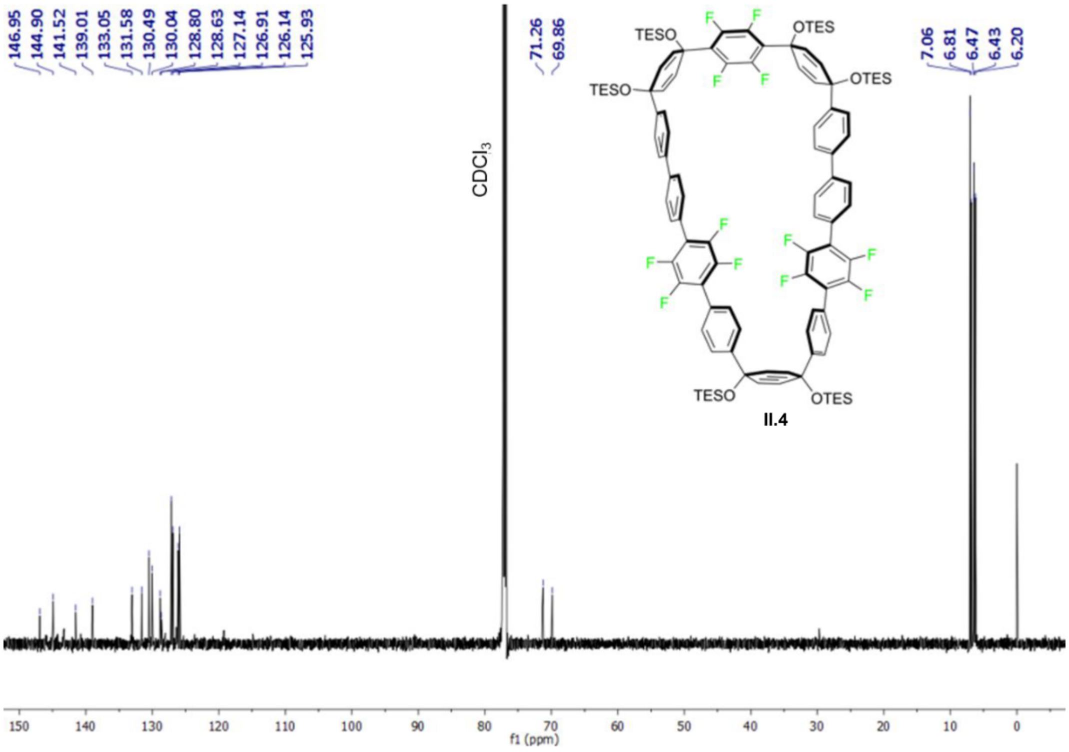

II.4

II.4.12. ^{19}F NMR Spectra.

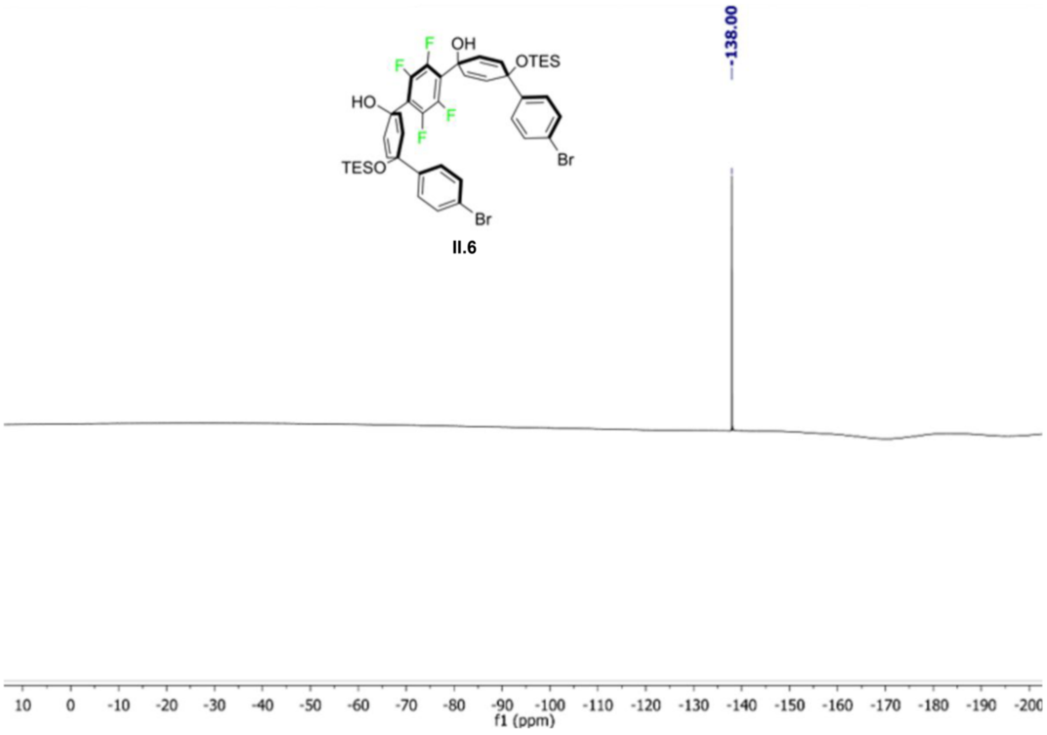

II.6

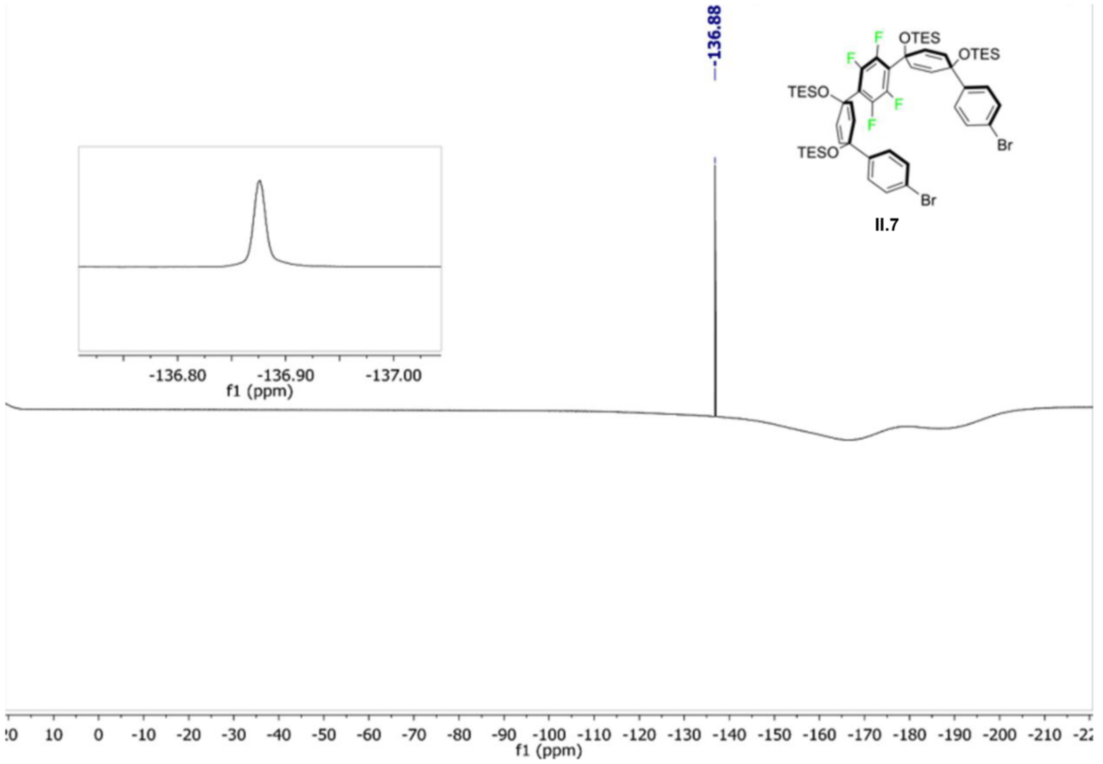
-136.88
OTES
OTES
F
F
F
F
TESO
TESO
Br
Br
II.7
-136.80
-136.90
-137.00
f1 (ppm)
10
0
-10
-20
-30
-40
-50
-60
-70
-80
-90
-100
-110
-120
-130
-140
-150
-160
-170
-180
-190
-200
-210
f1 (ppm)

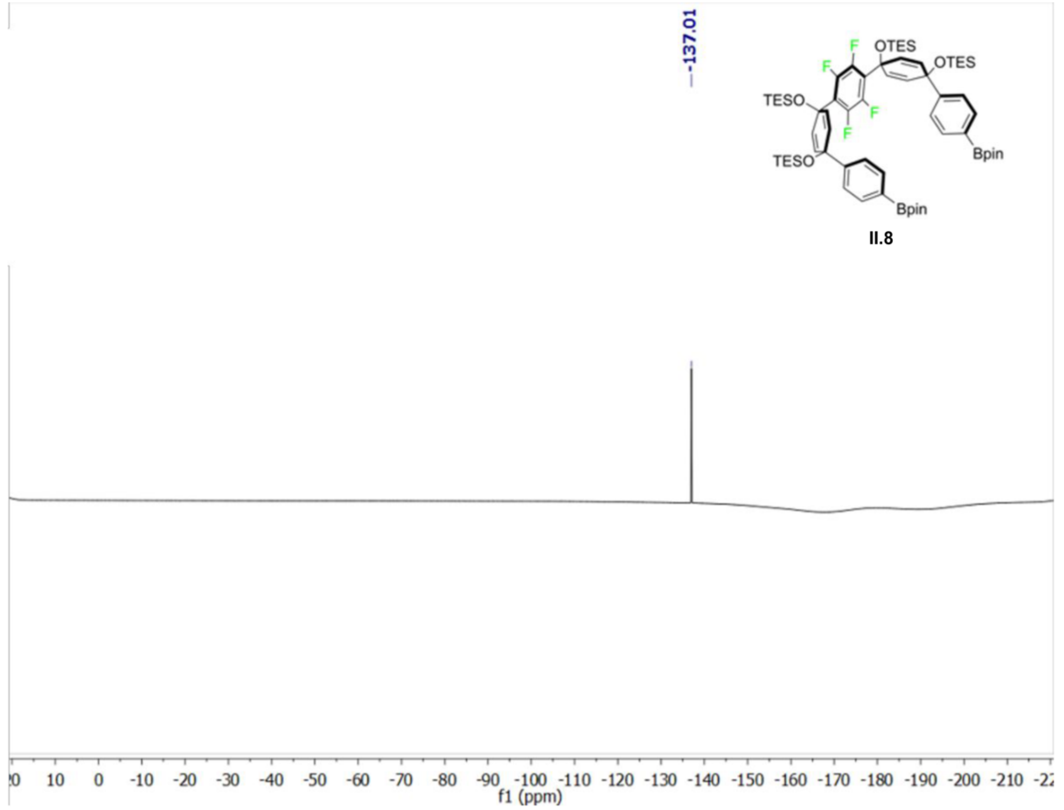
-137.01
OTES
OTES
F
F
F
F
TESO
TESO
Bpin
Bpin
II.8
10
0
-10
-20
-30
-40
-50
-60
-70
-80
-90
-100
-110
-120
-130
-140
-150
-160
-170
-180
-190
-200
-210
f1 (ppm)

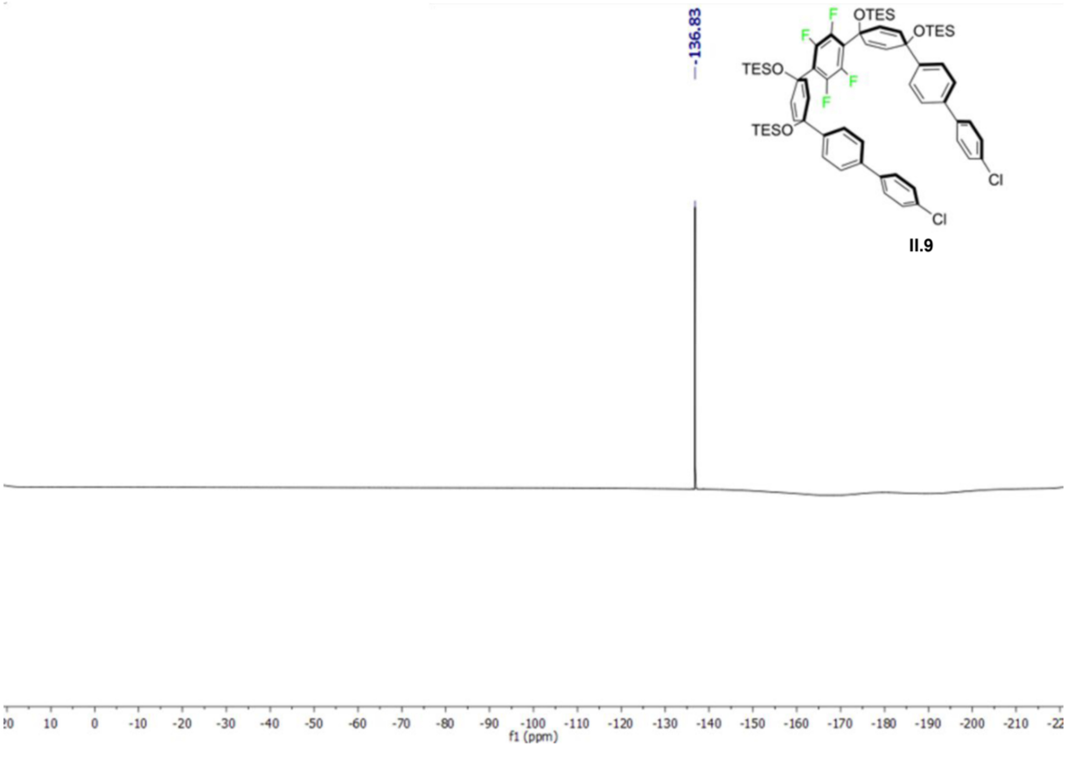
-136.83
F
F
F
F
OTES
OTES
TESO
TESO
Cl
Cl
20 10 0 -10 -20 -30 -40 -50 -60 -70 -80 -90 -100 -110 -120 -130 -140 -150 -160 -170 -180 -190 -200 -210 -22
f1 (ppm)

II.9

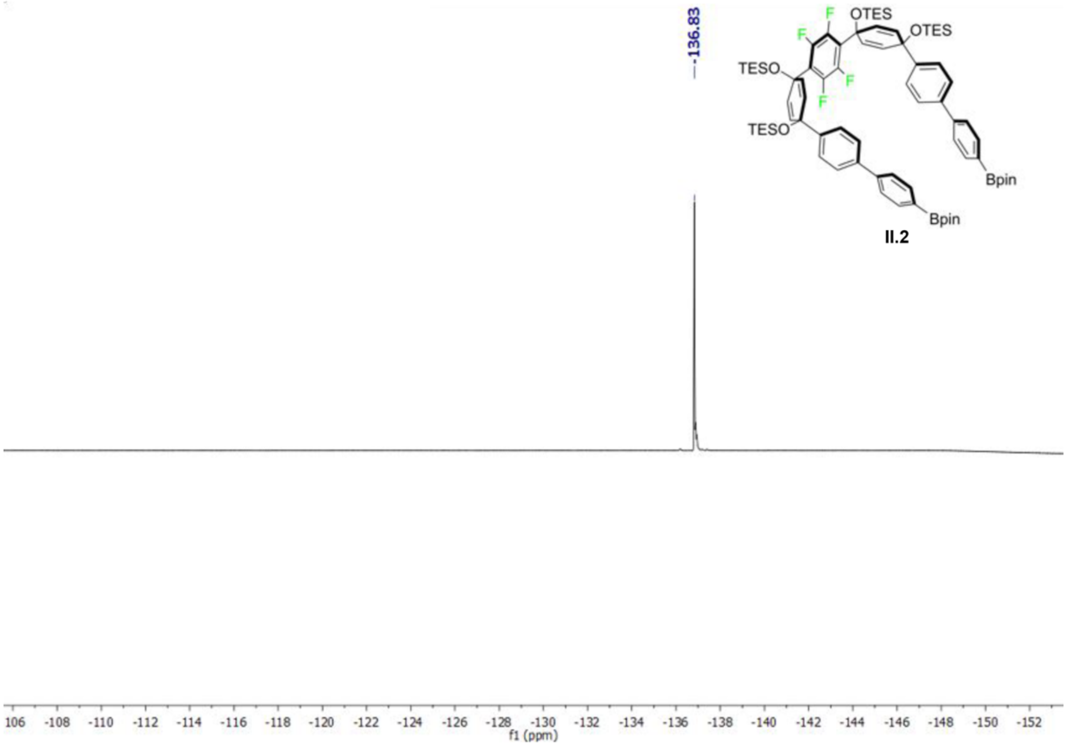
-136.83
F
F
F
F
OTES
OTES
TESO
TESO
Bpin
Bpin
106 -108 -110 -112 -114 -116 -118 -120 -122 -124 -126 -128 -130 -132 -134 -136 -138 -140 -142 -144 -146 -148 -150 -152
f1 (ppm)

II.2

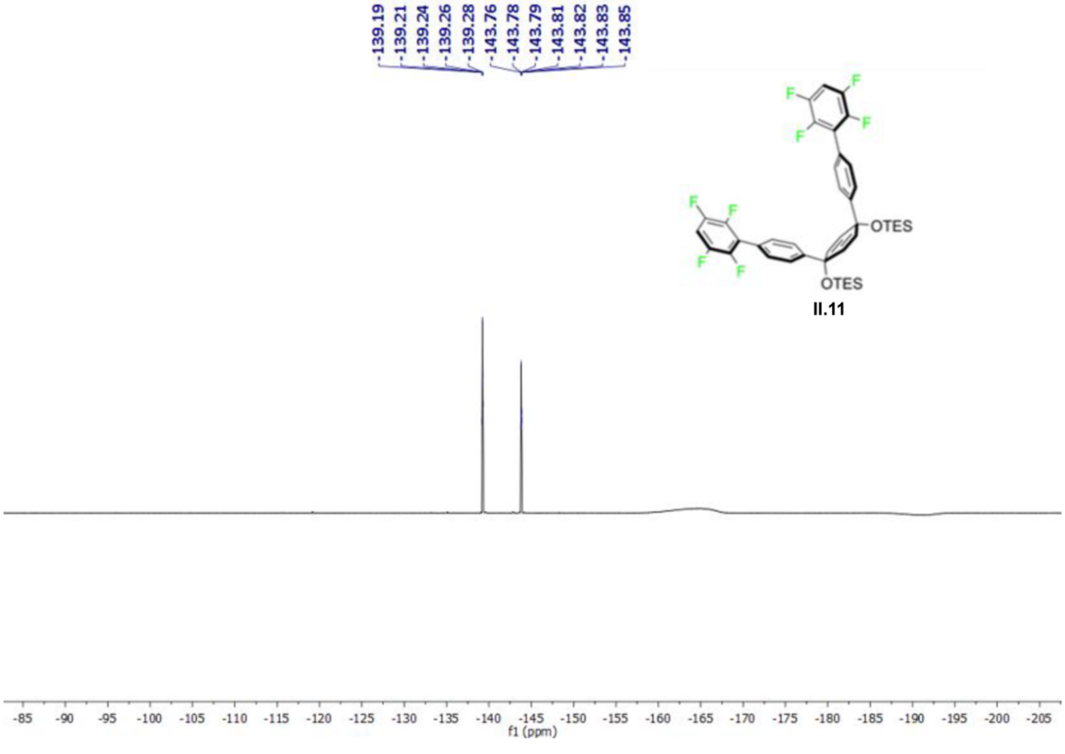
-139.19
-139.21
-139.24
-139.26
-139.28
-143.76
-143.78
-143.79
-143.81
-143.82
-143.83
-143.85
F
F
F
F
F
F
F
F
OTES
OTES
-85 -90 -95 -100 -105 -110 -115 -120 -125 -130 -135 -140 -145 -150 -155 -160 -165 -170 -175 -180 -185 -190 -195 -200 -205
f1 (ppm)

II.11

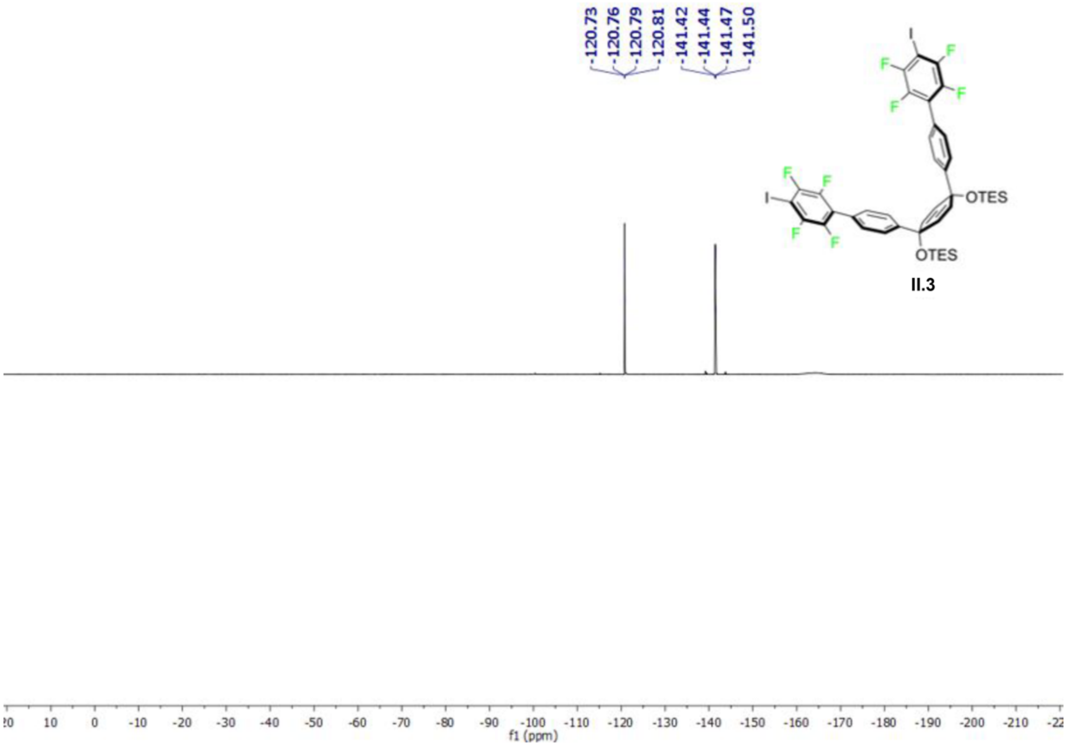
-120.73
-120.76
-120.79
-120.81
-141.42
-141.44
-141.47
-141.50
I
F
F
F
F
I
F
F
F
F
OTES
OTES
20 10 0 -10 -20 -30 -40 -50 -60 -70 -80 -90 -100 -110 -120 -130 -140 -150 -160 -170 -180 -190 -200 -210 -22
f1 (ppm)

II.3

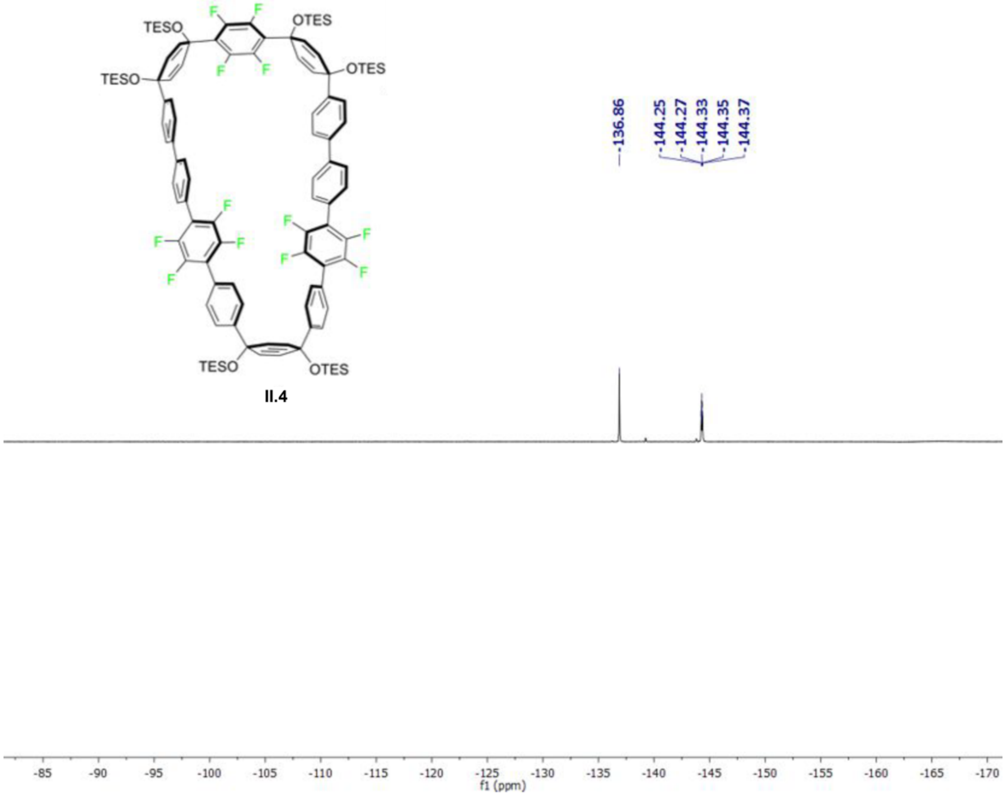
II.4
TESO
TESO
OTES
OTES
TESO
OTES
F
-136.86
-144.25
-144.27
-144.33
-144.35
-144.37
-85
-90
-95
-100
-105
-110
-115
-120
-125
-130
-135
-140
-145
-150
-155
-160
-165
-170
f1 (ppm)

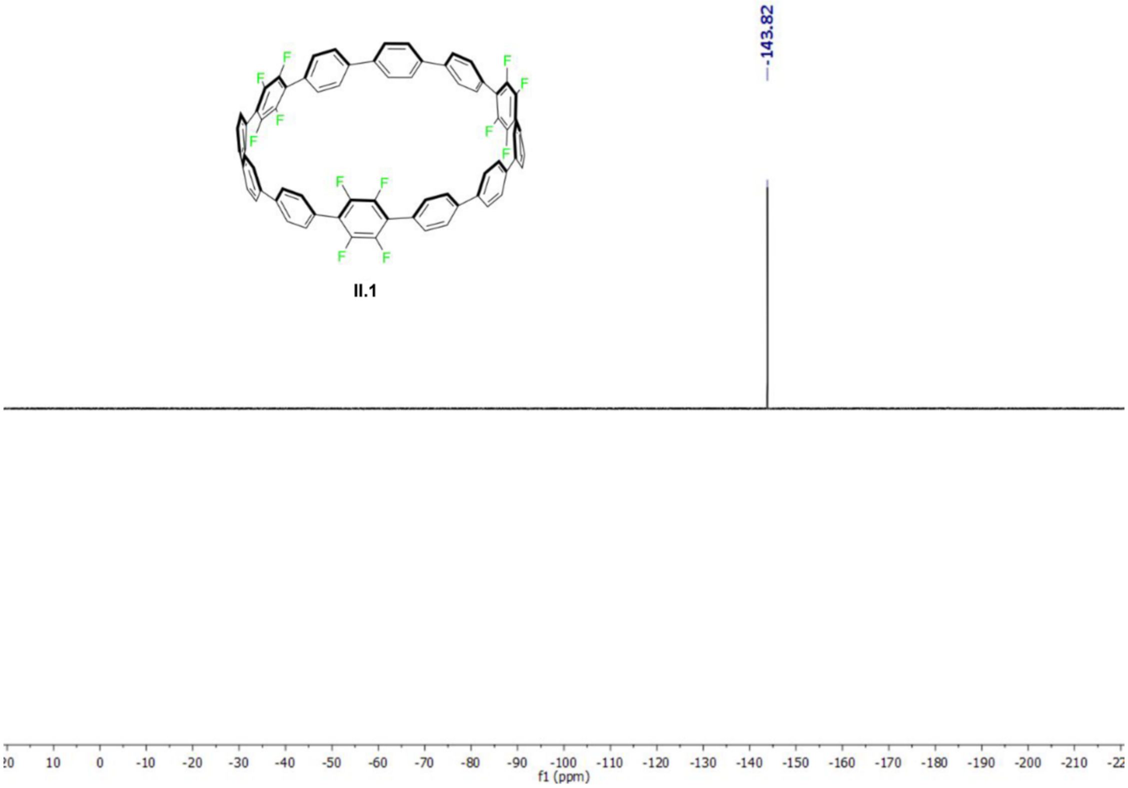
II.1
F
-143.82
10
0
-10
-20
-30
-40
-50
-60
-70
-80
-90
-100
-110
-120
-130
-140
-150
-160
-170
-180
-190
-200
-210
f1 (ppm)

II.5. Bridge to Chapter III.

In Chapter **II**, we disclosed the design and synthesis of a fluorinated nanohoop that, via organofluorine interactions, self-assembles into arrays of non-covalent nanotubes. Having demonstrated the success of our fluorination-based design strategy, we next sought to explore its generality in guiding tubular self-assembly for fluorinated CPPs of different diameters or with different fluorination symmetries (i.e. two-fold symmetry versus the three-fold symmetry exhibited by **II.1**). Additionally, we still questioned whether or not we could truly refer to the tubular assemblies formed by **II.1** as "CNT mimics" as we had not provided evidence of CNT-like behavior, such as permanently accessible channels. Chapter **III** examines our efforts to address these questions, first discussing the synthesis and crystal structure analyses of two new fluorinated nanohoops, followed by the results of N_2 uptake measurements on a solid sample of **II.1** in order to determine the accessibility of its CNT-like channels. We then close the chapter with a copmputational analysis of the organofluorine interactions observed in the crystal structures of these fluorinated nanohoops, providing critical details on the role these interactions play in their self-assembly.

CHAPTER III

PRECISION NANOTUBE MIMICS VIA SELF-ASSEMBLY OF PROGRAMMED CARBON NANOHOOPS

Chapter **III** is based primarily on work published in the *Journal of Organic Chemistry* in 2020. I am co-first author on this work along with Dr. Jeff M.Van Raden. Dr. Van Raden and I both contributed equally to the design, synthesis, and characterization of the molecules described in the manuscript and shared writing and editing duties along with Professor Ramesh Jasti. Dr. Lev N. Zakharov provided the X-ray crystallography data described in the manuscript. Andrés Pérez-Guardiola, Angel Jose Pérez-Jiménez, and Juan-Carlos Sancho-García carried out the computational work included in the manuscript and provided relevant written discussion. Checkers R. Marshall and Professor Carl K. Brozek acquired and analyzed the N_2 uptake data described in the manuscript as well as providing relevant figures and written discussion. N_2 uptake data for one molecule discussed in this chapter is not included in the above manuscript and instead will be part of a manuscript written by Dr. Tobias A. Schaub. I synthesized the necessary compound and Checkers R. Marshall and Professor Carl K. Brozek acquired and analyzed the N_2 uptake data.

The scalable production of homogeneous, uniform carbon nanomaterials represents a key synthetic challenge for contemporary organic synthesis as nearly all current fabrication methods provide heterogeneous mixtures of various carbonized products. For carbon nanotubes (CNTs) in particular, the inability to access structures with specific diameters or chiralities severely limits their potential applications. Here, we present a general approach to access solid-state CNT mimic structures via the self-assembly of fluorinated nanohoops, which can be synthesized in a scalable, size-selective fashion. X-ray crystallography reveals that these CNT mimics exhibit uniform channel diameters that are precisely defined by the diameter of their nanohoop constituents, which self-assemble in a tubular fashion via a combination of arene-perfluoroarene and C−H—F interactions. The nanotube-like assembly of these systems results in capabilities such as linear guest alignment and accessible channels, both of which are observed in CNTs but not in the analogous all-hydrocarbon nanohoop systems. Calculations suggest that the organofluorine interactions observed in the crystal structure are indeed critical in the self-assembly and robustness of the CNT mimic systems. This work establishes the self-assembly of carbon nanohoops via weak interactions as an attractive means to generate solid-state materials that mimic carbon nanotubes, importantly with the unparalleled tunability enabled by organic synthesis.

III.1. Introduction.

The remarkable properties of carbon nanomaterials continue to drive fundamental and applied research advancements across a multitude of fields.[1–3] Recently, the nanoscale confinement and smooth molecular topology afforded by materials such as carbon nanotubes (CNTs) and graphene have proven indispensable in the emerging area of nanofluidics,[4–7] promising revolutionary applications in water desalination and biomimetic channel construction. Carbon nanomaterials, however, are difficult to synthesize in a uniform, homogeneous manner, with most modern fabrication methods affording ill-defined heterogeneous mixtures of carbonized products. As a result of these limitations, a CNT of a particular diameter and chirality, for example, cannot be accessed directly. This is problematic as both CNT diameter and chirality dictate the observed behavior and thus the utility of the material.[1] The ability to control carbon connectivity within carbon nanomaterials with atom-level precision would therefore be broadly impactful as their materials properties could be finely tuned to meet specific applications, which would undoubtedly accelerate discoveries within the field.

By perfecting a balance between covalent and noncovalent interactions, nature has developed a powerful design strategy to construct highly complex, yet well-defined nanoarchitectures. This is perhaps best illustrated in molecular biology where covalently linked "programmed" small molecule building blocks engage in numerous secondary noncovalent interactions, ultimately giving rise to high functioning biological machinery.[8] Thus, as a guide, nature has provided synthetic chemists with important blueprints for developing new materials, a factor that has contributed to the development of homogeneous, well-defined materials such as metal−organic frameworks (MOFs)[9,10] and covalent-organic frameworks (COFs).[11,12] A key design feature is the inclusion of reversible, noncovalent interactions, which provides a pathway to structural homogeneity while requiring relatively little energy in contrast to current methods for traditional carbon nanomaterial synthesis. Inspired by these principles, we envisioned a noncovalent approach to the synthesis of well-defined CNT mimics, where key features such as diameter and chirality are programmed via simple small molecule building blocks. While self-assembled nanotube-like architectures are well-known,[13−15] those that successfully replicate the fully conjugated radial geometry of CNTs—a key property that gives rise to many of the observed confinement effects—remain largely underexplored.

Since the initial synthesis of the cycloparaphenylenes in 2008,[16] macrocycles with radial geometry have become increasingly common due to the advancement of appropriate strain-building synthetic methods.[17−22] Considering their structural relationship to CNTs, we envisioned that these relatively new macrocyclic structures could act as the desired small-molecule building blocks for self-assembled CNT-like solid-state materials. These "carbon nanohoops", however, do not naturally crystallize into tubular structures in the solid state. Instead, these molecules tend to self-assemble into staggered, herringbone-like packing motifs to minimize the void space created by the rigid macrocyclic structure.[23,24] We hypothesized that with the appropriate secondary interactions, these "CNT fragments" could be programmed to arrange into columnar arrays, similar to that of CNTs. To this end, recently, we reported the synthesis of a fluorinated nanohoop, **III.1**, that, in the solid state, readily self-assembles into nanotube-like columns that closely mimic CNT channels (Fig. III.1.).[25] Unlike traditional carbon nanomaterials, however, **III.1** is accessed via bottom-up organic synthesis, allowing for the diameter and connectivity of the self-assembled CNT mimics to be precisely defined. Through X-ray crystallographic analysis, we posited that this self-assembly arises from a combination of arene-perfluoroarene[26] and C−H—F[27] interactions. Moreover, we found it was possible to vertically assemble "forests" of these CNT mimics on graphite surfaces via mild solution casting, suggesting facile integration in a multitude of applications.

While fluorination successfully oriented the nanohoops into the desired CNT-like geometry, it was not clear the extent to which this self-assembly strategy could be regarded as a general strategy to CNT mimics. For example, in our initial report, we only examined the self-assembly of a single diameter nanohoop with a very specific fluorination pattern, raising the question of generality. Related to this, the underlying secondary interactions were not systematically investigated and therefore were not fully understood. We also recognized that in order for these materials to be considered genuine

CNT mimics, these self-assembled systems would also have to exhibit some degree of CNT functionality. Accordingly, in this work, we expand on our previous report by demonstrating that these fluorinated, self-assembling nanohoops exhibit structural features and functions that have been previously observed in traditional CNTs, ultimately establishing fluorinated nanohoops as a new CNT-like precision nanomaterial. First, we describe the synthesis of two new fluorinated derivates—a reduced diameter [10]CPP analog and a [12]CPP derivative with a lesser degree of fluorination, both of which assemble into the desired CNT mimic structures. Importantly, we illustrate the scalabilty of these materials through a new gram-scale synthesis of previously reported nanohoop **III.1**. Next, we show that the [10]CPP analog is capable of linearly aligning C_{60} molecules as observed in CNT@C_{60} peapod structures and that **III.1** shows microporosity at 77 K via N_2 uptake measurements. Neither of the above functionalities are observed in the respective nonfluorinated analogs, supporting our hypothesis that fluorination of the nanohoop backbone is an effective general strategy toward fabricating robust CNT solid-state mimics. Finally, a theoretical analysis of the CNT mimic systems is presented which supports our hypothesis that weak organofluorine interactions drive the self-assembly of the fluorinated nanohoop constituents. Moreover, the computational methods described here provide a predictive tool for the design of future solid-state CNT mimics.

III.2. Synthesis and X-ray Crystal Structure Analysis.

A primary aim of this study was to determine if the supramolecular design strategy we had employed with nanohoop **III.1** was amenable to nanohoops of varying diameter and fluorination patterns. Additionally, we sought to develop a modular synthetic strategy where access to fluorinated structures of differing diameter and fluorination patterns could be quickly obtained via common intermediates. Another key focus point was to improve the overall reaction efficiency over the low yielding synthetic route we had previously used to access **III.1**—a severe limitation that ultimately hindered our ability to explore the solid-state materials properties of **III.1**. Ultimately, we aimed to synthesize nanohoops **III.2** (a [10]CPP analog) and **III.3** (a [12]CPP analog), which each bear two symmetrically placed tetrafluorophenylene moieties.

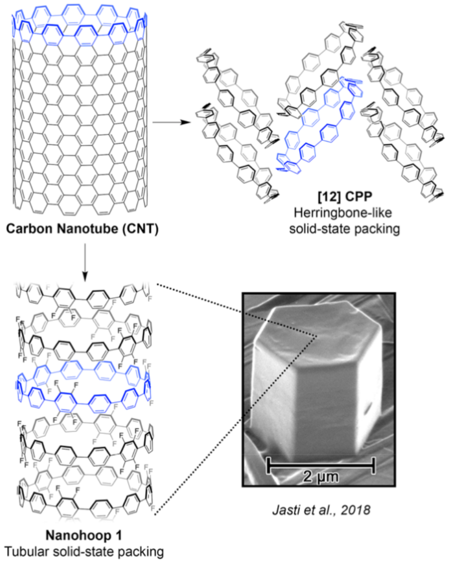

Figure III.1. CNT fragment [12]CPP exhibits a herringbone-like packing in the solid state, while nanohoop **III.1**, a fluorinated CNT fragment, self-assembles into nanotube-like columns. These columns can be fabricated in vertical "forests" on graphite substrates via mild solution casting, taking the form of hexagonal pillars.

Critical to our investigation was the acquisition of single crystals of **III.2** and **III.3** suitable for X-ray diffraction in order to unambiguously determine the solid-state packing of these materials and also to allow for the detailed analysis of arene-perfluoroarene and C−H—F interactions present in the solid-state arrangements.

With this in mind, we proceeded toward both **III.2** and **III.3** via our previously reported curved building blocks **III.4a**, **III.4b**, and **III.5**.[25] Importantly, each of these intermediates can be prepared on a multigram scale in excellent yield. Under dilute Suzuki-Miyaura cross-coupling conditions, triethylsilyl (TES) protected macrocycles **III.6a** and **III.6b** were synthesized in modest yields (Scheme III.1.). To overcome the highly strained nature of nanohoops and their derivatives, macrocyclic intermediates such as **III.6a** and **III.6b** are often prepared, where the embedded cyclohexadiene fragments act as "masked" benzene units.[17,19] Typically, after cleavage of the silyl protecting groups, the cyclohexadiene units can undergo reductive aromatization to give the final fully conjugated nanohoop.[19] In this case, however, we found that treatment of macrocycles **III.6a** and **III.6b** with tetrabutylammonium fluoride (TBAF) consistently resulted in decomposition. We reasoned that the electron-withdrawing nature of the fluorinated aryl rings can promote a retroaddition reaction, ultimately resulting in a cyclohexadienone and an unstable anionic tetrafluoraryl ring. After screening various conditions, we found that the addition of excess acetic acid to the reaction mixture allowed for clean conversion to the desired free-alcohol functionalized macrocycles. However, as reported by both the Yamago group[28] and our lab,[25] reductive aromatization with H_2SnCl_4 led to the desired products in low yield (15% and 12% for **III.2** and **III.3**, respectively). Through slight modification of the conditions reported by Yamago and co-workers,[28,29] we were able to improve the yield of both **III.2** (58% yield) and **III.3** (28% yield), providing ample material for our ongoing investigations.

Encouraged by this improvement, we then applied these optimized aromatization conditions to our original synthesis of nanohoop **III.1**. Unfortunately, we found that subjecting our previously reported cyclohexadiene-based macrocycle to these conditions gave a complex, insoluble mixture. With the hypothesis that fluorinated aryl rings adjacent to the cyclohexadiene may still undergo an undesired macrocyclic ring-opening type reaction, we developed a new synthetic route using “C” shaped intermediate **III.7** and previously reported “V” shaped intermediate **III.8**. In this case, macrocycle **III.9**, which does not contain fluorinated aryl rings adjacent to cyclohexadienes, smoothly undergoes reductive aromatization to produce **III.1** on gram scale. Given that we have already demonstrated the potential utility of **III.1** as a new, flexible optoelectronic nanomaterial, this improved synthetic route will accelerate further studies of its solid-state properties.

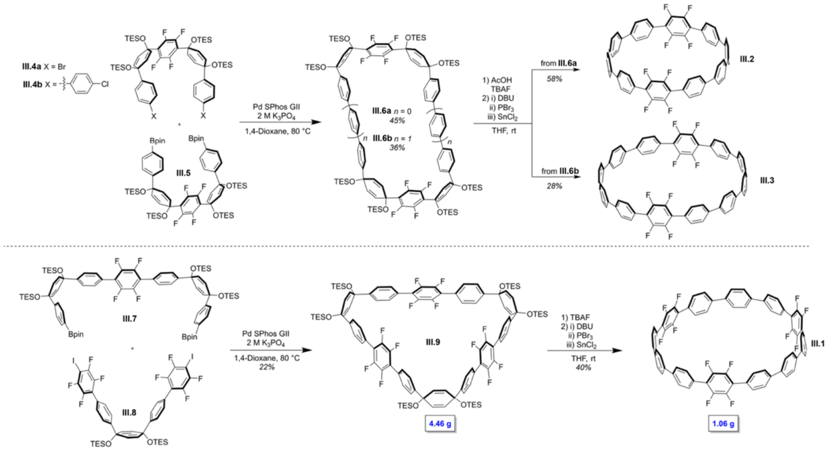
III.4a X = Br
III.4b X = Cl
TESO
OTES
F
X
+
Bpin
III.5
Pd SPhos GII
2 M K3PO4
1,4-Dioxane, 80 °C
III.6a n = 0
45%
III.6b n = 1
36%
n
1) AcOH
TBAF
2) i) DBU
ii) PBr3
iii) SnCl2
THF, rt
from III.6a
58%
III.2
from III.6b
28%
III.3
III.7
III.8
I
Pd SPhos GII
2 M K3PO4
1,4-Dioxane, 80 °C
22%
III.9
4.46 g
1) TBAF
2) i) DBU
ii) PBr3
iii) SnCl2
THF, rt
40%
III.1
1.06 g

Scheme III.1. Synthetic routes toward nanohoops **III.2**, **III.3**, and **III.1**.

As previously reported,[25] nanohoop **III.1** self-assembles into perfectly linear nanotube-like arrays in the solid state, forming channels that are precisely 1.63 nm in diameter (Fig. III.2a.). The 3-fold symmetry of the molecule allows for six arene-perfluoroarene interactions per hoop, each of which measures at 3.68 Å (Fig. III.2b).[31,32] This results in an ideal hexagonal circle-packing motif, which is the densest theoretical packing possible for circles of identical diameter.30 Vertical assembly in the solid-state architecture of **III.1** is guided by 18 C−H—F interactions per hoop dimer (Fig. III.2c), which range in distance from 2.53−2.62 Å (for completeness, C−F distances are also included for each crystal structure in Figure III.2).[27] The readily apparent organofluorine interactions observed in the crystal packing of **III.1** provide an excellent reference point when analyzing the X-ray crystal structures of **III.2** and **III.3**.

Following the synthesis of nanohoop **III.2**, needlelike single-crystals suitable for X-ray crystallography were obtained by slow evaporation of a THF solution of fluorinated nanohoop **III.2**. The solid-state packing of **III.**2 affords staggered nanotube-like columns (Fig. III.2d) with channel diameters of precisely 1.38 nm. As was observed previously for **III.1**, the horizontal arrangement of **III.2** was found to be guided by arene-perfluoroarene interactions. Four of these interactions can be found in the crystal structure of **III.2**, all measuring at 3.78 Å (Fig. III.2e.). Likewise, the vertical alignment of **III.2** in the solid state is dictated by a multitude of C−H—F interactions, as was also the case with **III.1**. A total of 16 C−H—F interactions were observed, measuring between 2.53−2.85 Å (Fig. III.2f.). It should be stressed that the packing of **III.2** is significantly different than that of parent [10]CPP,[33,34] which adopts a herringbone-type motif—a common observation in the all-hydrocarbon parent nanohoops.

Slow evaporation of **III.3** in dichloromethane (DCM) afforded needlelike crystals similar in appearance to those formed by **III.1** and **III.2**. Single-crystal XRD analysis revealed that **III.3** also self-assembles into tubular arrays (Fig. III.2g.), again in stark contrast to the herringbone-like packing of the all-hydrocarbon analog of [12]CPP. Upon closer inspection of the crystal structure of **III.3**, we observed four aryl-perfluoro aryl distances measuring at 3.69 Å (Fig. III.2h.) and 13 C−H—F interactions ranging between 2.48 and 2.84 Å (Fig. III.2i.). The solid-state packing of **III.3** in comparison to **III.1** is particularly interesting in that it shows how different tubular arrangements of nanohoops of identical size can be achieved through varying both the extent of fluorination in the nanohoop backbone and the symmetry of this fluorination.

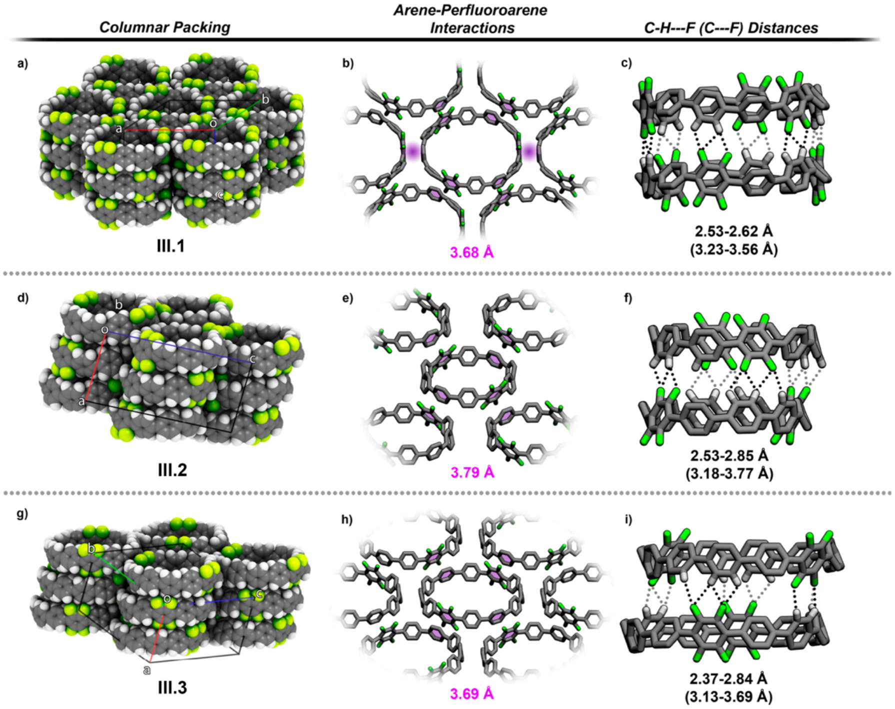
Columnar Packing
Arene-Perfluoroarene Interactions
C-H---F (C---F) Distances
a)
b)
c)
III.1
3.68 Å
2.53-2.62 Å
(3.23-3.56 Å)
d)
e)
f)
III.2
3.79 Å
2.53-2.85 Å
(3.18-3.77 Å)
g)
h)
i)
III.3
3.69 Å
2.37-2.84 Å
(3.13-3.69 Å)

Figure III.2. Columnar packing, arene-perfluoroarene interactions (highlighted in purple), and C−H—F distances (dotted lines, C−F distances shown in parentheses) observed in the crystal packings of nanohoops **III.1** (a-c), **III.2** (d-f), and **III.3** (g-i).

While the 3-fold symmetry of **III.1** results in linear channels (Fig. III.3a.) and an ideal hexagonal circle packing arrangement, the 2-fold symmetry of **III.3** affords staggered columns and a pseudohexagonal horizontal assembly. Also, due to the inclusion of only two tetrafluorophenylene moieties, **III.3** exhibits two fewer arene-perfluoroarene interactions and 23 fewer C− H—F interactions (Fig. III.2h, i.) than found in the crystal structure of **III.1**. Thus, we predict that organofluorine interactions may also allow for the further construction of tubular nanohoop-based assemblies with slightly varied morphologies but identical diameters.

The crystal structure analyses in this work suggest that fluorination is a relatively predictable and reliable strategy for accessing nanotube-like systems via nanohoop self-assembly. However, it should be noted that the 2-fold symmetry found in **III.1** and **III.2** has been shown to result in nontubular arrangements in fluorinated nanohoop systems. Indeed, Yamago and co-workers found that a 2-fold symmetric fluorinated [6]CPP analog exhibits herringbone-like packing, presumably since this staggered arrangement allows for the maximization of solid-state C−H—F interactions.[28] Likewise, the same study by Yamago provided an example of a 3-fold symmetric nanohoop (a [9]CPP analog) that assembles into tubular arrangements without the guidance of arene-perfluoroarene interactions, instead appearing to rely solely on C−H—F interactions. Therefore, we conclude that both nanohoop diameter and skeletal symmetry (i.e., the number of phenylene moieties present) are crucial factors to consider in the design of such systems.

III.3. Solid- and Solution-State Analysis of the C_{60}@III.2 Host—Guest Complex.

A notable application of CNT channels is the uptake and confinement of small molecule guests into 1D channels.[35–37] Thus, we were curious if the nanotube-like channels formed by fluorinated nanohoops are accessible to guests. As an initial approach, we sought to leverage the size and shape complementarity of fluorinated nanohoop **III.2**, a [10]CPP derivative, with C_{60}.[34,38] Indeed, macrocycles with radially oriented π-conjugation,[39] in particular [10]CPP and its derivatives,[40,41] have been shown to be strong hosts for C_{60} in both solution and the solid state. Similar to the case of C_{60}@ [10]CPP, we found that the addition of C_{60} to fluorinated nanohoop **III.2** resulted in a decrease in the fluorescence intensity of fluorinated nanohoop **III.2** (Fig. III.3a). From these fluorescence quenching data, we determined a binding constant (K_a) of $8.1 \pm 0.2 \times 10^5$ L^-1 mol between fluorinated nanohoop **III.2** and C_{60} (Fig. III.10.), a value that is lower than most binding constants reported [10]CPP hosts. For example, as compared to the parent [10]CPP host, the K_a is reduced (C_{60}@[10]CPP complex = $2.71 \pm 0.03 \times 10^6$ L^{-1} mol)[38] by nearly 30%. Despite this lowered affinity, the value is still relatively high among various fullerene hosts—a factor that allowed for a detailed investigation into the solid-state chemistry between nanohoop **III.2** and C_{60}. Dark red single-crystals of the C_{60}@**III.2** complex suitable for X-ray crystallography were grown via vapor diffusion of diethyl ether into a dilute THF/1,2-dichlorobenzene/toluene (1:1:1) solution of fluorinated nanohoop **III.2** and C_{60} (1:1). Interestingly, crystal structure analysis revealed cylindrical packing (Fig. III.3b.) but with the absence of perfluoroarene−arene interactions; however, numerous C−H—F interactions were found measuring from 2.54

to 2.87 Å (Fig. III.11.). These interactions appear to be the driving force behind the linear arrangement of the C_{60}@**III.2** complex in the solid state, as the analogous all-hydrocarbon [10]CPP@C_{60} complex has been previously shown to adopt a staggered packing motif (Fig. III.3c.).[34] The packing of C_{60}@**III.2** bears a striking aesthetic resemblance to CNT@C_{60} peapod structures, which have been shown to exhibit numerous exotic properties unique from bulk C_{60}. While not reported here, we expect that this arrangement can be adopted to align both endohedral[42,43] and exohedrally[41] functionalized fullerenes, a prospect that will likely result in new charge transport properties. Furthermore, given that the host−guest chemistry between nanohoops is just beginning to emerge, we anticipate that fluorinated nanohoops can potentially direct and preorganize other guest molecules into columnar 1D arrays in a highly size-selective manner leading to new strategies for applications such as templated polymerizations[44] and organic[45] electronic materials.

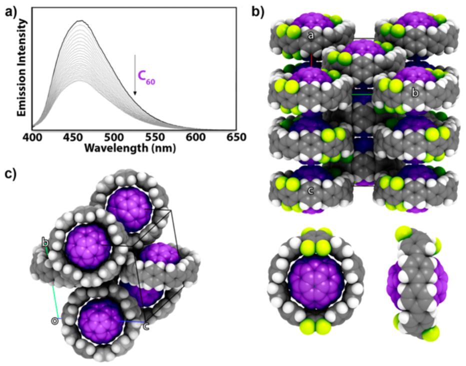

Figure III.3. a) Observed emission response of nanohoop **III.2** to increasing quantities of C_{60}. b) Peapod-like crystal packing of the C_{60}@**III.2** complex (top) and views of a single host−guest complex (bottom); c) X-ray crystal structure of the C_{60}@[10]CPP complex in the solid state. Fluorine atoms are colored in green, hydrogens are colored in white, carbons are colored in gray, and C_{60} has been colored purple.

III.4. N_2 Uptake Studies on Nanohoop III.1.

Encouraged by the thermal stability of nanohoop **III.1** as evidenced by thermogravimetric analysis (Fig. III.18.) and by the ability of the supramolecular assemblies of **III.1** to withstand the low-pressure conditions required for SEM measurements,[25] we sought to measure the material's surface area. Following evacuation to 2 μtorr at 125 °C, the N_2 uptake of **III.1** was collected at 77 K. The resulting data shown in Figure III.4 reveal a Type 1 isotherm. At low relative pressures P/P_0, high quantities of N_2 were adsorbed (Fig. III.19.), indicating the presence of microporosity, i.e., pore diameters below 2 nm. Brunauer−Emmett−Teller (BET) analysis of these data produces a surface area of 608 $m^2\ g^{-1}$ (Fig. III.20.). While this is a modest value in the general context of porous organic-based frameworks,[46−50] it is particularly high for an intrinsically porous system resulting from the assembly of macrocycles.[51−53] The calculated Saito-Foley cylindrical pore width of 0.74 nm for **III.1** is similar to the value reported previously for [12]CPP.[54] The crystallographic data, however, show an inner diameter of nanohoop **III.1** is 1.63 nm. The accuracy of the Saito-Foley equation is limited by assuming that pores are either completely full or empty and that the adsorbent packs perfectly.[55]

The related all-hydrocarbon [12]CPP exhibits little N_2 uptake when measured under the same conditions (Fig. III.4.), which is consistent with our findings that the organofluorine interactions underlying the supramolecular assembly of **III.1** are strong and ordered. Although **III.1** and the nonfluorinated [12]CPP are similar in size, a measurable surface area will arise only if the nanohoop pores are easily accessible to adsorbate molecules. A previous study on [12]CPP also found that the pores were inaccessible to N_2 at 77 K, whereas measuring at 195 K showed substantially higher uptake.[54] Interestingly, this same report discovered that CO_2 adsorption at 195 K revealed a Type 1 isotherm that afforded a BET surface area of 503 $m^2\ g^{-1}$. These observations suggested that the disordered assembly of [12]CPP prevented significant N_2 adsorption when rigidly fixed at low temperatures but permitted high uptake when allowed to reorient freely through thermally activated motion. While powder X-ray diffraction (PXRD) of [12]CPP after thermal activation has revealed it to be relatively disordered,[54] thermally activated **III.1** appears crystalline via PXRD. Interestingly, the activation process appears to actually induce ordering of the material, as PXRD measurements of a powder sample of **III.1** prior to heating and evacuation reveal a more amorphous character. We currently hypothesize that the observed crystallinity and microporosity of **III.1** after thermal activation can be attributed to the fluorination of the nanohoop backbone, as the all-hydrocarbon [12]CPP has been shown to be both amorphous and nonporous at 77 K after heating and evacuation. It is possible that, upon thermal activation, organofluorine interactions guide **III.1** into channels similar to those observed in the single crystal, which would then provide open pores for gas uptake.

Interestingly, although the tubular arrangement of **III.1** results in appreciable N_2 uptake, the same cannot be said for nanohoop **III.3**. A powder sample of **III.3** was found to exhibit negligible N_2 uptake at 77 K after evacuation to 2 μtorr at 125 °C (Fig. III.4.).[56] This implies that the tubular channels observed in the crystal structure of **III.3** may not be present in the powder sample after the evacuation process, with the sample instead possibly adopting a collapsed, herringbone-like morphology similar to that of [12]CPP. This hypothesis is loosely supported by PXRD analysis of **III.3** before and after activation (Fig. III.22.), which, unlike the analogous data for **III.1**, reveals a very low degree of crystalline order in the powder sample of **III.3** after evacuation and thus suggests the loss of the tubular morphology present in the single crystal. As our computational studies have shown (*vide infra*), the loss of a single fluorinated phenylene ring, and thus a loss of the associated organofluorine interactions, can have drastic energetic consequences on the stability of the solid-state stability of these fluorinated nanohoop systems. Thus, it is possible that the presence of fewer arene-perfluoroarene and C—H—F interactions in the crystal structure of **III.3** versus that of **III.1** renders the tubular assembly of **III.3** in the solid-state incapable of withstanding the aforementioned activation procedure, resulting in a collapsed, poorly ordered material that lacks N_2 uptake capabilities.

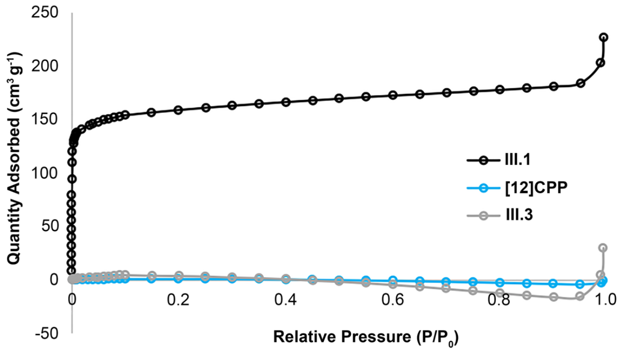

Figure III.4. Comparison of N_2 uptake isotherms of **III.1** (black), [12]CPP (blue), and **III.3** (gray) collected at 77 K.

III.5. Computational Analysis.

To gain a more detailed understanding of the factors that govern and ultimately dictate the observed molecular packing arrangements, we turned to Density Functional Theorem (DFT). Given that fundamental properties such as molecular size and shape act in concert with intermolecular forces to give the most effective solid-state packing, an important consideration in gaining this understanding is to first determine the magnitude of interaction energy between neighboring molecules in the solid state. This is readily accomplished by first determining the interaction energy of nanohoop dimeric units from experimentally obtained solid-state data.[57] The intermolecular interaction energy of each unit (ΔE) is calculated by subtracting the monomer energies (at the observed dimer geometry) from that particular dimer. To account for both intra- and intermolecular noncovalent interactions, the D3(BJ) method[58,59] for dispersion-corrected DFT is applied, using the B3LYP functional[60] and the large cc-pVTZ basis set to avoid superposition errors. Calculations were carried out using the Gaussian 09 (D.01) package.[61]

To investigate this approach with fluorinated nanohoops, we opted to first investigate the forces involved in the solid-state molecular packing of **III.2**. As our design strategy relies on expected arene-perfluoroarene interactions, it would follow that fluorinated aryl rings of nanohoops such as **III.2** would possess a positive aromatic quadrupole moment (Qzz), similar to that observed in the case of hexafluorobenzene.[62] Indeed, the computationally determined Qzz for the fluorinated aryl rings of nanohoop **III.2** of were found to be 1.21×10^{-38} C m^2—a value of opposite sign for the model compound benzene (Qzz = -29.2×10^{-40} C m^2).[62] Additionally, when compared to 1,2,4,5-tetrafluorobenzene (Qzz = 13.6×10^{-40} C m^2),[63] the impact of the nanohoop framework is particularly apparent as the Qzz is considerably higher. Taken together, these findings highlight the underlying electronic structure involved in the observed solid-state arene-perfluoroarene interactions. Next, to understand energetic contributions of arene-perfluoroarene interactions in the crystal packing of **III.2**, we explored the various lateral interactions observed in the nanohoop's crystal structure, represented by the dimers in Figure III.5. Importantly, it was found that the dimer in which a tetrafluorophenylene ring of one nanohoop is aligned face-to-face with a non-fluorinated phenylene in the adjacent hoop (Fig. III.5a.) exhibits a markedly high interaction energy

($\Delta E = -11.28$ kcal/mol) compared to the other three dimers studied (Fig. III.5b-d.). Indeed, as illustrated experimentally by Patrick and Prosser,[26] benzene and hexafluorobenzene are known to form energetically favorable dimeric units due to opposite electric quadrupole moments (benzene, $Qzz = -29.0 \times 10^{-40}$ C m^2 and hexafluorobenzene, $Qzz = 31.7 \times 10^{-40}$ C m^2)[62] which provides support for these observed interactions in **III.2**. Additionally, similar to that observed in the solid state of **III.2**, arene-perfluoroarene-based dimers are typically arranged in slightly shifted (π-stacked) sandwich-like structures with alternating molecular positive and negative quadrupole moments.[64] Referring to the experimentally determined lateral configuration of **III.2** (Fig. III.2e.), it is clear that every pair of molecules belonging to the same layer is precisely arranged to maximize these face-to-face interactions between unsubstituted and tetrafluorosubstituted units, presumably induced by the large stabilization energy of −11.28 kcal/mol calculated for this configuration. Thus, these energetically dominant interactions effectively drive the self-assembly of the system.

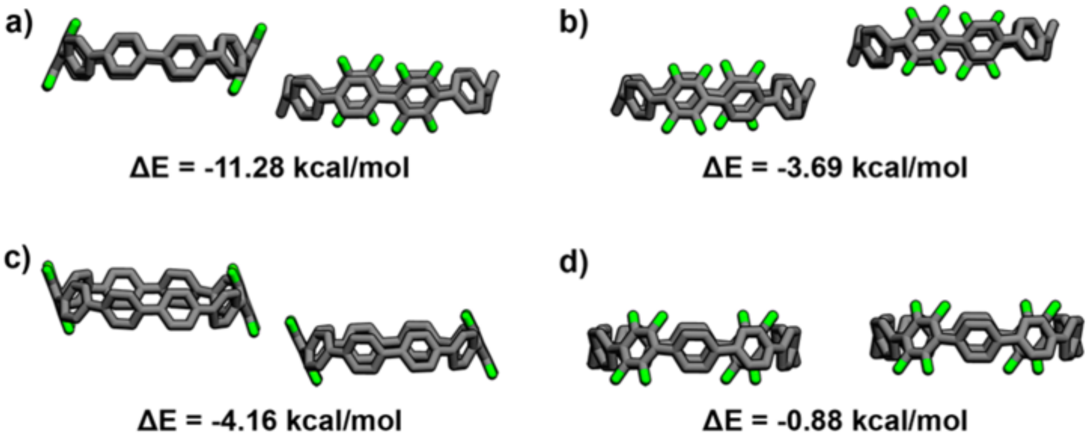

Figure III.5. Set of lateral-like dimers extracted from the crystal structure of nanohoop **III.2** along with their respective interactions energies.

While the lateral interactions can be explained on the basis of face-to-face arene-perfluoroarene interactions, the radial geometry of the macrocycles prohibits these interactions in the vertical direction. Bearing this in mind, we next sought to understand the origin as well as identity of the secondary interactions that drive the vertical assembly. Accordingly, a vertical nanohoops dimer was identified, and the interaction energy was, to our surprise, determined to be higher (23.08 vs 11.28 kcal/mol) than that determined for the lateral dimeric structure. As discussed in the solid-state analysis, we attribute this result to multiple C−H—F interactions. The aryl C−H—F contacts here are comprised between 2.53 and 2.85 Å, depending on the relative orientations between interacting rings, and are thus found below or close to the sum of the van der Waals radii of H (120 pm) and F (147 pm). Importantly, this dimer displays a remarkably large interaction energy of −23.08 kcal/mol as compared to the determined value of −17.32 kcal/mol for the corresponding offset-tubular dimer (Fig. III.23.) found in the herringbone-like packing of the parent hydrocarbon [10]CPP.[57] Intrigued by the unexpectedly large contribution of these C−H—F interactions, we then examined the theoretical energetic repercussions of systematically removing tetrafluorinated aryl rings from the vertical dimer of **III.2**. As expected, a consistent decrease in interaction energy was observed in going from four to zero tetrafluorinated aryl rings (Fig. III.6b-e.). To examine this result experimentally, we then prepared a [10]CPP derivative embedded with a single tetrafluoro aryl ring (Scheme III.3). As revealed by single crystal X-ray analysis, nanohoop **III.2S** packed into a herringbone type motif (Fig. III.12.), confirming our theoretical predictions, and, perhaps more importantly, suggesting that this approach may act as a predictive design tool for future investigations. Particularly noteworthy is the modest difference in interaction energy (<2 kcal/mol) between the tubular dimer shown in Figure III.6e (i.e., a theoretical solid-state columnar arrangement of [10]CPP) and that determined for the offset-tubular arrangement of [10]CPP (Fig. III.23.). This modest difference provides a rationale for the observed solid-state arrangement of [10]CPP, where polymorphism can be predicted. Ultimately, these findings highlight important considerations when designing these cylindrical structures. Additionally, while this analysis was carried out with **III.2**, we found that the vertical, secondary interactions in **III.1** (Fig. III.24.) also had stronger interaction energies than those in the lateral direction (Fig. III.25.)—a feature that likely plays a role in the observed packing of C_{60}@**III.2**, where face-to-face interactions are not present.

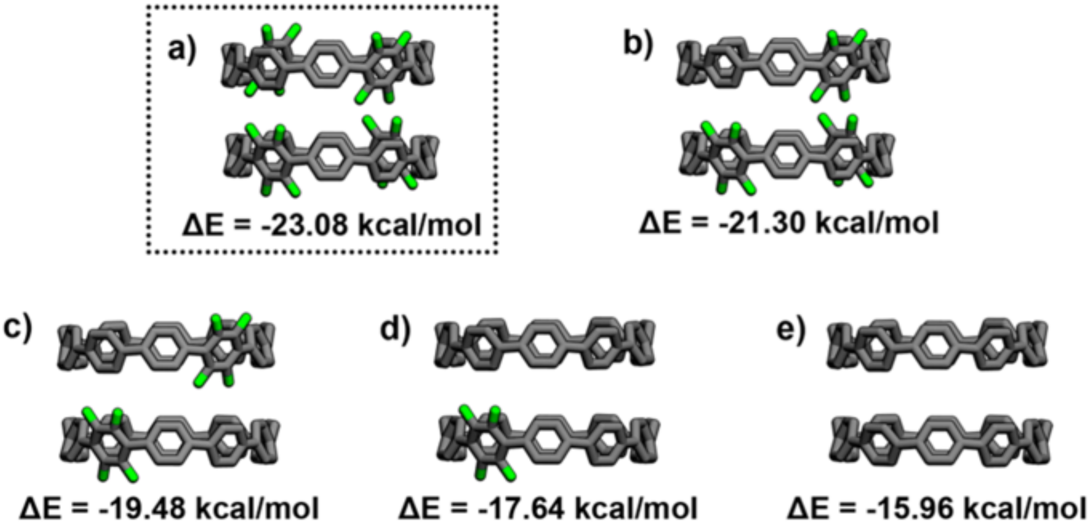

Figure III.6. a) Calculated interaction energy for the vertical dimer extracted from the crystal structure of nanohoop 2, along with the structures and respective interaction energies for this dimer upon the removal of fluorine atoms (b-e).

III.6. Conclusion and Outlook.

In conclusion, we have presented a scalable, size-selective strategy for accessing functional CNT mimic systems. Two novel fluorinated nanohoops (**III.2** and **III.3**) were synthesized via a general route using common intermediates, and a new synthetic approach was developed to access previously reported nanohoop **III.1** on the gram scale. Through X-ray crystallographic analysis, it was determined that nanohoops **III.1**, **III.2**, and **III.3** all self-assemble into CNT mimic systems in the solid state via organofluorine interactions and boast uniform channel diameters defined by the diameters of their respective constituent nanohoops. Aside from the aesthetic similarities between CNTs and the mimic systems disclosed herein, CNT-like properties were also found to emerge as a result of tubular nanohoop alignment. Specifically, nanohoop **III.2** was shown capable of linear C_{60} alignment, while nanohoop **III.1** exhibits accessible channels at 77 K with a BET surface area of 608 $m^2\ g^{-1}$. Neither of these functionalities are observed in the analogous nonfluorinated nanohoop systems, implying that the arene-perfluoroarene and C−H—F interactions observed in the crystal structures of the CNT mimics are effective in maintaining a tubular architecture. We further supported this hypothesis via a theoretical analysis of the crystal structure of nanohoop **III.2**, the results of which strongly suggest that organofluorine interactions are indeed energetically dominant in the self-assembly of the fluorinated nanohoop systems. The ability to fabricate these CNT mimics in a discrete, size-selective fashion is expected to benefit studies in nanofluidics and general nanoscale confinement, where access to atomically precise nanopores is difficult due to the inability to selectively produce CNTs or graphene nanopores. Furthermore, we believe the combined experimental and theoretical analysis of the CNT mimics presented may serve as an initial blueprint for the predictable design of other tubular systems based on the self-assembly of curved macrocycles, opening the door to a variety of new precision nanomaterials.

III.7. Experimental Section

III.7.1. General Information

^{1}H NMR spectra were recorded at 500 MHz on a Varian VNMR spectrometer, 500 MHz on a Bruker spectrometer, or 600 MHz on a Bruker spectrometer. All ^{1}H NMR spectra are referenced to TMS (δ 0.00 ppm), CH_2Cl_2 (δ 5.32 ppm), or $(CH_3)_3CO$ (δ 2.05 ppm). All ^{13}C NMR spectra are references to a residual $CHCl_3$ (δ 77.16 ppm), CH_2Cl_2 (54.00 ppm), or $(CH_3)_3CO$ (δ 29.84 ppm). All ^{19}F spectra were indirectly referenced via the Bruker TopSpin 3.5 software suite to $CFCl_3$. All reagents were obtained commercially and used without further purification unless otherwise noted. All glassware was flame-dried and cooled under an inert atmosphere of nitrogen unless otherwise noted. Moisture sensitive reactions were carried out under an inert atmosphere of nitrogen using standard syringe/septa technique. Absorbance spectra for **III.2** and **III.3** were collected in dichloromethane (DCM) in a 1 cm quartz cuvette on an Agilent Cary 60 UV−vis spectrophotometer. The emission spectra for **III.2** and **III.3** were collected in DCM on a Horiba Jobin Yvon Fluoromax-4 fluorometer. Silica column chromatography was conducted with Zeochem Zeoprep 60 Eco 40-63 μM silica gel while alumina chromatography utilized Sorbent Technologies 50-200 um Basic Activity II−II alumina. Intermediates **III.4a**, **III.4b**, **III.5**, and **III.8** were prepared as reported in reference 25. Intermediates **III.5S** and **III.10** were prepared as reported in reference 65.

III.7.2. Synthetic Schemes

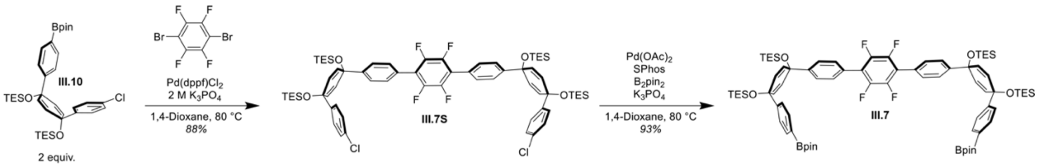

Scheme III.2. Synthetic route towards intermediate **III.7**.

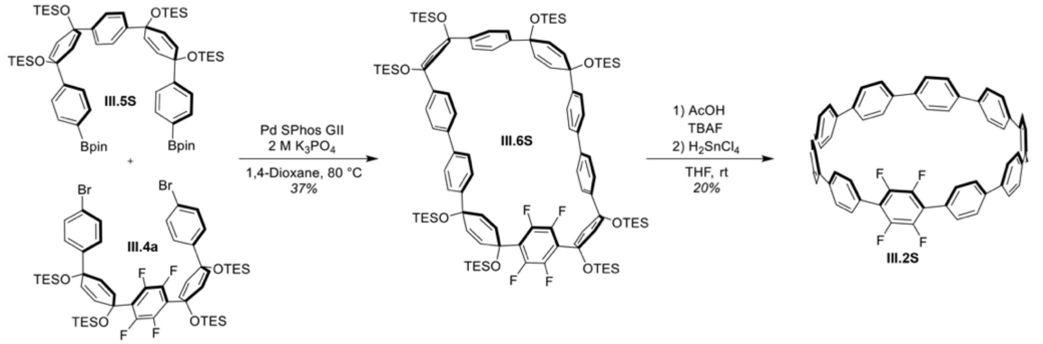

Scheme III.3. Synthetic route towards nanohoop **III.2S**.

III.7.3. Synthetic Procedures.

Synthesis of Macrocycle III.6a. To a flame-dried 250 mL round-bottom flask equipped with a stir bar was added **III.4a** (0.268 g, 2.36 mmol, 1.00 equiv), **III.5** (0.290 g, 2.36 mmol, 1.00 equiv), and SPhos-Pd-G2 (16.9 mg, 0.0236 mmol, 0.100 equiv). The flask was evacuated and backfilled with N_2 5 times, followed by addition of 1,4-dioxane (118 mL). This solution was then vigorously sparged with N_2 for 2 h at which point the solution was placed into an oil bath at 80 °C. At this point, an aqueous solution of 2 M K_3PO_4 (11.8 mL, 23.6 mmol, 10.0 equiv) was added, quickly turning the colorless solution bright yellow. The solution was allowed to stir for 1 h, at which point the solution was allowed to cool to room temperature followed by removal of the solvent via rotary evaporation. The resulting yellow/brown oil was extracted with hexanes (3 × 100 mL), followed by washing of the combined organic phases with H_2O (3 × 100 mL), brine (1 × 100 mL), and finally placed over sodium sulfate. After solvent removal, the brown oil was dissolved in hexanes and then filtered over a fritted funnel. The brown solids were washed with plenty of hexanes, and the resulting yellow filtrate was concentrated to a yellow oil. The addition of acetone caused the precipitation of a white solid, which after collection via filtration and washing with acetone yielded **III.6a** as a white solid (0.207 g, 45%). ^{1}H NMR (500 MHz, $CDCl_3$) δ 7.15 (d, *J* = 8.4 Hz, 8H), 7.07 (d, *J* = 8.5 Hz, 8H), 6.37 (d, *J* = 10.2 Hz, 8H), 6.00 (d, *J* = 10.4 Hz, 8H), 1.01− 0.81 (m, 72H), 0.76−0.53 (m, 48H). ^{13}C{^{1}H} NMR (126 MHz, $CDCl_3$) δ 144.1, 139.7, 133.5, 129.0, 127.0, 125.5, 71.3, 70.2, 7.2, 6.9, 6.6, 6.3. ^{19}F NMR (471 MHz, $CDCl_3$) δ −136.43 (s). δ LRMS (TOF, MALDI) (m/z): $[M]^+$ calculated for $C_{108}H_{152}O_8F_8Si_8$, 1952.951; found, 1954.126.

Synthesis of Nanohoop III.2. To a flame-dried 50 mL round-bottom flask equipped with a stir bar was added **III.6a** (0.077 g, 0.0365 mmol, 1.00 equiv) followed by THF (20 mL). To this solution was then added glacial acetic acid (0.105 mL, 1.83 mmol, 50.0 equiv), followed by tetrabutylammonium fluoride (1 M in THF, 0.914 mL, 0.914 mmol, 25 equiv) dropwise. The resulting colorless solution was then stirred for 18 h at which point H_2O (10 mL) was added, followed by removal of THF via rotary evaporation. The white solid was then filtered and washed with H_2O (30 mL) to afford the deprotected intermediate as a white solid. Without further purification, the intermediate was placed in a flame-dried 50 mL round-bottom flask equipped with a stir bar followed by THF (8 mL). To the resulting cloudy-white solution was added 1,8-diazabicyclo[5.4.0]undec-7-ene (0.027 mL, 0.292 mmol, 8 equiv), followed by PBr_3 (0.044 mL, 0.292 mmol, 8 equiv), resulting in an obvious white precipitate. After ~5 min of stirring, anhydrous $SnCl_2$ (0.055 g, 0.292 mmol, 8 equiv) was added as a solid, turning the solution yellow. After 1 h of stirring, the solution was quenched with 10% NaOH (5 mL), and THF was removed via rotary evaporation. To the resulting yellow suspension was added 125 mL of H_2O, followed by excessive extractions with DCM (6 × 50 mL). This was followed by washes with H_2O (3 × 50 mL) and brine (1 × 50 mL). The organic layer was then dried over sodium sulfate and filtered, followed by solvent removal via rotary evaporation. Purification via column chromatography (0−40% DCM/ Hexanes), using basic alumina as the stationary phase, afforded **III.2** as an off-white solid (0.019 g, 58%). ^{1}H NMR (500 MHz, $CDCl_3$) δ 7.71−7.45 (m, 32H). ^{19}F NMR (471 MHz, $CDCl_3$) δ −143.52 (s). Due to insolubility, ^{13}C NMR data could not be obtained. δ HRMS (TOF, ES+) (m/z): $[M]^+$ calculated for $C_{60}H_{32}F_8$, 904.2376; found, 904.2380.

Synthesis of Macrocycle III.6b. To a flame-dried 250 mL round-bottom flask equipped with a stir bar was added **III.5** (0.334 g, 0.271mmol, 1.00 equiv), **III.4b** (0.325 g, 0.271 mmol, 1.00 equiv), and SPhos-Pd-G2 (0.039 g, 0.0542 mmol, 0.200 equiv). The flask was evacuated and backfilled with N_2 5 times, followed by addition of 1,4-dioxane 2 (90 mL). This solution was then vigorously sparged with N_2 for 1 h at which point the solution was placed into an oil bath at 80 °C. At this point, an aqueous solution of 2 M K_3PO_4 (9.03 mL, 4.52 mmol, 17.0 equiv) was added. The solution was allowed to stir for 12 h, after which the solution was brought to room temperature, and the solvent was removed under reduced pressure. Water (50 mL) was added, followed by extraction with DCM (3 × 50 mL). The combined organic phases were washed with water (3 × 50 mL) and brine (1 × 50 mL) and dried over sodium sulfate. The solvent was removed via rotary evaporation, and the resulting brown solid was purified via column chromatography (0−40% DCM/Hexanes) using basic alumina as the stationary phase. This afforded **III.6b** as a white solid (0.199 g, 35%). ^{1}H NMR (500 MHz, $CDCl_3$) δ 7.36 (d, *J* = 7.9 Hz, 8H), 7.28 (d, *J* = 7.7 Hz, 8H), 6.40 (d, *J* = 9.7 Hz, 8H), 5.99 (d, *J* = 9.3 Hz, 8H), 0.99 (t, *J* = 7.8 Hz, 36H), 0.94 (t, *J* = 8.0 Hz, 36H), 0.69 (q, *J* = 7.9 Hz, 24H), 0.61 (q, *J* = 7.8 Hz, 24H). ^{13}C{^{1}H} NMR (126 MHz, $CDCl_3$) δ 144.1, 139.6, 139.1, 133.2, 128.6, 127.1, 126.6, 125.7, 71.4, 69.9, 7.1, 6.8, 6.4, 6.2. ^{19}F NMR (471 MHz, $CDCl_3$) δ −136.37 (s). δ HRMS (MALDI, TOF), m/z calculated for $C_{120}H_{160}F_8O_8Si_8$ $(M)^+$ 2106.02, found 2106.02.

Synthesis of Nanohoop III.3. To a flame-dried 100 mL round-bottom flask equipped with a stir bar was added **III.6b** (0.036 g, 0.0171 mmol, 1.00 equiv) followed by THF (10 mL). To this solution was then added glacial acetic acid (0.049 mL, 0.854 mmol, 50.0 equiv), followed by tetrabutylammonium fluoride (1 M in THF, 0.427 mL, 0. mmol, 25 equiv) dropwise. The resulting colorless solution was then stirred for 18 h at which point H_2O (10 mL) was added, followed by removal of THF via rotary evaporation. The white solid was then filtered and washed with H_2O (30 mL) to afford the deprotected intermediate as a white solid. Without further purification, the intermediate was placed in a flame-dried 50 mL round-bottom flask equipped with a stir bar followed by THF (8 mL). To the resulting cloudy-white solution was added 1,8-diazabicyclo[5.4.0]undec-7-ene (0.020 mL, 0.137 mmol, 8 equiv), followed by PBr_3 (0.013 mL, 0.137 mmol, 8 equiv) dropwise, resulting in a white precipitate. After ~5 min of stirring, anhydrous $SnCl_2$ (0.026 g, 0.137 mmol, 8 equiv) was added as a solid, turning the solution yellow. After 1 h of stirring, the solution was quenched with 10% NaOH (5 mL), and THF was removed via rotary evaporation. To the resulting yellow suspension was added 125 mL of H_2O, followed by excessive extractions with DCM (6 × 50 mL). This was followed by washes with H_2O (3 × 50 mL) and brine (1 × 50 mL). The organic layer was then dried over sodium sulfate and filtered, followed by solvent removal via rotary evaporation. Purification via column chromatography (0−40% DCM/ Hexanes) afforded **III.3** as an off-white solid (0.005 g, 28%). ^{1}H NMR (500 MHz, $CDCl_3$) δ 7.70−7.63 (m, 30H), 7.57 (d, J = 8.4 Hz, 10H). ^{19}F NMR (471 MHz, $CDCl_3$) δ −143.86 (s). Due to insolubility, ^{13}C NMR data could not be obtained. δ HRMS (MALDI, TOF), m/z calculated for $C_{72}H_{40}F_8$ $(M)^+$ 1056.30, found 1056.30.

Synthesis of III.7S. (See Scheme III.2.) To a 250 mL flame-dried flask was added **III.10** (18.56 g, 28.0 mmol, 2 equiv), 1,4-dibromo-2,3,5,6-tetrafluorobenzene (4.27 g, 14.0 mmol, 1 equiv), and [1,1′-bis(diphenylphosphino)ferrocenedichloropalladium (1.01 g, 1.39 mmol, 0.100 equiv). After the solids were added, the flask was evacuated and backfilled with nitrogen 3 times. The flask was then purged with N_2 for 20 min. 1,4-Dioxane (100.0 mL) was then added to the flask, after which aqueous 2 M K_3PO_4 (0.660 mL, 1.32 mmol, 5.5 equiv), sparged for 1 h prior to use, was added. The solution was then placed in an 80 °C oil bath and allowed to stir for 12 h. The next day, the reddish-black solution was allowed to come to room temperature before removing the solvent under reduced pressure. The resulting reddish-black sludge was dissolved in DCM and run through a plug of Celite with a small pad of silica on top. This was followed by removal of DCM solvent from the eluent via rotary evaporation. The resulting yellow oil was washed with MeOH, causing the product to precipitate as a white solid. Vacuum filtration, followed by additional MeOH rinses, afforded **III.7S** as a white solid (14.70 g, 88%). ^{1}H NMR (500 MHz, $CDCl_3$) δ 7.45 (dd, 8H), 7.32 (d, J = 8.5 Hz, 4H), 7.26 (d, 4H), 6.09−5.97 (dd, 8H), 0.97 (dt, J = 11.2, 7.9 Hz, 36H), 0.65 (dq, J = 21.6, 7.9 Hz, 24H). ^{13}C{^{1}H} NMR (126 MHz, $CDCl_3$) δ 146.8, 144.5, 133.1, 131.6, 131.5, 130.0, 128.3, 127.4, 126.4, 126.3, 71.4, 71.1, 7.0, 6.5. ^{19}F NMR (471 MHz, $CDCl_3$) δ −144.35. MS could not be obtained.

Synthesis of III.7. To a 100 mL flame-dried flask was added Pd(OAc)$_2$ (0.135 g, 0.602 mmol, 0.05 equiv), 2-dicyclohexylphosphino-2′6′-dimethoxybiphenyl (0.618 g, 1.50 mmol, 0.125 equiv), bis(pinacolato)diboron (15.30 g, 60.2 mmol, 5 equiv), **III.7S** (14.45 g, 12.0 mmol, 1 equiv), and K$_3$PO$_4$ (5.91 g, 60.2 mmol, 5 equiv). After the solids were added, the flask was evacuated and backfilled with nitrogen 5 times. The flask was then purged with N$_2$ for 20 min. 1,4-Dioxane (100.0 mL) was then added to the flask, and the solution was sparged for 20 min before being placed in an 80 °C oil bath overnight. The next day, the black solution was brought to room temperature, and the solvent was removed under reduced pressure. The resulting black sludge was dissolved in DCM and run through a plug of Celite with a small pad of silica on top. After removing the DCM solvent from the eluent via rotary evaporation, the resulting dark-orange oil was washed with methanol, causing the product to precipitate as a white solid. Vacuum filtration afforded **III.7** as a white solid (15.54 g, 93%). ^{1}H NMR (500 MHz, CDCl$_3$) δ 7.74 (d, J = 8.0 Hz, 4H), 7.45 (d, J = 8.4 Hz, 4H), 7.40 (d, J = 8.2 Hz, 8H), 6.05 (d, J = 10.1 Hz, 4H), 5.99 (d, J = 10.1 Hz, 4H), 1.33 (s, 24H), 0.94 (dt, J = 25.1, 7.9 Hz, 36H), 0.67 (q, J = 7.9 Hz, 12H), 0.57 (q, J = 7.9 Hz, 12H). ^{13}C{^{1}H} NMR (126 MHz, CDCl$_3$) δ 149.0, 147.0, 145.0, 143.2, 134.8, 131.6, 131.4, 129.9, 128.2, 126.3, 126.0, 125.9, 125.3, 83.8, 71.5, 24.9, 7.1, 7.0, 6.5, 6.4. ^{19}F NMR (471 MHz, CDCl$_3$) δ −144.37. δ HRMS (TOF, ES+) (m/z): [M]$^+$ calculated for $C_{78}H_{108}B_2O_8F_4NaSi_4$, 1405.7141; found, 1405.7163.

Synthesis of Macrocycle III.9. To a flame-dried 2000 mL round-bottom flask equipped with a stir bar was added **III.7** (14.44 g, 10.40 mmol, 1.00 equiv), **III.8** (10.80 g, 10.40 mmol, 1.00 equiv), and SPhos-Pd-G2 (1.50 g, 2.08 mmol, 0.200 equiv). The flask was evacuated and backfilled with N$_2$ 5 times, followed by 30 min of purging with N$_2$. Next, 1,4-dioxane (1000 mL) was added to the flask via cannula to afford a 10 mM solution. This solution was then vigorously sparged with N$_2$ for 2 h at which point the solution was placed into an oil bath at 80 °C. At this point, an aqueous solution of 2 M K$_3$PO$_4$ (103.9 mL, 207.8 mmol, 20.0 equiv) was added. The solution was allowed to stir for 12 h, after which the solution was brought to room temperature, and the solvent was removed under reduced pressure. The resulting brown oil was dissolved in DCM and run through a plug of Celite with a small pad of silica on top. The eluent was then dried via rotary evaporation to afford a sticky white solid. Purification via column chromatography

(0−40% DCM/Hexanes) afforded **III.9** as a white solid (4.46 g, 22%) (alternatively, the crude material can be washed with hexanes to precipitate the product at a loss of yield). ^{1}H NMR (500 MHz, CDCl$_3$) δ 7.53 (d, *J* = 8.2 Hz, 12H), 7.45 (d, *J* = 8.0 Hz, 12H), 6.10 (s, 12H), 0.99 (t, *J* = 7.9 Hz, 54H), 0.68 (q, *J* = 7.9 Hz, 36H). ^{13}C{^{1}H} NMR (126 MHz, CDCl$_3$) δ 147.0, 145.2, 143.1, 131.5, 130.0, 126.4, 126.1, 71.5, 7.1, 6.5. ^{19}F NMR (471 MHz, CDCl$_3$) δ −144.38. MALDI TOF, m/z calculated for $C_{108}H_{126}F_{12}O_6Si_6$ (M)$^+$ 1915.80, found 1915.96.

Synthesis of Nanohoop III.1. To a flame-dried 50 mL round-bottom flask equipped with a stir bar was added 9 (0.174 g, 0.091 mmol, 1.00 equiv) followed by THF (10 mL). To this solution was then addedtetrabutylammonium fluoride (1 M in THF, 2.27 mL, 2.27 mmol, 25.0 equiv) dropwise. This solution was then stirred for 2 h at which point H2O (10 mL) was added, followed by removal of THF via rotary evaporation. The resulting suspension was vacuum filtered, washed with water, and allowed to fully dry. Without further purification, the crude white solid was placed in a flame-dried 250 mL round-bottom flask equipped with a stir bar followed by THF (100 mL). The flask was then placed in an ice bath (0 °C) and allowed to cool for 30 min. After 30 min, 1,8-diazabicyclo[5.4.0]undec-7-ene (0.027 mL, 0.292 mmol, 8 equiv) was added, followed by PBr3 (0.044 mL, 0.292 mmol, 8 equiv) dropwise, resulting in a white precipitate. After ~5 min of stirring, anhydrous SnCl2 (0.055 g, 0.292 mmol, 8 equiv) was added as a solid, turning the solution yellow. After 1 h of stirring, a majority of the THF solvent was removed via rotary evaporation, and the concentrated reaction mixture was poured directly onto a basic alumina plug. Flushing the plug with DCM caused only the product to elute. The eluent was dried under reduced pressure to afford **III.1** as an off-white solid (1.06 g, 40%). ^{1}H NMR (500 MHz, CDCl$_3$) δ 7.69 (d, *J* = 6.2 Hz, 24H), 7.59 (d, *J* = 8.2 Hz, 12H). ^{19}F NMR (471 MHz, CDCl$_3$) δ −143.82. Due to insolubility, ^{13}C NMR data could not be obtained. MALDI TOF, *m/z* calculated for $C_{72}H_{36}F_{12}$ (M)$^+$ 1128.2625, found 1128.0602.

Synthesis of Macrocycle III.6S. (See Scheme III.3.) To a flame-dried 250 mL round-bottom flask equipped with a stir bar was added **III.4a** (0.338 g, 2.92 mmol, 1.00 equiv), **III.5S** (0.330 g, 2.92 mmol, 1.00 equiv), and SPhos-Pd-G2 (20.0 mg, 0.0292 mmol, 0.100 equiv). The flask was evacuated and backfilled with N_2 5 times, followed by addition of 1,4-dioxane (146 mL). This solution was then vigorously sparged with N_2 for 2 h at which point the solution was placed into an oil bath at 80 °C. At this point, an aqueous solution of 2 M K_3PO_4 (14.6 mL, 29.2 mmol, 10.0 equiv) was added, quickly turning the colorless solution bright yellow, turning to a white suspension over the course of 1 h. The solution was allowed to stir for 2 h, at which point the solution was cooled to room temperature followed by removal of the solvent via rotary evaporation. The resulting yellow/brown oil aqueous phase was extracted with hexanes (3 × 100 mL), followed by washing of the combined organic phases with H_2O (3 × 100 mL), brine (1 × 100 mL), and finally placed over sodium sulfate. After solvent removal, the brown oil was dissolved in hexanes and then filtered using a fritted funnel. The brown solids were washed with plenty of hexanes, and the resulting yellow filtrate was concentrated to a yellow oil. The yellow oil was loaded onto silica gel (0−40% DCM/Hexanes) to afford macrocycle **III.6S** as a white solid (0.203 g, 37%). ^{1}H NMR (600 MHz, $CDCl_3$) δ 7.33 (d, *J* = 8.4 Hz, 4H), 7.29 (d, *J* = 8.4 Hz, 4H), 7.26− 7.20 (m, 8H), 7.12 (s, 4H), 6.40 (d, *J* = 10.1 Hz, 4H), 6.00 (d, *J* = 10.3 Hz, 4H), 5.95 (d, *J* = 10.3 Hz, 4H), 5.92 (d, *J* = 10.2 Hz, 4H), 0.99−0.87 (m, 72H), 0.62 (m, 48H). ^{13}C{^{1}H} NMR (151 MHz, $CDCl_3$) δ 146.2, 145.0, 144.9, 144.3, 139.7, 139.6, 133.4, 131.8, 131.6, 131.5, 131.3, 128.8, 128.2, 127.0, 126.8, 126.3, 125.9, 125.9, 125.7, 125.7, 123.9, 71.6, 71.4, 71.6, 70.1, 7.2, 7.2, 6.9, 6.6, 6.6, 6.3. 1^{9}F NMR (471 MHz, $CDCl_3$) δ −136.43 (s). δ LRMS (TOF, MALDI) (m/z): $[M]^+$ calculated for $C_{108}H_{156}O_8F_4Si_8$, 1880.99; found, 1882.1.

Synthesis of 2S. (See Scheme III.3.) To a flame-dried 100 mL round-bottom flask equipped with a stir bar was added **III.6S** (0.203 g, 0.108 mmol, 1.00 equiv) followed by THF (20 mL). To this solution was then added glacial acetic acid (0.620 mL, 10.8 mmol, 100.0 equiv), followed by tetrabutylammonium fluoride (1 M in THF, 2.16 mL, 2.16 mmol, 20.0 equiv) dropwise. The resulting colorless solution was then stirred for 18 h at which point H_2O (10 mL) was added, followed by removal of THF via rotary evaporation. The white solid was then filtered and washed with H_2O (30 mL) and DCM (3 × 10 mL) to give crude, deprotected **III.6S** (0.0941 g, 90%). The resulting white solid then added to a flame-dried 100 mL round-bottom flask equipped with a stir bar, followed by THF (40 mL). To this suspension was added H_2SnCl_4 (0.40 M in THF, 0.0971 mmol, 1.21 mL, 5.00 equiv), resulting in a faint-yellow/white suspension which was stirred at room temperature for 18 h. Aqueous (18 w/w%) ammonia (10 mL) was added followed by filtration using a fritted funnel. The resulting faint blue filtrate was then collected in a round-bottom flask, followed by removal of THF via rotary evaporation and gave an off-white/teal solid. This solid was then dissolved in DCM (100 mL), washed with H_2O (3 × 50 mL) and brine (1 × 50 mL), and then placed over sodium sulfate. After removal of solvent, the resulting solid was loaded onto silica gel (0−100% DCM/Hexanes) to give **III.2S** as an off-white/yellow solid (17.9 mg, 20%). ^{1}H NMR (500 MHz, $CDCl_3$) δ 7.70−7.47 (m, 36H). $^{13}C\{^1H\}$ NMR (126 MHz, $CDCl_3$) δ 140.9, 138.6, 138.4, 138.3, 138.2, 138.2, 138.0, 137.9, 130.9, 127.8, 127.5, 127.4, 127.4, 127.3, 127.0, 126.8. ^{19}F NMR (471 MHz, $CDCl_3$) δ −143.54 (s). δ HRMS (TOF, ES+) (m/z): $[M]^+$ calculated for $C_{60}H_{36}F_4$, 832.2753; found, 832.2748.

III.7.4. ^{1}H NMR Spectra.

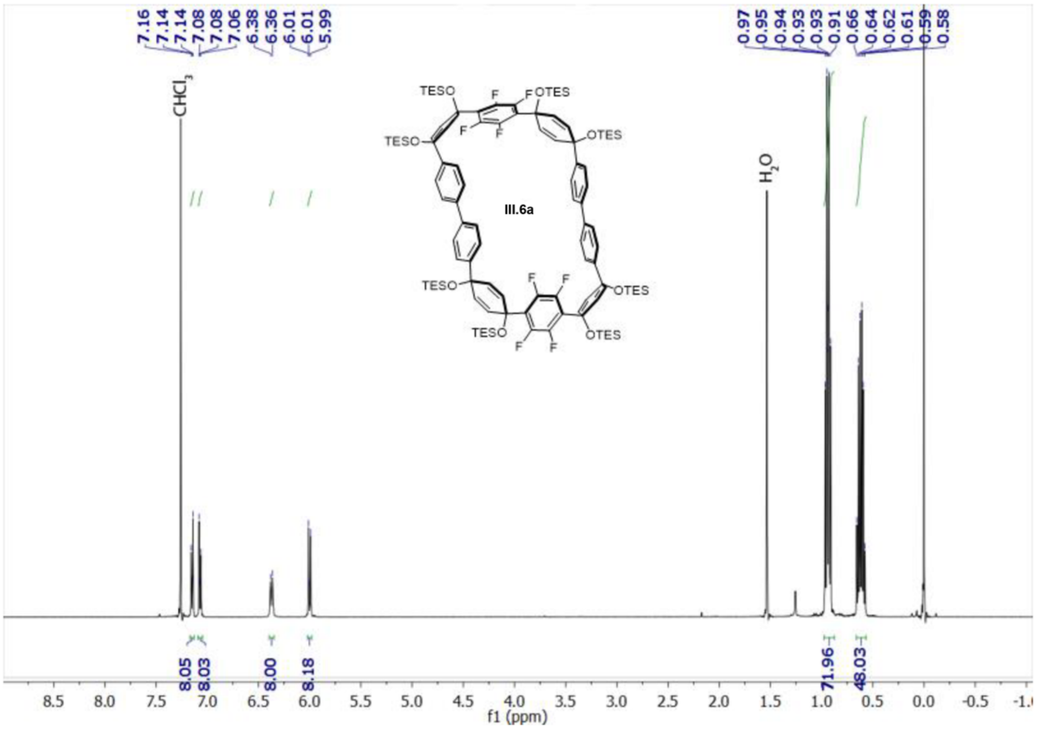

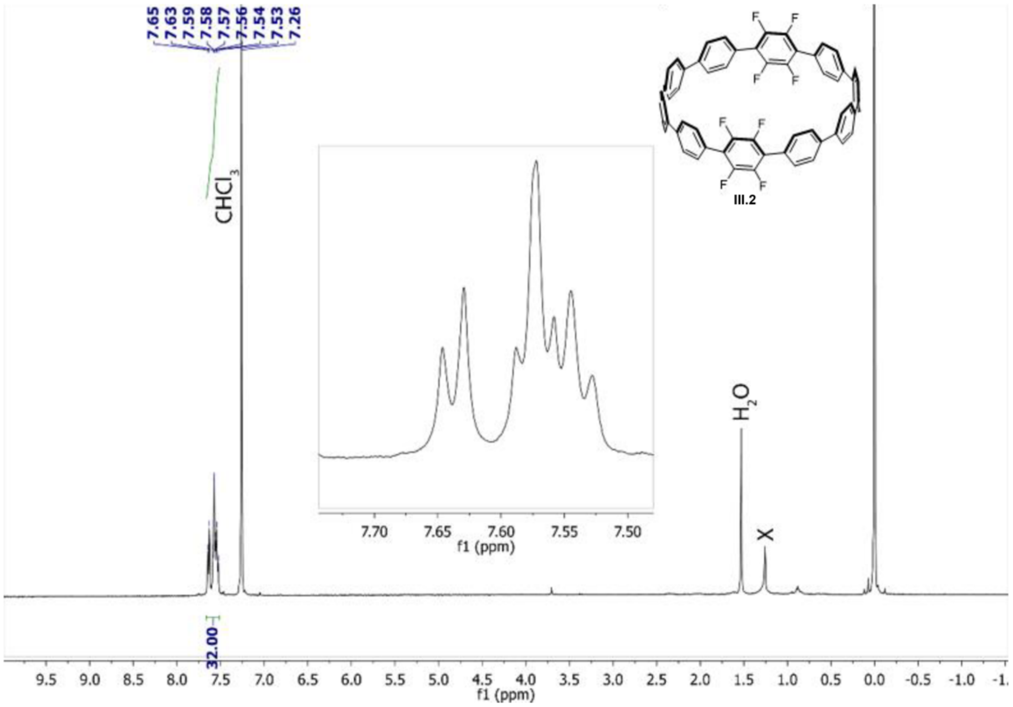
7.65
7.63
7.59
7.58
7.57
7.56
7.54
7.53
7.26
CHCl3
H2O
X
32.00
III.2
7.70
7.65
7.60
7.55
7.50
f1 (ppm)
9.5 9.0 8.5 8.0 7.5 7.0 6.5 6.0 5.5 5.0 4.5 4.0 3.5 3.0 2.5 2.0 1.5 1.0 0.5 0.0 -0.5 -1.0
f1 (ppm)

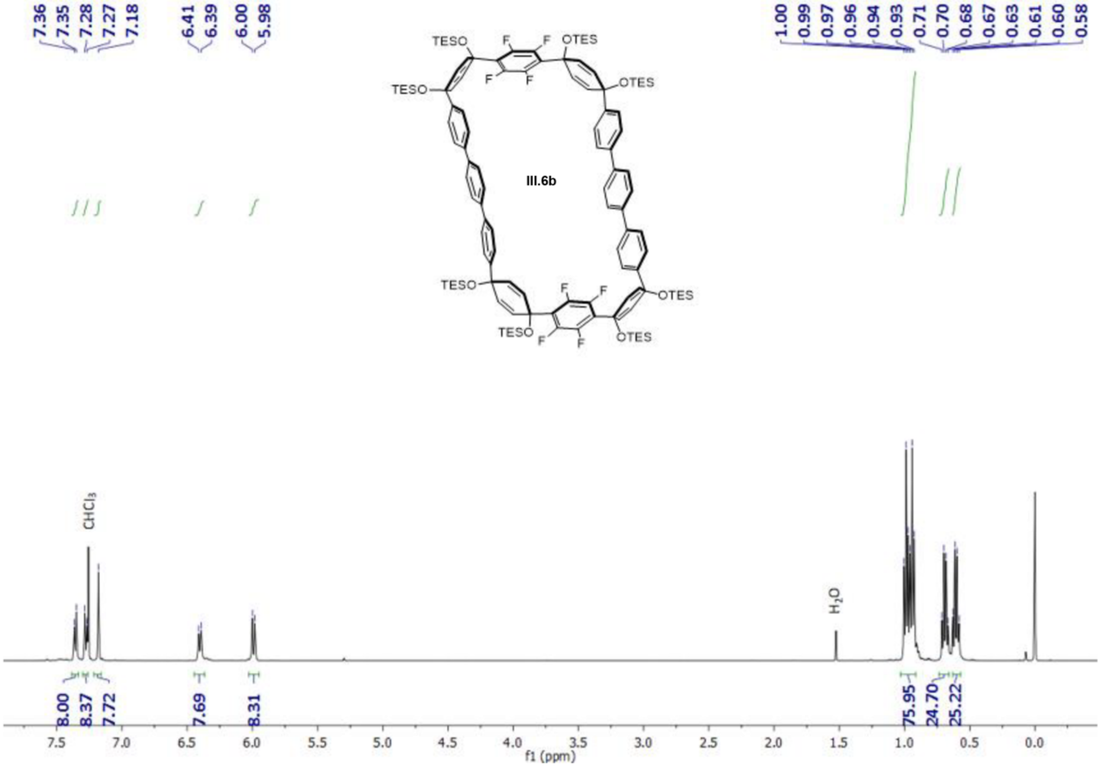
7.36
7.35
7.28
7.27
7.18
6.41
6.39
6.00
5.98
1.00
0.99
0.97
0.96
0.94
0.93
0.71
0.70
0.68
0.67
0.63
0.61
0.60
0.58
TESO
OTES
F
III.6b
CHCl3
H2O
8.00
8.37
7.72
7.69
8.31
75.95
24.70
25.22
7.5 7.0 6.5 6.0 5.5 5.0 4.5 4.0 3.5 3.0 2.5 2.0 1.5 1.0 0.5 0.0
f1 (ppm)

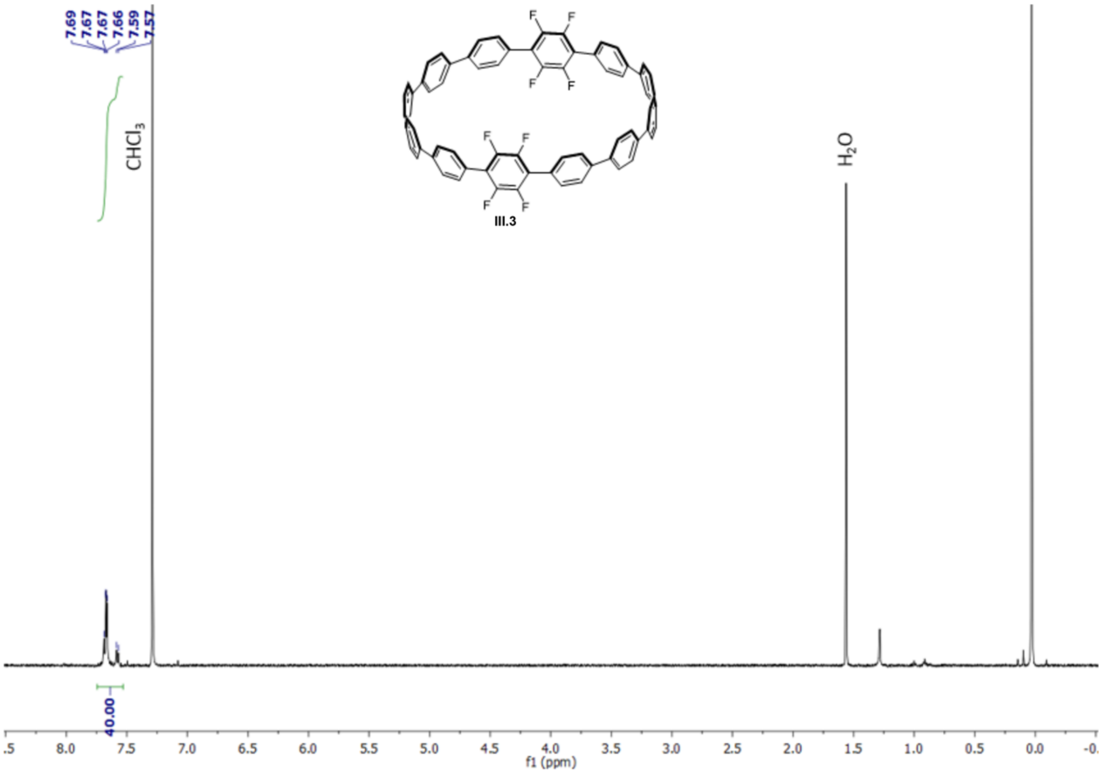
7.69
7.67
7.67
7.66
7.59
7.57
CHCl$_3$
H$_2$O
III.3
F
40.00
.5
8.0
7.5
7.0
6.5
6.0
5.5
5.0
4.5
4.0
3.5
3.0
2.5
2.0
1.5
1.0
0.5
0.0
-0.
f1 (ppm)

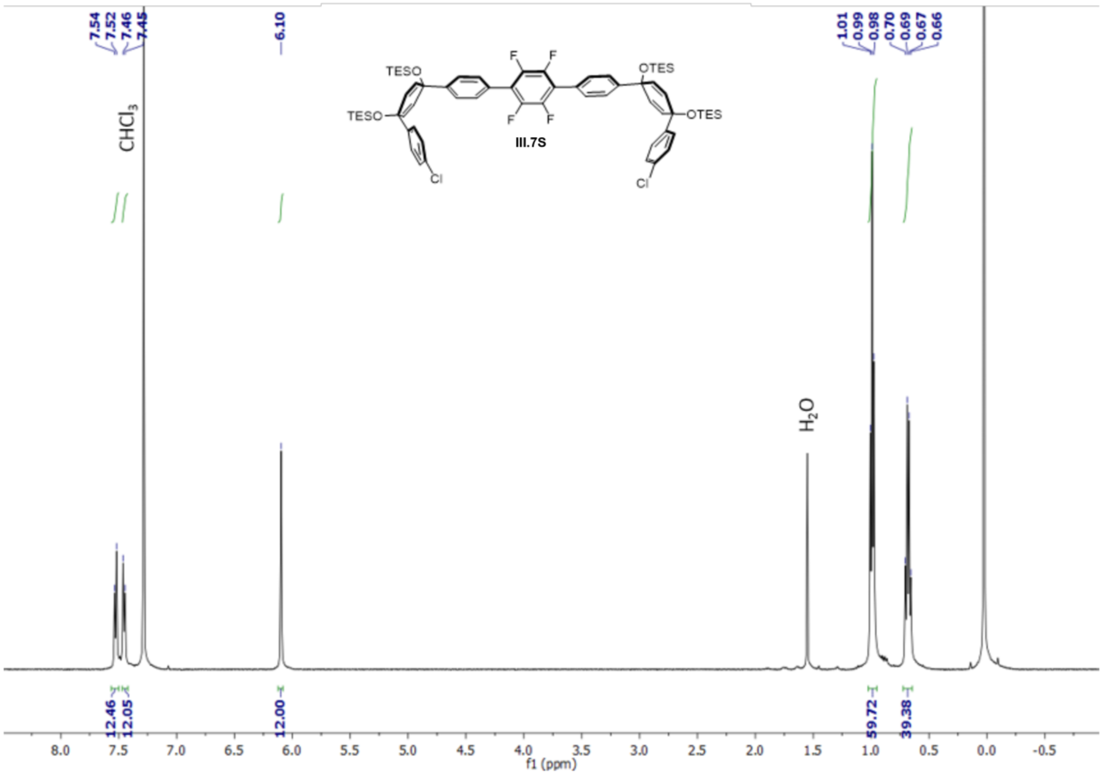
7.54
7.52
7.46
7.45
6.10
1.01
0.99
0.98
0.70
0.69
0.67
0.66
CHCl$_3$
H$_2$O
TESO
OTES
F
Cl
III.7S
12.46
12.05
12.00
59.72
39.38
8.0
7.5
7.0
6.5
6.0
5.5
5.0
4.5
4.0
3.5
3.0
2.5
2.0
1.5
1.0
0.5
0.0
-0.5
f1 (ppm)

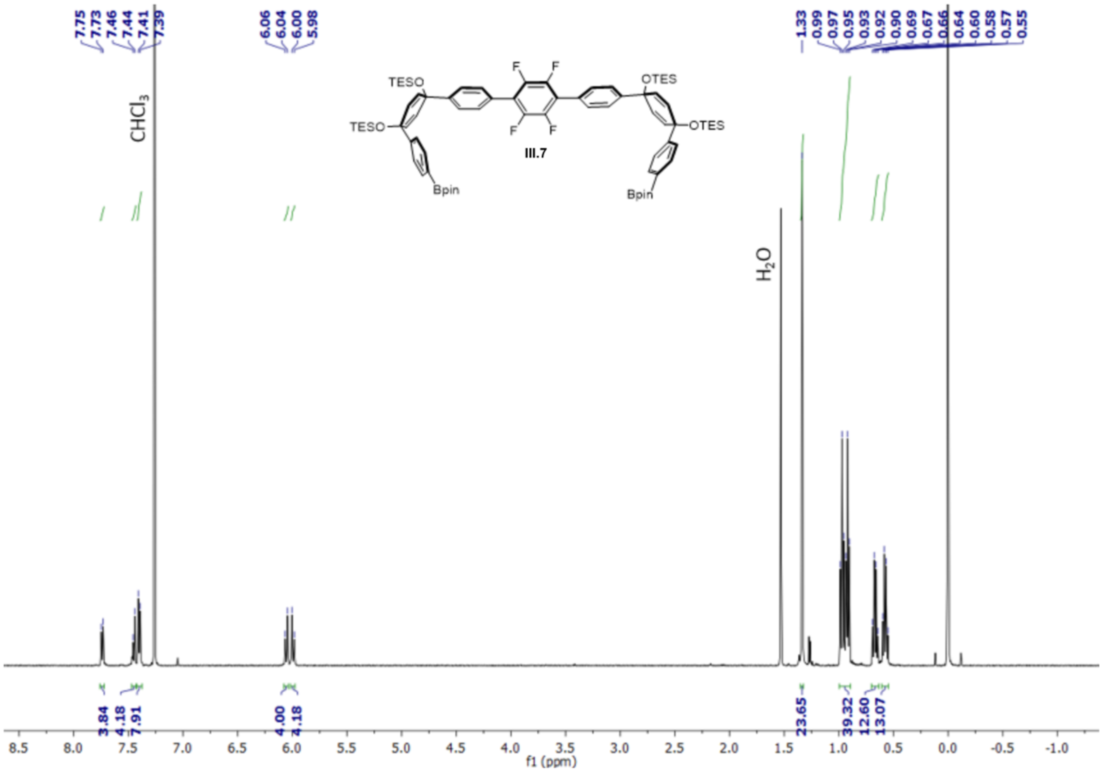
7.75
7.73
7.46
7.44
7.41
7.39
6.06
6.04
6.00
5.98
1.33
0.99
0.97
0.95
0.93
0.92
0.90
0.69
0.67
0.66
0.64
0.60
0.58
0.57
0.55
CHCl$_3$
TESO
TESO
F
F
F
F
OTES
OTES
Bpin
Bpin
III.7
H$_2$O
3.84
4.18
7.91
4.00
4.18
23.65
39.32
12.60
13.07
8.5 8.0 7.5 7.0 6.5 6.0 5.5 5.0 4.5 4.0 3.5 3.0 2.5 2.0 1.5 1.0 0.5 0.0 -0.5 -1.0
f1 (ppm)

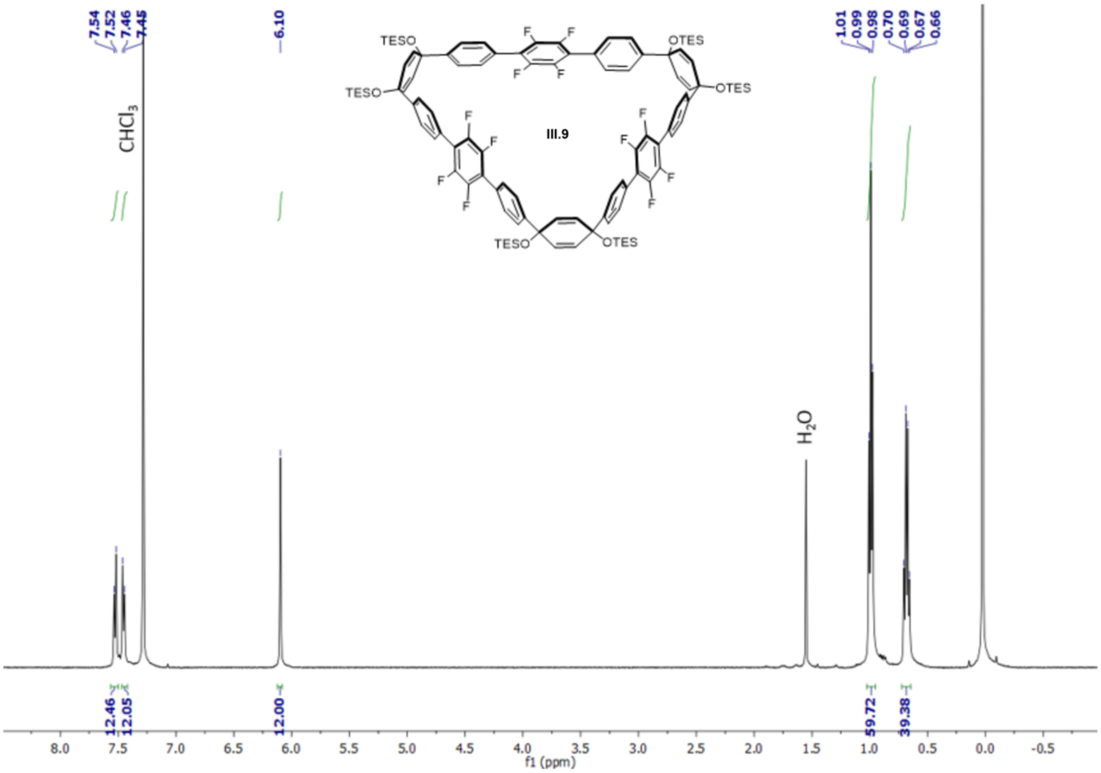
7.54
7.52
7.46
7.45
6.10
1.01
0.99
0.98
0.70
0.69
0.67
0.66
CHCl$_3$
TESO
TESO
TESO
OTES
OTES
OTES
F
III.9
H$_2$O
12.46
12.05
12.00
59.72
39.38
8.0 7.5 7.0 6.5 6.0 5.5 5.0 4.5 4.0 3.5 3.0 2.5 2.0 1.5 1.0 0.5 0.0 -0.5
f1 (ppm)

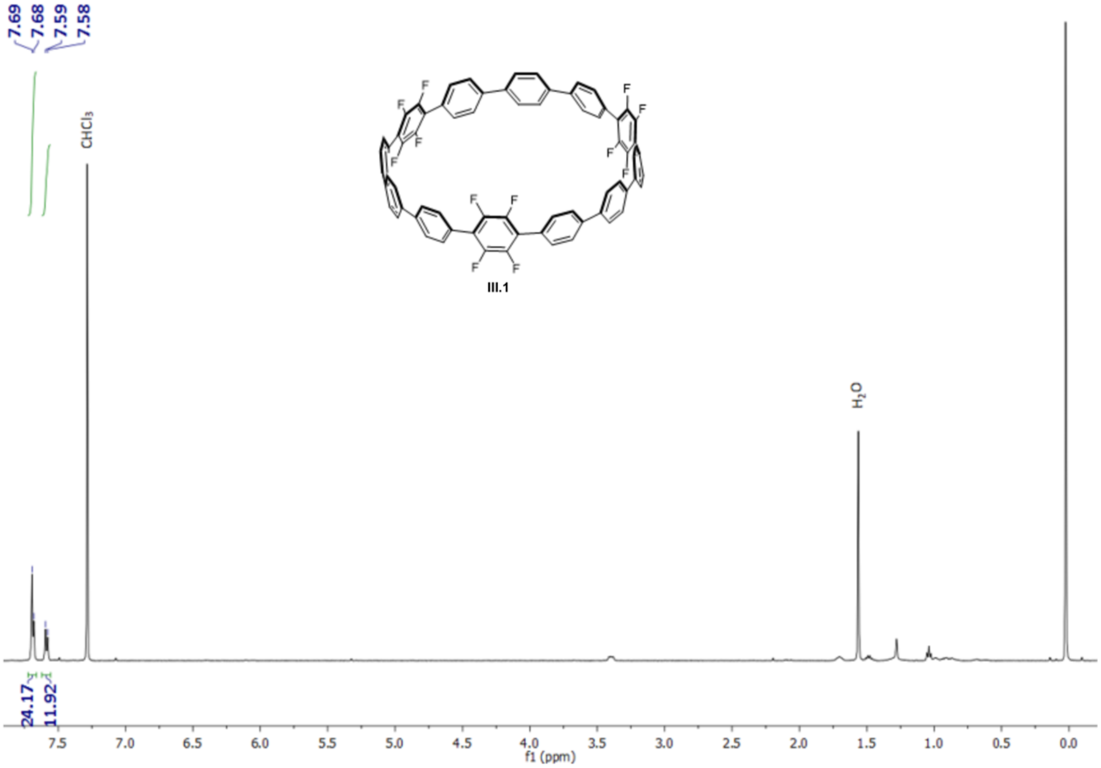
III.1

7.69
7.68
7.59
7.58
CHCl₃
H₂O
24.17
11.92
7.5
7.0
6.5
6.0
5.5
5.0
4.5
4.0
3.5
3.0
2.5
2.0
1.5
1.0
0.5
0.0
f1 (ppm)
F

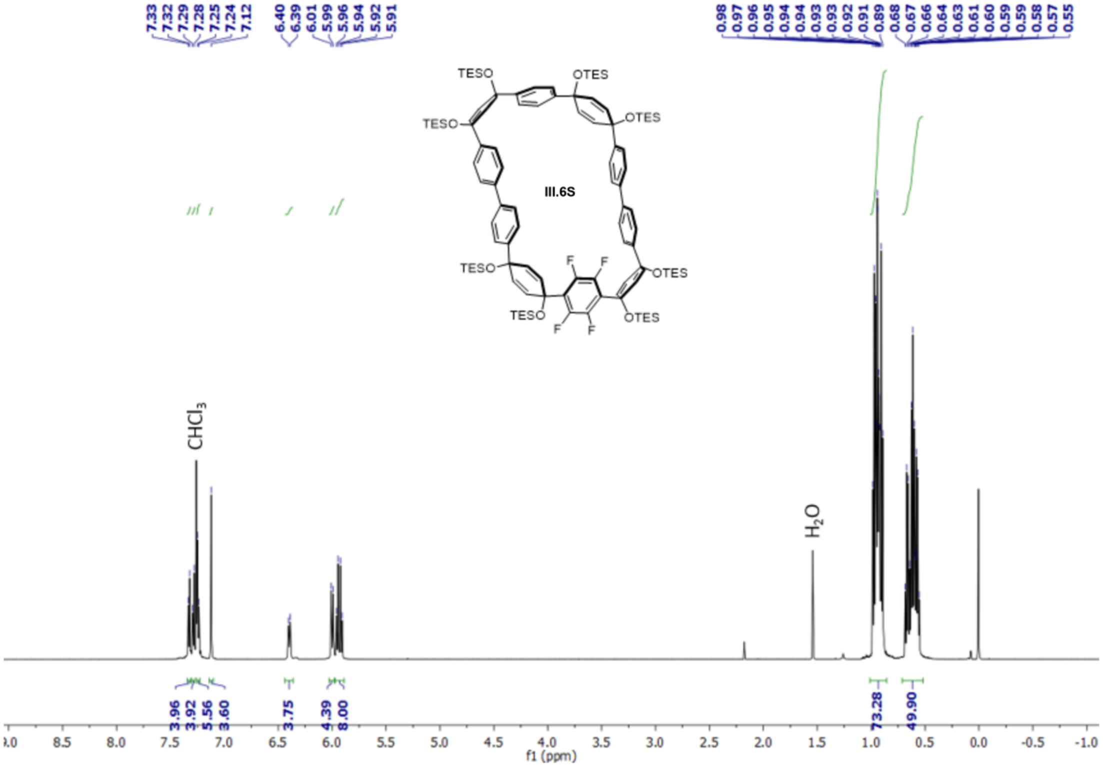
III.6S

7.33
7.32
7.29
7.28
7.25
7.24
7.12
6.40
6.39
6.01
5.99
5.96
5.94
5.92
5.91
0.98
0.97
0.96
0.95
0.94
0.94
0.93
0.93
0.92
0.91
0.89
0.68
0.67
0.66
0.64
0.63
0.61
0.60
0.59
0.59
0.58
0.57
0.55
TESO
OTES
F
CHCl₃
H₂O
3.96
3.92
5.56
3.60
3.75
4.39
8.00
73.28
49.90
9.0
8.5
8.0
7.5
7.0
6.5
6.0
5.5
5.0
4.5
4.0
3.5
3.0
2.5
2.0
1.5
1.0
0.5
0.0
-0.5
-1.0
f1 (ppm)

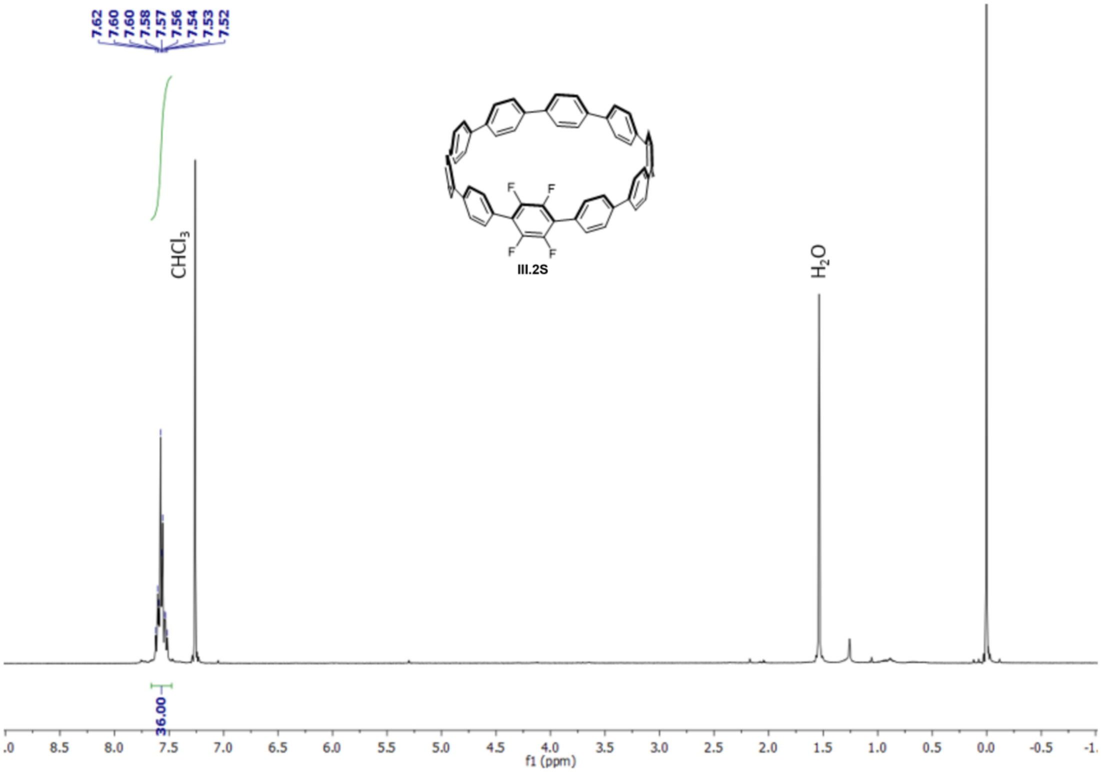

III.7.5. ^{13}C NMR Spectra.

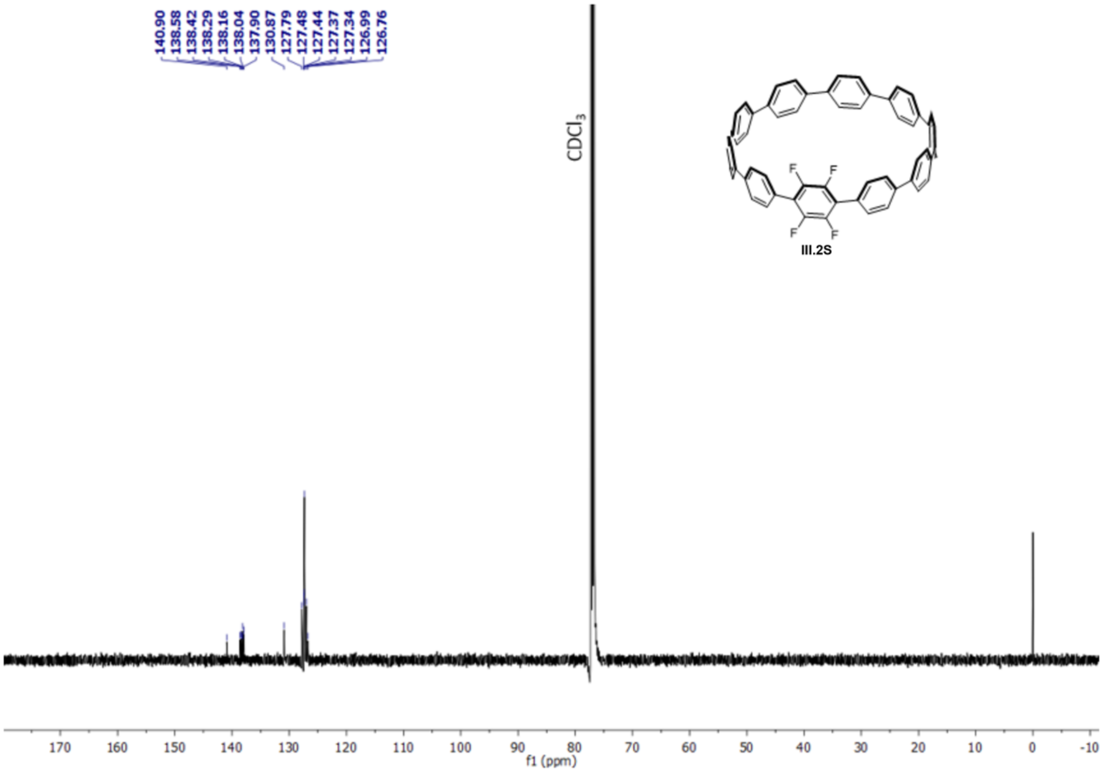

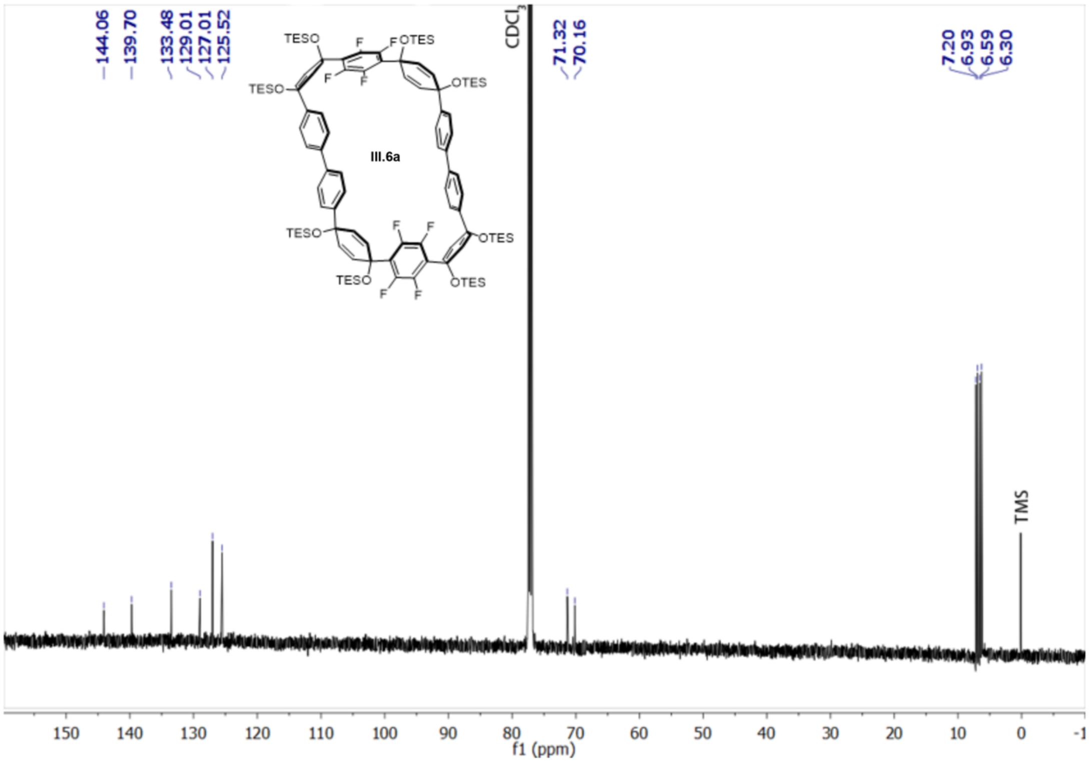
144.06
139.70
133.48
129.01
127.01
125.52
CDCl3
71.32
70.16
7.20
6.93
6.59
6.30
TMS
III.6a
TESO
OTES
F
150 140 130 120 110 100 90 80 70 60 50 40 30 20 10 0 -1
f1 (ppm)

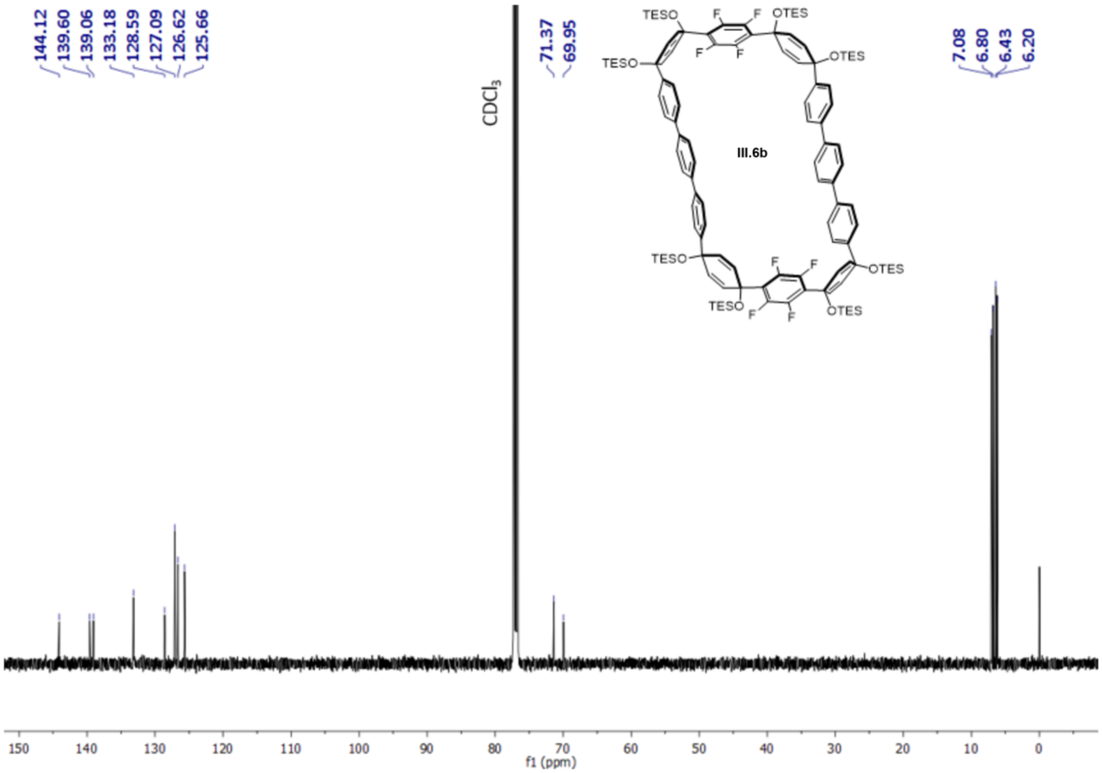
144.12
139.60
139.06
133.18
128.59
127.09
126.62
125.66
CDCl3
71.37
69.95
7.08
6.80
6.43
6.20
III.6b
TESO
OTES
F
150 140 130 120 110 100 90 80 70 60 50 40 30 20 10 0
f1 (ppm)

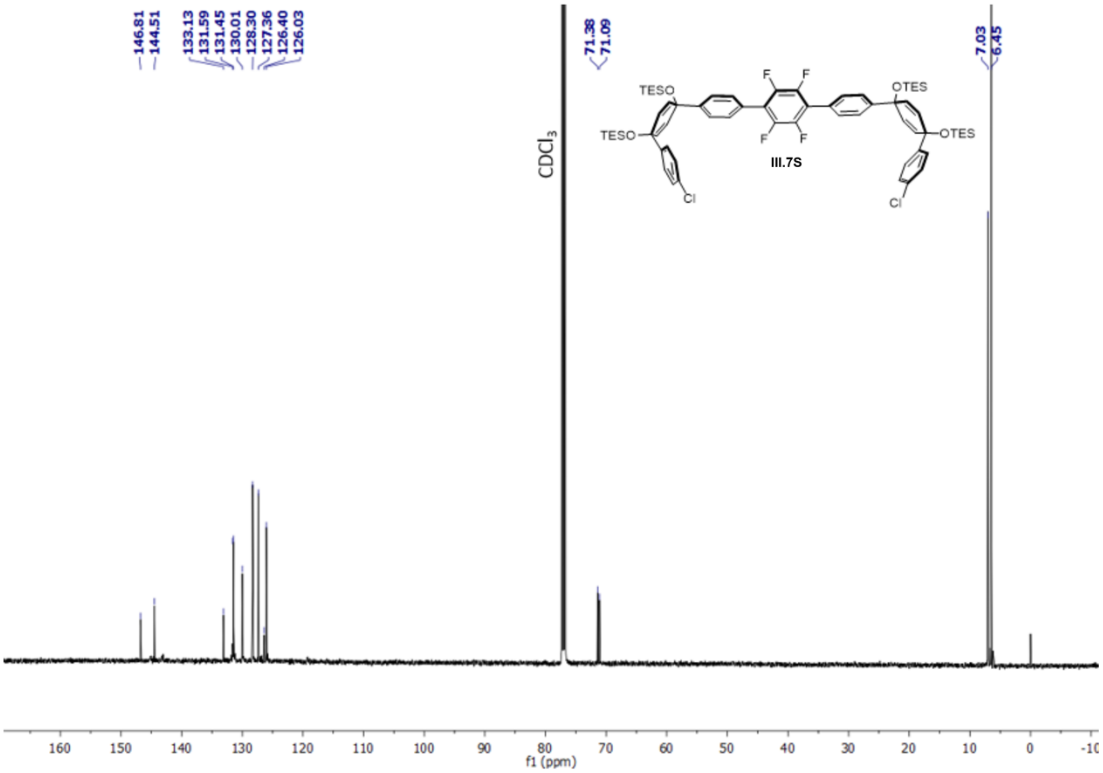
146.81
144.51
133.13
131.59
131.45
130.01
128.30
127.36
126.40
126.03
71.38
71.09
7.03
6.45
CDCl$_3$
TESO
TESO
F
F
F
F
OTES
OTES
Cl
Cl
III.7S
160
150
140
130
120
110
100
90
80
70
60
50
40
30
20
10
0
-10
f1 (ppm)

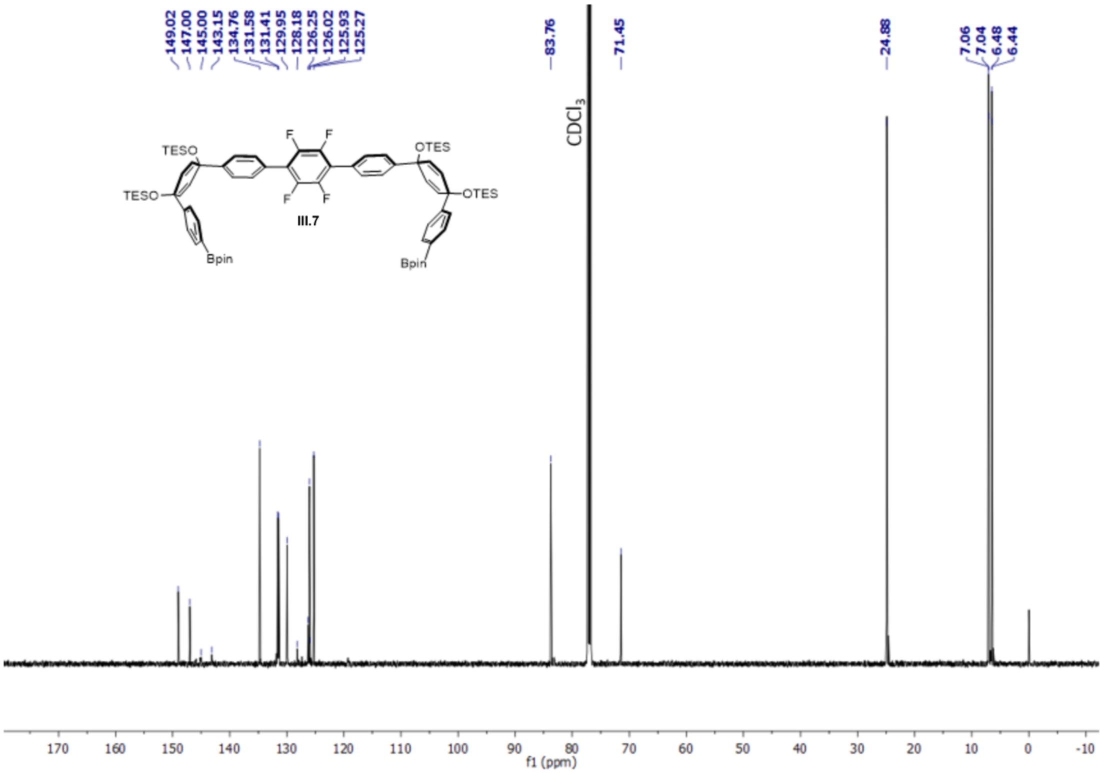
149.02
147.00
145.00
143.15
134.76
131.58
131.41
129.95
128.18
126.25
126.02
125.93
125.27
83.76
71.45
24.88
7.06
7.04
6.48
6.44
CDCl$_3$
TESO
TESO
F
F
F
F
OTES
OTES
Bpin
Bpin
III.7
170
160
150
140
130
120
110
100
90
80
70
60
50
40
30
20
10
0
-10
f1 (ppm)

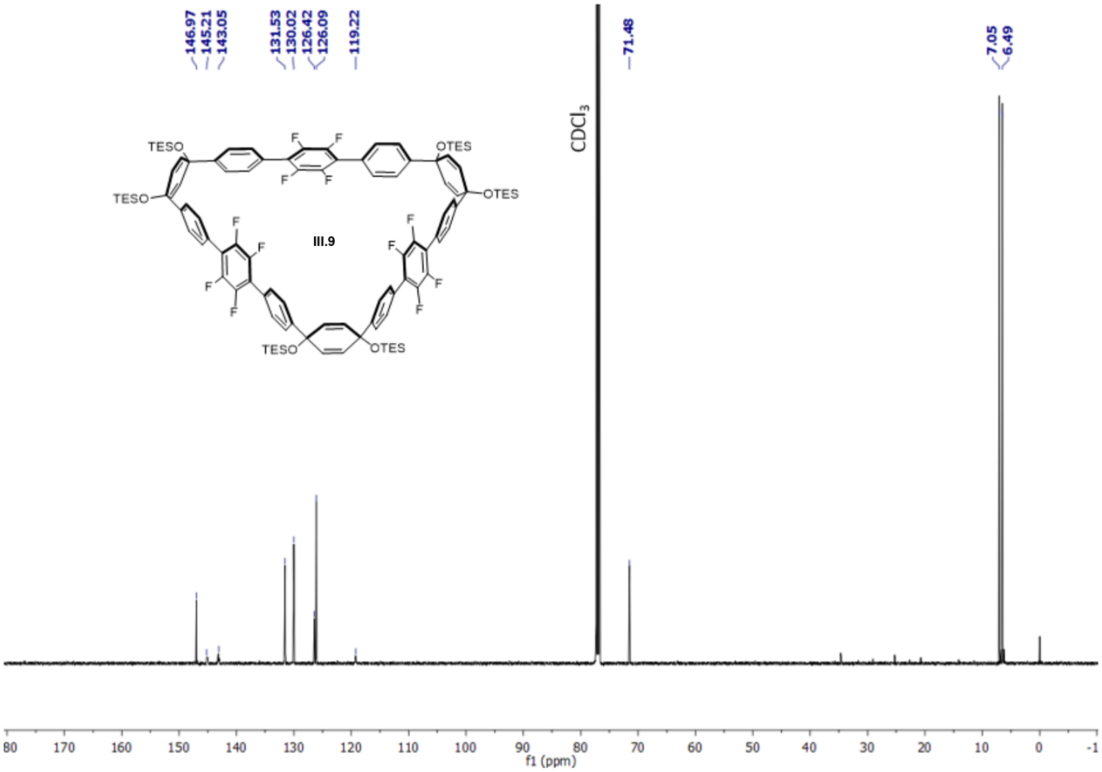
146.97
145.21
143.05
131.53
130.02
126.42
126.09
119.22
71.48
7.05
6.49
CDCl3
TESO
TESO
OTES
OTES
TESO
OTES
F
F
F
F
F
F
F
F
F
F
F
F
III.9
80
170
160
150
140
130
120
110
100
90
80
70
60
50
40
30
20
10
0
-1
f1 (ppm)

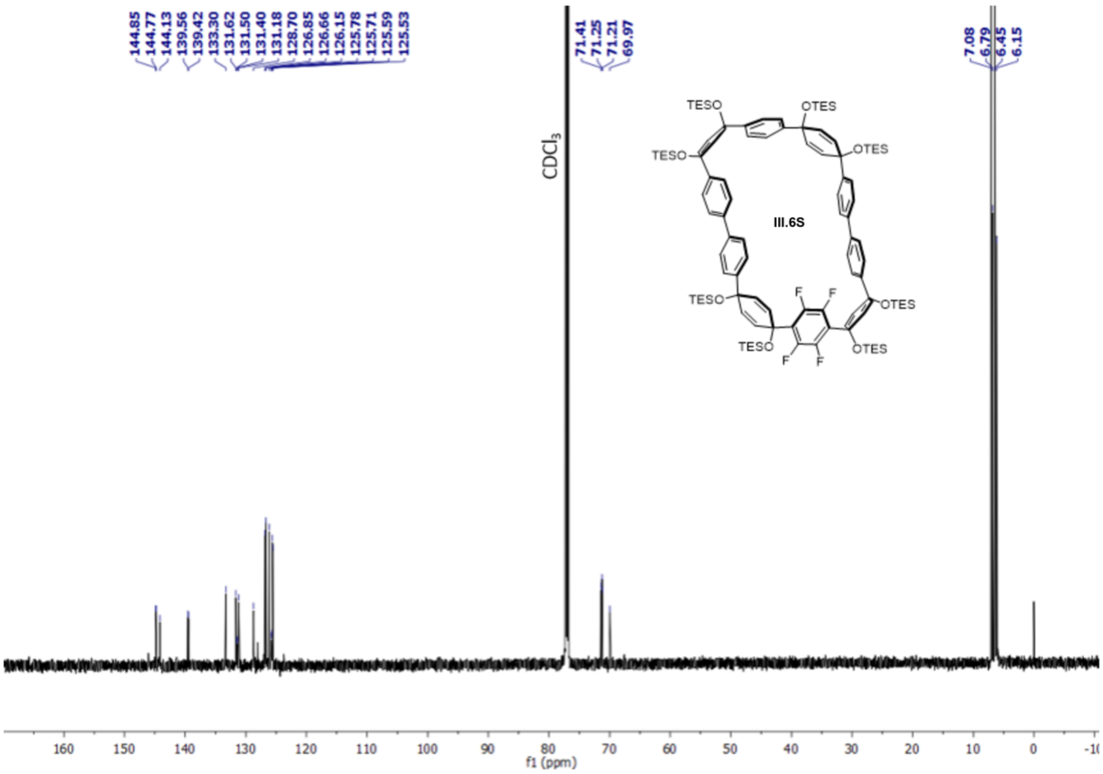
144.85
144.77
144.13
139.56
139.42
133.30
131.62
131.50
131.40
131.18
128.70
126.85
126.66
126.15
125.78
125.71
125.59
125.53
71.41
71.25
71.21
69.97
7.08
6.79
6.45
6.15
CDCl3
TESO
OTES
TESO
OTES
III.6S
TESO
OTES
TESO
OTES
F
F
F
F
160
150
140
130
120
110
100
90
80
70
60
50
40
30
20
10
0
-1(
f1 (ppm)

III.7.6. ^{19}F NMR Spectra.

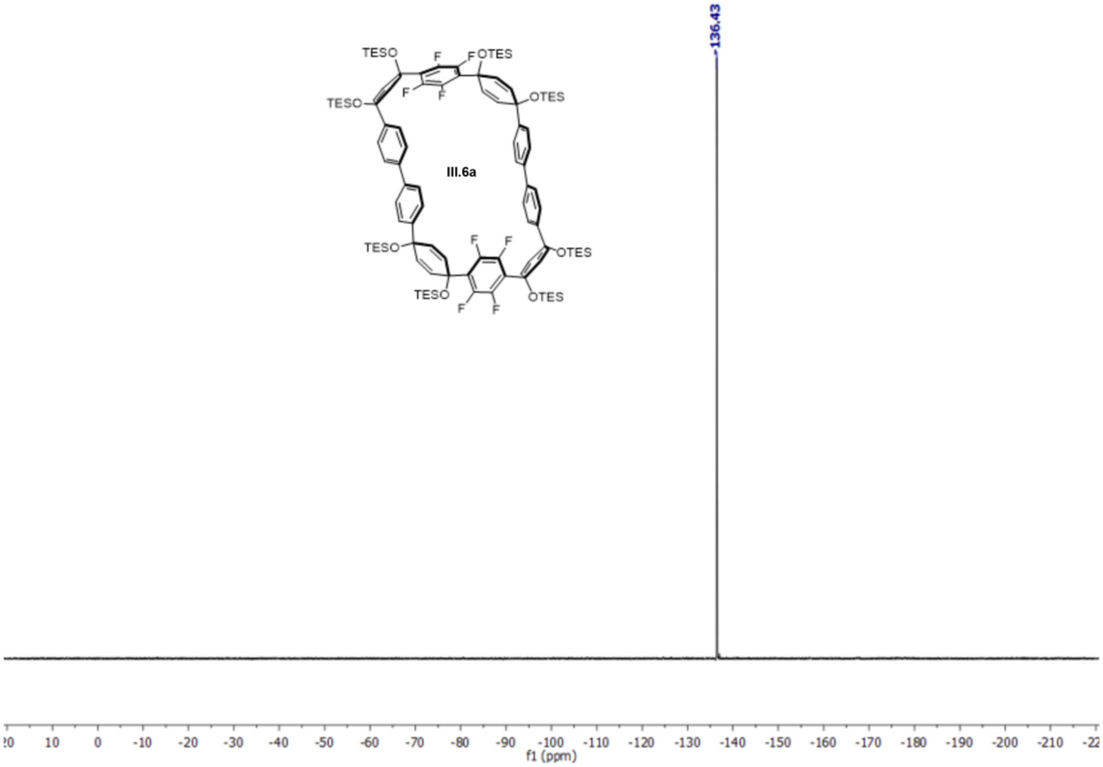

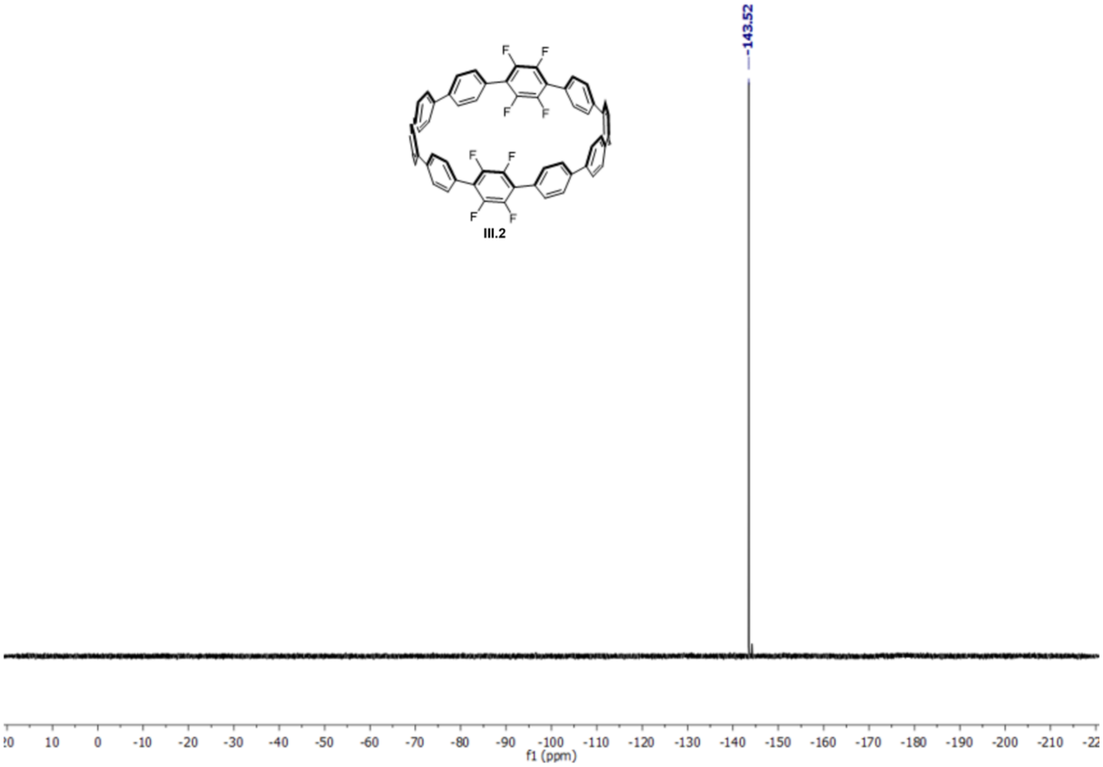

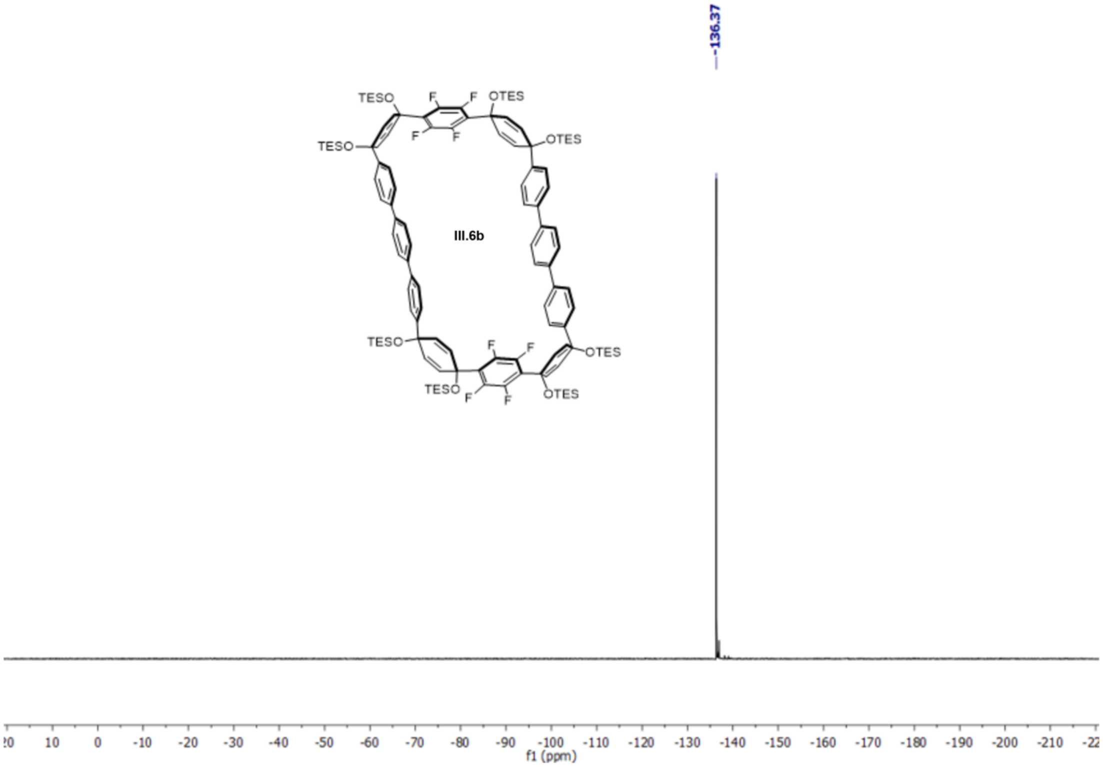
-136.37
TESO
F
F
OTES
TESO
F
F
OTES
III.6b
TESO
F
F
OTES
TESO
F
F
OTES
20
10
0
-10
-20
-30
-40
-50
-60
-70
-80
-90
-100
-110
-120
-130
-140
-150
-160
-170
-180
-190
-200
-210
-220
f1 (ppm)

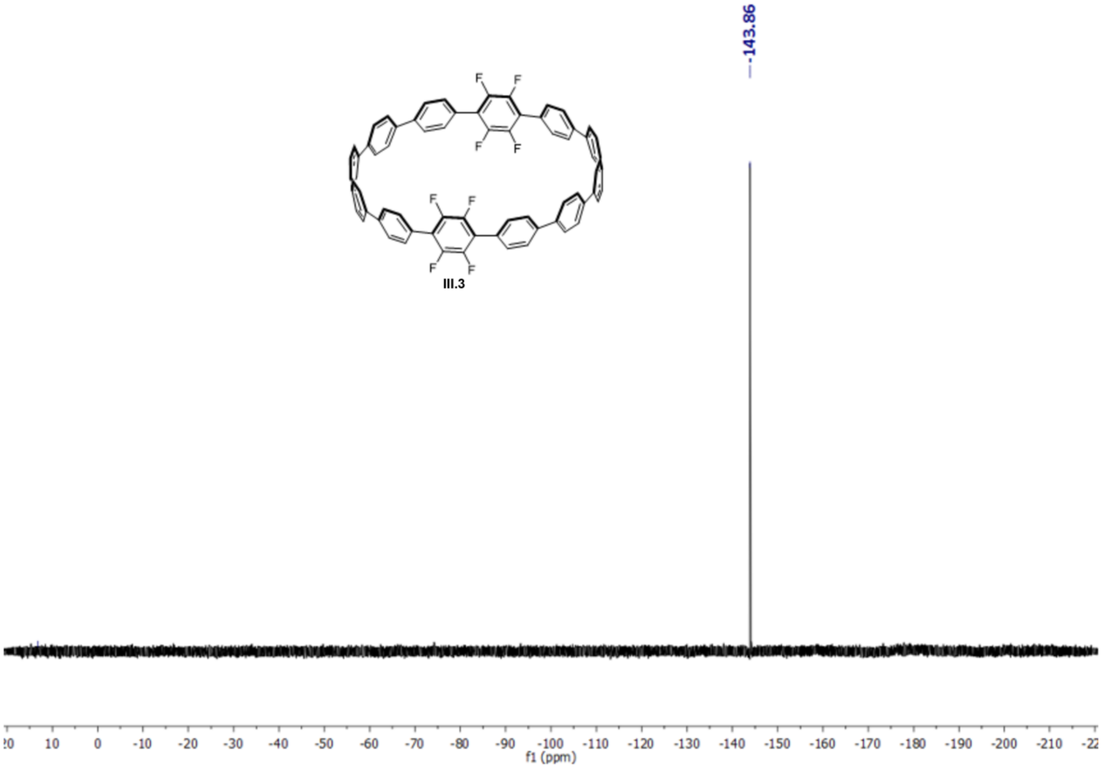
-143.86
F
F
F
F
F
F
F
F
III.3
20
10
0
-10
-20
-30
-40
-50
-60
-70
-80
-90
-100
-110
-120
-130
-140
-150
-160
-170
-180
-190
-200
-210
-220
f1 (ppm)

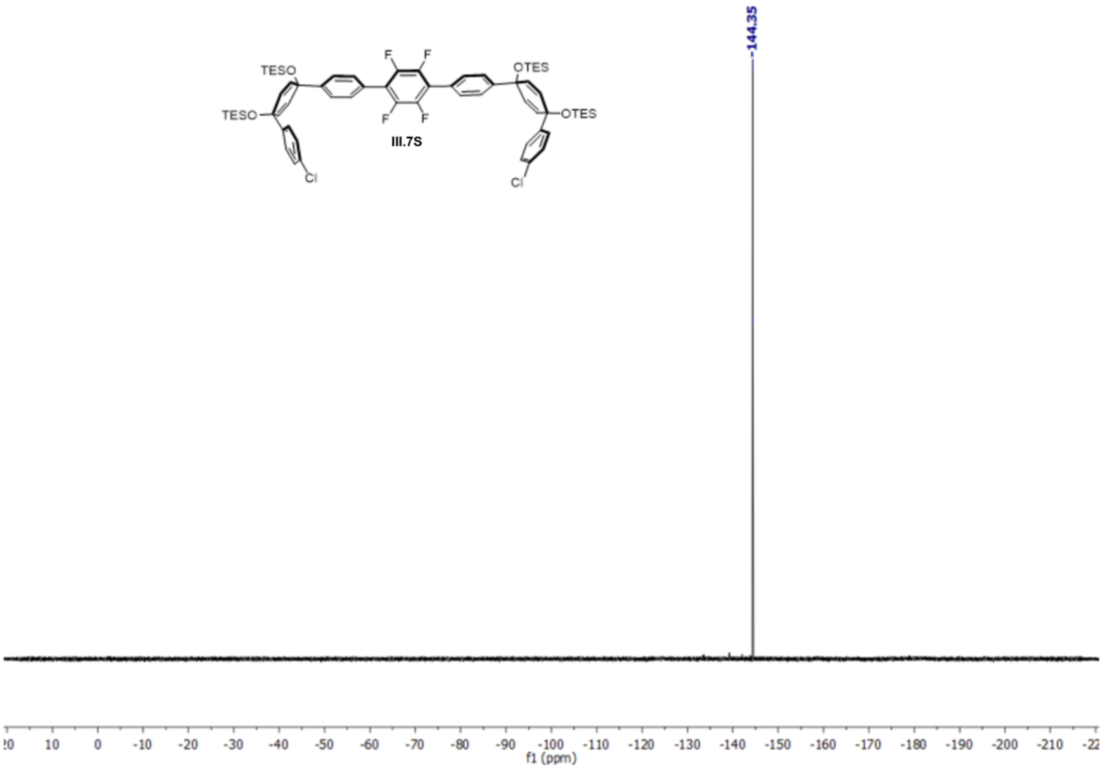
-144.35
TESO
TESO
F
F
F
F
OTES
OTES
III.7S
Cl
Cl
20 10 0 -10 -20 -30 -40 -50 -60 -70 -80 -90 -100 -110 -120 -130 -140 -150 -160 -170 -180 -190 -200 -210 -22
f1 (ppm)

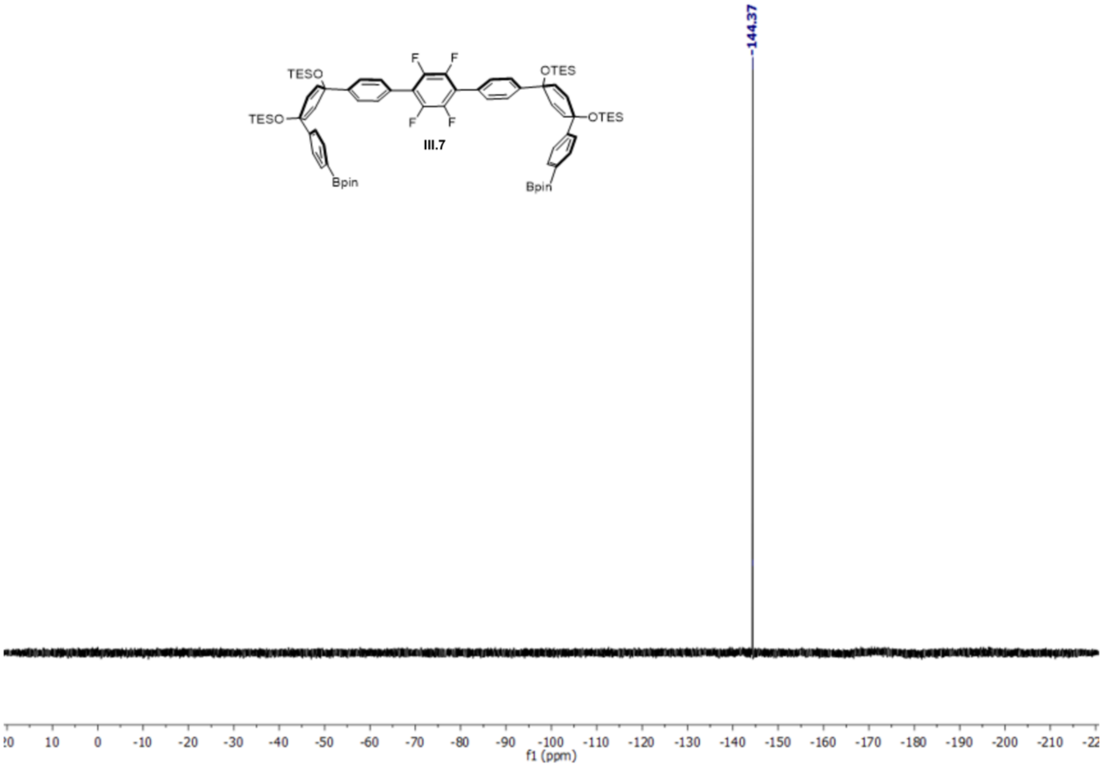
-144.37
TESO
TESO
F
F
F
F
OTES
OTES
III.7
Bpin
Bpin
20 10 0 -10 -20 -30 -40 -50 -60 -70 -80 -90 -100 -110 -120 -130 -140 -150 -160 -170 -180 -190 -200 -210 -22
f1 (ppm)

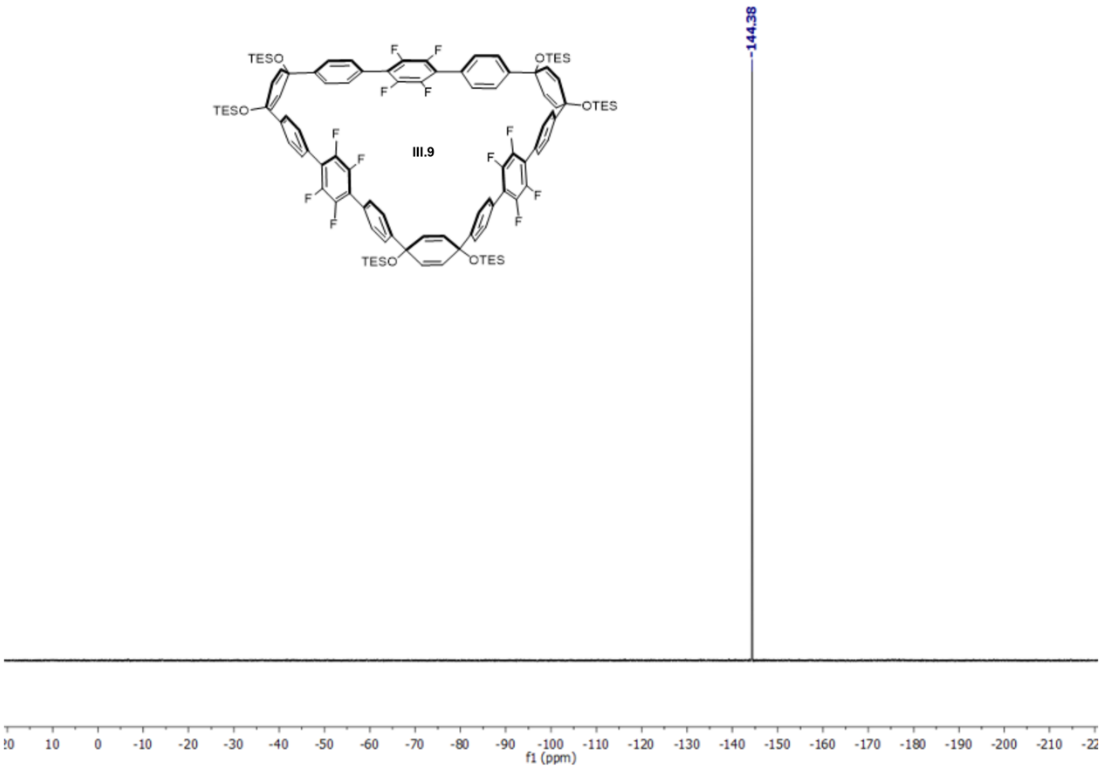
-144.38
TESO
TESO
OTES
OTES
TESO
OTES
F
III.9
10
0
-10
-20
-30
-40
-50
-60
-70
-80
-90
-100
-110
-120
-130
-140
-150
-160
-170
-180
-190
-200
-210
f1 (ppm)

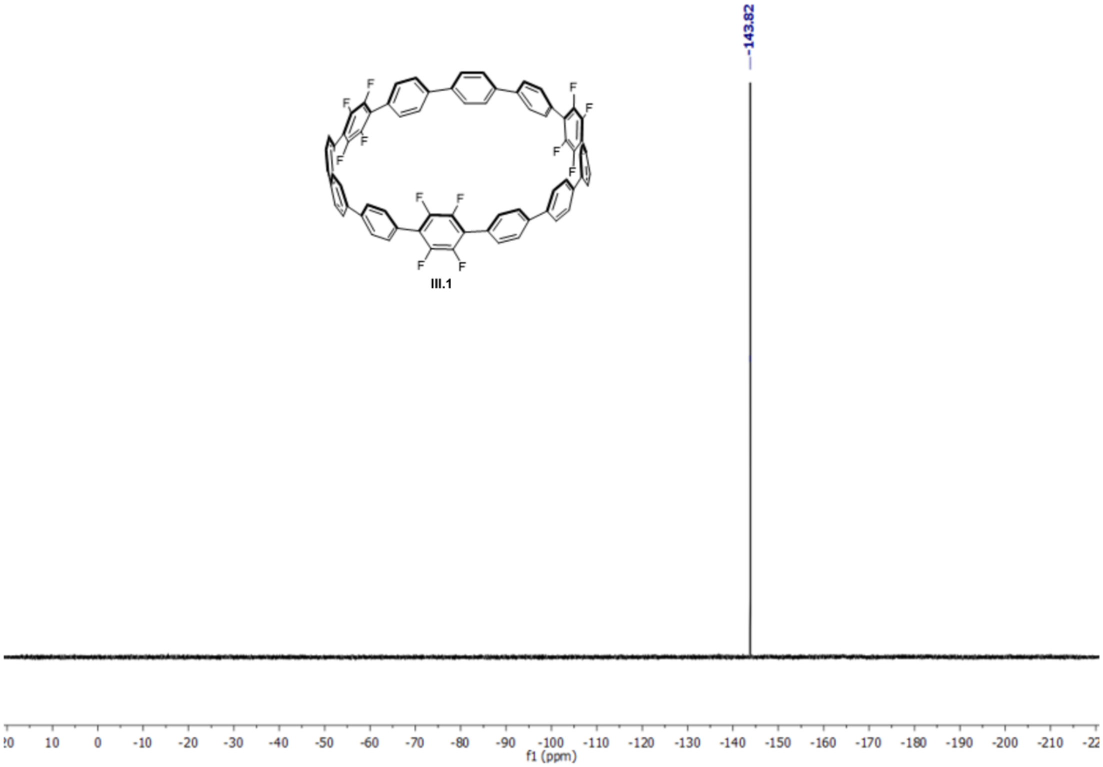
-143.82
F
III.1
10
0
-10
-20
-30
-40
-50
-60
-70
-80
-90
-100
-110
-120
-130
-140
-150
-160
-170
-180
-190
-200
-210
f1 (ppm)

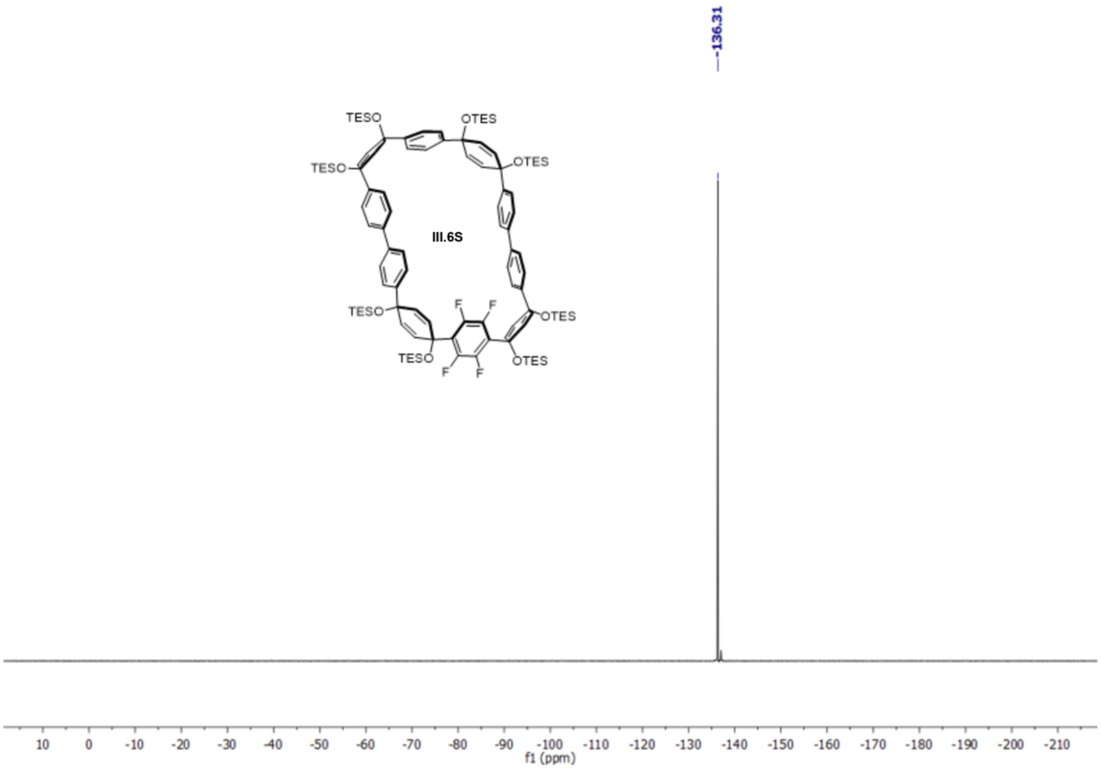
-136.31
TESO
OTES
III.6S
F
10 0 -10 -20 -30 -40 -50 -60 -70 -80 -90 -100 -110 -120 -130 -140 -150 -160 -170 -180 -190 -200 -210
f1 (ppm)

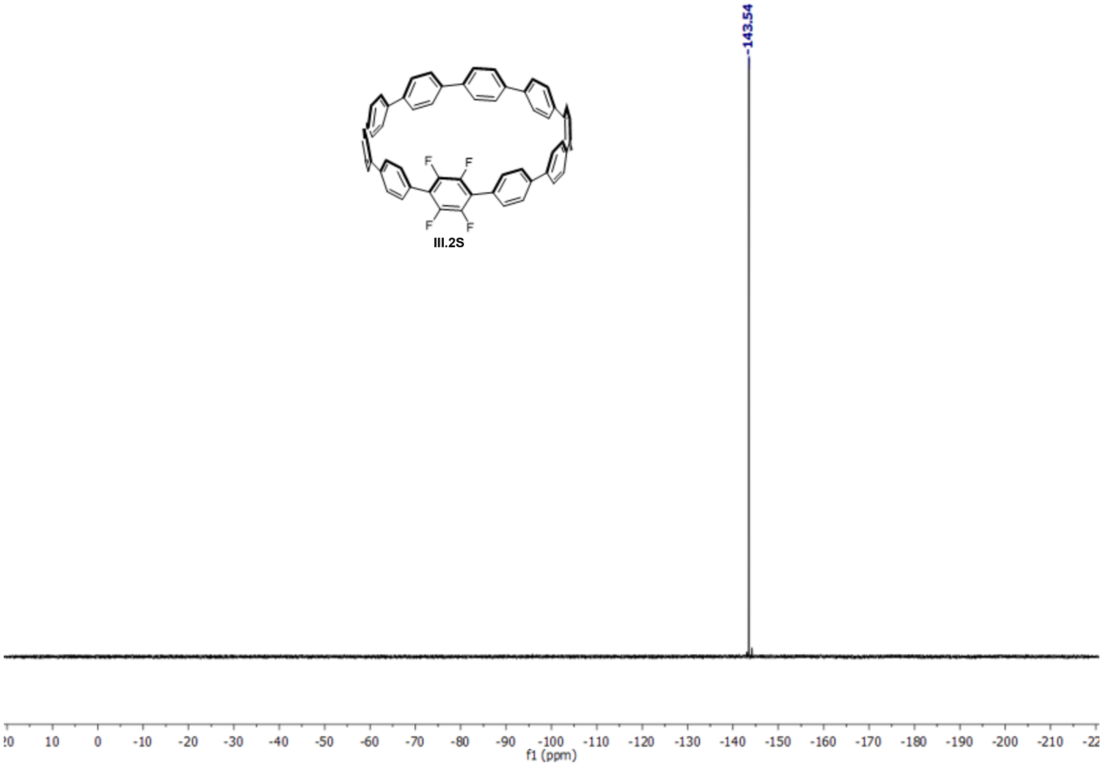
-143.54
F
III.2S
20 10 0 -10 -20 -30 -40 -50 -60 -70 -80 -90 -100 -110 -120 -130 -140 -150 -160 -170 -180 -190 -200 -210 -22
f1 (ppm)

III.7.7. Photophysical Data.

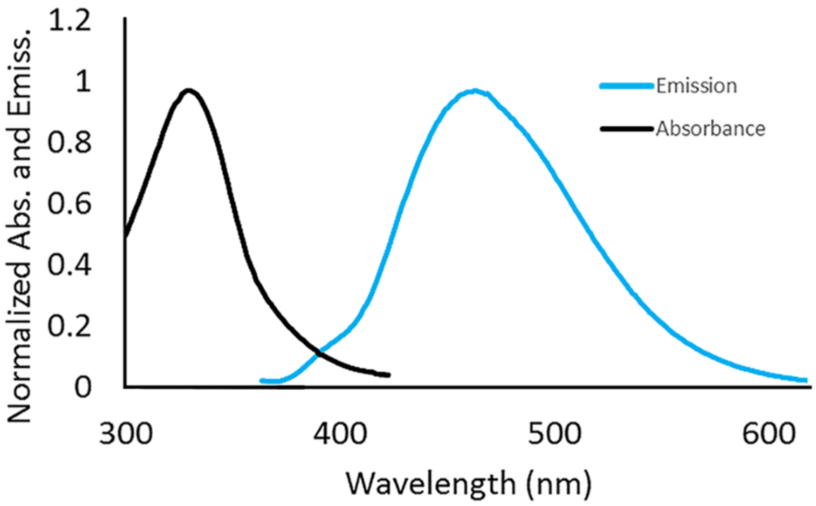

Figure III.7. Absorbance (black) and emission (blue) spectra for nanohoop **III.2**.

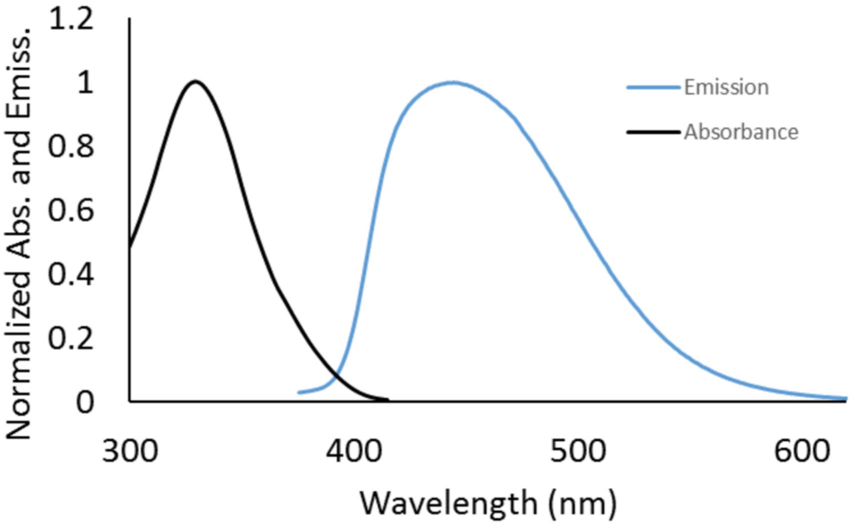

Figure III.8. Absorbance (black) and emission (blue) spectra for nanohoop **III.3**.

III.7.8. Binding Constant (*K*$_a$) Determination.

Binding constants were determined via fluorescence quenching experiments as reported by the Sessler[66] and Yamago[38] groups. In a typical experiment, a solution of C_{60} in toluene (1.01×10^{-5} mol L^{-1}) was added to a solution of fluorinated nanohoop **III.2** in toluene (5.00×10^{-7} mol L^{-1}). The change in fluorescence emission intensity at 460 nm was then monitored for each addition (Fig. III.9).

The K_a data was then determined by fitting the data to eq III.1:

$$F/F_o = \left(1 + \frac{k_f}{k_{sf}} * K_a * [C_{60}]\right) / (1 + K_a * [C_{60}]) \qquad \text{(III.1)}$$

where F, F_o, k_f, k_s, K_a, and $[C_{60}]$ denote fluorescence intensity, fluorescence of fluorinated nanohoop **III.2** prior to the addition of C_{60}, a proportionality constant of the complex, a proportionality constant of the host, the binding constant of C_{60}, and the concentration of C_{60}, respectively. The data from Figure III.9 have been fit to eq III.1 and are shown in Figure III.10.

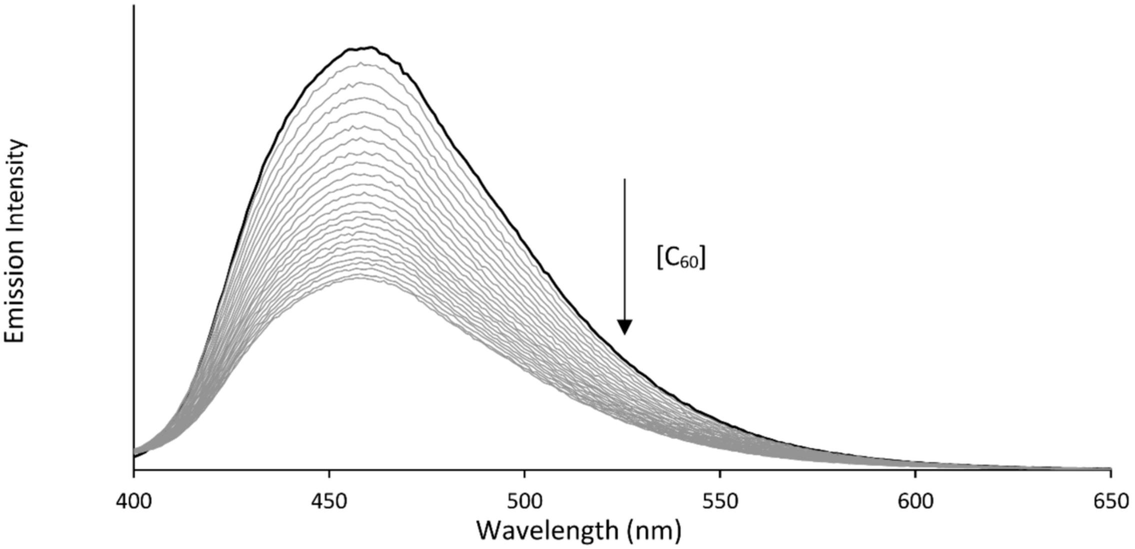

Figure III.9. Change in emission intensity fluorinated nanohoop **III.2** with increasing concentration of C_{60}. The initial concentration of **III.2** was 5.00 X 10^{-7} mol L^{-1}, while the concentration of C_{60} was varied from 0.00 – 2.88 x 10^{-7} mol L^{-1}.

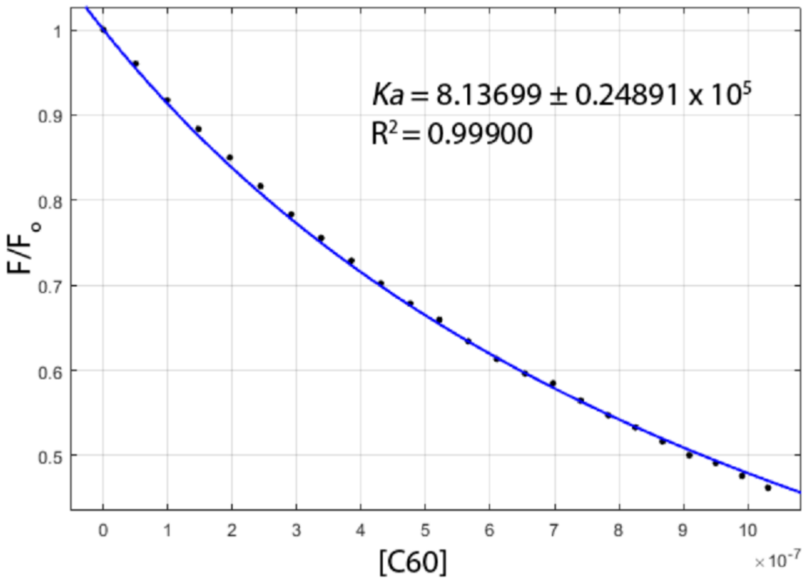

Figure III.10. Correlation of [C_{60}] on the fluorescence intensity of fluorinated nanohoop **III.2** in toluene. The change in fluorescence at 460 nm (obtained from Figure III.9) was fit to eq III.1 to obtain the K_a.

III.7.9. Crystallographic Data.

Diffraction intensities for **III.2** were collected at 173 K on a Bruker Apex2 CCD diffractometer using an Incoatec Cu IμS source, CuKα radiation, 1.54178 Å. Space groups were determined based on systematic absences. Absorption corrections were applied by SADABS.[67] Structures were solved by direct methods and Fourier techniques and refined on *F*2 using full matrix least-squares procedures. All non-H atoms were refined with anisotropic thermal parameters except for the C and O atoms in solvent THF molecules in **III.2** which were refined with isotropic thermal parameters. All H atoms in **III.2** were refined in calculated positions in a rigid group model. Six THF molecules are in **III.2**, with two THF molecules being located outside the hoop. Four THF molecules in **III.2** are located inside the hoops. Positions of the THF molecules in **III.2** in the hoop were found on the residual density map and refined. Thermal atomic parameters for THF molecules located in the hoop in **III.2** are large and show that these molecules seem to be disordered. One short H···H contact between these THF molecules (H18c···H21C, 1.94 Å) also indicates that the THF molecules located in the hoop are disordered. X-ray diffraction from crystals of **III.2** at high angles was very weak. Even by using a strong Incoatec Cu IμS source it was possible to collect diffraction data only up to $2\theta_{\max}$ = 98.79°. Regardless, the collected data provide an appropriate number of measured reflections per refined parameters: 7163 reflections per 833 refined parameters. All calculations were performed by the Bruker SHELXL-2014/7 package.[68]

Diffraction intensities for **III.3** were collected at 173 K on a Bruker Apex2 CCD diffractometer using CuKα radiation, λ = 1.54178 Å. Space groups were determined based on intensity statistics. Absorption corrections were applied by SADABS.[67] Structures were solved by direct methods and Fourier techniques and refined on *F*2 using full matrix least-squares procedures. All non-H atoms were refined with anisotropic thermal parameters. All H atoms were refined in calculated positions in a rigid group model. There are two symmetrically independent main molecules in the crystal structure. The molecules form columns in the crystal. Two solvent molecules CH_2Cl_2 filling a space between the columns in the packing are ordered. These solvent molecules were found and refined. Three pentane and two dichloromethane solvent molecules filling a space inside the hoop are highly disordered and were treated by SQUEEZE.[69] Correction of the X-ray data by SQUEEZE is 490 electron/cell; the required value is 420 electron/cell for four CH_2Cl_2 and six C_5H_{12} molecules in the full unit cell. All calculations were performed by the Bruker SHELXL-2014 package.[68]

Diffraction intensities for C_{60}@**III.2** were collected at 173 K on a Bruker Apex2 CCD diffractometer using an Incoatec Cu IμS source, CuKα radiation, 1.54178 Å. Space groups were determined based on systematic absences. Absorption corrections were applied by SADABS.[67] Structures were solved by direct methods and Fourier techniques and refined on *F*2 using full matrix least-squares procedures. All non-H atoms were refined without any restrictions and with anisotropic thermal parameters. H atoms in the hoop were refined in calculated positions in a rigid group model. The crystal structure has additional solvent molecules which are highly disordered and fill out a space between the main molecules. Based on the residual density map we suggest that in the crystal structure there are highly disordered solvent molecules; one toluene molecule is disordered in a general position, and four O_2Et_2 solvent molecules are disordered over an inversion center. These disordered solvent molecules have been treated by SQUEEZE,[69] but they are added to the formula of the compound. Correction of the X-ray data by SQUEEZE is 1224 electron/unit cell; the required number of electrons is 1072 for eight toluene and 16 diethyl ether molecules in the full unit cell. Comments about using SQUEEZE have been added in the final CIF file. All calculations were performed by the Bruker SHELXL-2014/7.[68]

Diffraction intensities for **III.2S** were collected at 173 K on a Bruker Apex2 CCD diffractometer using CuKα radiations, 1.54178 Å. Space groups were determined based on systematic absences. The beta angle in the monoclinic system is close to 90°, but the structure was determined in the lowest possible space group $P21/c$ to avoid a possible disorder due to using high symmetry. Absorption corrections were applied by SADABS.[67] Structures were solved by direct methods and Fourier techniques and refined on $F2$ using full matrix least-squares procedures. All non-H atoms were refined with anisotropic thermal parameters. All H atoms were refined in calculated positions in a rigid group model. Refinement of the structure without restrictions shows that in all C_6-rings of the hoop the C−H distances are longer vs the standard C−H distance of 0.95 Å and C−F bond lengths are shorter vs the standard C−F distance of 1.35 Å. It indicates that four F atoms in the structure are disordered over many positions. After checking several options for the disorder, we found that the model in which four F atoms are disordered over all ten C_6-rings does not provide the best final data. Thus, the final refinement has been done for the model where four F atoms are disordered over six positions corresponding to the six C_6-rings which are slightly out from the central part of the hoop. Such a S32 conformation seems to be related to more steric repulsions for C_6F_4 groups vs the C_6H_6 groups. The disordered H and F atoms were taken in the refinement with appropriate occupation factors. The structure was refined with restrictions; the standard C−H and C−F distances were used as the targets for corresponding bonds and C_6F_4 groups were refined as flat groups. RIGU restriction has been also applied for thermal parameters. The residual density map shows that inside the main hoop there are one or two disordered solvent molecules. Our attempts to model this disorder with full or partially occupied positions of pentane/hexane molecules failed. These disordered solvent molecules have been treated by SQUEEZE.[69] The correction of the X-ray data by SQUEEZE, 80 electrons, corresponds to two possible solvent pentane molecules, C_5H_{12}, 84 electrons. Taking into account that these positions could be partially occupied, only one pentane molecule per the main molecule was added into the final formula. Diffraction from crystals of **III.2S** was very weak at high angles. Even using a strong Incoatec IμS Cu-source it was possible to collect diffraction data only to $2\theta_{\max} = 99.64°$. Regardless, the collected data provide in the refinements an appropriate number of reflections per independent refined parameters. All calculations were performed by the Bruker SHELXL-2014 package.[68]

Crystallographic Data for III.2. $C_{84}H_{80}F_8O_6$, $C_{60}H_{32}F_8 \cdot 6(OC_4H_8)$, $M = 1337.48$, $0.12 \times 0.08 \times 0.05$ mm, $T = 173(2)$ K, monoclinic, space group $P21/c$, $a = 13.4645(7)$ Å, $b = 19.5258(12)$ Å, $c = 26.8045(16)$ Å, $\beta = 94.711(4)°$, $V = 7023.2(7)$ Å^3, $Z = 4$, $D_c = 1.265$ Mg/m^3, $\mu(\mathrm{Cu}) = 0.764$ mm^{-1}, $F(000) = 2816$, $2\theta_{\max} = 98.79°$, 26273 reflections, 7163 independent reflections [$R_{\mathrm{int}} = 0.0655$], R1 = 0.0769, wR2 = 0.2115, and GOF = 1.021 for 7163 reflections (833 parameters) with $I > 2\sigma(I)$, R1 = 0.1071, wR2 = 0.2453, and GOF = 1.022 for all reflections, max/min residual electron density +0.559/ −0.506 eÅ^{-3}.

Crystallographic Data for 3. $C_{91}H_{84}Cl_8F_8$, $C_{72}H_{40}F_8 \cdot 4(CH_2Cl_2) \cdot 3(C_5H_{12})$, $M = 1613.18$, $0.15 \times 0.08 \times 0.03$ mm, $T = 173(2)$ K, triclinic, space group P-1, $a = 13.3910(4)$ Å, $b = 20.0066(6)$ Å, $c = 20.2292(6)$ Å, $\alpha = 119.204(2)°$, $\beta = 97.369(2)°$, $\gamma = 102.306(6)°$, $V = 4447.3(2)$ Å^3, $Z = 2$, $D_c = 1.205$ Mg/m^3, $\mu(\mathrm{Cu}) = 2.795$ mm^{-1}, $F(000) = 1676$, $2\theta_{\max} = 133.39°$, 61640 reflections, 15617 independent reflections [$R_{\mathrm{int}} = 0.0524$], R1 = 0.0499, wR2 = 0.1240, and GOF = 1.045 for 15617 reflections (775 parameters) with $I > 2\sigma(I)$, R1 = 0.0691, wR2 = 0.1313, and GOF = 1.045 for all reflections, max/min residual electron density +0.434/−0.404 eÅ^{-3}.

Crystallographic Data for C_{60}@III.2. $C_{150}H_{88}F_8O_4$, $C_{120}H_{32}F_8 \cdot 4(OC_4H_{10}) \cdot 2(C_7H_8)$, $M = 2106.20$, $0.12 \times 0.06 \times 0.02$ mm, $T = 173(2)$ K, monoclinic, space group $C2/c$, $a = 25.1372(10)$ Å, $b = 20.9252(9)$ Å, $c = 19.7816(8)$ Å, $\beta = 108.436(2)°$, $V = 9871.1(7)$ Å^3, $Z = 4$, $D_c = 1.417$ Mg/m^3, $\mu(\mathrm{Cu}) = 0.759$ mm^{-1}, $F(000) = 4368$, $2\theta_{\max} = 133.13°$, 39936 reflections, 8726 independent reflections [$R_{\mathrm{int}} = 0.0514$], R1 = 0.0964, wR2 = 0.2870, and GOF = 1.030 for 8726 reflections (577 parameters) with $I > 2\sigma(I)$, R1 = 0.1143, wR2 = 0.3028, and GOF = 1.030 for all reflections, max/min residual electron density +1.271/−0.391 eÅ^{-3}.

Crystallographic Data for 2S. $C_{65}H_{48}F_4$, $M = 905.03$, 0.08 × 0.04 × 0.03 mm, $T = 173(2)$ K, monoclinic, space group $P21/c$, $a = 30.539(2)$ Å, $b = 8.1703(7)$ Å, $c = 21.1171(16)$ Å, $\beta = 90.018(5)°$, $V = 5269.0(7)$ Å^3, $Z = 4$, $D_c = 1.141$ Mg/m^3, μ(Cu) = 0.597 mm^{-1}, $F(000) = 1896$, $2\theta_{max} = 99.64°$, 19529 reflections, 5331 independent reflections [$R_{int} = 0.0810$], R1 = 0.1338, wR2 = 0.3765, and GOF = 1.194 for 5331 reflections (613 parameters) with $I > 2\sigma(I)$, R1 = 0.2033, wR2 = 0.4214, and GOF = 1.115 for all reflections, max/min residual electron density +0.586/−0.518 eÅ^{-3}.

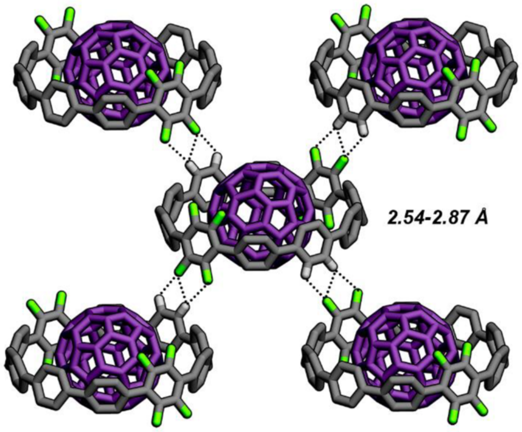

Figure III.11. C—H---F interactions (dotted lines) observed in the crystal packing of C_{60}@**III.2**. C---F distances measure from 3.20-3.81 Å.

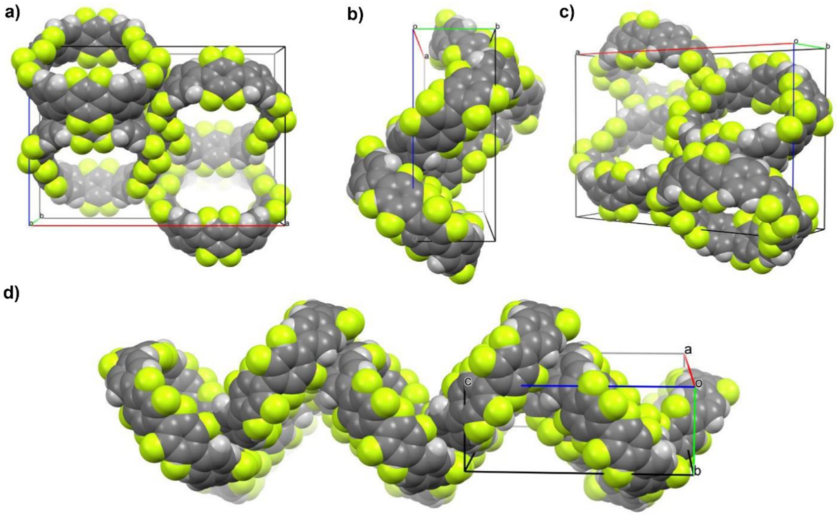

Figure III.12. (a-d) Observed solid-state packing of fluorinated nanohoop **III.2S**, with fluorine atoms disordered across six phenylene moieties.

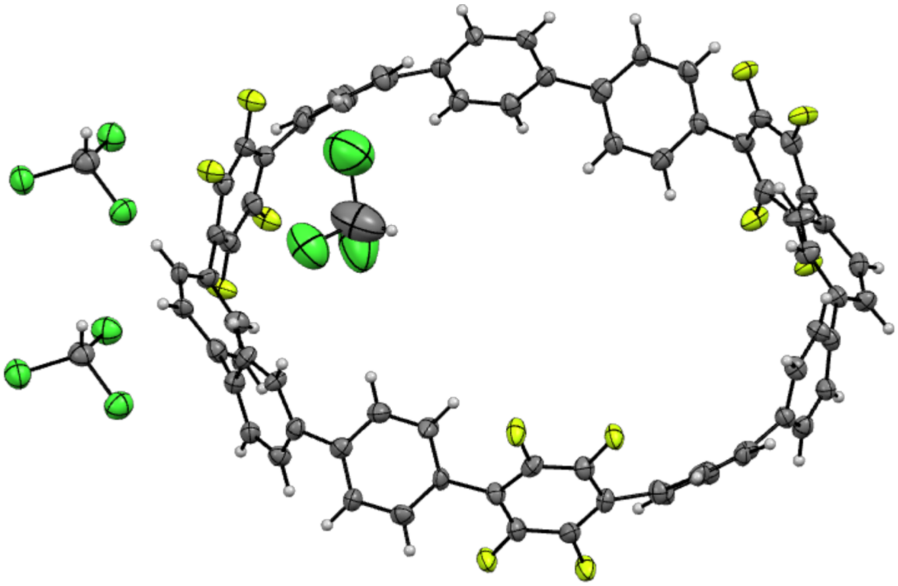

Figure III.13. Molecular structure of nanohoop **III.1**, with ellipsoids drawn at the 50% probability level. Crystals were grown via slow evaporation from $CHCl_3$.

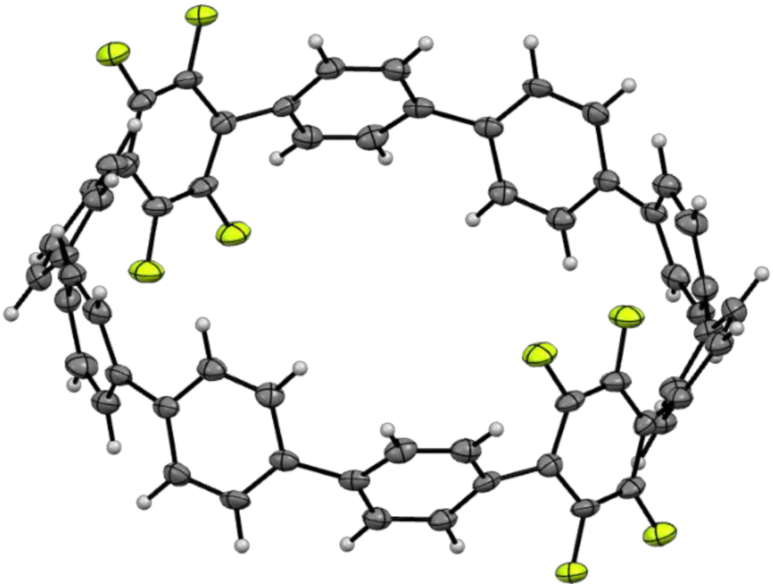

Figure III.14. Molecular structure of nanohoop **III.2**, with ellipsoids drawn at the 50% probability level. Crystals were grown via layering of pentane onto a solution of **III.2** in THF.

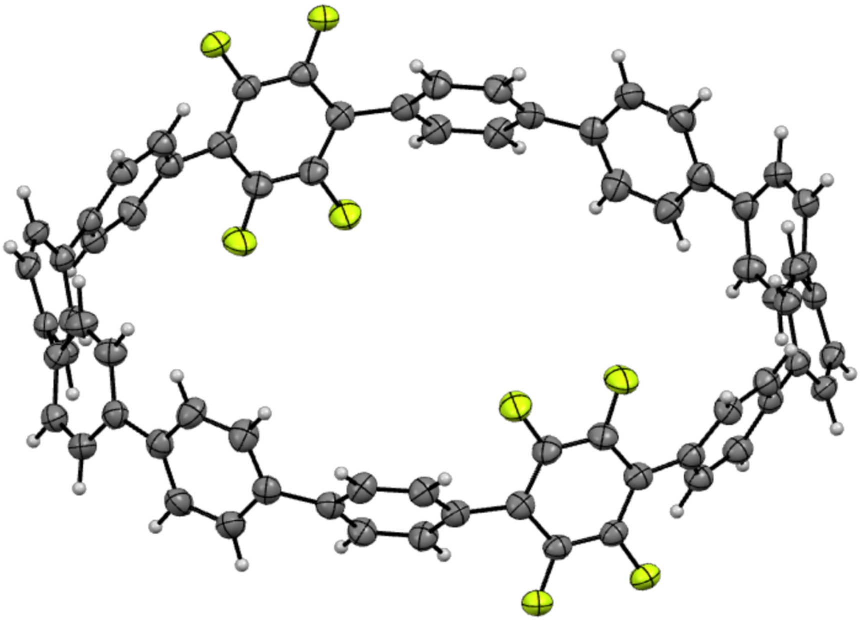

Figure III.15. Molecular structure of nanohoop **III.3**, with thermal ellipsoids drawn at the 50% probability level. Crystals were grown via slow evaporation from CH_2Cl_2.

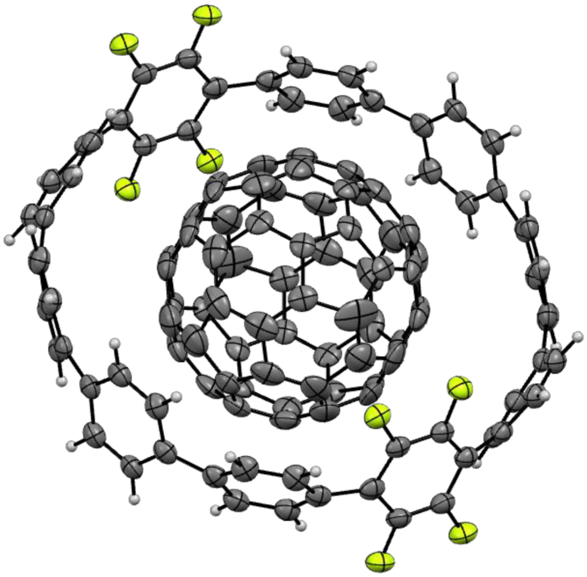

Figure III.16. Molecular structure of C_{60}@**III.2**, with thermal ellipsoids drawn at the 50% probability level. Crystals were grown via vapor diffusion of diethyl ether into a dilute THF/1,2-dichlorobenzene/toluene (1:1:1) solution of fluorinated nanohoop **III.2** and C_{60} (1:1).

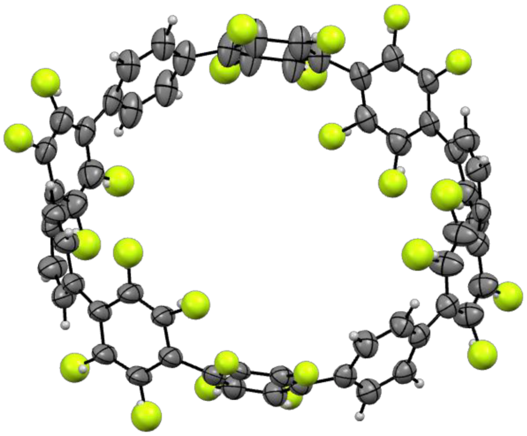

Figure III.17. Molecular structure of **III.2S**, with thermal ellipsoids drawn at the 50% probability level. Fluorine atoms were found to be disordered throughout the structure. Crystals were grown via layering pentane onto a solution of **III.2S** in THF.

III.7.10. Thermogravimetric (TGA) Analysis of Nanohoop III.1.

TGA analysis was carried out on a TA Instruments Thermogravimetric Analyzer (TGA Q500) instrument. A small quantity of nanohoop **III.1** (4.9870 mg, as measured by the instrument) was placed on an aluminum sample pan, and the sample was heated from room temperature to 600.00 °C at 10.00 °C per minute under N_2 atmosphere (Fig. III.18.).

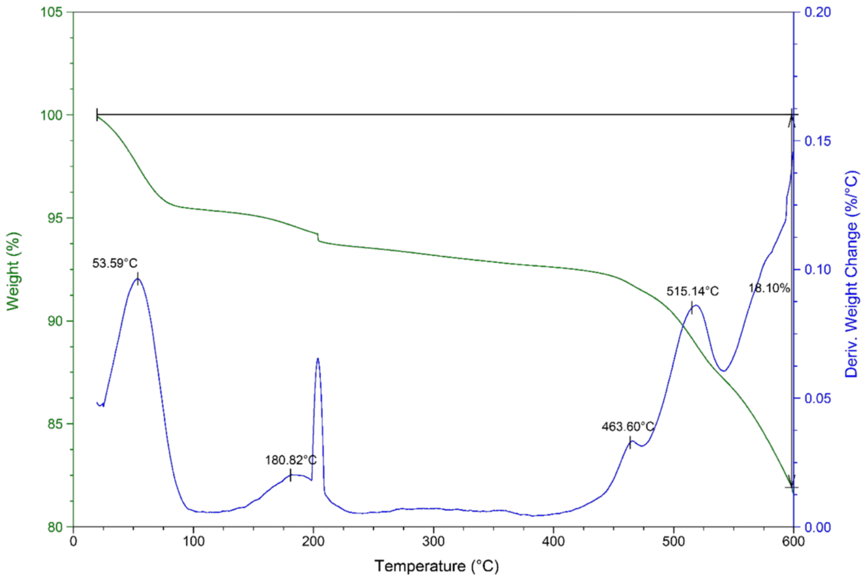

Figure III.18. TGA analysis of nanohoop **III.1**. The sharp mass loss at ~210 °C is attributed to a physical loss of material from the sample pan.

III.7.11. N_2 Uptake Studies.

Gas uptake measurements were performed using a Micromeritics ASAP 2020 Plus. Prior to analysis, samples were evacuated to 2 μtorr and held at 125 °C for approximately 24 h. Following this activation procedure, sample mass was determined from the difference between the empty sample tube and the sample tube loaded with evacuated material. N_2 uptake was measured isothermally using a liquid nitrogen bath (77 K). Pressure ranges for BET surface area analysis were selected based on guidelines detailed previously.[70] Activation temperatures were chosen based on the high temperatures of thermal stability indicated by thermogravimetric analysis (Fig. III.18. for nanohoop **III.1**, ref 54 for [12]CPP). Activation was considered complete when the sample outgassing rate fell below 2 μtorr min^{-1}. See Figures III.19. and III.20. for N_2 isotherm data and the BET plot, respectively.

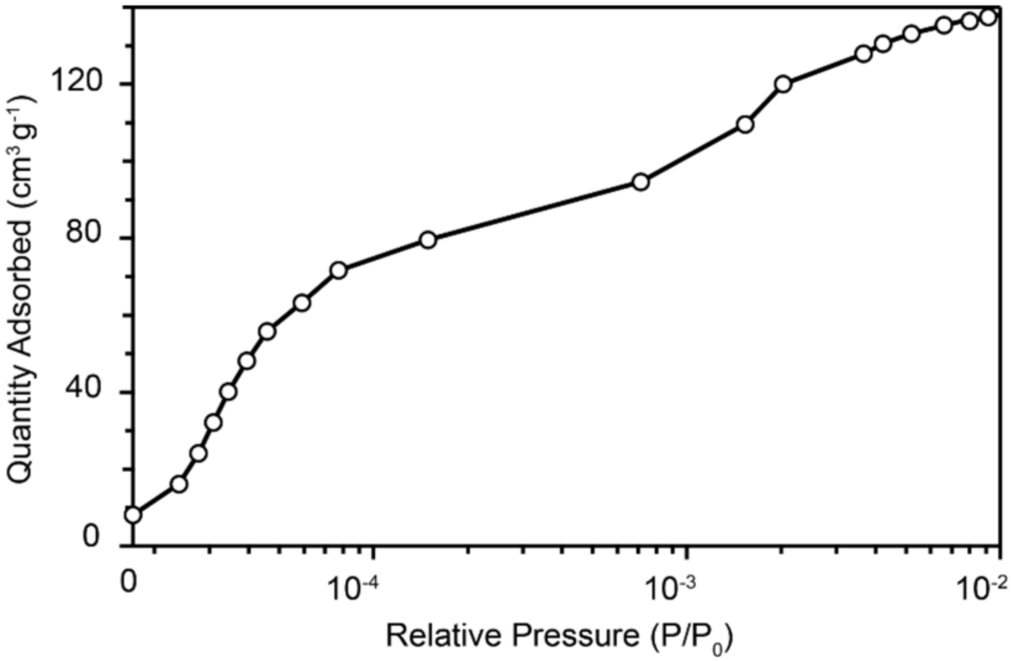

Figure III.19. N_2 uptake isotherm of nanohoop **III.1** shown at low relative pressures (P/P_0) in semi-log scale.

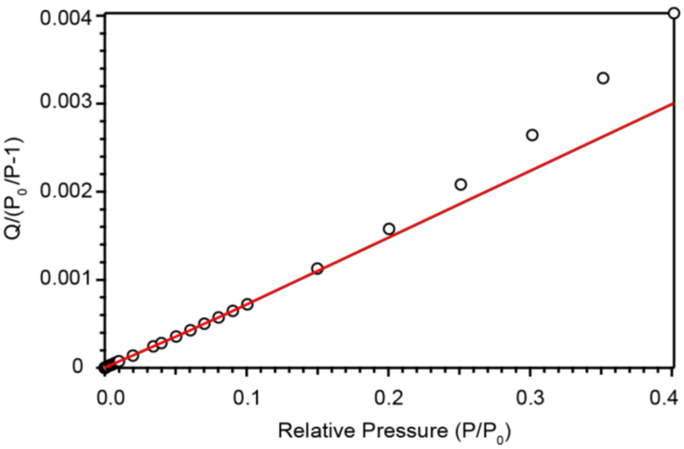

Figure III.20. Brunauer-Emmett-Teller (BET) plot of nanohoop **III.1**. Analysis was based on a linear fit (shown in red) to N_2 isotherm data at relative pressures between 10^{-5} – 10^{-1} P/P_0.

III.7.12. Powder X-ray Diffraction (PXRD) Analysis.

Powder X-ray Diffraction (PXRD) scans were taken in the range of 1.0−40.0° 2*θ* on a Bruker D2 Phaser system using a zero-background Si sample holder. PXRD patterns were collected of the as-synthesized powder and of the powder after it was evacuated at 200 °C for 48 h (Fig. III.21.).

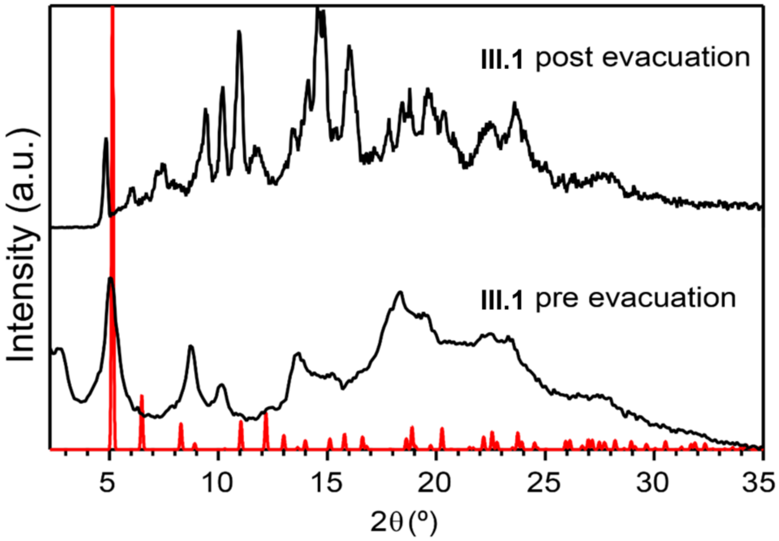

Figure III.21. Powder X-ray diffraction (PXRD) data for nanohoop **III.1** before (bottom) and after (top) evacuation to 2 *μ*torr at 125 °C. Calculated PXRD pattern for **III.1** based on the provided crystal structure is shown in red (calculated using Mercury visualization software[71]).

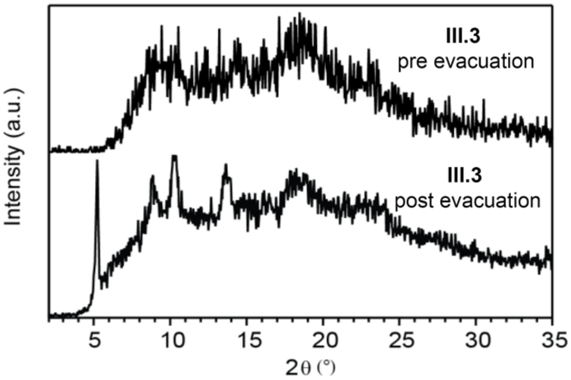

Figure III.22. Powder X-ray diffraction (PXRD) data for nanohoop **III.3** before (bottom) and after (top) evacuation to 2 μtorr at 125 °C.

III.7.13. Estimation of Cohesive Energies of III.2, III.2S, and III.1.

We can estimate the molecular cohesive or lattice energy from the individual interaction energies of the dimers through the following expression

$$U = \Sigma_i^{\text{dimers}} m_i \Delta E^{(i)}$$

with m_i being the number of symmetry-unique pairs taking one central molecule as reference, and $\Delta E^{(i)}$ being each of the interaction energies calculated before. The result must be half-divided to avoid a double counting of interactions, and it leads to a value of 65.6 kcal/mol, considerably higher than the value found before for pristine [12]CPP (57.6 kcal/mol).[57]

III.7.14 Additional Computational Data.

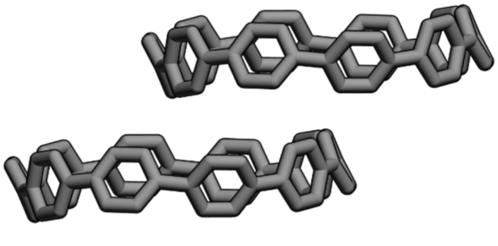

Figure III.23. Offset-tubular dimer extracted from the herringbone-like crystal structure of [10]CPP.[72]

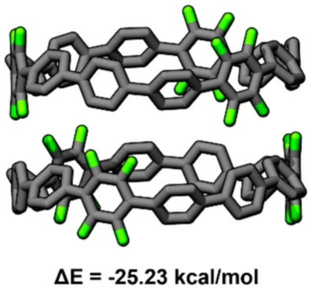

Figure III.24. Tubular-like dimer extracted from the crystalline structure of nanohoop **III.1**.

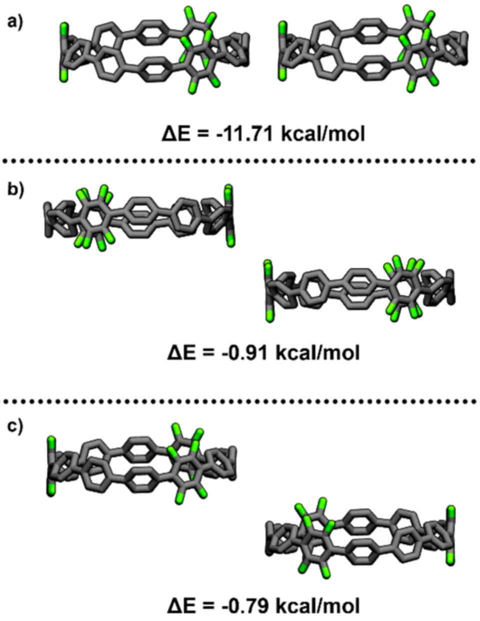

Figure III.25. Set of lateral-like dimers extracted from the crystalline structure of nanohoop **III.1**.

III.7.15. Bridge to Chapter IV.

In Chapter **III**, we demonstrated that fluorination of the CPP backbone can be used as a relatively general strategy to afford CNT mimic structures of varying diameter. In the case of fluorinated nanohoop **III.1**, we also discovered unique properties that were not exhibited by the non-fluorinated analog, namely the ability to uptake N_2 in the solid state. Considering this, we sought to explore what other nanohoop properties could be elicited or improved via fluorination-induced tubular assembly. We observed that the arene-perfluoroarene interactions observed in the crystal structures of the fluorinated nanohoops discussed in Chapter **III** induce improved π-π contacts between nanohoops, a critical feature for effective charge transfer in organic materials. In Chapter **IV**, we examine how the face-to-face arrangements observed in the crystal structures of fluorinated nanohoops may result in improved charge transport , potentially bolstering the viability of CPPs as organic electronic materials. Via preliminary solid-state conductivity measurements, we show that fluorination of the [10]CPP backbone results in a modest 10-fold increase in conductivity versus the non-fluorinated analog, which we tentatively attribute to the improved π-π contacts that we expect to be present in the solid-state arrangement of the fluorinated nanohoop.

CHAPTER IV

IMPROVING THE SOLID-STATE CONDUCTIVITY OF NANOHOOPS VIA ARENE-PERFLUOROARENE-INDUCED FACE-TO-FACE PACKING

Chapter **IV** is based on unpublished work, the concept of which was designed by myself, Dr. Jeff Van Raden, Dr. Evan Darzi, Professor Mark Lonergan, and Professor Ramesh Jasti. Dr. Jeff Van Raden carried out the synthesis of the fluorinated [10]CPP analog used in these studies and provided all cyclic voltammetry (CV) data and computational results. I fabricated the nanohoop-based organic field-effect transistors (OFETs) used in these studies and measured their conductivities. Professors Mark Lonergan and Ramesh Jasti contributed conceptually and to experimental design in regard to device measurements.

Organic electronics offer the promise of large-scale, solution-based device fabrication that is far less energy intensive and costly than the processes used to manufacture traditional silicon-based electronics. Additionally, the greater flexibility of organic electronic materials, particularly in thin-film form, can allow for the further development of novel technologies such as "foldable" electronics. While most research on potential candidates for effective organic semiconductors has focused on linear conjugated systems, relatively little work has been done to explore the viability of conjugated macrocycles as new scaffolds for the development of new organic charge-carriers. One major roadblock in the development of macrocyclic organic semiconductors is a lack of methods by which one can control their solid-state self-assembly, which is a critical factor in determining the efficiency of charge-transfer in organic solids. We present preliminary data suggesting that the solid-state conductivities of cycloparaphenylenes (CPPs), or "nanohoops", can be enhanced by inducing face-to-face aryl contacts between neighboring hoops. Via the fabrication and measurement of two-contact thin-film devices, a fluorinated [10]CPP analog (**IV.1**), which exhibits a multitude of arene-perfluoroarene interactions in the solid-state, is found to exhibit a conductivity ten times greater than that of non-fluorinated [10]CPP, which exhibits no face-to-face contacts in the solid-state. Both computational data and cyclic voltammetry (CV) experiments reveal that **IV.1** and [10]CPP have relatively similar electronic properties on the molecular level, suggesting that the observed difference in conductivity is not electronic in nature. Thus, we hypothesize that the observed order-of-magnitude increase in conductivity arises from morphological differences in the two materials, although further studies are required to more conclusively support this.

IV.1. Introduction

Organic electronic materials have been studied intensely throughout the last two decades due to the great promise they offer in next-generation electronic technologies.[1-3] From a design standpoint, organic materials boast remarkable versatility compared to their inorganic counterparts as organic synthesis allows for atom-precise molecular alterations to be made in order to finely tune electronic properties or solid-state morphologies. Additionally, most organic materials can be solution cast under mild conditions, allowing for fabrication processes that are typically far less energy-intensive, and thus less costly, than the high-temperature processes involved in the fabrication of typical silicon-based devices.[4-5] Solution-cast films of organic materials have also been shown to be remarkably flexible, making them ideal candidates for use in the inevitable wave of "foldable" electronics[1-5] that are expected to be appearing on store shelves in the coming years. Thus, the continued exploration of new scaffolds for use in the development of organic electronics remains a topic of great interest in the scientific community.

Despite the wide appeal of organic electronics, most studies have focused on the use of linear conjugated systems, those typically being acenes and their derivatives (Fig. IV.1).[7-10] This is not without good reason, as these structural motifs are relatively easy to functionalize, allowing for facile tuning of their electronics and solubility, and their flat geometries often lead to desirable face-to-face stacking in the solid state that facilitates effective π-π contacts.[1, 4, 7-8] While excellent progress has been made in the field of linear acene-based organic electronics, with some materials exhibiting formidable charge mobilities (μ) in thin-film form,[9-10] emerging research suggests that macrocyclic small molecule scaffolds may offer a competitive advantage in many areas. First, their circular architectures could, in theory, provide enhanced contacts between neighboring molecules in the solid state.[11] Additionally, macrocycles inherently exhibit internal cavities and thus can potentially host a variety of guest molecules in order to further tune electronic properties.[11-12] One of the most convincing arguments for the effectiveness of macrocyclic organic electronics is provided by Nuckolls et al., who have shown that *n*-type perylenediimide-based macrocycles vastly outperform their linear counterparts when used as the active layer in an organic photovoltaic (OPV) device.[12] Despite these promising results, however, research on macrocyclic small molecules in the context of organic electronics remains quite sparse.

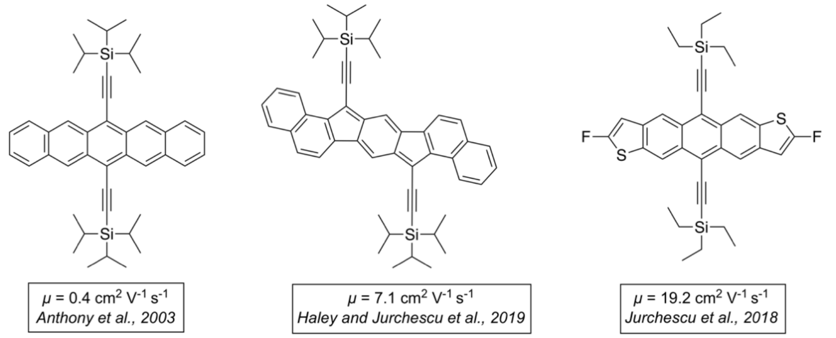
Si
F
S
μ = 0.4 cm^2 V^{-1} s^{-1}
Anthony et al., 2003
μ = 7.1 cm^2 V^{-1} s^{-1}
Haley and Jurchescu et al., 2019
μ = 19.2 cm^2 V^{-1} s^{-1}
Jurchescu et al., 2018

Figure IV.1. Examples of linear conjugated organic electronic materials and their respective thin-film charge mobilities (references 8-10, from left to right).

With this in mind, we were encouraged to begin exploring cycloparaphenylenes (CPPs) as a new potential class of macrocyclic organic electronic materials. The CPP scaffold offers a variety of advantages for the development of organic charge-transport materials, including facile functionalization,[13-16] high solubility without the need for solubilizing groups, and the ability to host electronically-active guests such as fullerenes.[17-18] Additionally, as mentioned in Chapter **I**, the electronics of CPPs can be altered simply by changes in hoop diameter,[19] thus providing another functional handle of sorts that is not often seen in other small molecule scaffolds. Considering these advantageous properties, it should come as no surprise that the notion of using CPPs in the context of organic electronics has already been heavily contemplated by researchers. As discussed in detail in Chapter **I**, a collaboration between our lab and the Lonergan lab explored the altered electronic properties of *N*-methylpyridinium-containing CPPs towards their potential use in organic electronics.[20] Likewise, numerous computational efforts,[21-22] most notably by the Houk group,[23] have suggested that CPP single crystals may exhibit formidable charge mobilities if implemented into OFET device architectures.

While much groundwork has been laid to aid in the exploration of CPPs as organic electronic materials, there currently exists only one example of CPPs actually being implemented into device architectures in order to study their electronic behavior. Yamago and coworkers have recently reported the synthesis of a tetraalkoxy [10]CPP derivative that, via thin-film space-charge limited current (SCLC) measurements, was found to have an electron mobility of 4.5×10^{-6} cm^2 V^{-1} s^{-1}.[24] Although this serves as a helpful baseline for future study of CPP-based devices, a lack of characterization of the morphologies of the thin films used in this study makes it difficult to connect these results to the solid-state arrangements of the tetraalkoxy nanohoops in the films. Inspired by our previous success in predictably controlling the solid-state self-assembly of CPPs via fluorination of the nanohoop backbone,[25-26] we set out to explore more thoroughly how solid-state morphology impacts the electronic behavior of bulk CPP samples. Specifically, we were interested in determining whether or not the face-to-face packing observed in nanohoop **IV.1** (Fig. IV.2a, c.), a fluorinated [10]CPP analog, would result in improved electronic communication in the solid-state versus the herringbone-like packing of [10]CPP (Fig. IV.2b, d.). Towards this, we examined the electronic behavior of both nanohoop **IV.1** and non-fluorinated [10]CPP when incorporated into thin-film OFET device architectures. Through this, we were able to determine that the conductivity of **IV.1** was, on average, an order of magnitude higher than that of non-fluorinated [10]CPP.

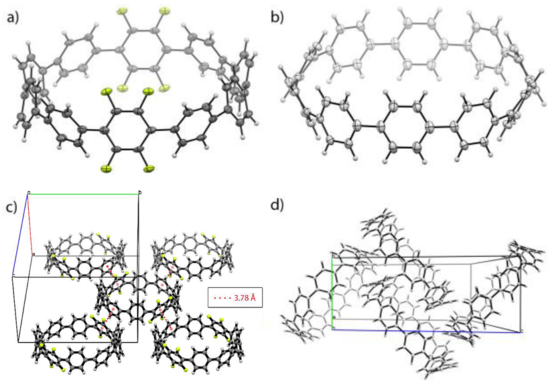

Figure IV.2. ORTEP representations (50% probability) of (a) **IV.1**, (b) [10]CPP and observed solid-state packing of (c) **IV.1** and (d) [10]CPP (carbon atoms in gray, hydrogen atoms in white, fluorine atoms in yellow).

IV.2. Results and Discussion.

In order to study the electronic behavior of both **IV.1** and [10]CPP, both materials, synthesized as previously reported,[17, 26] were spin cast onto pre-fabricated OFET devices to afford devices with bottom-gate bottom-contact geometries (see Section IV.4. for further details on device fabrication and measurement). Current was then measured between -10 and 10 V under ambient conditions, resulting in linear I-V curves for both materials (Figure IV.3b.). Our results showed a dramatic difference between these two nanohoops, where the measured conductivity of fluorinated nanohoop **IV.1** was 2.67 x 10^{-7} S cm^{-1}—more than an order of magnitude greater than that found for the parent all-carbon [10]CPP (3.33 x 10^{-8} S cm^{-1}). Given that π-π interactions between adjacent molecules in the solid-state is a critical element for obtaining efficient electronic communication, we expect that the observed perfluoroarene-arene interactions (Fig. IV.2c.) in fluorinated nanohoop **IV.1** play a strong role in this improved conductivity over [10]CPP. To more conclusively support this hypothesis, future work will focus on elucidating the morphology of the thin-films formed by both **IV.1** and [10]CPP through the use of X-ray diffraction. Preliminary optical microscope analysis of thin films of both nanohoops does, however, suggest noticeable differences in morphology between the two materials (Fig. IV.4.). It should be noted that charge mobilities for both **IV.1** and [10]CPP could not be determined using the above experimental approach as neither material exhibited a response to applied gate voltage. Given the success that the Yamago group has had in using SCLC measurements to determine the electron mobility of the tetraalkoxy CPP they had synthesized,[24] we plan to explore a similar approach in the future to determine how the differences in solid-state morphology between **IV.1** and [10]CPP manifest in regard to their charge mobilites.

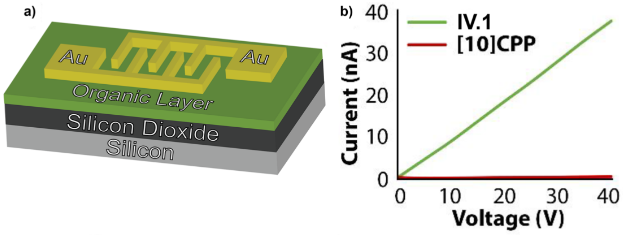

Figure IV.3. (a) Schematic of two-contact devices used; (b) I-V curves of **IV.1** (green) and [10]CPP (red).

In an attempt to deconvolute the differences in conductivity between **IV.1** from any inherent electronic differences the nanohoops might exhibit, the electronic structure of **IV.1** was investigated via density functional theorem (DFT) analysis. It was found that the highest occupied molecular orbital (HOMO) and lowest unoccupied molecular orbital (LUMO) energy levels of fluorinated nanohoop **IV.1** were comparable to those in [10]CPP,[27] with both the HOMO and LUMO energy levels in **IV.1** each being lowered by approximately 0.200 eV relative to [10]CPP (Fig. IV.5.). As a result of this equivalent drop in HOMO and LUMO energy level, the DFT calculated HOMO-LUMO gaps of **IV.1** and [10]CPP are nearly identical (3.53 and 3.54 eV, respectively). To corroborate these DFT calculated values, cyclic voltammetry was then performed on fluorinated nanohoop **IV.1**, where it was found that the oxidation potential of **IV.1** is nearly 200 mV lower than that of [10]CPP[27] (Fig. IV.8.). It is worth noting the large HOMO-LUMO gap energy levels of both [10]CPP and **IV.1**, which is consistent with the relatively low conductivities observed for both materials. Regardless, the fact that fluorination of the CPP backbone can induce dramatic changes in solid-state morphology with little impact on electronic properties suggests that it may be an effective strategy in enhancing charge transport in CPP derivatives with more desirable electronic properties, such as the *N*-methylpyridinium nanohoops previously reported by our lab.

IV.3. Conclusion and Outlook.

In conclusion, we have provided preliminary data showing that fluorination of the CPP backbone can afford enhanced electronic properties in the solid-state. Via conductivity measurements on thin-film devices using either nanohoop **IV.1** or [10]CPP as the electronically active layer, **IV.1** was found to exhibit a conductivity ten times higher than that of [10]CPP. Based on crystal structure analyses of the two materials, we tentatively attribute this noticeable difference in conductivities to the presence of more face-to-face interactions, and thus better π-π overlap, in the solid state morphology of **IV.1** versus [10]CPP. CV data reveal relatively minor differences in the electronic properties of **IV.1** and [10]CPP, suggesting that the observed ten-fold increase in conductivity does not arise from differences in the electronic structure of the molecules. Most critical in regard to future work is rigorous analysis of the thin-film morphologies of **IV.1** and [10]CPP via XRD and potentially atomic force microscopy (AFM) in order to more conclusively connect the solid-state assemblies of the systems to the differences in conductivity we have observed. Additionally, the fabrication and measurement of single-crystal OFET devices using both **IV.1** and [10]CPP would not only help elucidate their inherent electronic properties (i.e. without the structural variability that comes with thin-film casting), but would also allow for comparisons to be made to established computational work on the electronic behavior of CPP single crystals.[21, 23]

IV.4. Device Fabrication and Conductivity Measurements.

The pre-fabricated substrates used for this study were purchased from Fraunhofer IPMS (4th generation "Position 2" OFET structures). These substrates consisted of a 150 mm n-doped silicon wafer layered with a 230 ± 10 nm SiO_2 gate oxide and 30 nm interdigitated Au source/drain electrodes deposited onto a 10 nm ITO adhesion layer. Each substrate provided 16 transistor devices with variable gap spacings of 2.5, 5, 10, and 20 μm (4 of each per substrate), gap widths of 10mm, and contact areas of 0.5 x 0.5 mm^2. Substrates were received from the manufacturer protected with AZ7217 resist. Prior to fabrication, substrates were cleaned by rinsing with acetone (necessary to remove the resist) followed by a methanol rinse, blow-drying the substrates with a stream of N_2 gas in between each rinse. Finally, substrates were plasma cleaned for 2 minutes directly before spin coating (it is important to prevent solvent from contacting substrate surfaces after plasma cleaning). Once the substrates were prepared, thin-film devices of **IV.1** and [10]CPP for use in conductivity measurements were fabricated using the following procedure. A 2 mM concentrated solution of **IV.1** in THF (10 mg/6 mL) was prepared for spin coating onto the substrates described above. Spin coating was carried out under ambient conditions by flooding substrates with the solution described above and spinning at 750 RPM for 60 seconds. These devices were then allowed to air-dry for at least 15 minutes before taking measurements. Devices of [10]CPP were fabricated by following this exact procedure with a 20 mg/ 7 mL solution of [10]CPP in THF.

Conductivity was measured via two-contact measurements using a Sigmatone 1160 Series probe station and a Keithley 236 source-measure unit. All measurements were taken under ambient atmosphere and temperature. Current was measured as voltage was swept between 10 and -10 V, producing symmetric I-V curves (only current from 0 to 10 V shown in text). Conductivity was calculated using the following equations:

$$G = \frac{I}{V}$$

$$\sigma = \frac{G \cdot L}{t \cdot w}$$

where G is electrical conductance, L is the gap spacing (variable between 2.5. 5. 10, and 20 μm in these studies), t is film thickness (25 nm on average for both materials, as measured by optical profilometry, and w is the gap width of the interdigitated electrodes (10 mm for all devices).

IV.5. Thin-Film Characterization via Optical Microscopy.

The respective film morphologies of fluorinated [10]CPP and [10]CPP devices were analyzed via optical microscopy using a Leica DM2500 M optical microscope at 100x magnification.

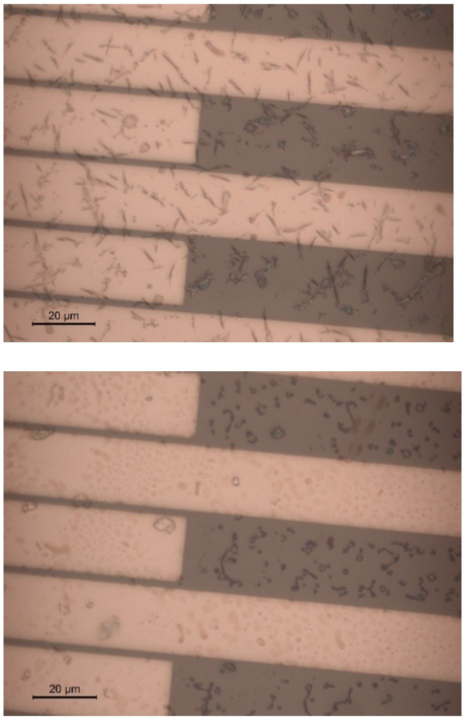

Figure IV.4. Optical microscope images of thin-films of **IV.1** (top) and [10]CPP (bottom), both prepared as described in Chapter **IV.4**.

IV.6. Computational Data.

Calculations for **IV.1** were carried out with Gaussian 09 package[28] using B3LYP/6-31g* level of theory. Frontier molecular orbital energy levels for [10]CPP are taken from reference **27.**

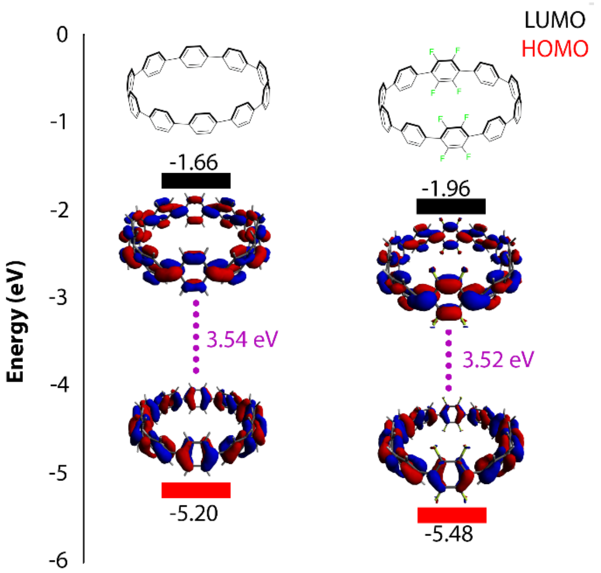

Figure IV.5. DFT calculated frontier molecular orbitals (FMO) and their respective energy levels for [10]CPP (left) and **IV.1** (right). The energy level between each FMO is colored in purple.

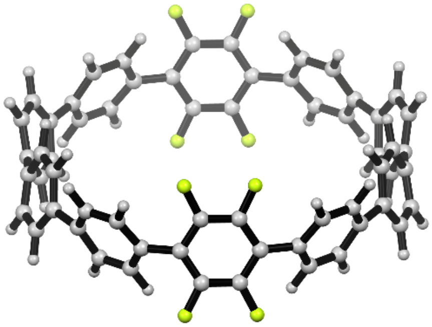

Figure IV.6. Minimized structure of **IV.1**.

C	6.8545033418	-1.4540696563	0.1094030782
C	7.3007608099	-0.6949496525	-0.9859022303
C	7.3007659429	0.6949241091	-0.9858913504
C	6.8545120732	1.4540310052	0.1094249660

C	6.5775675517	0.6953652947	1.2571850478
C	6.5775638474	-0.6954210806	1.2571741626
C	6.3789618949	-2.8573457884	-0.0072946789
C	6.3789799927	2.8573127307	-0.0072569389
F	7.6678821020	1.3107479521	-2.1270327948
F	7.6678705130	-1.3107588637	-2.1270536020
F	6.1593148293	1.2920756062	2.3883783417
F	6.1593092730	-1.2921500350	2.3883569206
C	5.7082983647	3.2430961503	-1.1837915504
C	4.8711841916	4.3502794413	-1.1969106313
C	4.6653220547	5.1255803612	-0.0420672124
C	5.4815809096	4.8482178002	1.0683881827
C	6.3195366173	3.7361255387	1.0894594053
C	6.3194984636	-3.7361623906	1.0894173198
C	5.4815358237	-4.8482495032	1.0683309098
C	4.6652875841	-5.1255996073	-0.0421350583
C	4.8711590663	-4.3502886807	-1.1969692906
C	5.7082825952	-3.2431123854	-1.1838358214
C	3.4565858739	5.9835429574	0.0419994584
C	3.4565460903	-5.9835545464	0.0419142960
C	2.6848914819	5.9564160107	1.2164634328
C	1.3589670503	6.3735596306	1.2164304016
C	0.7413137834	6.8403017072	0.0429869125
C	1.5664916714	7.0365976113	-1.0802314597
C	2.8929913239	6.6152118953	-1.0819215882
C	2.6849025522	-5.9565027958	1.2164126742
C	1.3589760780	-6.3736407005	1.2164075200
C	0.7412738623	-6.8403023422	0.0429591627
C	1.5663975308	-7.0365141601	-1.0803135668
C	2.8928996916	-6.6151341063	-1.0820311490
C	-0.7412705126	6.8403019718	-0.0432319138

C	-0.7413123811	-6.8402957804	-0.0431876546
C	-1.5664432517	7.0367094265	1.0799703001
C	-2.8929429412	6.6153252980	1.0817081657
C	-3.4565446616	5.9835476671	-0.0421481146
C	-2.6848562228	5.9563079528	-1.2166139679
C	-1.3589301666	6.3734471275	-1.2166273825
C	-1.5664342768	-7.0365978759	1.0800703675
C	-2.8929331197	-6.6152084027	1.0818281249
C	-3.4565792856	-5.9835296221	-0.0420616030
C	-2.6849392930	-5.9563848422	-1.2165605157
C	-1.3590151207	-6.3735304729	-1.2165946370
C	-4.6652816626	5.1255939928	0.0420119444
C	-4.6653142388	-5.1255726087	0.0420669276
C	-5.4816012300	4.8481972840	-1.0683906804
C	-6.3195700613	3.7361134628	-1.0893760017
C	-6.3789629003	2.8573417402	0.0073749994
C	-5.7082115796	3.2431575243	1.1838587083
C	-4.8710903579	4.3503364707	1.1968946502
C	-4.8711461226	-4.3503164466	1.1969455359
C	-5.7082646561	-3.2431354417	1.1838917290
C	-6.3789849670	-2.8573152020	0.0073924791
C	-6.3195589486	-3.7360767379	-1.0893644391
C	-5.4815966261	-4.8481655545	-1.0683601363
C	-6.8545128670	1.4540618350	-0.1092364451
C	-6.8545255143	-1.4540346353	-0.1092256080
C	-6.5777274690	0.6954000563	-1.2570365025
C	-6.5777336604	-0.6953860861	-1.2570307503
C	-7.3006216363	-0.6949182670	0.9861473293
C	-7.3006167150	0.6949561190	0.9861418364
F	-7.6675609973	-1.3107333415	2.1273502270
F	-7.6675596743	1.3107810309	2.1273383893

F	-6.1596304835	1.2921166968	-2.3882840582
F	-6.1596433954	-1.2921202317	-2.3882715749
H	5.7618174954	2.6165101288	-2.0654768170
H	4.2741623429	4.5406952658	-2.0829029664
H	5.4143213751	5.4721330326	1.9547303780
H	6.8753361489	3.5130210462	1.9918164608
H	6.8752880996	-3.5130641953	1.9917824559
H	5.4142580855	-5.4721680112	1.9546696708
H	4.2741417262	-4.5406955833	-2.0829669545
H	5.7618123095	-2.6165192518	-2.0655154786
H	3.0834558804	5.4806552728	2.1068271791
H	0.7612730513	6.2107003175	2.1074515553
H	1.1497092785	7.4723750953	-1.9836453138
H	3.4832250832	6.7290165341	-1.9867143353
H	3.0835119309	-5.4808115388	2.1067938304
H	0.7613195289	-6.2108497043	2.1074668326
H	1.1495680358	-7.4722176121	-1.9837417035
H	3.4830943711	-6.7288700049	-1.9868582926
H	-1.1496554823	7.4725726371	1.9833403437
H	-3.4831714616	6.7292204790	1.9864927794
H	-3.0834241033	5.4804602710	-2.1069294479
H	-0.7612402105	6.2104980131	-2.1076348041
H	-1.1496047290	-7.4723796991	1.9834606680
H	-3.4831252645	-6.7290178570	1.9866476007
H	-3.0835472376	-5.4806146849	-2.1069000309
H	-0.7613599051	-6.2106665031	-2.1076415405
H	-5.4143847176	5.4720798503	-1.9547590805
H	-6.8754171659	3.5129779394	-1.9916966445
H	-5.7616889583	2.6166018934	2.0655685445
H	-4.2740199572	4.5407779603	2.0828485141
H	-4.2741006567	-4.5407671228	2.0829147088

H	-5.7617650540	-2.6165827478	2.0656026447
H	-6.8753739850	-3.5129286571	-1.9917023914
H	-5.4143490511	-5.4720405324	-1.9547317750

IV.7. Cyclic Voltammetry Data.

Cyclic voltammetry experiments (scan rate = 100 mV/s) were performed using a CH Instruments 1200B potentiostat running CH Instruments software. Measurements were conducted in degassed 0.100 M $n\mathrm{Bu_4PF_6}$ (recrystallized 3 x from methanol) in tetrahydrofuran under an N_2 atmosphere with a glassy carbon working electrode, platinum counter electrode, and an Ag reference electrode. The ferrocene/ferrocenium couple was used as an internal reference.

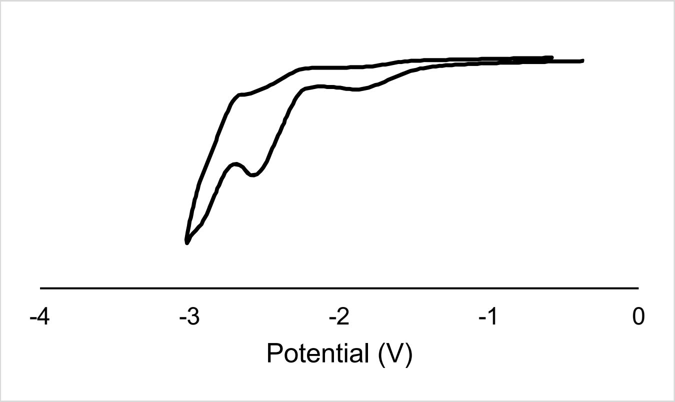

Figure IV.7. Reduction curve of **IV.1**.

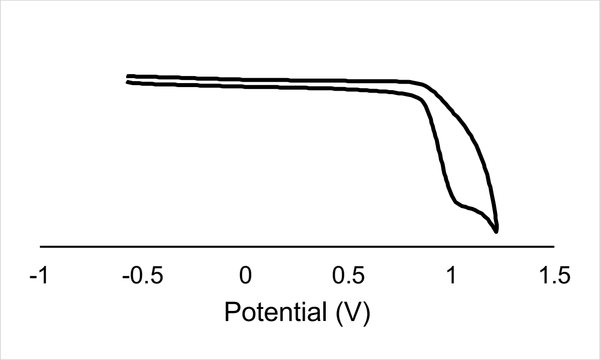

Figure IV.8. Oxidation curve of **IV.1**.

IV.8. Bridge to Chapter V.

Chapters **II-IV** have focused on the design, synthesis, and potential applications of cylindrical CNT mimics constructed from the non-covalent self-assembly of fluorinated nanohoops. While the use of non-covalent organofluorine interactions had proven fruitful in producing tubular CNT-like structures, we began contemplating strategies by which we could construct fully covalent nanohoop-based CNT mimics. This, we presumed, would potentially provide more robust tubular structures with channels that more closely emulate those of CNTs. In Chapter V, we disclose our work towards the construction of such structures through the use of dynamic covalent chemistry. Our strategy involves the synthesis of nanohoops with hydroxy functionalities, which, through preliminary NMR evidence, are shown to be capable of condensation reactions with boronic acids. This, we hypothesize, will allow for the facile construction of CPP-based extended structures in future work.

CHAPTER V

SYNTHESIS OF HYDROXY FUNCTIONALIZED NANOHOOPS TOWARDS THE CONSTRUCTION OF COVALENT NANOTUBE MIMICS AND RELATED STRUCTURES

Chapter **IV** is based on unpublished work, the concept of which was designed by myself and Professor Ramesh Jasti. I carried out the synthesis and characterization of the compounds described in this chapter.

The study of carbon nanomaterials is currently limited by a lack of methodologies that allow for the precise synthesis of covalently-linked extended structures. This is especially true for carbon nanotubes (CNTs) and related tubular structures as the problem is compounded by the fact that curved systems are inherently difficult to synthesize. Cycloparaphenylenes (CPPs), or nanohoops, serve as ideal building blocks for the construction of CNT mimics or finite tubular cage compounds due to their curved geometry and scalable, modular synthesis. However, there still remains a lack of strategies to covalently link nanohoops in a precise manner so as to afford cylindrical structures. Given that dynamic covalent chemistry (DCC) has proven useful in the synthesis of otherwise inaccessible two-dimensional extended structures such as covalent organic frameworks (COFs) as well as complex molecular cages, we saw this as a promising avenue to explore in our efforts to access covalently-linked CPP-based structures. Herein, we present the synthesis of a novel [12]CPP analog containing a catechol moiety, which we show to be capable of readily forming boronic ester linkages with boronic acids. Thus, we predict that catechol-embedded CPPs will offer a viable route towards the construction of a variety of extended tubular structures and curved cages with tunable diameters and functionalities.

V.1. Introduction.

Carbon-based nanomaterials, such as carbon nanotubes (CNTs) and graphene, have shown great promise in an overwhelming variety of applications.[1-3] However, the potential of these materials is inherently limited by their inhomogenous syntheses that result in structures of mixed lengths, widths, and, in the case of CNTs, chiralities.[1] Given that graphene, CNTs, and other carbon nanomaterials are comprised primarily of carbon-carbon bonds (assuming pristine composition), it would seem that an obvious solution to this problem would be the use of synthetic organic methodologies that allow for atom-precise bond manipulation. However, traditional synthetic strategies simply do not translate when creating the vast number of carbon-carbon bonds present in extended carbon materials due to the inevitable formation of kinetically-trapped defects. While great progress has recently been made in the precise synthesis of graphene structures, particularly in the case of graphene nanoribbons,[4-5] major progress in the size-selective synthesis of CNTs has yet to be achieved. This is arguably due to the more complex curved geometry of CNTs, which, even on the single-molecule scale, is difficult to imitate using organic synthesis.

Nature, too, is aware of the difficulty in constructing complex, extended systems of irreversible covalent bonds. Instead, natural systems, such as the multicomponent light-harvesting complexes used by plants in photosynthesis,[6] rely on reversible, thermodynamic processes that allow for the precise self-assembly of smaller molecules. Inspired by this, synthetic chemists have begun exploring strategies to produce both extended materials and larger discrete structures using the reversible assembly of small molecule synthons. One approach that has proven successful in this endeavor is the use of dynamic covalent chemistry (DCC), which relies on dynamic bond forming processes that can be precisely controlled such that they equilibrate to a desired thermodynamic product.[7] DCC is most notable for its use in the synthesis of covalent organic frameworks (COFs) (Fig. V.1a.), where incredibly simple processes such as the reversible formation of boronic esters or imine bonds are used to produce well-ordered frameworks (Fig. V.1a.).[8-10] Likewise, DCC has also been used to synthesize a variety of smaller discrete systems, such as molecular cages (Fig. V.1b.), that would be difficult to access through kinetic processes.[11-13] Aside from its self-assembly capabilities, DCC is attractive in that synthons are only limited by their ability to be functionalized with the appropriate complimentary groups necessary for reversible bond formation. Thus, DCC-based structures can, in theory, be endlessly optimized in order to fine tune any desired properties.

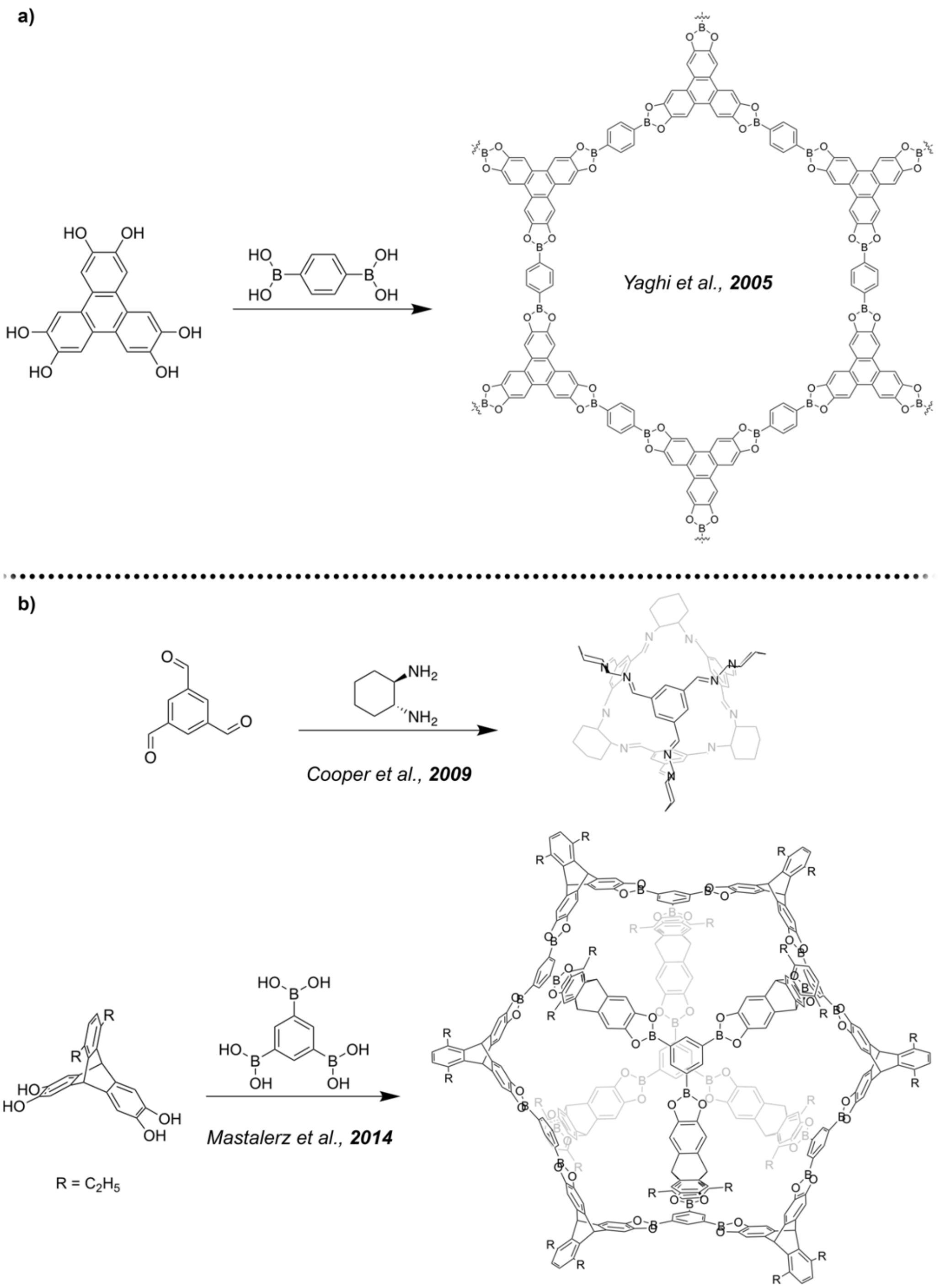
a)
HO
OH
HO
OH
HO
OH
B
Yaghi et al., 2005
b)
NH2
NH2
N
Cooper et al., 2009
HO
OH
B
R
R = C2H5
Mastalerz et al., 2014

Figure V.1. a) Example of a covalent organic framework synthesized using dynamic covalent bond formation (reference 8); b) Examples of organic cage compounds synthesized using dynamic processes (references 12 and 13).

Considering the versatility of DCC in constructing complex systems that are otherwise difficult to access, we wondered if this approach could be applied to the precise synthesis of CNT-like structures. Towards this, we viewed cycloparaphenylenes (CPPs), or nanohoops, as an ideal supramolecular synthon as they inherently exhibit a curved geometry identical to that of CNTs. Our lab has already shown that CPPs can be used to fabricate non-covalent CNT mimics through the use of organofluorine interactions.[14-15] Since CPPs are synthesized from the bottom up, the diameters of these systems can be precisely controlled, providing a potential advantage over CNTs. Additionally, it was found that these CNT mimics can indeed emulate CNT functions, such as small molecule uptake (via permanently accessible channels) and linear guest alignment.[15] Thus, we predict that fully covalent analogs of these systems would be even more robust and potentially capable of more exotic CNT functionality such as ultra-fast mass transport. On the small-molecule level, CPP synthons are also expected to allow for the synthesis of cylindrical organic cages with highly tunable pores. Herein, we present the synthesis of a novel [12]CPP analog, monohydroxy-functionalized **V.1** (Scheme V.1), as an initial effort to explore the DCC capabilities of CPPs. Importantly, via preliminary NMR data, we show that **V.1** appears to be readily capable of reacting with boronic acids to form boronic ester linkages, implying that this is a viable approach toward the construction of discrete nanohoop-based cages and extended tubular structures.

V.2. Results and Discussion.

With the long-term goal of this work being the construction of covalently-linked CNT mimics, the necessary nanohoop synthons had to be designed in such a way so as to allow for linear vertical linkages between nanohoops. Conveniently, the boronic ester linkages formed through the condensation of catechol and boronic acid components (a common DCC motif) provide the desired linear geometry. Thus, one could imagine that a condensation reaction involving an appropriately designed hydroxy functionalized nanohoop and 1,4-benzenediboronic acid would result in the formation of linear CNT-like framework (Fig. V.2a.). Likewise, a hexahydroxy nanohoop such as **V.2** would be capable of forming nanohoop-based cages under similar conditions (Fig. V.2b.). However, as a hydroxy functionalized CPP had not yet been reported, we decided to first synthesize nanohoop **V.1. (**Scheme V.1.), a [12]CPP analog containing a catechol moiety, to not only establish the synthetic viability and stability of such a system but also as a means of testing simple boronic acid condensations on the CPP backbone. To access **V.1**, we envisioned a synthetic route utilizing methoxy functionalities that could be deprotected at the end of the synthesis to reveal the desired hydroxy groups. Numerous groups have synthesized nanohoops bearing methoxy groups,[16-17] so we were confident in our ability to access a nanohoop with the desired 1,2-methoxy functionality. The synthesis of **V.1** hinged on the macrocyclization of coupling partners **V.3** and **V.4** dilute Suzuki-Miyaura cross-coupling conditions (Scheme V.1.) (see Section V.4.2. and for synthetic schemes used to access **V.3** and **V.4**). Macrocycle **V.5**, carried on crude, was then subjected to treatment with tetrabutylammonium fluoride (TBAF) to remove the triethylsilyl protecting groups present on the molecule, affording an alcohol-functionalized intermediate. This deprotected intertmediate, without further purification, was subjected to mild tin-mediated aromatization conditions[18] to afford methoxy-protected nanohoop **V.6** in an 11% yield over three steps. Finally, standard BBr_3 deprotection conditions were used to remove the remaining methoxy groups, resulting in the formation of **V.1** in 80% yield.

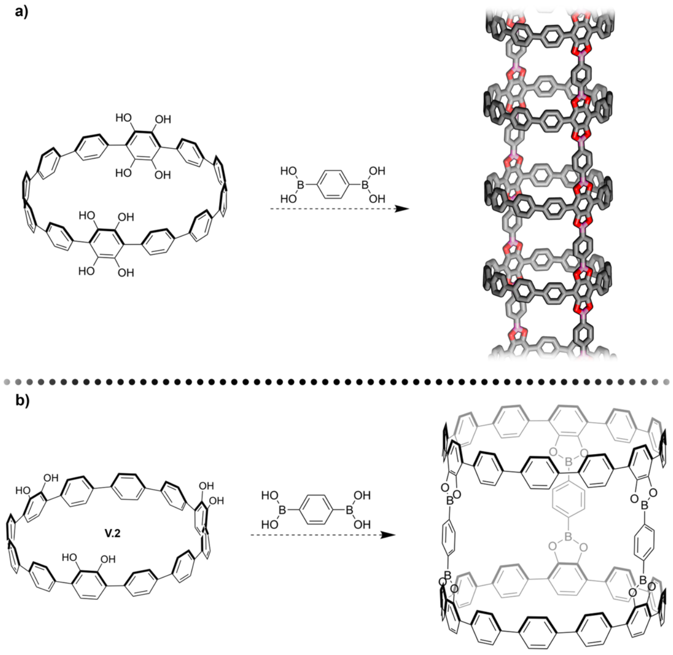

Figure V.2. a) Proposed synthesis of a CPP-based nanotube via a condensation reaction between a hydroxy-functionalized nanohoop and 1,4-benzenediboronic acid; b) Synthesis of a CPP-based cage using proposed nanohoop **V.2** as a synthon.

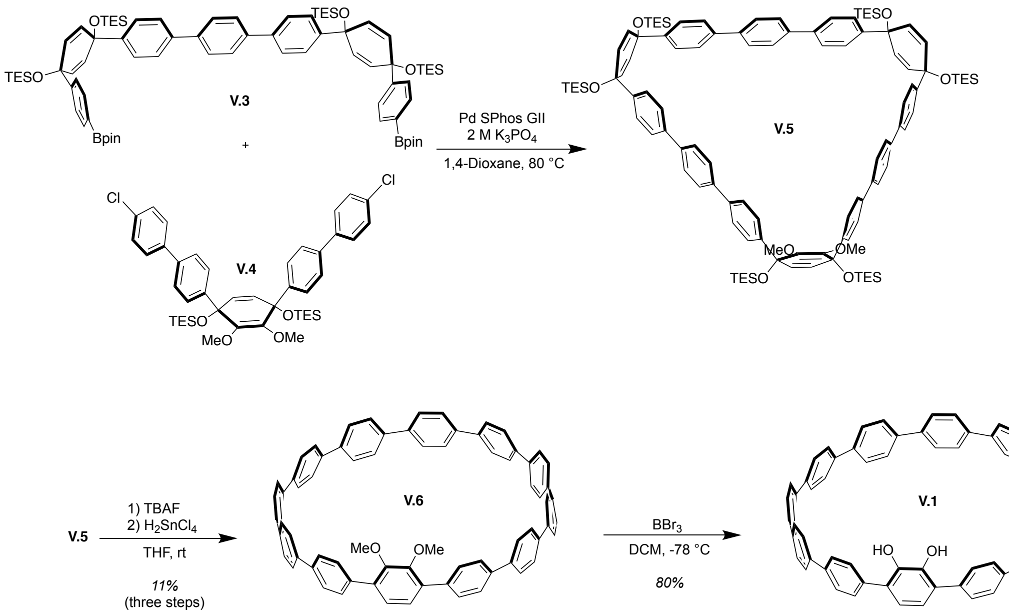
OTES
TESO
TESO
OTES
V.3
Bpin
+
Bpin
Pd SPhos GII
2 M K_3PO_4
1,4-Dioxane, 80 °C
Cl
Cl
V.4
TESO
OTES
MeO
OMe
OTES
TESO
TESO
OTES
V.5
MeO
OMe
TESO
OTES
V.5
1) TBAF
2) H_2SnCl_4
THF, rt
11%
(three steps)
V.6
MeO
OMe
BBr$_3$
DCM, -78 °C
80%
V.1
HO
OH

Scheme V.1. Synthetic route used to access nanohoop **V.1**.

Upon the successful synthesis of **V.1**, we next sought to test the viability of this hydroxy-functionalized nanohoop as a DCC synthon. We chose to begin with a simple condensation reaction of **V.1** with 4-*tert*-butylphenylboronic acid (Fig V.3.). After overnight refluxing in a toluene/methanol solution, condensation product **V.7** appeared to form quantitatively via ^{1}H NMR (Fig. V.3.) (due to the small scale of the reaction, a proper yield could not be determined). Upon the apparent success of this experiment, we next sought to access a slightly more complex structure, namely dimer **V.8** (Fig. V.3.) which consists of two equivalents of **V.1** linked by boronic ester linkages to a central phenylene moiety. While ^{1}H NMR evidence is less conclusive than in the case of **V.7**, we observe the complete disappearance of **V.1** in the spectrum along with multiple peaks that we can tentatively assign to various protons in **V.8** (Fig. V.4.). Most notable of these is a singlet downfield at approximately 8.4 ppm which we attribute to the phenylene linking the two hoops. Being a convenient linker for DCC strategies, 1,4-benzenediboronic acid has been used quite extensively in the literature, and in most cases the aryl protons on this moiety exhibit a dramatic downfield shift upon the formation of boronic ester linkages between other aromatic units.[13, 19] Aside from this, we have assigned the protons on the nanohoop backbone under the hypothesis that the expected doublets would shift further upfield the farther they were located from the phenylene linker (Fig. V.4.). We note that the remaining, unassigned protons of the nanohoop backbone appear to coalesce into a large signal between 7.7 and 7.6 ppm that we were not able to deconvolute. Additionally, we find that the integration of this signal (not shown) is much larger than expected for the remaining protons of the nanohoop. While we do not yet have an explanation for this, we currently attribute it to the extremely small scale of the reaction coupled with the large amount of protons the signal is presumably representing. Attempts to isolate **V.8** were unsuccessful, with NMR showing the apparent partial decomposition of **V.8** into its constituent components, and thus a true yield was unattainable. Regardless, we quite confidently conclude that **V.8** is indeed forming, which is a promising result for future nanohoop-based DCC work. Preliminary work has now begun on the synthesis of nanohoop **V.2** (Fig. V.2b.), as our successful experiments with **V.1** lead us to believe that the formation of a nanohoop-based cage using **V.2** (see Figure V.2b.) should indeed be possible.

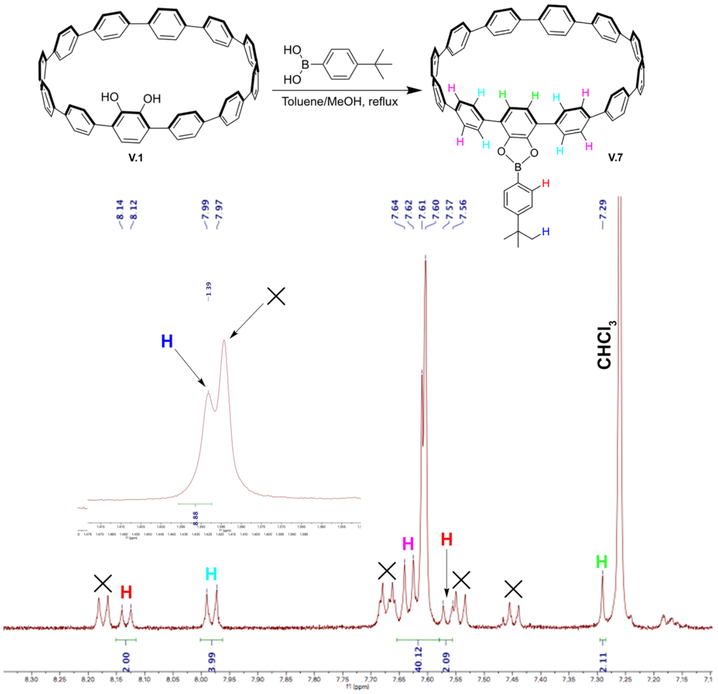

Figure V.3. (top) Synthetic scheme to access **V.7**; (bottom) Proton NMR spectrum of **V.7** showing proton assignments (black "X" marks represent excess 4-*tert*-butylphenylboronic acid).

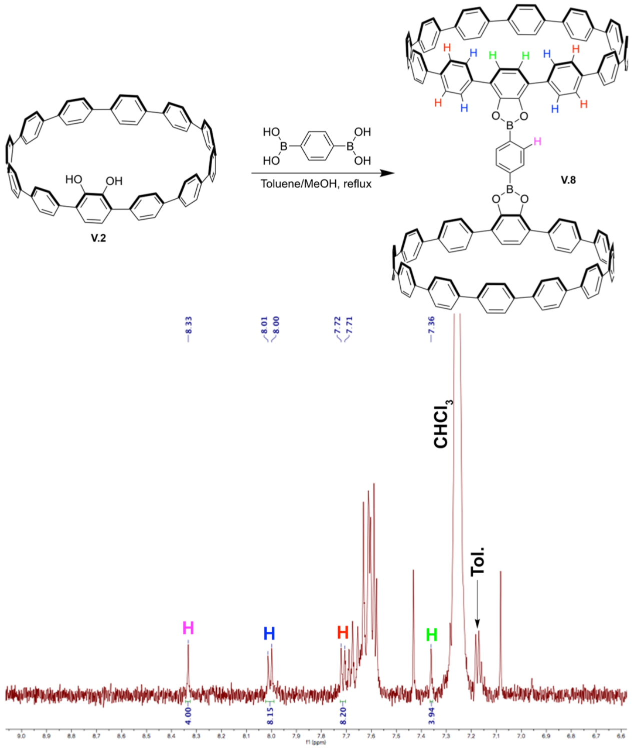

Figure V.4. (top) Synthetic scheme to access **V.8**; (bottom) Proton NMR spectrum of **V.8** showing proton assignments (residual toluene is clearly highlighted).

V.3. Conclusion and Outlook.

In this chapter, we have disclosed our preliminary work towards nanohoop-based cages and extended CNT mimics using dynamic covalent strategies. A novel hydroxy-functionalized nanohoop, **V.1**, was successfully synthesized, establishing a viable route toward the future synthesis of catechol-containing nanohoops. Importantly, preliminary ^{1}H NMR results revealed that nanohoop **V.1** can undergo simple condensation reactions, allowing for the formation of adducts **V.7** and **V.8**. Our experiments with **V.1** suggest that it may indeed be possible to construct nanohoop-based cages with proposed hexahydroxy-functionalized **V.2** and an appropriate linker, such as 1,4-benzenediboronic acid. Such a prospect is exciting in that these cages would be remarkably tunable, with diameters that can be controlled via alterations to the constituent nanohoops and lengths that can be changed by using longer or shorter boronic acid linkers. One could also imagine further functionalizing the nanohoop backbone to elicit further utility. For example, pyridines can be incorporated into a catechol-functionalized nanohoop to allow for metal binding[20] or even enhanced CO_2 uptake in the solid state (a theoretically predicted property of nitrogen-doped nanohoops).[21] Alternatively, the addition of sulfonate groups could bestow water solubility upon these cages,[22] allowing for the exploration of biological applications. Perhaps more intriguing is that all of the aforementioned advantages of nanohoop-based cages could, in theory, also be applied to the covalent CNT mimic structures that we have also proposed, potentially allowing for an unprecedented level of control over the synthesis of nanotube structures that cannot be achieved using current CNT syntheses. Ultimately, it is our hope that this preliminary work will aid in the discovery of new CNT-like materials that were previously inaccessible.

V.4. Experimental Section.

V.4.1. General Information.

^1H NMR spectra were recorded at 500 MHz on a Varian VNMR spectrometer, 500 MHz on a Bruker spectrometer, or 600 MHz on a Bruker spectrometer. All ^1H NMR spectra are referenced to TMS (δ 0.00 ppm), CH_2Cl_2 (δ 5.32 ppm), or $(CH_3)_3CO$ (δ 2.05 ppm). All reagents were obtained commercially and used without further purification unless otherwise noted. All glassware was flame-dried and cooled under an inert atmosphere of nitrogen unless otherwise noted. Moisture sensitive reactions were carried out under an inert atmosphere of nitrogen using standard syringe/septa technique. Silica column chromatography was conducted with Zeochem Zeoprep 60 Eco 40-63 μM silica gel while alumina chromatography utilized Sorbent Technologies 50-200 um Basic Activity II−II alumina. Intermediate **V.9** was prepared as previously reported in reference 23. Intermediate **V.14** was prepared as previously reported in reference 24.

V.4.2. Synthetic Schemes

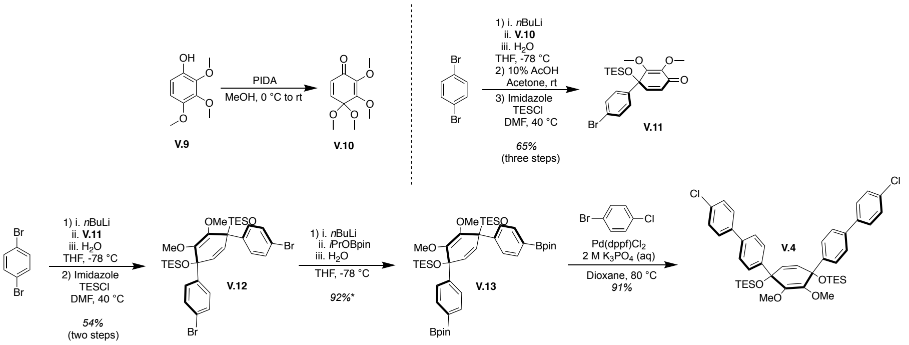
OH
V.9
PIDA
MeOH, 0 °C to rt
O
V.10
Br
Br
1) i. nBuLi
ii. V.10
iii. H₂O
THF, -78 °C
2) 10% AcOH
Acetone, rt
3) Imidazole
TESCl
DMF, 40 °C
65%
(three steps)
TESO
V.11
1) i. nBuLi
ii. V.11
iii. H₂O
THF, -78 °C
2) Imidazole
TESCl
DMF, 40 °C
54%
(two steps)
OMe
TESO
MeO
V.12
1) i. nBuLi
ii. iPrOBpin
iii. H₂O
THF, -78 °C
92%*
Bpin
V.13
Br
Cl
Pd(dppf)Cl₂
2 M K₃PO₄ (aq)
Dioxane, 80 °C
91%
V.4
OTES
OMe

Scheme V.2. Synthetic route used to access intermediate **V.4**.

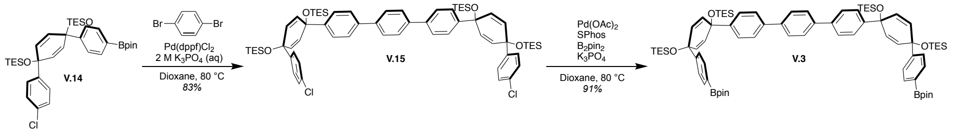

Scheme V.3. Synthetic scheme used to access intermediate **V.5**.

V.4.3. Synthetic Procedures.

Synthesis of V.10. A flame-dried 500 mL round-bottom flask with a stir bar was charged with **V.9** (4.43 g, 24.1 mmol), which was subsequently dissolved in 90 mL of MeOH. The flask was then placed in an ice bath. Diacetoxyiodobenzene (PIDA) (9.30 g, 28.9 mmol) was then added slowly as a solid over the course of an hour, causing the solution to slowly turn from bright yellow to orange. Once all of the PIDA had been added, the solution was allowed to stir overnight. The next day, the solution was quenched with saturated sodium bicarbonate solution (50 mL). Water was added (100 mL), and the resulting solution was extracted with dichloromethane (DCM) (3 x 100 mL). The combined organic phases were then washed with water (3 x 100 mL), KOH (1 x 50 mL) and brine (1 x 100 mL) before being dried over sodium sulfate and filtered. Solvent was then removed under reduced pressure to afford a yellow oil. The oil was purified via column chromatography using basic alumina. A 10% EtOAc/Hexanes mobile phase was first used to remove impurities, followed by a 22-25% EtOAc/Hexanes gradient to elute the product. Rotary evaporation then afforded **V.10** as a deep yellow oil (4.37 g, 85%). ^{1}H NMR (500 MHz, Chloroform-d) δ 6.50 (d, J = 10.3 Hz, 1H), 6.27 (d, J = 10.3 Hz, 1H), 4.18 (s, 3H), 3.76 (s, 3H), 3.33 (s, 6H).

Synthesis of V.11. To a flame-dried 500 mL round-bottom flask with a stir bar was charged 1,4-dibromobenzene (1.24 g, 5.27 mmol, 1.2 equiv). The flask was evacuated and backfilled with N_2 before being capped with a rubber septum and being kept under N_2. To the flask was added 150 mL of dry tetrahydrofuran (THF) and the solution was stirred until all solids had dissolved. The flask was then placed in a dry ice bath and allowed to cool over the course of an hour. After 1 hour, *n*-butyllithium (2.00 mL, 2.42 M, 4.83 mmol, 1.1 equiv) was added dropwise. After 15 minutes, **V.11** (0.941 g, 4.39 mmol, 1 equiv) was added quickly via syringe. The solution was allowed to stir for an hour before being quenched with deionized H_2O (50 mL). The flask was placed under reduced pressure to remove excess THF, after which 100 mL of EtOAc was added. The organic layer was drained, and two more EtOAc extractions (50 mL) were performed. The combined organic phases were then washed with water (3 x 50 mL), followed by brine (1 x 50 mL) before being dried over sodium sulfate and filtered. Solvent was then removed under reduced pressure and the resulting oil was dissolved in approximately 20 mL of acetone, followed by the addition of 20 mL of 10% AcOH. This solution was allowed to stir overnight. The next day, the solution was quenched with saturated sodium bicarbonate solution (50 mL), after which 100 mL of EtOAc and 50 mL of water were added. The organic layer was drained, and two more EtOAc extractions (50 mL) were performed. The organic phase was then washed with water (3 x 50 mL), followed by brine (1 x 50 mL) before being dried over sodium sulfate and filtered. Solvent was then removed under reduced pressure and the resulting solid (1.28 g, 75% crude yield) was placed in a flame-dried 250 mL round-bottom flask with a stir bar. Imidazole (0.804 g, 11.8 mmol, 3 equiv) was added, and the flask was evacuated and backfilled with N_2 before being capped with a rubber septum and being kept under N_2. The solids were dissolved in dry dimethylformamide (approximately 50 mL), after which triethylsilyl chloride (TESCl) (1.32 mL, 7.87 mmol, 2 equiv) was added dropwise. The flask was then heated to 40 °C in an oil bath and the solution was allowed to stir overnight. The next day, the flask was placed in an ice bath the solution was quenched with saturated sodium bicarbonate solution (50 mL). 50 mL of water was added, and the solution was extracted with ethyl ether (3 x 50 mL). The combined organic phases were then washed with 5% LiCl solution (5 x 50 mL) and brine (1 x 50 mL) before being dried over sodium sulfate and filtered. Solvent was removed under reduced pressure and the resulting oil was purified via column chromatography using silica as the stationary phase. A 5-8% EtOAc/Hexanes mobile phase was used. It should be noted that it may take repeated purification cycles to completely remove the silanol byproduct. The product, **V.11**, was isolated as an oil with some silanol byproduct remaining (1.5 g, 65% over three steps). ^1H NMR (500 MHz, Chloroform-d) δ 7.46 (d, J = 8.7 Hz, 2H), 7.30 (d, J = 8.7 Hz, 2H), 6.44 (d, J = 9.9 Hz, 1H), 6.10 (d, J = 9.9 Hz, 1H), 3.93 (s, 3H), 3.76 (s, 3H), 0.98 (t, J = 7.9 Hz, 9H), 0.66 (q, J = 7.8 Hz, 6H).

Synthesis of V.12. To a flame-dried 250 mL round-bottom flask with a stir bar was charged 1,4-dibromobenzene (0.966 g, 4.10 mmol, 1.2 equiv). The flask was evacuated and backfilled with N_2 before being capped with a rubber septum and being kept under N_2. To the flask was added 50 mL of dry tetrahydrofuran (THF) and the solution was stirred until all solids had dissolved. The flask was then placed in a dry ice bath and allowed to cool over the course of an hour. After 1 hour, *n*-butyllithium (1.55 mL, 2.42 M, 3.75 mmol, 1.1 equiv) was added dropwise. After 15 minutes, **V.11.** (1.50 g, 3.41 mmol, 1 equiv) was added quickly via syringe. The solution was allowed to stir for an hour before being quenched with deionized H_2O (25 mL). The flask was placed under reduced pressure to remove excess THF, after which 50 mL of EtOAc was added. The organic layer was drained, and two more EtOAc extractions (50 mL) were performed. The combined organic phases were then washed with water (3 x 50 mL), followed by brine (1 x 50 mL) before being dried over sodium sulfate and filtered. Solvent was then removed under reduced pressure and the resulting solid (1.76 g, 86% crude yield) was placed in a flame-dried 250 mL round-bottom flask with a stir bar. Imidazole (0.603 g, 8.85 mmol, 3 equiv) was added, and the flask was evacuated and backfilled with N_2 before being capped with a rubber septum and being kept under N_2. The solids were dissolved in dry dimethylformamide (approximately 50 mL), after which triethylsilyl chloride (TESCl) (0.99 mL, 5.90 mmol, 2 equiv) was added dropwise. The flask was then heated to 40 °C in an oil bath and the solution was allowed to stir overnight. The next day, the flask was placed in an ice bath the solution was quenched with saturated sodium bicarbonate solution (50 mL). 50 mL of water was added, and the solution was extracted with ethyl ether (3 x 50 mL). The combined organic phases were then washed with 5% LiCl solution (5 x 50 mL) and brine (1 x 50 mL) before being dried over sodium sulfate and filtered. Solvent was removed under reduced pressure and the resulting oil was purified via column chromatography using silica as the stationary phase. A 5-8% EtOAc/Hexanes mobile phase was used. The product, **V.12**, was isolated as a sticky solid (1.32 g, 54% over two steps). ^{1}H NMR (500 MHz, Chloroform-d) δ 7.45 – 7.39 (d, 4H), 7.32 – 7.27 (d, 4H), 5.79 (s, 4H), 3.57 (s, 6H), 0.95 (t, *J* = 7.9 Hz, 18H), 0.67 – 0.60 (q, 12H).

Synthesis of V.13. To a flame-dried 100 mL round-bottom flask with a stir bar was charged **V.12** (1.32 g, 1.86 mmol, 1 equiv). The flask was evacuated and backfilled with N_2 before being capped with a rubber septum and being kept under N_2. To the flask was added 35 mL of dry tetrahydrofuran (THF) and the solution was stirred until all solids had dissolved. The flask was then placed in a dry ice bath and allowed to cool over the course of 40 minutes. After 40 minutes, *n*-butyllithium (1.84 mL, 2.42 M, 4.46 mmol, 2.4 equiv) was added dropwise, turning the solution a deep green. After 15 minutes, 2-isopropoxy-4,4,5,5-tetramethyl-1,3,2-dioxaborolane (1.52 mL, 7.43 mmol, 4 equiv) was added quickly via syringe, causing the solution to turn yellow over the course of an hour. The solution was allowed to stir for an hour before being quenched with deionized H_2O (25 mL). The flask was placed under reduced pressure to remove excess THF, after which 50 mL of DCM was added. The organic layer was drained, and two more DCM extractions (50 mL) were performed. The combined organic phases were then washed with water (3 x 50 mL), followed by brine (1 x 50 mL) before being dried over sodium sulfate and filtered. Solvent was removed under reduced pressure, affording the product, **V.13**, as a solid, which was used without further purification (1.38 g, 92% crude yield). 1H NMR (500 MHz, Chloroform-d) δ 7.77 – 7.71 (d, 4H), 7.54 – 7.42 (d, 4H), 5.81 – 5.75 (s, 2H), 3.60 – 3.50 (s, 6H), 1.34 (s, 24H), 0.95 (t, 18H), 0.64 (d, 12H) (*NMR data taken from crude, post-workup spectrum*).

Synthesis of V.4. To a 100 mL flame-dried flask was added **V.13** (1.38 g, 1.71 mmol, 1 equiv), 1-bromo-4-chlorobenzene (1.31 g, 6.86 mmol, 4 equiv), and [1,1′-bis(diphenylphosphino)ferrocenedichloropalladium (0.124 g, 0.17 mmol, 0.100 equiv). After the solids were added, the flask was evacuated and backfilled with nitrogen 3 times. The flask was then purged with N_2 for 20 min. 1,4-Dioxane (15 mL) was then added to the flask, after which aqueous 2 M K_3PO_4 (4.72 mL, 9.43 mmol, 5.5 equiv), sparged for 1 h prior to use, was added. The solution was then placed in an 80 °C oil bath and allowed to stir overnight. The next day, the black solution was allowed to come to room temperature before removing the solvent under reduced pressure. The resulting reddish-black sludge was dissolved in DCM and run through a silica plug. This was followed by removal of DCM solvent from the eluent via rotary evaporation. The resulting oil was purified via column chromatography (EtOAc/Hexanes) to afford the product as a waxy

dark yellow solid after solvent removal (1.21 g, 91%). ^{1}H NMR (500 MHz, Chloroform-d) δ 7.52 (m, *J* = 14.9, 8.3 Hz, 12H), 7.39 (d, *J* = 8.5 Hz, 4H), 5.87 (s, 2H), 3.63 (s, 6H), 0.98 (t, *J* = 7.9 Hz, 18H), 0.68 (q, *J* = 7.9 Hz, 12H).

Synthesis of V.15. To a 100 mL flame-dried flask was added **V.14** (0.668 g, 1.02 mmol, 2.1 equiv), 1,4-dibromobenzene (0.120 g, 0.51 mmol, 1 equiv), and [1,1′-bis(diphenylphosphino)ferrocenedichloropalladium (0.037 g, 0.051 mmol, 0.100 equiv). After the solids were added, the flask was evacuated and backfilled with nitrogen 3 times. The flask was then purged with N_2 for 20 min. 1,4-Dioxane (10 mL) was then added to the flask, after which aqueous 2 M K_3PO_4 (1.40 mL, 4.89 mmol, 5.5 equiv), sparged for 1 h prior to use, was added. The solution was then placed in an 80 °C oil bath and allowed to stir overnight. The next day, the black solution was allowed to come to room temperature before removing the solvent under reduced pressure. The resulting dark red sludge was dissolved in DCM and run through a silica plug. This was followed by removal of DCM solvent from the eluent via rotary evaporation. Column chromatography using silica as the stationary phase and a 5-8% EtOAc/Hexanes gradient as the mobile phase allowed **V.15** to be isolated as a waxy oil (0.477 g, 83%). ^{1}H NMR (500 MHz, Chloroform-d) δ 7.66 (s, 4H), 7.56 (d, *J* = 8.7 Hz, 4H), 7.39 (d, *J* = 8.2 Hz, 4H), 7.29 (d, *J* = 8.8 Hz, 4H), 7.24 (d, *J* = 8.7 Hz, 4H), 6.05 (d, *J* = 10.1 Hz, 4H), 5.97 (d, *J* = 10.2 Hz, 4H), 0.94 (m, 36H), 0.62 (m, 24H).

Synthesis of V.3. To a 100 mL flame-dried flask was added $Pd(OAc)_2$ (0.005 g, 0.023 mmol, 0.05 equiv), 2-dicyclohexylphosphino-2′6′-dimethoxybiphenyl (0.023 g, 0.056 mmol, 0.125 equiv), bis(pinacolato)diboron (0.573 g, 2.25 mmol, 5 equiv), **V.15** (0.509 g, 0.451 mmol, 1 equiv), and K_3PO_4 (0.479 g, 2.25 mmol, 5 equiv). After the solids were added, the flask was evacuated and backfilled with nitrogen 5 times. The flask was then purged with N_2 for 20 min. 1,4-Dioxane (10 mL) was then added to the flask, and the solution was sparged for 20 min before being placed in an 80 °C oil bath overnight. The next day, the black solution was brought to room temperature, and the solvent was removed under reduced pressure. The resulting black sludge was dissolved in DCM and run through a short plug of silica. After removing the DCM solvent from the eluent via rotary evaporation, the resulting oil was washed with methanol, causing the product to precipitate as a white solid. Vacuum filtration afforded **V.3** as a white solid (0.51 g, 86%).

Synthesis of V.5. To a flame-dried 250 mL round-bottom flask equipped with a stir bar was added **V.3** (0.493 g, 0.376 mmol, 1.00 equiv), **V.4** (0.291 g, 0.376 mmol, 1.00 equiv), and SPhos-Pd-G2 (0.054 g, 0.075 mmol, 0.200 equiv). The flask was evacuated and backfilled with N_2 5 times, followed by addition of 1,4-dioxane (125 mL). This solution was then vigorously sparged with N_2 for 1 h at which point the solution was placed into an oil bath at 80 °C. At this point, an aqueous solution of 2 M K_3PO_4 (12.5 mL) was added. The solution was allowed to stir overnight. The next day the solution was cooled to room temperature followed by removal of the solvent via rotary evaporation. The resulting black sludge was dissolved in DCM and run through a short plug of silica. After removing the DCM solvent from the eluent via rotary evaporation, the resulting waxy white solid, crude **V.5**, was carried directly on to the synthesis of **V.6** (vide infra).

Synthesis of V.6. To a flame-dried 100 mL round-bottom flask equipped with a stir bar was added **V.5** (0.611 g, 0.347 mmol, 1.00 equiv) followed by THF (10 mL). To this solution was then added tetrabutylammonium fluoride (1 M in THF, 2.78 mL, 2.78 mmol, 8 equiv) dropwise. The solution was then stirred for overnight, followed by removal of THF via rotary evaporation, resulting in a cloudy yellow oil. Water (10 mL) was then added, affording a white suspension which was vacuum filtered and washed with more water (about 30 mL) to afford a white solid. The resulting white solid then added to a flame-dried 250 mL round-bottom flask equipped with a stir bar, followed by THF (35 mL), resulting in a beige suspension. To this suspension was added H_2SnCl_4 (0.08 M in THF, 2.78 mmol, 34.7 mL, 8 equiv), resulting in a yellow suspension which was stirred at room temperature for 3 hours. The solution was then quenched with saturated sodium bicarbonate solution (25 mL), followed by the removal of THF via rotary evaporation. An extraction was then performed using DCM (3 x 50 mL). The combined organic phases were washed with water (3 x 50 mL) and brine (1 x 50 mL) before being dried over sodium sulfate and filtered. Solvent was removed via reduced pressure, and the resulting yellow solid was dry loaded onto a basic alumina column via adsorption onto Celite. A mobile phase gradient of 20-30% EtOAc/Hexanes was first used to remove impurities, followed by a gradient of 70-80% EtOAc/Hexanes to elute only the product. Rotary evaporation of the column fractions afforded **V.6** as an off-white powdery solid (0.04 g, 11% over three steps). ^{1}H NMR (500 MHz, Chloroform-d) δ 7.70 – 7.55 (m, 44H), 6.77 (s, 2H), 3.95 (s, 6H).

Synthesis of V.1. To a flame-dried 50 mL round-bottom flask with a stir bar was added **V.6** (0.008 g, 0.008 mmol, 1 equiv). The flask was evacuated and backfilled with N_2 before being capped with a rubber septum and being kept under N_2. Next, 5 mL dry DCM was added and the flask was placed in a dry ice bath. After 20 minutes, BBr_3 (0.004 mL, 0.041 mmol, 5 equiv) was added (due to difficulty in measuring such a small volume in the syringes available, it is likely that much more BBr_3 was added than intended, qualitatively about one drop). This solution was allowed to run overnight, with the dry ice bath being allowed to expire. The next day, 1 mL of MeOH was added and the solution was exposed to reduced pressure to remove DCM. This resulted in a white suspension, which was filtered on a Celite plug and washed with copious amounts of MeOH to remove impurities. The plug was then flushed with DCM, which, after rotary evaporation, afforded **V.1** as a yellow solid (0.0062, 80%). ^{1}H NMR (500 MHz, Chloroform-d) δ 7.74 – 7.53 (m, 44H), 6.64 (s, 2H), 5.74 (s, 2H).

Synthesis of V.7. To a flame-dried 25 mL round-bottom flask with a stir bar was added **V.1** (0.001 g, 0.001 mmol, 1 equiv) and 4-*tert*-butylphenylboronic acid. The solids were dissolved in a mixture of dry toluene (5 mL) and MeOH (1 mL). A Dean-Stark trap and condenser were fitted to the flask, and the solution was stirred at reflux overnight. The next day, an aliquot of the solution was taken and concentrated for NMR analysis. Proton NMR revealed the full consumption of **V.1** and the presence of what appeared to be **V.7** along with remaining excess 4-*tert*-butylphenylboronic acid.

Synthesis of V.8. To a flame-dried 25 mL round-bottom flask with a stir bar was added **V.1** (0.003 g, 0.004 mmol, 2 equiv) and 1,4-benzenediboronic acid. The solids were dissolved in a mixture of dry toluene (5 mL) and MeOH (1 mL). A Dean-Stark trap and condenser were fitted to the flask, and the solution was stirred at reflux. After 6 hours, an aliquot of the solution was taken and concentrated for NMR analysis. Proton NMR revealed the full consumption of **V.1** and the presence of what appeared to be **V.8**.

V.4.4. ^{1}H NMR Spectra.

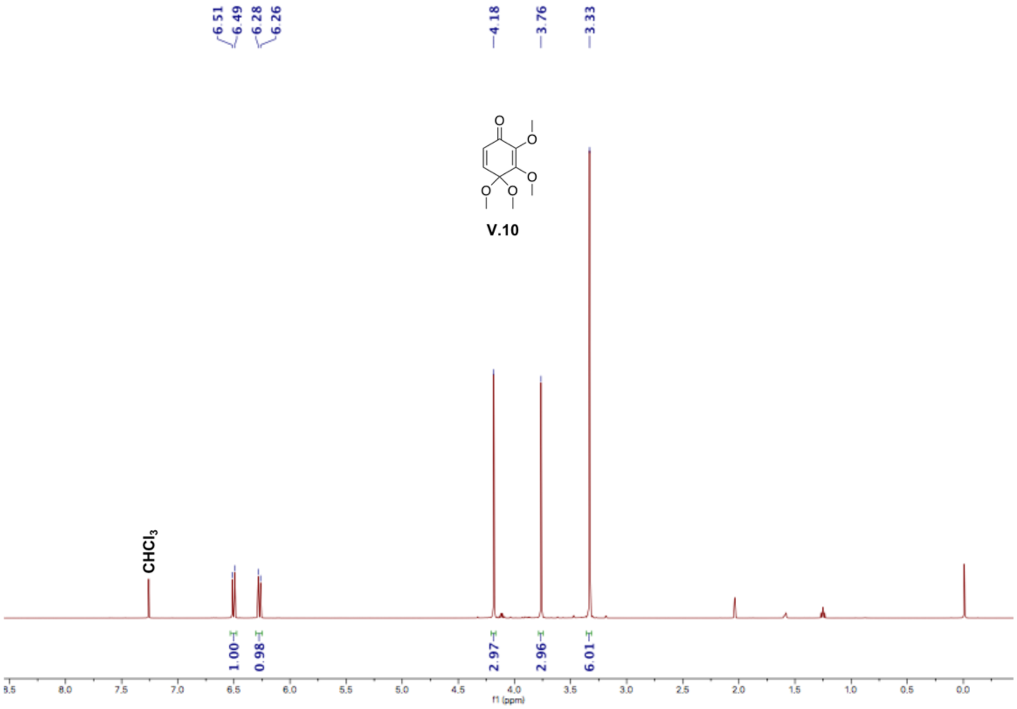
V.10

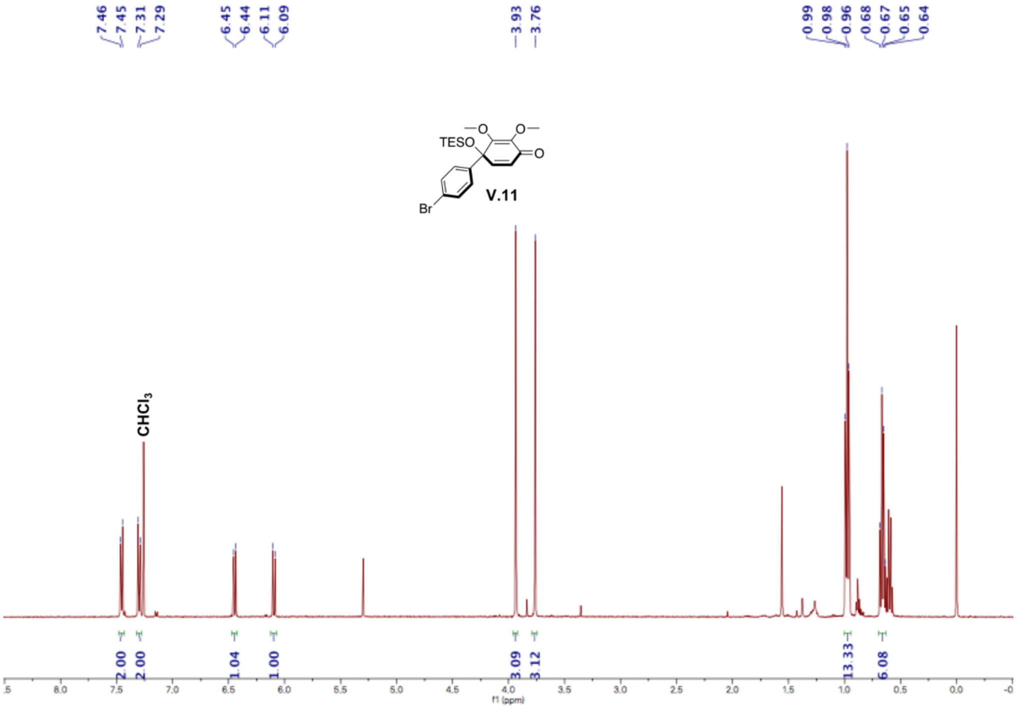
V.11

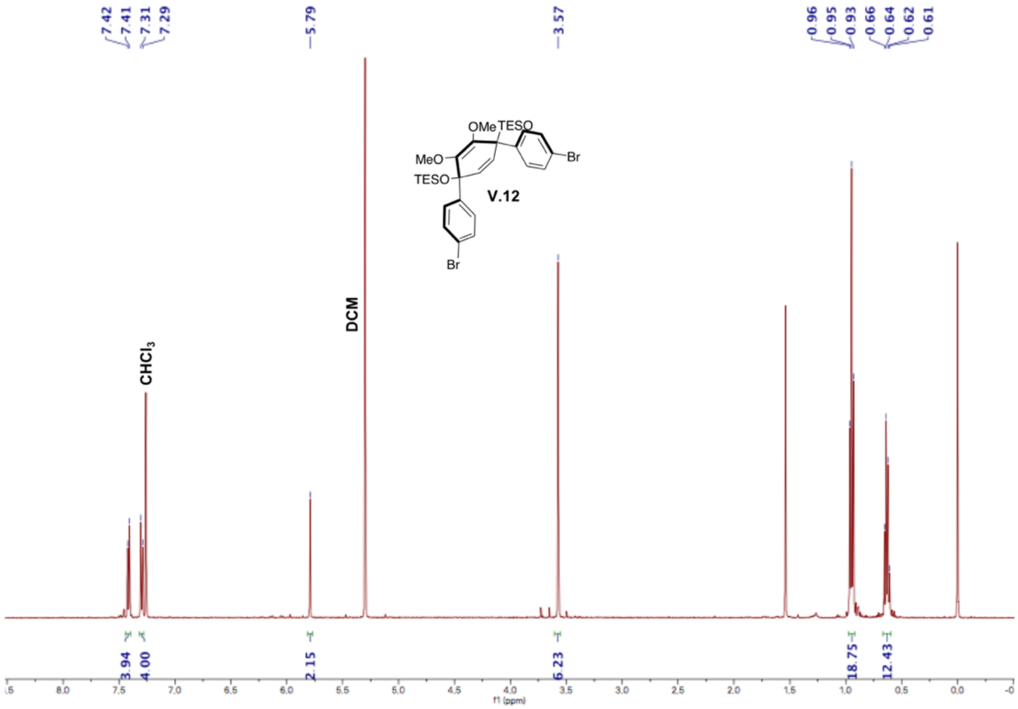

7.42
7.41
7.31
7.29
5.79
3.57
0.96
0.95
0.93
0.66
0.64
0.62
0.61
OMe
TESO
MeO
TESO
Br
Br
V.12
DCM
CHCl$_3$
3.94
4.00
2.15
6.23
18.75
12.43
f1 (ppm)

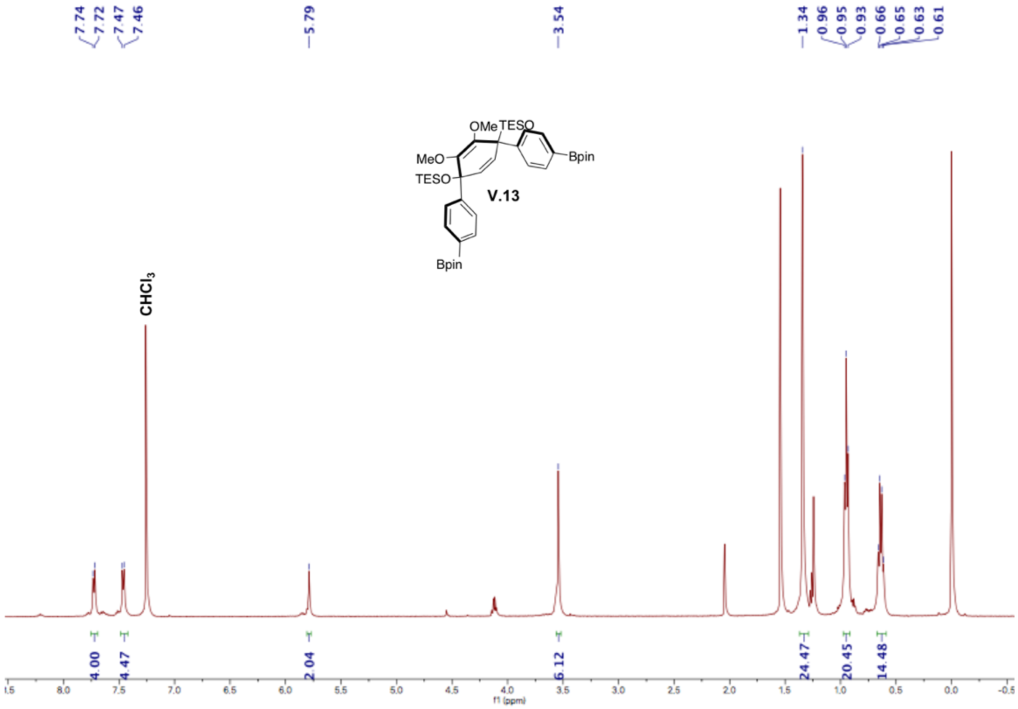

7.74
7.72
7.47
7.46
5.79
3.54
1.34
0.96
0.95
0.93
0.66
0.65
0.63
0.61
OMe
TESO
MeO
TESO
Bpin
Bpin
V.13
CHCl$_3$
4.00
4.47
2.04
6.12
24.47
20.45
14.48
f1 (ppm)

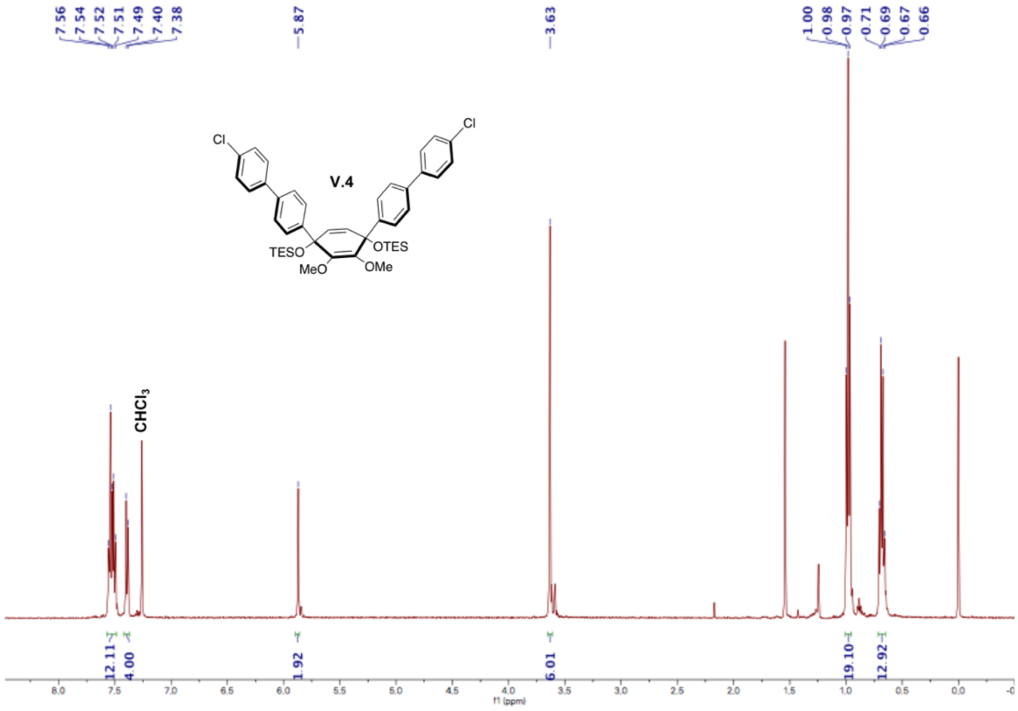
7.56
7.54
7.52
7.51
7.49
7.40
7.38
5.87
3.63
1.00
0.98
0.97
0.71
0.69
0.67
0.66
Cl
Cl
V.4
TESO
OTES
MeO
OMe
CHCl3
12.11
4.00
1.92
6.01
19.10
12.92
8.0
7.5
7.0
6.5
6.0
5.5
5.0
4.5
4.0
3.5
3.0
2.5
2.0
1.5
1.0
0.5
0.0
f1 (ppm)

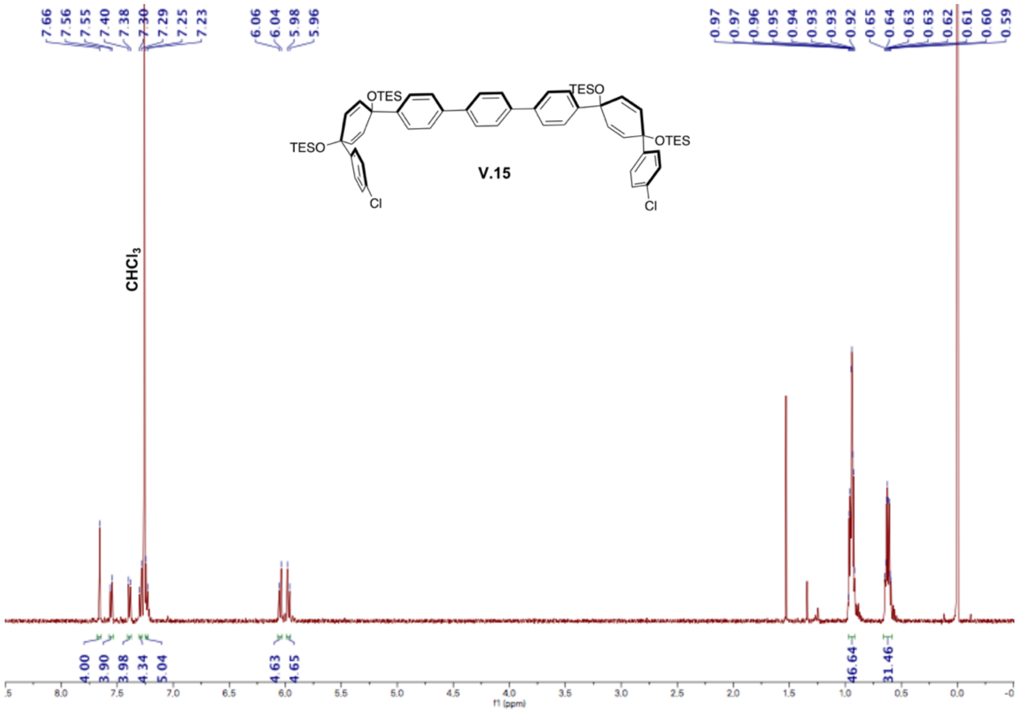
7.66
7.56
7.55
7.40
7.38
7.30
7.29
7.25
7.23
6.06
6.04
5.98
5.96
0.97
0.97
0.96
0.95
0.94
0.93
0.93
0.92
0.65
0.64
0.63
0.63
0.62
0.61
0.60
0.59
OTES
TESO
TESO
OTES
Cl
Cl
V.15
CHCl3
4.00
3.90
3.98
4.34
5.04
4.63
4.65
46.64
31.46
8.0
7.5
7.0
6.5
6.0
5.5
5.0
4.5
4.0
3.5
3.0
2.5
2.0
1.5
1.0
0.5
0.0
f1 (ppm)

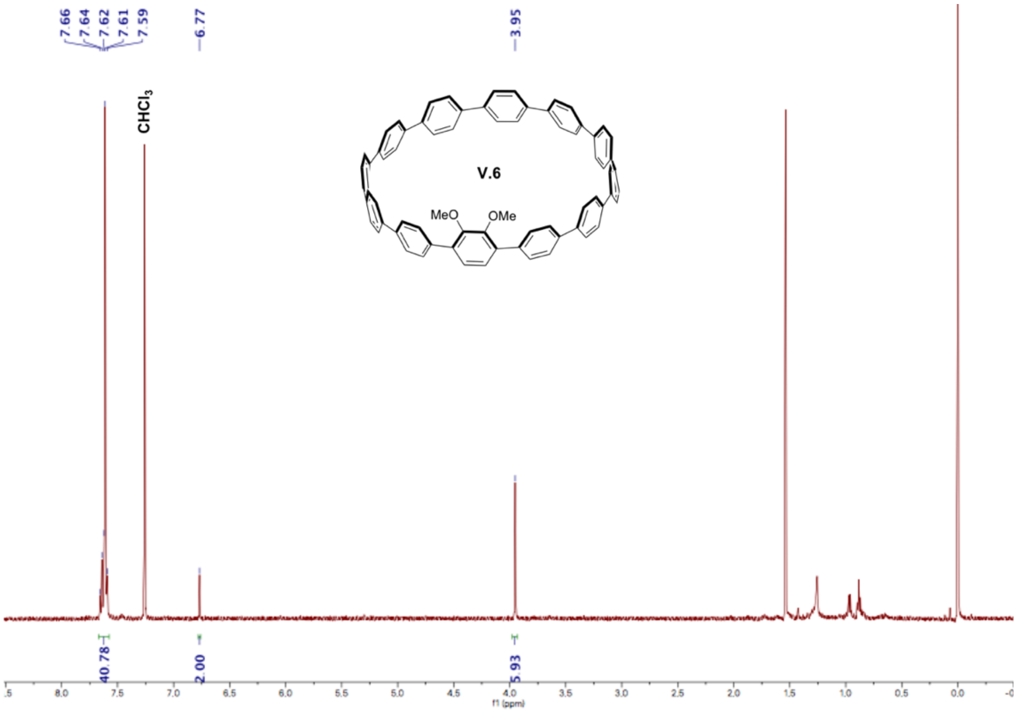
7.66
7.64
7.62
7.61
7.59
6.77
3.95
CHCl$_3$
V.6
MeO
OMe
40.78
2.00
5.93
8.0
7.5
7.0
6.5
6.0
5.5
5.0
4.5
4.0
3.5
3.0
2.5
2.0
1.5
1.0
0.5
0.0
f1 (ppm)

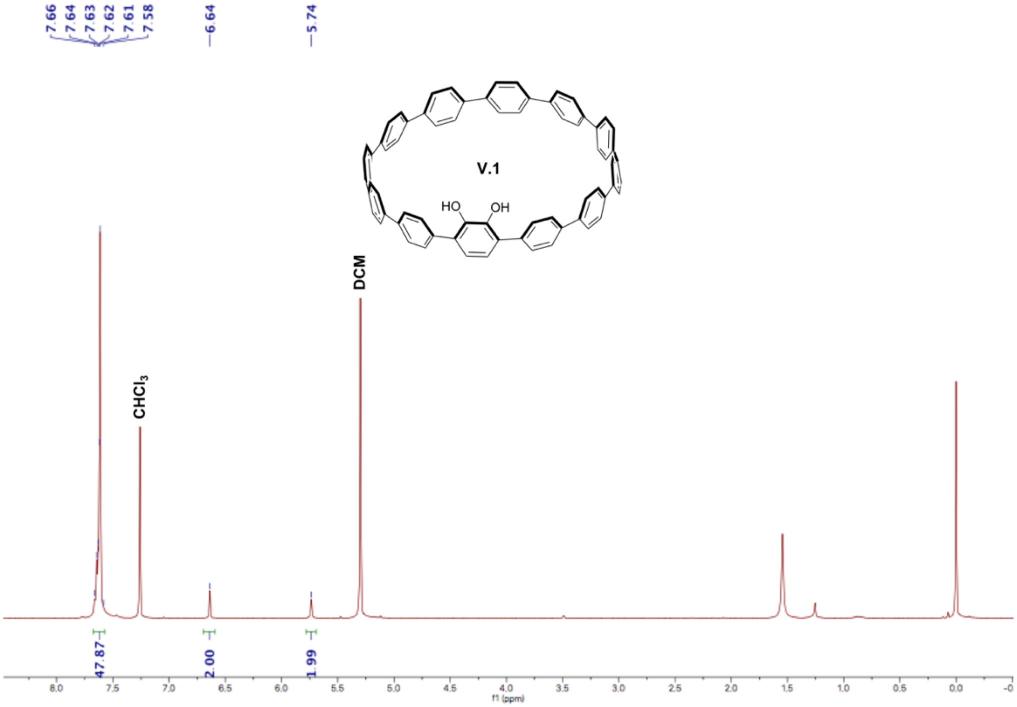
7.66
7.64
7.63
7.62
7.61
7.58
6.64
5.74
CHCl$_3$
DCM
V.1
HO
OH
47.87
2.00
1.99
8.0
7.5
7.0
6.5
6.0
5.5
5.0
4.5
4.0
3.5
3.0
2.5
2.0
1.5
1.0
0.5
0.0
f1 (ppm)

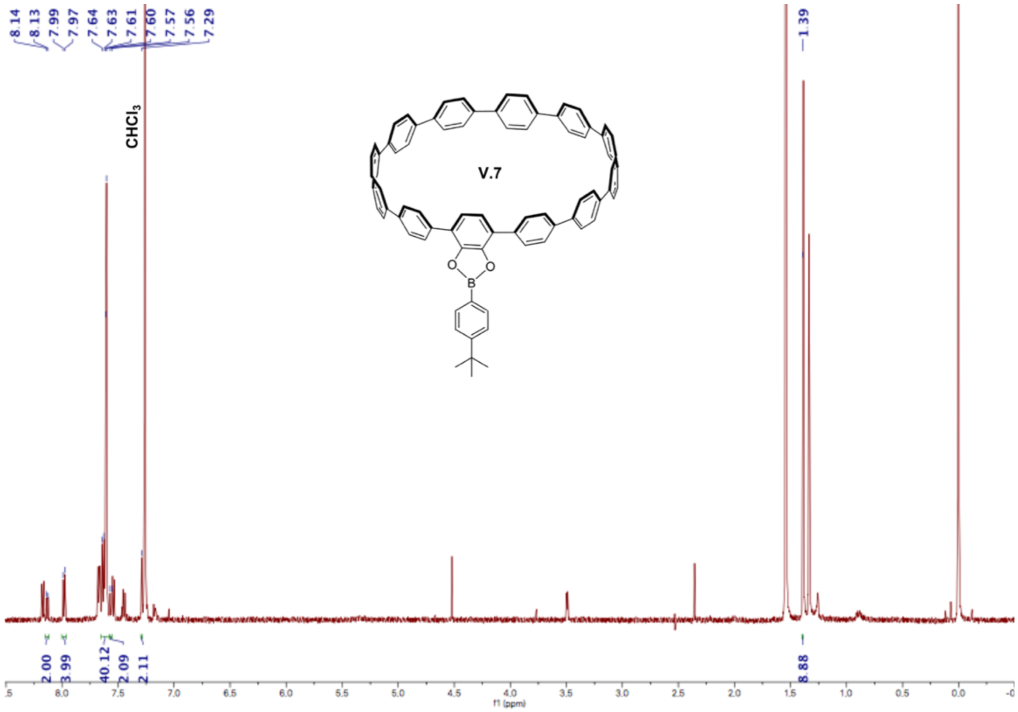
8.14
8.13
7.99
7.97
7.64
7.63
7.61
7.60
7.57
7.56
7.29
1.39
CHCl3
V.7
O
B
O
2.00
3.99
40.12
2.09
2.11
8.88
.5
8.0
7.5
7.0
6.5
6.0
5.5
5.0
4.5
4.0
3.5
3.0
2.5
2.0
1.5
1.0
0.5
0.0
-0
f1 (ppm)

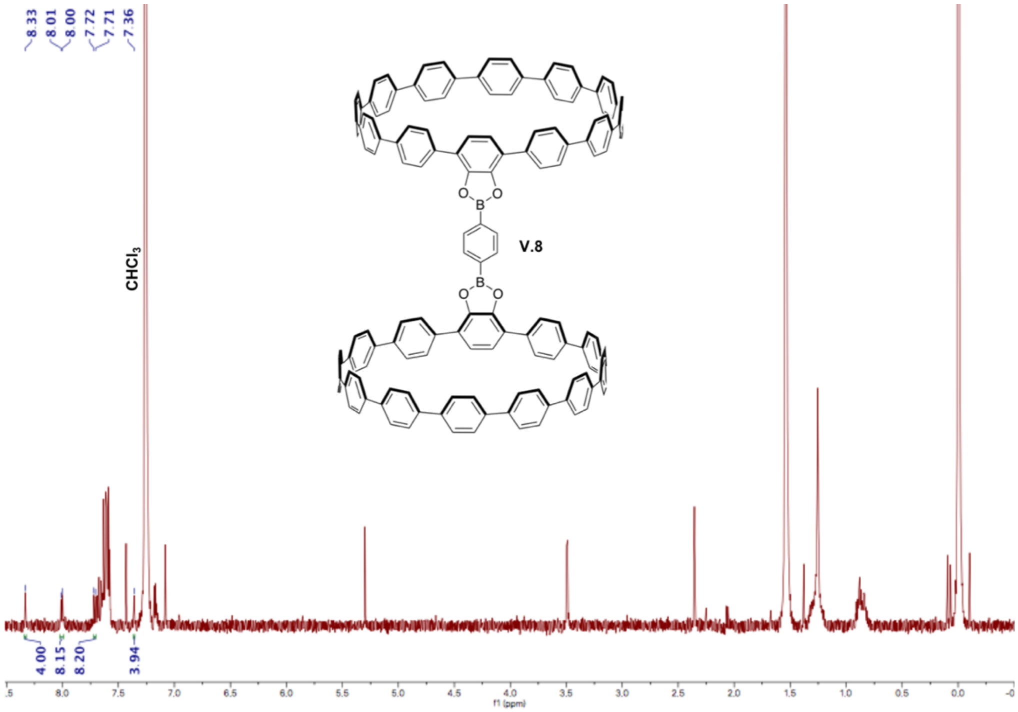
8.33
8.01
8.00
7.72
7.71
7.36
CHCl3
V.8
O
B
O
4.00
8.15
8.20
3.94
.5
8.0
7.5
7.0
6.5
6.0
5.5
5.0
4.5
4.0
3.5
3.0
2.5
2.0
1.5
1.0
0.5
0.0
-0
f1 (ppm)

CHAPTER VI

CONCLUDING REMARKS

This dissertation summarizes the efforts of our research group in designing nanotube-like solid-state materials using cycloparaphenylenes as supramolecular synthons. We have shown that, via judicious fluorination, nanohoops can self-assemble into tubular solid-state arrays with tunable diameters. Furthermore, these materials were shown to be capable of appreciable N_2 uptake, linear guest alignment, and even spontaneous nanowire formation via mild solution casting. To improve the practical viability of these materials, we have developed a modular synthetic route that can be used to access fluorinated nanohoops on the gram scale. In order to expand the utility of nanohoops in the synthesis of cylindrical materials, we have also begun preliminary work on the synthesis of catechol-containing nanohoops that we intend to use in the construction of boronic ester-linked nanotubes and cages. Thus far, have shown that a nanohoop containing a single catechol moiety is not only synthetically accessible but is readily capable of undergoing condensation reactions with boronic acids, implying that our strategy to access more complex boronic ester-linked structures using hydroxy-functionalized nanohoops is indeed feasible. Overall, this work has produced a number of design principles and synthetic strategies that may be useful in the future development of exotic carbon nanomaterials comprised of curved macrocyclic building blocks.

REFERENCES CITED

Chapter I

1. Jasti, R.; Bhattacharjee, J; Neaton, J. B.; Bertozzi, C. R. *J. Am. Chem. Soc.* **2008**, *130*, 17646–17647.

2. Darzi, E. R.; Sisto, T. J.; Jasti, R. *J. Org. Chem.* **2012**, *77,* 6624–6628.

3. Iwamoto, T.; Watanabe, Y.; Sakamoto, Y.; Suzuki, T.; Yamago, S. *J. Am. Chem. Soc.* **2011**, *133*, 8354–8361.

4. Segawa, Y.; Fukazawa, A.; Matsuura, S.; Omachi, H.; Yamaguchi, S.; Irle, S.; Itami, K. *Org. Biomol. Chem.* **2012**, *10*, 5979-5984.

5. Li, P.; Sisto, T. J.; Darzi, E. R.; Jasti, R. *Org. Lett.* **2014**, *16*, 182–185.

6. Fujitsuka, M.; Iwamoto, T.; Kayahara, E.; Yamago, S.; Majima, T. *ChemPhysChem* **2013**, *14*, 1570–1572.

7. Hines, D. A.; Darzi, E. R.; Jasti, R.; Kamat, P. V. *J. Phys. Chem. A* **2014**, *118*, 1595–1600.

8. Xia, J.; Bacon, J. W.; Jasti, R. *Chem. Sci.* **2012**, *3*, 3018–3021.

9. Kayahara, E.; Patel, V. K.; Xia, J.; Jasti, R.; Yamago, S. *Synlett* **2015**, *26*, 1615–1619.

10. Kayahara, E.; Sun, L.; Onishi, H.; Suzuki, K.; Fukushima, T.; Sawada, A.; Kaji, H.; Yamago, S. *J. Am. Chem. Soc.* **2017**, *139*, 18480-18483.

11. Li, P.; Wong, B. M.; Zakharov, L. N.; Jasti, R. *Org. Lett.* **2016**, *18*, 1574–1577.

12. Van Raden, J. M.; Louie, S.; Zakharov, L. N.; Jasti, R. *J. Am. Chem. Soc.* **2017**, *139*, 2936–2939.

13. Evans, P. J.; Zakharov, L. N.; Jasti, R. *J. Photochem. Photobiol. A Chem.* **2019**, *382*, 111878.

14. Matsui, K.; Segawa, Y.; Itami, K. *Org. Lett.* **2012**, *14*, 1888–1891.

15. Tran-Van, A.-F.; Huxol, E.; Basler, J. M.; Neubuger, M.; Adjizian, J.-J.; Ewels, C. P.; Wegner, H. A. *Org. Lett.* **2014**, *16*, 1594-1597.

16. Kubota, N.; Segawa, Y.; Itami, K. *J. Am. Chem. Soc.* **2015**, *137*, 1356–1361.

17. Hashimoto, S.; Kayahara, E.; Mizuhata, Y.; Tokitoh, N.; Takeuchi, K.; Ozawa, F.; Yamago, S. *Org. Lett.*, **2018**, *20*, 5973-5976.

18. Van Raden, J. M.; White, B. M.; Zakharov, L. N.; Jasti, R. *Angew. Chem. Int. Ed.* **2019**, *58*, 7341–7345.

19. White, B. M.; Zhao, Y.; Kawashima, T. E.; Branchaud, B. P.; Pluth, M. D.; Jasti, R. *ACS Cent. Sci.* **2018**, *4*, 1173-1178.

20. Ozaki, N.; Sakamoto, H.; Nishihara, T.; Fujimori, T.; Hijikata, Y.; Kimura, R.; Irle, S.; Itami, K. *Angew. Chem. Int. Ed.* **2017**, *56*, 11196-11202.

21. Della Sala, P.; Buccheri, N.; Sanzone, A.; Sassi, M.; Neri, P.; Talotta, C.; Rocco, A.; Pinchetti, V.; Beverina, L.; Brovelli, S.; Gaeta, C. *Chem. Commun.* **2019**, *55*, 3160-3163.

22. Xu, Y.; Wang, B.; Kaur, R.; Minameyer, M. B.; Bothe, M.; Drewello, T.; Guldi, D. M.; von Delius, M. *Angew. Chem. Int. Ed.* **2018**, *57*, 11549-11553.

23. Huang, Q.; Zhuang, G.; Jia, H.; Qian, M.; Cui, S.; Yang, S.; Du, P. *Angew. Chem. Int. Ed.* **2019**, *58*, 6244-6249.

24. Sakamoto, H.; Fujimori, T.; Li, X.; Kaneko, K.; Kan, K.; Ozaki, N.; Hijikata, Y.; Irle, S.; Itami, K. *Chem. Sci.* **2016**, *7*, 4204-4210.

25. Tang, H.; Gu, Z.; Li, C.; Li, Z.; Wu, W.; Jiang, X. *Biomater. Sci.* **2019**, *7*, 2552-2558.

26. Leonhardt, E. J.; Van Raden, J. M.; Miller, D. J.; Zakharov, L. N.; Alemán, B. J.; Jasti, R. *Nano Lett.* **2018**, *18*, 7991-7997.

27. Darzi, E. R.; Jasti, R. *Chem. Soc. Rev.* **2015**, *44*, 6401–6410.

28. Golder, M. R.; Jasti, R. *Acc. Chem. Res.* **2015**, *48*, 557–566.

29. Lewis, S. E. *Chem. Soc. Rev.* **2015**, *44*, 2221–2304.

30. Wu, D., Cheng, W., Ban, X. & Xia, J. *Asian J. Org. Chem.* **2018**, *7,* 2161–2181.

31. Majewski, M. A.; Stępień, M. *Angew. Chem. Int. Ed.* **2019**, *58*, 86–116.

32. Povie, G.; Segawa, Y.; Nishihara, T.; Miyauchi, Y.; Itami, K. *Science* **2017**, *356*, 172–175.

33. Povie, G.; Segawa, Y.; Nishihara, T.; Miyauchi, Y.; Itami, K. *J. Am. Chem. Soc.* **2018**, *140*, 10054–10059.

34. Segawa, Y.; Kuwayama, M.; Hijikata, Y.; Fushimi, M.; Nishihara, T.; Pirillo, J.; Shirasaki, J.; Kubota, N.; Itami, K. *Science* **2019**, *365*, 272–276.

35. Banerjee, M.; Shukla, R.; Rathore, R. *J. Am. Chem. Soc.* **2009**, *131*, 1780–1786.

36. Segawa, Y.; Omachi, H.; Itami, K. *Org. Lett.* **2010**, *12*, 2262–2265.

37. Chen, H.; Golder, M. R.; Wang, F.; Jasti, R.; Swan, A. K. *Carbon* **2014**, *67*, 203–213.

38. Adamska, L.; Nayyar, I.; Chen, H.; Swan, A. K.; Oldani, N.; Fernandez-Alberti, S.; Golder, M. R.; Jasti, R.; Doorn, S. K.; Tretiak, S. *Nano Lett.* **2014**, *14*, 6539-6546.

39. Evans, P. J.; Darzi, E. R.; Jasti, R. *Nat. Chem.* **2014**, *6*, 404–408.

40. Xia, J.; Jasti, R. *Angew. Chem. Int. Ed.* **2012**, *51*, 2474–2476.

41. Lovell, T. C.; Colwell, C. E.; Zakharov, L. N.; Jasti, R. *Chem. Sci.* **2019**, *10*, 3786–3790.

42. Yamago, S.; Watanabe, Y.; Iwamoto, T. *Angew. Chem. Int. Ed.* **2010**, *49*, 757–759.

43. Jasti, R.; Bertozzi, C. R. *Chem. Phys. Lett.* **2010**, *494*, 1–7.

44. Sisto, T. J.; Golder, M. R.; Hirst, E. S.; Jasti, R. *J. Am. Chem. Soc.* **2011**, *133*, 15800–15802.

45. Kayahara, E.; Patel, V. K.; Yamago, S. *J. Am. Chem. Soc.* **2014**, *136*, 2284–2287.

46. Balzani, V.; Credi, A.; Francisco, M.; Stoddart, J. F. *Angew. Chem. Int. Ed.* **2000**, *39*, 3348–3391.

47. Bruns, C. J.; Stoddart, J. F. *The Nature of the Mechanical Bond: From Molecules to Machines* (Wiley-VCH, 2016).

48. Langton, M. J.; Beer, P. D. *Acc. Chem. Res.* **2014**, *47*, 1935–1949.

49. Denis, M.; Qin, L.; Turner, P.; Jolliffe, K. A.; Goldup, S. M. *Angew. Chem. Int. Ed.* **2018**, *57*, 5315–5319.

50. Denis, M.; Pancholi, J.; Jobe, K.; Watkinson, M.; Goldup, S. M. *Angew. Chem. Int. Ed.* **2018**, *57*, 5310–5314.

51. Sagara, Y.; Karman, M.; Verde-Sesto, E.; Matsuo, K.; Kim, Y.; Tamaoki, N.; Weder, C. *J. Am. Chem. Soc.* **2018**, *140*, 1584-1587.

52. Movsisyan, L. D.; Franz, M.; Hampel, F.; Thompson, A. L.; Tykwinski, R. R. *J. Am. Chem. Soc.* **2016**, *138*, 1366-1376.

53. Arunkumar, E.; Forbes, C. C.; Noll, B. C.; Smith, B. D. *J. Am. Chem. Soc.* **2005**, *127*, 3288–3289.

54. Aucagne, V.; Hänni, K. D.; Leigh, D. A.; Lusby, P. J.; Walker, D. B. *J. Am. Chem. Soc.* **2006**, *128*, 2186–2187.

55. Denis, M.; Goldup, S. M. *Nat. Rev. Chem.* **2017**, *1*, 0061.

56. Garland, M.; Yim, J. J.; Bogyo, M. *Cell Chem. Biol.* **2016**, *23*, 122–136.

57. Lavis, L. D.; Raines, R. T. *ACS Chem. Biol.* **2008**, *3*, 142–155.

58. Liu, Z.; Lavis, L. D.; Betzig, E. *Mol. Cell* **2015**, *58*, 644–659.

59. Lavis, L. D.; Raines, R. T. *ACS Chem. Biol.* **2014**, *9*, 855–866.

60. Lavis, L. D. *Biochemistry* **2017**, *56*, 5165–5170.

61. Grimm, J. B.; English, B. P.; Chen, J. J.; Slaughter, J. P.; Zhang, Z. J.; Revyakin, A.; Patel, R., Macklin, J. J.; Normanno, D.; Singer, R. H.; Lionnet, T.; Lavis, L. D. *Nat. Methods* **2015**, *12*, 244-250.

62. Grimm, J. B.; Muthusamy, A. K.; Liang, Y.; Brown, T. A.; Lemon, W. C.; Patel, R.; Lu, R.; Macklin, J. J.; Keller, P. J.; Ji, N.; Lavis, L. D. *Nat. Methods* **2017**, *14*, 987−994.

63. Butkevich, A. N.; Lukinavičius, G.; D'Este, E.; Hell, S. W. *J. Am. Chem. Soc.* **2017**, *139*, 12378–12381.

64. Dojindo Molecular Technologies. Cell counting kit-8: Technical Manual. *Dojindo* https://www.dojindo.com/ TechnicalManual/Manual_CK04.pdf (2016).

65. Dunn, K. W.; Kamocka, M. M.; McDonald, J. H. *Am. J. Physiol. Cell Physiol.* **2011**, *300*, C723–C742.

66. Consoli, G. M. L.; Granata, G.; Fragrassi, G.; Grossi, M.; Sallese, M.; Geraci, C. *Org. Biomol. Chem.* **2015**, *13*, 3298-3307.

67. Consoli, G. M. L.; Granata, G.; Geraci, C. *Org. Biomol. Chem.* **2011**, *9*, 6491–6495.

68. Zhu, M.; Yang, C. *Chem. Soc. Rev.* **2013**, *42*, 4963–4976.

69. Shimizu, M.; Hiyama, T. *Chem. Asian J.* **2010**, *5*, 1516–1531.

70. Han, T.-H.; Lee, Y.; Choi, M.-R.; Woo, S.-H.; Bae, S.-H.; Hong, B. H.; Ahn, J.-H.; Lee, T.-W. *Nat. Photonics* **2012**, *6*, 105-110.

71. Tanaka, T.; Nishio, I.; Sun, S.-T.; Ueno-Nishio, S. *Science* **1982**, *218*, 467–469.

72. Zhang, Q. M.; Li, H.; Poh, M.; Xia, F.; Cheng, Z.-Y.; Xu, H.; Huang, C. *Nature* **2002**, *419*, 284-287.

73. Asamitsu, A.; Tomioka, Y.; Kuwahara, H.; Tokura, Y. *Nature* **1997**, *388*, 50–52.

74. Fernandez, C. A.; Martin, P. C.; Schaef, T.; Bowden, M. E.; Thallapally, P. K.; Dang, L.; Xu, W.; Chen, X.; McGrail, B. P. *Sci. Rep.* **2014**, *4*, 6114.

75. Hasell, T.; Schmidtmann, M.; Cooper, A. I. *J. Am. Chem. Soc.* **2011**, *133*, 14920–14923.

76. 76. Hertzsch, T.; Budde, F.; Weber, E.; Hulliger, J. *Angew. Chem. Int. Ed.* **2002**, *41*, 2281–2284.

77. Guan, L.; Suenaga, K.; Shi, Z.; Gu, Z.; Iijima, S. *Nano Lett.* **2007**, *7*, 1532–1535.

78. Teitelbaum, R. C.; Ruby, S. L.; Marks, T. J. *J. Am. Chem. Soc.* **1978**, *100*, 3215–3217.

79. Konishi, T.; Tanaka, W.; Kawai, T.; Fujikawa, T. *J. Synchrotron Radiat.* **2001**, *8*, 737–739.

80. Cui, Y.; Yue, Y.; Qian, G.; Chen, B. *Chem. Rev.* **2012**, *112*, 1126–1162.

81. Mukherjee, S.; Thilagar, P. *Dyes Pigments* **2014**, *110*, 2–27.

82. Iwamoto, T.; Watanabe, Y.; Sadahiro, T.; Haino, T.; Yamago, S. *Angew. Chem. Int. Ed.* **2011**, *50*, 8342–8344.

83. Debije, M. G.; Verbunt, P. P. C. *Adv. Energy Mater.* **2012**, *2*, 12–35.

84. Meinardi, F.; Colombo, A.; Velizhanin, K. A.; Simonutti, R.; Lorenzon, M.; Beverina, L.; Viswanatha, R.; Klimov, V. I.; Brovelli, S. *Nat. Photonics* **2014**, *8*, 392-399.

85. Meinardi, F.; Akkerman, Q. A.; Bruni, F.; Park, S.; Mauri, M.; Dang, Z.; Manna, L.; Brovelli, S. *ACS Energy Lett.* **2017**, *2*, 2368-2377.

86. Papucci, C.; Geervliet, T. A.; Franchi, D.; Bettucci, O.; Mordini, A.; Reginato, G.; Picchioni, F.; Pucci, A.; Calamante, M.; Zani, L. *Angew. Chem. Int. Ed.* **2018**, *2018*, 2657-2666.

87. Sol, J. A. H. P.; Dehm, V.; Hecht, R.; Würthner, F.; Schenning, A. P. H. J.; Debije, M. G. *Angew. Chem. Int. Ed.* **2018**, *57*, 1030-1033.

88. Krumer, Z.; van Sark, W. G. J. H. M.; Schropp, R. E. I.; de Mello Donegá, C. *Sol. Energy Mater. Sol. Cells* **2017**, *167*, 133–139.

89. Ball, M.; Zhang, B.; Zhong, Y.; Fowler, B.; Xiao, S.; Ng, F.; Steigerwald, M.; Nuckolls, C. *Acc. Chem. Res.* **2019**, *52*, 1068-1078.

90. Van Raden, J. M.; Darzi, E. R.; Zakharov, L. N.; Jasti, R. *Org. Biomol. Chem.* **2016**, *14,* 5721–5727.

91. Hines, D.; Darzi, E. R.; Jasti, R.; Kamat, P. *J. Phys. Chem. A* **2015**, *119*, 8083–8089.

92. Darzi, E. R.; Hirst, E. S.; Weber, C. D.; Zakharov, L. N.; Lonergan, M. C.; Jasti, R. *ACS Cent. Sci.* **2015**, *1*, 335-342.

93. Kuwabara, T.; Orii, J.; Segawa, Y.; Itami, K. *Angew. Chem. Int. Ed.* **2015**, *54*, 9646–9649.

94. Canola, S.; Graham, C.; Pérez-Jiménez; A. J., Sancho-García, J. C.; Negri, F. *Phys. Chem. Chem. Phys.* **2019**, *21*, 2057–2068.

95. Hu, L.; Guo, Y.; Yan, X.; Zeng, H.; Zhou, J. *Phys. Lett. A* **2017**, *381*, 2107–2111.

96. Pérez-Guardiola, A., Pérez-Jiménez, A. J., Muccioli, L. & Sancho-García, J. C. *Adv. Mater. Interfaces* **2019**, *6*, 1801948.

97. Sancho-García, J. C.; Moral, M.; Pérez-Jiménez, A. J. *J. Phys. Chem. C* **2016**, *120*, 9104–9111.

98. Lin, J. B.; Darzi, E. R.; Jasti, R.; Yavuz, I.; Houk, K. N. *J. Am. Chem. Soc.* **2019**, *141*, 952–960.

99. Segawa, Y.; Miyamoto, S.; Omachi, H.; Matsuura, S.; Šenel, P.; Sasamori, T.; Tokitoh, N.; Itami, K. *Angew. Chem. Int. Ed.* **2011**, *50*, 3244-3248.

100. Kayahara, E., Sakamoto, Y., Suzuki, T. & Yamago, S. *Org. Lett.* **2012**, *14*, 3284–3287.

101. Segawa, Y.; Šenel, P.; Matsuura, H.; Omachi, H.; Itami, K. *Chem. Lett.* **2011**, *40*, 423–425.

102. Sibbel, F.; Matsui, K.; Segawa, Y.; Studer, A.; Itami, K. *Chem. Commun.* **2014**, *50*, 954–956.

103. Fukushima, T.; Sakamoto, H.; Tanaka, K.; Hijikata, Y.; Irle, S.; Itami, K. *Chem. Lett.* **2017**, *46*, 855-857.

104. Yavuz, I.; Lopez, S. A.; Lin, J. B.; Houk, K. N. *J. Mater. Chem. C* **2016**, *4*, 11238–11243.

105. Zabula, A. V.; Filatov, A. S.; Xia, J.; Jasti, R.; Petrukhina, M. A. *Angew. Chem. Int. Ed.* **2013**, *52*, 5033–5036.

106. Spisak, S. N.; Wei, Z.; Darzi, E.; Jasti, R.; Petrukhina, M. A. *Chem. Commun.* **2018**, *54*, 7818–7821.

107. Golder, M. R.; Wong, B. M.; Jasti, R. *Chem. Sci.* **2013**, *4*, 4285–4291.

108. Kayahara, E.; Kouyama, T.; Kato, T.; Takaya, H.; Yasuda, N.; Yamago, S. *Angew. Chem. Int. Ed.* **2013**, *52*, 13722–13726.

109. Toriumi, N.; Muranaka, A.; Kayahara, E.; Yamago, S.; Uchiyama, M. *J. Am. Chem. Soc.* **2015**, *137*, 82–85.

110. Kayahara, E.; Kouyama, T.; Kato, T.; Yamago, S. *J. Am. Chem. Soc.* **2016**, *138*, 338–344.

111. Masumoto, Y.; Toriumi, N.; Muranaka, A.; Kayahara, E.; Yamago, S.; Uchiyama, M. *J. Phys. Chem. A* **2018**, *122*, 5162–5167.

112. Meijer, E. J.; De Leeuw, D. M.; Setayesh, S.; van Veenendaal, E.; Huisman, B.-H.; Blom, P. W. M.; Hummelen, J. C.; Scherf, U.; Klapwijk, T. M. *Nat. Mater.* **2003**, *2*, 678–682.

113. Blom, P. W. M.; de Jong, M. J. M.; Vleggaar, J. J. *Appl. Phys. Lett.* **1996**, *68*, 3308–3310.

114. Lei, T.; Wang, J.-Y.; Pei, J. *Chem. Mater.* **2014**, *26*, 594–603.

115. Reese, C.; Bao, Z. *Mater. Today* **2007**, *10*, 20–27.

116. Li, C.-Z., Yip, H.-L. & Jen, A. K.-Y. *J. Mater. Chem.* **2012**, *22*, 4161–4177.

117. Guldi, D. M.; Illescas, B. M.; Atienza, C. M.; Wielopolski, M.; Martín, N. *Chem. Soc. Rev.* **2009**, *38*, 1587–1597.

118. Babu, S. S.; Möhwald, H.; Nakanishi, T. *Chem. Soc. Rev.* **2010**, *39*, 4021–4035.

119. Smith, B. W.; Monthioux, M.; Luzzi, D. E. *Nature* **1998**, *396*, 323–324.

120. Smith, B. W.; Luzzi, D. E. *Chem. Phys. Lett.* **2000**, *321*, 169–174.

121. Hornbaker, D. J.; Kahng, S.-J.; Misra, S.; Smith, B. W.; Johnson, A. T.; Mele, E. J.; Luzzi, D. E.; Yazdani, A. *Science* **2002**, *295*, 828-831.

122. Barnes, J. C.; Dale, E. J.; Prokofjevs, A.; Narayanan, A.; Gibbs-Hall, I. C.; Juríček, M.; Stern, C. L.; Sarjeant, A. A.; Botros, Y. Y.; Stupp, S. I.; Stoddart, J. F. *J. Am. Chem. Soc.* **2015**, *137*, 2392-2399.

123. Iwamoto, T.; Watanabe, Y.; Takaya, H.; Haino, T.; Yasuda, N.; Yamago, S. **2013**, *19*, 14061-14068.

124. Shinohara, H. *Rep. Prog. Phys.* **2000**, *63*, 843–892.

125. Chaur, M. N.; Melin, F.; Ortiz, A. L.; Echegoyen, L. *Angew. Chem. Int. Ed.* **2009**, *48*, 7514–7538.

126. Rodrígues-Fortea, A.; Balch, A. L.; Poblet, J. M. *Chem. Soc. Rev.* **2011**, *40*, 3551–3563.

127. Kimura, K.; Ikeda, N.; Maruyama, Y.; Okazaki, T.; Shinohara, H.; Bandow, S.; Iijima, S. *Chem. Phys. Lett.* **2003**, *379*, 340-344.

128. Iwamoto, T.; Slanina, Z.; Mizorogi, N.; Guo, J.; Akasaka, T.; Nagase, S.; Takaya, H.; Yasuda, N.; Kato, T.; Yamago, S. *Chem. Eur. J.* **2014**, *20*, 14403-14409.

129. Ueno, H.; Nishihara, T.; Segawa, Y.; Itami, K. *Angew. Chem. Int. Ed.* **2015**, *54*, 3707–3711.

130. Isobe, H.; Hitosugi, S.; Yamasaki, T.; Iizuka, R. *Chem. Sci.* **2013**, *4*, 1293–1297.

131. Sato, S., Yamasaki, T. & Isobe, H. *Proc. Natl Acad. Sci. USA* **111**, 8374–8379 (2014).

132. Isobe, H.; Nakamura, K.; Hitosugi, S.; Sato, S.; Tokoyama, H.; Yamakado, H.; Ohno, K.; Kono, H. *Chem. Sci.* **2015**, *6*, 2746–2753.

133. Lim, G. N.; Obondi, C. O.; D'Souza, F. *Angew. Chem. Int. Ed.* **2016**, *55*, 11517–11521.

134. Molina-Ontoria, A.; Wielopolski, M.; Gebhardt, J.; Gouloumis, A.; Clark, T.; Guldi, D. M.; Martín, N. *J. Am. Chem. Soc.* **2011**, *133*, 2370–2373.

135. Yamamoto, M.; Föhlinger, J.; Petersson, J.; Hammarström, L.; Imahori, H. *Angew. Chem. Int. Ed.* **2017**, *56*, 3329–3333.

136. Yu, H.-Z.; Baskin, J. S.; Zewail, A. H. *J. Phys. Chem. A* **2002**, *106*, 9845–9854.

137. Guldi, D. M.; Prato, M. *Acc. Chem. Res.* **2000**, *33*, 695–703.

138. Omachi, H.; Nakayama, T.; Takahashi, E.; Segawa, Y.; Itami, K. *Nat. Chem.* **2013**, *5*, 572–576.

139. Scott, L. T. *Angew. Chem. Int. Ed.* **2003**, *42*, 4133–4135.

140. Tan, L.-L.; Li, H.; Tao, Y.; Zhang, S. X.-A.; Wang, B.; Yang, Y.-W. *Adv. Mater.* **2014**, *26*, 7027–7031.

141. Lim, S.; Kim, H.; Selvapalam, N.; Kim, K.-J.; Cho, S. J.; Seo, G.; Kim, K. *Angew. Chem. Int. Ed.* **2008**, *47*, 3352–3355.

142. Matsuda, R.; Tsujino, T.; Sato, H.; Kubota, Y.; Morishige, K.; Takata, M.; Kitagawa, S. *Chem. Sci.* **2010**, *1*, 315–321.

143. Zhang, D.; Q., G.-B.; Zhao, Y.-X.; Qiao, S.-L.; Yang, C.; Wang, H. *Adv. Mater.* **2015**, *27*, 6125–6130.

144. Zheng, X.; Tang, H.; Xie, C.; Zhang, J.; Wu, W.; Jiang, X. *Angew. Chem. Int. Ed.* **2015**, *54*, 8094–8099.

145. Jiang, X.; Xin, H.; Gu, J.; Xu, X.; Xia, W.; Chen, S.; Xie, Y.; Chen, L.; Chen, Y.; Sha, X.; Fang, X. *Biomaterials* **2013**, *34*, 1739–1746.

146. Liu, C.; Zhen, X.; Wang, X.; Wu, W.; Jiang, X. *Soft Matter* **2011**, *7*, 11526–11534.

147. Sorkin, A.; Goh, L. K. *Exp. Cell Res.* **2009**, *315*, 683–696.

148. Thalladi, V. R.; Weiss, H.-C.; Bläser, D.; Boese, R.; Nangia, A.; Desiraju, G. R. *J. Am. Chem. Soc.* **1998**, *120*, 8702–8710.

149. Coates, G. W.; Dunn, A. R.; Henling, L. M.; Dougherty, D. A.; Grubbs, R. H. *Angew. Chem. Int. Ed.* **1997**, *36*, 248–251.

150. Patrick, C. R.; Prosser, G. S. *Nature* **1960**, *187*, 1021.

151. Kissel, P.; Murray, D. J.; Wulftange, W. J.; Catalano, V. J.; King, B. T. *Nat. Chem.* **2014**, *6*, 774–778.

152. Salonen, L. M.; Ellermann, M.; Diederich, F. *Angew. Chem. Int. Ed.* **2011**, *50*, 4808–4842.

153. Falcaro, P.; Okada, K.; Hara, T.; Ikigaki, K.; Tokudome, Y.; Thornton, A. W.; Hill, A. J.; Williams, T.; Doonan, C.; Takahashi, M. *Nat. Mater.* **2017**, *16*, 342–348.

154. Holt, J. K.; Park, H. G.; Wang, Y.; Stadermann, M.; Artyukhin, A. B.; Grigoropoulos, C. P.; Noy, A.; Bakajin, O. *Science* **2006**, *312*, 1034–1037.

155. Tunuguntla, R. H.; Allen, F. I.; Kim, K.; Belliveau, A.; Noy, A. *Nat. Nanotechnol.* **2016**, *11*, 639–644.

156. Wang, H.; Wang, B.; Quek, X.-Y.; Wei, L.; Zhao, J.; Li, L.-J.; Chan-Park, M. B.; Yang, Y.; Chen, Y. *J. Am. Chem. Soc.* **2010**, *132*, 16747–16749.

157. Sanchez-Valencia, J. R.; Dienel, T.; Gröning, O.; Shorubalko, I.; Mueller, A.; Jansen, M.; Amsharov, K.; Ruffieux, P.; Fasel, R. *Nature* **2014**, *512*, 61–64.

Chapter II

1. Jariwala, D.; Sangwan, V. K.; Lauhon, L. J.; Marks, T. J.; Hersam, M. C. *Chem. Soc. Rev.* **2013**, *42*, 2824−2860.

2. Wang, H.; Wang, B.; Quek, X.-Y.; Wei, L.; Zhao, J.; Li, L.-J.; Chan-Park, M. B.; Yang, Y.; Chen, Y. *J. Am. Chem. Soc.* **2010**, *132*, 16747−16749.

3. He, M.; Chernov, A. I.; Fedotov, P. V.; Obraztsova, E. D.; Rikkinen, E.; Zhu, Z.; Sainio, J.; Jiang, H.; Nasibulin, A. G.; Kauppinen, E. I.; Niemela,̈M.; Krause, A. O. I. *Chem. Commun.* **2011**, *47*, 1219−1221.

4. Sanchez-Valencia, J. R.; Dienel, T.; Gröning, O.; Shorubalko, I.; Mueller, A.; Jansen, M.; Amsharov, K.; Ruffieux, P.; Fasel, R. *Nature* **2014**, *512*, 61−64.

5. Holt, J. K.; Park, H. G.; Wang, Y.; Stadermann, M.; Artyukhin, A. B.; Grigoropoulos, C. P.; Noy, A.; Bakajin, O. *Science* **2006**, *312*, 1034−1037.

6. Tunuguntla, R. H.; Allen, F. I.; Kim, K.; Belliveau, A.; Noy, A. *Nat. Nanotechnol.* **2016**, *11*, 639−644.

7. Hata, K.; Futaba, D. N.; Mizuno, K.; Namai, T.; Yumura, M.; Iijima, S. *Science* **2004**, *306*, 1362−1364.

8. Fornasiero, F.; Park, H. G.; Holt, J. K.; Stadermann, M.; Grigoropoulos, C. P.; Noy, A.; Bakajin, O. *Proc. Natl. Acad. Sci. U. S. A.* **2008**, *105*, 17250−17255.

9. Qu, L.; Vaia, R. A.; Dai, L. *ACS Nano* **2011**, *5*, 994−1002.

10. Bsoul, A.; Sultan Mohamed Ali, M.; Nojeh, A.; Takahata, K. *Appl. Phys. Lett.* **2012**, *100*, 213510.

11. Miyake, T.; Yoshino, S.; Yamada, T.; Hata, K.; Nishizawa, M. *J. Am. Chem. Soc.* **2011**, *133*, 5129−5134.

12. Smalley, R. E.; Li, Y.; Moore, V. C.; Price, B. K.; Colorado, R.; Schmidt, H. K.; Hauge, R. H.; Barron, A. R.; Tour, J. M. *J. Am. Chem. Soc.* **2006**, *128*, 15824−15829.

13. Xia, J.; Golder, M. R.; Foster, M. E.; Wong, B. M.; Jasti, R. *J. Am. Chem. Soc.* **2012**, *134*, 19709−19715.

14. Sisto, T. J.; Tian, X.; Jasti, R. *J. Org. Chem.* **2012**, *77*, 5857− 5860.

15. Omachi, H.; Nakayama, T.; Takahashi, E.; Segawa, Y.; Itami, K. *Nat. Chem.* **2013**, *5*, 572−576.

16. Jasti, R.; Bhattacharjee, J.; Neaton, J. B.; Bertozzi, C. R. *J. Am. Chem. Soc.* **2008**, *130*, 17646−17647.

17. Darzi, E. R.; Sisto, T. J.; Jasti, R. *J. Org. Chem.* **2012**, *77,* 6624− 6628.

18. Xia, J.; Jasti, R. *Angew. Chem., Int. Ed.* **2012**, *51*, 2474−2476.

19. Patel, V. K.; Kayahara, E.; Yamago, S. *Chem. Eur. J.* **2015**, *21*, 5742−5749.

20. Evans, P. J.; Darzi, E. R.; Jasti, R. *Nat. Chem.* **2014**, *6*, 404−408.

21. Tran-Van, A.-F.; Huxol, E.; Basler, J. M.; Neuburger, M.; Adjizian, J.-J.; Ewels, C. P.; Wegner, H. A. *Org. Lett.* **2014**, *16*, 1594− 1597.

22. Van Raden, J. M.; Louie, S.; Zakharov, L. N.; Jasti, R. *J. Am. Chem. Soc.* **2017**, *139*, 2936−2939.

23. White, B. M.; Zhao, Y.; Kawashima, T. E.; Branchaud, B. P.; Pluth, M. D.; Jasti, R. *ACS Cent. Sci.* **2018**, *4*, 1173−1178.

24. Povie, G.; Segawa, Y.; Nishihara, T.; Miyauchi, Y.; Itami, K. *Science* **2017**, *356*, 172−175.

25. Povie, G.; Segawa, Y.; Nishihara, T.; Miyauchi, Y.; Itami, K. *J. Am. Chem. Soc.* **2018**, *140*, 10054−100059.

26. Fujitsuka, M.; Cho, D. W.; Iwamoto, T.; Yamago, S.; Majima, T. *Phys. Chem. Chem. Phys.* **2012**, *14*, 14585−14588.

27. Darzi, E. R.; Jasti, R. *Chem. Soc. Rev.* **2015**, *44*, 6401−6410.

28. Sakamoto, H.; Fujimori, T.; Li, X.; Kaneko, K.; Kan, K.; Ozaki, N.; Hijikata, Y.; Irle, S.; Itami, K. *Chem. Sci.* **2016**, *7*, 4204−4210.

29. Kayahara, E.; Sun, L.; Onishi, H.; Suzuki, K.; Fukushima, T.; Sawada, A.; Kaji, H.; Yamago, S. *J. Am. Chem. Soc.* **2017**, *139*, 18480− 18483.

30. Ozaki, N.; Sakamoto, H.; Nishihara, T.; Fujimori, T.; Hijikata, Y.; Kimura, R.; Irle, S.; Itami, K. *Angew. Chem., Int. Ed.* **2017**, *56*, 11196−11202.

31. Mori, T.; Tanaka, H.; Dalui, A.; Mitoma, N.; Suzuki, K.; Matsumoto, M.; Aggarwal, N.; Patnaik, A.; Acharya, S.; Shrestha, L. K.; Sakamoto, H.; Itami, K.; Ariga, K. *Angew. Chem. Int. Ed.* **2018**, *57*, 9679−9683.

32. Ball, M.; Zhong, Y.; Fowler, B.; Zhang, B.; Li, P.; Etkin, G.; Paley, D. W.; Decatur, J.; Dalsania, A. K.; Li, H.; Xiao, S.; Ng, F.; Steigerwald, M. L.; Nuckolls, C. *J. Am. Chem. Soc.* **2016**, *138*, 12861− 12867.

33. Bezdek, A.; Kuperberg, W. *Mathematika* **1990**, *37*, 74−80.

34. Peigney, A.; Laurent, C.; Flahaut, E.; Bacsa, R. R.; Rousset, A. *Carbon* **2001**, *39*, 507−514.

35. Anthony, J. E.; Brooks, J. S.; Eaton, D. L.; Parkin, S. R. *J. Am. Chem. Soc.* **2001**, *123*, 9482−9483.

36. Segawa, Y.; Miyamoto, S.; Omachi, H.; Matsuura, S.; Šenel, P.; Sasamori, T.; Tokitoh, N.; Itami, K. *Angew. Chem. Int. Ed.* **2011**, *50*, 3244−3248.

37. Patrick, C. R.; Prosser, G. S. *Nature* **1960**, *187*, 1021.

38. Coates, G. W.; Dunn, A. R.; Henling, L. M.; Dougherty, D. A.; Grubbs, R. H. *Angew. Chem. Int. Ed. Engl.* **1997**, *36*, 248−251.

39. Kissel, P.; Murray, D. J.; Wulftange, W. J.; Catalano, V. J.; King, B. T. *Nat. Chem.* **2014**, *6*, 774−778.

40. Thalladi,V.R.;Weiss, H.-C.;Blas̆er, D.; Boese, R.; Nangia, A.; Desiraju, G. R. *J. Am. Chem. Soc.* **1998**, *120*, 8702−8710.

41. Hashimoto, S.; Kayahara, E.; Mizuhata, Y.; Tokitoh, N.; Takeuchi, K.; Ozawa, F.; Yamago, S. *Org. Lett.* **2018**, *20*, 5973−5976.

42. Suzuki, A. *Angew. Chem. Int. Ed.* **2011**, *50*, 6722−6737.

43. Rio, J.; Erbahar, D.; Rayson, M.; Briddon, P.; Ewels, C. P. *Phys. Chem. Chem. Phys.* **2016**, *18*, 23257−23263.

44. Li, P.; Zakharov, L. N.; Jasti, R. *Angew. Chem. Int. Ed.* **2017**, *56*, 5237−5241.

45. Falcaro, P.; Okada, K.; Hara, T.; Ikigaki, K.; Tokudome, Y.; Thornton, A. W.; Hill, A. J.; Williams, T.; Doonan, C.; Takahashi, M. *Nat. Mater.* **2017**, *16*, 342−348.

46. Peŕez-Guardiola, A.; Peŕez-Jimeńez, A. J.; Sancho-García, J. C. *Mol. Syst. Des. Eng.* **2017**, *2*, 253.

47. Chen, H.; Golder, M. R.; Wang, F.; Jasti, R.; Swan, A. K. *Carbon* **2014**, *67*, 203−213.

48. Cooper, A. I. *ACS Cent. Sci.* **2017**, *3*, 544−553.

49. Tan, J. C.; Cheetham, A. K. *Chem. Soc. Rev.* **2011**, *40*, 1059−1080.

50. Beaujuge, P. M.; Frećhet, J. M. J. *J. Am. Chem. Soc.* **2011**, *133*, 20009−20029.

51. Valeur, B. *Molecular Fluorescence*; Wiley-VCH Verlag GmbH & Co. KGaA: Weinheim, Germany, 2001.

52. Iwamoto, T.; Watanabe, Y.; Sakamoto, Y.; Suzuki, T.; Yamago, S. *J. Am. Chem. Soc.* **2011**, *133*, 8354−8361.

53. Kuwabara, T.; Orii, J.; Segawa, Y.; Itami, K. *Angew. Chem. Int. Ed.* **2015**, *54*, 9646−9649.

54. Jackson, E. P.; Sisto, T. J.; Darzi, E. D.; Jasti, R. *Tetrahedron.* **2016**, *72*, 3754–3758.

55. Patel, V. K.; Kayahara, E.; Yamago, S. *Chem. Eur. J.* **2015**, *21*, 5742–5749.

56. Sheldrick, G. M. *Bruker/Siemens Area Detector Absorption Correction Program*, Bruker AXS, Madison, WI, **1998**.

57. Van der Sluis, P.; Spek, A. L. *Acta Cryst.* **1990**, *A46*, 194−201.

58. Sheldrick, G. M. *Acta Cryst.* **2015**, *C71*, 3−8.

Chapter III

1. Jariwala, D.; Sangwan, V. K.; Lauhon, L. J.; Marks, T. J.; Hersam, M. C. *Chem. Soc. Rev.* **2013**, *42*, 2824−2860.

2. Hong, G.; Diao, S.; Antaris, A. L.; Dai, H. *Chem. Rev.* **2015**, *115*, 10816−10906.

3. Yang, Z.; Ren, J.; Zhang, Z.; Chen, X.; Guan, G.; Qui, L.; Zhang, Y.; Peng, H. *Chem. Rev.* **2015**, *115*, 5159−5223.

4. Holt, J. K.; Park, H. G.; Wang, Y.; Stadermann, M.; Artyukhin, A. B.; Grigoropoulos, C. P.; Noy, A.; Bakajin, O. *Science* **2006**, *312*, 1034−1037.

5. Tunuguntla, R. H.; Allen, F. I.; Kim, K.; Belliveau, A.; Noy, A. *Nat. Nanotechnol.* **2016**, *11*, 639−644.

6. Radha, B.; Esfandiar, A.; Wang, F. C.; Rooney, A. P.; Gopinadhan, K.; Keerthi, A.; Mischenko, A.; Janardanan, A.; Blake, P.; Fumagalli, L.; Lozada-Hidalgo, M.; Garaj, S.; Haigh, S. J.; Grigorieva, I. V.; Wu, H. A.; Geim, A. K. *Nature* **2016**, *538*, 222−225.

7. Tunuguntla, R. H.; Henley, R. Y.; Yao, Y.-C.; Pham, T. A.; Wanunu, M.; Noy, A. *Science* **2017**, *357*, 792−796.

8. Zhang, S. *Nat. Biotechnol.* **2003**, *21*, 1171−1178.

9. Li, H.; Eddaoudi, M.; O'Keeffe, M.; Yaghi, O. M. *Nature* **1999**, *402*, 276−279.

10. Lee, J. Y.; Farha, O. K.; Roberts, J.; Scheidt, K. A.; Nguyen, S. B. T.; Hupp, J. T. *Chem. Soc. Rev.* **2009**, *38*, 1450−1459.

11. Côté, A. P.; Benin, A. I.; Ockwig, N. W.; O'Keeffe, M.; Matzger, A. J.; Yaghi, O. M. *Science* **2005**, *310*, 1166−1170.

12. Ding, S.-Y.; Gao, J.; Wang, Q.; Zhang, Y.; Song, W.-G.; Su, C.-Y.; Wang, W. *J. Am. Chem. Soc.* **2011**, *133*, 19816−19822.

13. Khazanovich, N.; Granja, J. R.; McRee, D. E.; Milligan, R. A.; Ghadiri, M. R. *J. Am. Chem. Soc.* **1994**, *116*, 6011−6012.

14. Hong, B. H.; Lee, J. Y.; Lee, C.-W.; Kim, J. C.; Bae, S. C.; Kim, K. S. *J. Am. Chem. Soc.* **2001**, *123*, 10748−10749.

15. Shimizu, L. S.; Smith, M. D.; Hughes, A. D.; Shimizu, K. D. *Chem. Commun.* **2001**, *0,* 1592−1593.

16. Jasti, R.; Bhattacharjee, J.; Neaton, J. B.; Bertozzi, C. R. *J. Am. Chem. Soc.* **2008**, *130*, 17646−17647.

17. Darzi, E. R.; Sisto, T. J.; Jasti, R. *J. Org. Chem.* **2012**, *77*, 6624−6628.

18. Xia, J.; Jasti, R. *Angew. Chem., Int. Ed.* **2012**, *51*, 2474−2476.

19. Patel, V. K.; Kayahara, E.; Yamago, S. *Chem. Eur. J.* **2015**, *21*, 5742−5749.

20. Evans, P. J.; Darzi, E. R.; Jasti, R. *Nat. Chem.* **2014**, *6*, 404−408.

21. Ball, M.; Fowler, B.; Li, P.; Joyce, L. A.; Li, F.; Liu, T.; Paley, D.; Zhong, Y.; Li, H.; Xiao, S.; Ng, F.; Steigerwald, M. L.; Nuckolls, C. *J. Am. Chem. Soc.* **2015**, *137*, 9982−9987.

22. Povie, G.; Segawa, Y.; Nishihara, T.; Miyauchi, Y.; Itami, K. *Science* **2017**, *356*, 172−175.

23. Darzi, E. R.; Jasti, R. *Chem. Soc. Rev.* **2015**, *44*, 6401− 6410.

24. Segawa, Y.; Miyamoto, S.; Omachi, H.; Matsuura, S.; Šenel, P.; Sasamori, T.; Tokitoh, N.; Itami, K. *Angew. Chem. Int. Ed.* **2011**, *50*, 3244−3248.

25. Leonhardt, E. J.; Van Raden, J. M.; Miller, D.; Zakharov, L. N.; Alemań, B.; Jasti, R. *Nano Lett.* **2018**, *18*, 7991−7997.

26. Patrick, C. R.; Prosser, G. S. *Nature* **1960**, *187*, 1021.

27. Thalladi, V. R.; Weiss, H.-C.; Blaŝer, D.; Boese, R.; Nangia, A.; Desiraju, G. R. *J. Am. Chem. Soc.* **1998**, *120*, 8702−8710.

28. Hashimoto, S.; Kayahara, E.; Mizuhata, Y.; Tokitoh, N.; Takeuchi, K.; Ozawa, F.; Yamago, S. *Org. Lett.* **2018**, *20*, 5973− 5976.

29. Schwaben, J.; Münster, N.; Breuer, T.; Klues, M.; Harms, K.; Witte, G.; Koert, U. *Eur. J. Org. Chem.* **2013**, *2013*, 1639−1643.

30. Bezdek, A.; Kuperberg, W. *Mathematika* **1990**, *37*, 74−80.

31. Coates, G. W.; Dunn, A. R.; Henling, L. M.; Dougherty, D. A.; Grubbs, R. H. *Angew. Chem. Int. Ed. Engl.* **1997**, *36*, 248−251.

32. Kissel, P.; Murray, D. J.; Wulftange, W. J.; Catalano, V. J.; King, B. T. *Nat. Chem.* **2014**, *6*, 774−778.

33. Kayahara, E.; Sakamoto, Y.; Suzuki, T.; Yamago, S. *Org. Lett.* **2012**, *14*, 3284−3287.

34. Xia, J.; Bacon, J. W.; Jasti, R. *Chem. Sci.* **2012**, *3*, 3018−3021.

35. Koga, K.; Gao, G. T.; Tanaka, H.; Zeng, X. C. *Nature* **2001**, *412*, 802−805.

36. Hornbaker, D. J.; Kahng, S.-J.; Misra, S.; Smith, B. W.; Johnson, A. T.; Mele, E. J.; Luzzi, D. E.; Yazdani, A. *Science* **2002**, *295*, 828−831.

37. Chuvilin, A.; Bichoutskaia, E.; Gimenez-Lopez, M. C.; Chamberlain, T. W.; Rance, G. A.; Kuganathan, N.; Biskupek, J.; Kaiser, U.; Khlobystov, A. N. *Nat. Mater.* **2011**, *10*, 687−692.

38. Iwamoto, T.; Watanabe, Y.; Sadahiro, T.; Haino, T.; Yamago, S. *Angew. Chem. Int. Ed.* **2011**, *50*, 8342−8344.

39. Sato, S.; Yamasaki, T.; Isobe, H. *Proc. Natl. Acad. Sci. U. S. A.* **2014**, *111*, 8374−8379.

40. Xu, Y.; Wang, B.; Kaur, R.; Minameyer, M. B.; Bothe, M.; Drewello, T.; Guldi, D. M.; von Delius, M. *Angew. Chem., Int. Ed.* **2018**, *57*, 11549−11553.

41. Xu, Y.; Kaur, R.; Wang, B.; Minameyer, M. B.; Gsañger, S.; Meyer, B.; Drewello, T.; Guldi, D. M.; von Delius, M. *J. Am. Chem. Soc.* **2018**, *140*, 13413−13420.

42. Iwamoto, T.; Slanina, Z.; Mizorogi, N.; Guo, J.; Akasaka, T.; Nagase, S.; Takaya, H.; Yasuda, N.; Kato, T.; Yamago, S. *Chem. Eur. J.* **2014**, *20*, 14403− 14409.

43. Ueno, H.; Nishihara, T.; Segawa, Y.; Itami, K. *Angew. Chem. Int. Ed.* **2015**, *54*, 3707−3711.

44. Britz, D. A.; Khlobystov, A. N.; Porfyrakis, K.; Ardavan, A.; Briggs, G. A. D. *Chem. Commun.* **2005**, *0*, 37−39.

45. Barnes, J. C.; Dale, E. J.; Prokofjevs, A.; Narayanan, A.; Gibbs-Hall, I. C.; Juríček, M.; Stern, C. L.; Sarjeant, A. A.; Botros, Y. Y.; Stupp, S. I.; Stoddart, J. F. *J. Am. Chem. Soc.* **2015**, *137*, 2392−2399.

46. Cooper, A. I. *ACS Cent. Sci.* **2017**, *3*, 544−553.

47. Ding, S.-Y.; Wang, W. *Chem. Soc. Rev.* **2013**, *42*, 548−568.

48. Waller, P. J.; Gandara, F.; Yaghi, O. M. *Acc. Chem. Res.* **2015**, *48*, 3053−3063.

49. Furukawa, H.; Cordova, K. E.; O'Keefe, M.; Yaghi, O. M. *Science* **2013**, *341*, 1230444.

50. Cui, Y.; Li, B.; He, H.; Zhou, W.; Chen, B.; Qian, G. *Acc. Chem. Res.* **2016**, *49*, 483−493.

51. Lim, S.; Kim, H.; Selvapalam, N.; Kim, K.; Cho, S. J.; Seo, G.; Kim, K. *Angew. Chem. Int. Ed.* **2008**, *47*, 3352−3355.

52. Dewal, M.; Xu, Y.; Yang, J.; Mohammed, F.; Smith, M.; Shimizu, L. *Chem. Commun.* **2008**, *33*, 3909− 3911.

53. Tan, L.; Li, H.; Tao, Y.; Zhang, S. X.; Wang, B.; Yang, Y. *Adv. Mater.* **2014**, *26*, 7027−7031.

54. Sakamoto, H.; Fujimori, T.; Li, X.; Kaneko, K.; Kan, K.; Ozaki, N.; Hijikata, Y.; Irle, S.; Itami, K. *Chem. Sci.* **2016**, *7*, 4204−4210.

55. Webb, P. A.; Orr, C. *Analytical Methods in Fine Particle Technology*; Micromeritics Instrument Corp.: **1997**.

56. Schaub, T. A.; Prantl, E. A.; Khon, J.; Bursch, M.; Marshall, C. R.; Leonhardt, E. J.; Lovell, T. C.; Zakharov, L. N.; Brozek, C. K.; Waldvogel, S. R.; Grimme, S.; Jasti, R. *J. Am. Chem. Soc.* **2020**, *Available Online*.

57. Reche-Tamayo, M.; Moral, M.; Peŕez-Jimeńez, A. J.;Sancho-García, J. C. J. *Phys. Chem. C* **2016**, *120*, 22627−22634.

58. Grimme, S.; Antony, J.; Ehrlich, S.; Krieg, H. *J. Chem. Phys.* **2010**, *132*, 154104.

59. Grimme, S.; Ehrlich, S.; Goerigk, L. *J. Comput. Chem.* **2011**, *32*, 1456−1465.

60. Becke, A. D. *J. Chem. Phys.* **1993**, *98*, 5648−5652.

61. Frisch, M. J.; Trucks, G. W.; Schlegel, H. B.; Scuseria, G. E.; Robb, M. A.; Cheeseman, J. R.; Scalmani, G.; Barone, V.; Petersson, G. A.; Nakatsuji, H.; Li, X.; Caricato, M.; Marenich, A.; Bloino, J.; Janesko, B. G.; Gomperts, R.; Mennucci, B.; Hratchian, H. P.; Ortiz, J. V.; Izmaylov, A. F.; Sonnenberg, J. L.; Williams-Young, D.; Ding, F.; Lipparini, F.; Egidi, F.; Goings, J.; Peng, B.; Petrone, A.; Henderson, T.; Ranasinghe, D.; Zakrzewski, V. G.; Gao, J.; Rega, N.; Zheng, G.; Liang, W.; Hada, M.; Ehara, M.; Toyota, K.; Fukuda, R.; Hasegawa, J.; Ishida, M.; Nakajima, T.; Honda, Y.; Kitao, O.; Nakai, H.; Vreven, T.; Throssell, K.; Montgomery, J. A., Jr.; Peralta, J. E.; Ogliaro, F.; Bearpark, M.; Heyd, J. J.; Brothers, E.; Kudin, K. N.; Staroverov, V. N.; Keith, T.; Kobayashi, R.; Normand, J.; Raghavachari, K.; Rendell, A.; Burant, J. C.; Iyengar, S. S.; Tomasi, J.; Cossi, M.; Millam, J. M.; Klene, M.; Adamo, C.; Cammi, R.; Ochterski, J. W.; Martin, R. L.; Morokuma, K.; Farkas, O.; Foresman, J. B.; Fox, D. J. *Gaussian 09*, Revision D.01; Gaussian, Inc.: Wallingford, CT, **2016**.

62. Battaglia, M. R.; Buckingham, A. D.; Williams, J. H. *Chem. Phys. Lett.* **1981**, *78*, 421−423.

63. Shimizu, K.; Costa Gomes, M. F.; Pádua, A. A. H.; Rebelo, L. P. N.; Lopes, J. N. C. *J. Phys. Chem. B* **2009**, *113*, 9894−9900.

64. Martinez, C. R.; Iverson, B. L. *Chem. Sci.* **2012**, *3*, 2191−2201.

65. Lovell, T. C.; Colwell, C. E.; Zakharov, L. N.; Jasti, R. *Chem. Sci.* **2019**, *10*, 3786−3790.

66. Black, C. B.; Andrioletti, B.; Try, A. C.; Ruiperez, C.; Sessler, J. L. *J. Am. Chem. Soc.* **1999**, *121*, 10438−10439.

67. Sheldrick, G. M. *Bruker/Siemens Area Detector Absorption Correction Program*; Bruker AXS: Madison, WI, **1998**.

68. Sheldrick, G. M. *Acta Crystallogr., Sect. C: Struct. Chem.* **2015**, *C71*, 3−8.

69. Van der Sluis, P.; Spek, A. L. *Acta Crystallogr., Sect. A: Found. Crystallogr.* **1990**, *A46*, 194− 201.

70. Rouquerol, J.; Llewellyn, P.; Rouquerol, F. *Stud. Surf. Sci. Catal.* **2007**, *160*, 49−56.

71. Macrae, C. F.; Bruno, I. J.; Chisholm, J. A.; Edgington, P. R.; McCabe, P.; Pidcock, E.; Rodriguez-Monge, L.; Taylor, R.; van de Streek, J.; Wood, P. A. *J. Appl. Cryst.* **2008**, *41*, 466−470.

72. Reche-Tamayo, M.; Moral, M.; Pérez-Jiménez, A. J.; Sancho-García, J. C. *J. Phys. Chem. C* **2016**, *120*, 22627–22634.

Chapter IV

1. Anthony, J. E. *Chem. Rev.* **2006**, *106*, 5028–5048.

2. Wang, C.; Dong, H.; Hu, W.; Liu, Y.; Zhu, D. *Chem. Rev.* **2012**, *112*, 2208–2267.

3. Liao, C.; Zhang, M.; Yu, M. Y.; Hua, T.; Li, L.; Yan, F. *Adv. Mater.* **2015**, *27*, 7493–7527.

4. Sun, Y; Liu, Y.; Zhu, D. *J. Mater. Chem.* **2005**, *15*, 53–65.

5. Sirringhaus, H. *Adv. Mater.* **2014**, *26*, 1319-1335.

6. Wu, W.; Liu, Y.; Zhu, D. *Chem. Soc. Rev.* **2010**, *39*, 1489–1502.

7. Anthony, J. E. *Angew. Chem. Int. Ed.* **2008**, *47*, 452–483.

8. Sheraw, C. D.; Jackson, T. N.; Eaton, D. L.; Anthony, J. E. *Adv. Mater.* **2003**, *15*, 2009–2011.

9. Zeidell, A. M.; Jennings, L.; Frederickson, C. K.; Ai, Q.; Dressler, J. J.; Zakharov, L. N.; Risko, C.; Haley, M. M.; Jurchescu, O. D. *Chem. Mater.* **2019**, *31*, 6962–6970.

10. Lamport, Z. A.; Barth, K. J.; Lee, H.; Gann, E.; Engmann, S.; Chen, H.; Guthold, M.; McCulloch, I.; Anthony, J. E.; Richter, L. J.; DeLongchamp, D. M.; Jurchescu, O. D. *Nat. Commun.* **2018**, *19*, 5130.

11. Ball, M.; Zhang, B.; Zhong, Y.; Fowler, B.; Xiao, S.; Ng, F.; Steigerwald, M.; Nuckolls, C. *Acc. Chem. Res.* **2019**, *52*, 1068–1078.

12. Ball, M.; Zhong, Y.; Fowler, B.; Zhang, B.; Li, P.; Etkin, G.; Paley, D. W.; Decatur, J.; Dalsania, A. K.; Li, H.; Xiao, S.; Ng, F.; Steigerwald, M. L.; Nuckolls, C. *J. Am. Chem. Soc.* **2016**, *138*, 12861–12867.

13. Van Raden, J. M.; Louie, S.; Zakharov, L. N.; Jasti, R. *J. Am. Chem. Soc.* **2017**, *139*, 2936–2939.

14. Evans, P. J.; Zakharov, L. N.; Jasti, R. *J. Photochem. Photobiol. A: Chemistry* **2019**, *382*, 111878.

15. Tran-Van, A.-F.; Huxol, E.; Basler, J. M.; Neubuger, M.; Adjizian, J.-J.; Ewels, C. P.; Wegner, H. A. *Org. Lett.* **2014**, *16*, 1594–1597.

16. Hashimoto, S.; Kayahara, E.; Mizuhata, Y.; Tokitoh, N.; Takeuchi, K.; Ozawa, F.; Yamago, S. *Org. Lett.*, **2018**, *20*, 5973–5976.

17. Xia, J.; Bacon, J. W.; Jasti, R. *Chem. Sci.* **2012**, *3*, 3018–3021.

18. Iwamoto, T.; Watanabe, Y.; Sadahiro, T.; Haino, T.; Yamago, S. *Angew. Chem. Int. Ed.* **2011**, *50*, 8342–8344.

19. Darzi, E. R.; Jasti, R. *Chem. Soc. Rev.* **2015**, *44*, 6401–6410.

20. Darzi, E. R.; Hirst, E. S.; Weber, C. D.; Zakharov, L. N.; Lonergan, M. C.; Jasti, R. *ACS Cent. Sci.* **2015**, *1*, 335–342.

21. Sancho-Garcia, J. C.; Moral, M.; Perez-Jimenez, A. J. *J. Phys. Chem. C* **2016**, *120*, 9104–9111.

22. Canola, S.; Graham, C.; Perez-Jimenez, A. J.; Sancho-Garcia, J. C.; Negri, F. *Phys. Chem. Chem. Phys.* **2019**, *21*, 2057–2068.

23. Lin, J. B., Darzi, E. R., Jasti, R., Yavuz, I. & Houk, K. N. Solid-State Order and Charge Mobility in [5]-[12] Cycloparaphenylenes. *J. Am. Chem. Soc.* **2019**, *141*, 952–960.

24. Kayahara, E.; Sun, L.; Onishi, H.; Suzuki, K.; Fukushima, T.; Sawada, A.; Kaji, H.; Yamago, S. *J. Am. Chem. Soc.* **2017**, *139*, 18480–18483.

25. Leonhardt, E. J.; Van Raden, J. M.; Miller, D. J.; Zakharov, L. N.; Alemán, B. J.; Jasti, R. *Nano Lett.* **2018**, *18*, 7991–7997.

26. Van Raden, J. M.; Leonhardt, E. J.; Zakharov, L. N.; Pérez-Guardiola, A.; Pérez-Jiménez, A. J.; Marshall, C. R.; Brozek, C. K.; Sancho-García, J.-C.; Jasti, R. *J. Org. Chem.* **2020**, *85*, 129–141.

27. Iwamoto, T.; Watanabe, Y.; Sakamoto, Y.; Suzuki, T.; Yamago, S. *J. Am. Chem. Soc.* **2011**, *133*, 8354–8361.

28. Frisch, M. J.; Trucks, G. W.; Schlegel, H. B.; Scuseria, G. E.; Robb, M. A.; Cheeseman, J. R.; Scalmani, G.; Barone, V.; Petersson, G. A.; Nakatsuji, H.; Li, X.; Caricato, M.; Marenich, A.; Bloino, J.; Janesko, B. G.; Gomperts, R.; Mennucci, B.; Hratchian, H. P.; Ortiz, J. V.; Izmaylov, A. F.; Sonnenberg, J. L.; Williams-Young, D.; Ding, F.; Lipparini, F.; Egidi, F.; Goings, J.; Peng, B.; Petrone, A.; Henderson, T.; Ranasinghe, D.; Zakrzewski, V. G.; Gao, J.; Rega, N.; Zheng, G.; Liang, W.; Hada, M.; Ehara, M.; Toyota, K.; Fukuda, R.; Hasegawa, J.; Ishida, M.; Nakajima, T.; Honda, Y.; Kitao, O.; Nakai, H.; Vreven, T.; Throssell, K.; Montgomery, J. A., Jr.; Peralta, J. E.; Ogliaro, F.; Bearpark, M.; Heyd, J. J.; Brothers, E.; Kudin, K. N.; Staroverov, V. N.; Keith, T.; Kobayashi, R.; Normand, J.; Raghavachari, K.; Rendell, A.; Burant, J. C.; Iyengar, S. S.; Tomasi, J.; Cossi, M.; Millam, J. M.; Klene, M.; Adamo, C.; Cammi, R.; Ochterski, J. W.; Martin, R. L.; Morokuma, K.; Farkas, O.; Foresman, J. B.; Fox, D. J. *Gaussian 09*, Revision D.01; Gaussian, Inc.: Wallingford, CT, **2016**.

Chapter V

1. Jariwala, D.; Sangwan, V. K.; Lauhon, L. J.; Marks, T. J.; Hersam, M. C. *Chem. Soc. Rev.* **2013**, *42*, 2824−2860.

2. Hong, G.; Diao, S.; Antaris, A. L.; Dai, H. *Chem. Rev.* **2015**, *115*, 10816−10906.

3. Yang, Z.; Ren, J.; Zhang, Z.; Chen, X.; Guan, G.; Qui, L.; Zhang, Y.; Peng, H. *Chem. Rev.* **2015**, *115*, 5159−5223.

4. Sisto, T. J.; Zhong, Y.; Zhang, B.; Trinh, M. T.; Miyata, K.; Zhong, X.; Zhu, X. Y.; Steigerwald, M. L.; Ng, F.; Nuckolls, C. *J. Am. Chem. Soc.* **2017**, *139*, 5684−5651.

5. Koga, Y.; Kaneda, T.; Saito, Y.; Murakami, K.; Itami, K. *Science* **2018**, *359*, 435−439.

6. Johnson, M. P. *Essays Biochem.* **2016**, *60*, 255−273.

7. Rowan, S. J.; Cantrill, S. J.; Cousins, G. R. L.; Sanders, J. K. M.; Stoddart, J. F. *Angew. Chem. Int. Ed.* **2002**, *41*, 899−952.

8. Côté, A. P.; Benin, A. I.; Ockwig, N. W.; O'Keefe, M.; Matzger, A. J.; Yaghi, O. M. *Science* **2005**, *310*, 1166−1170.

9. Ding, S.-Y.; Wang, W. *Chem. Soc. Rev.* **2013**, *42*, 548−568.

10. Waller, P. J.; Gandara, F.; Yaghi, O. M. *Acc. Chem. Res.* **2015**, *48*, 3053−3063.

11. Jin, Y.; Wang, Q.; Taynton, P.; Zhang, W. *Acc. Chem. Res.* **2014**, *47*, 1575−1586.

12. Tozawa, T.; Jones, J. T. A; Swamy, S. I.; Jiang, S.; Adams, D. J.; Shakespeare, S.; Clowes, R.; Bradshaw, D.; Hasell, T.; Chong, S. Y.; Tang, C.; Thompson, S.; Parker, J.; Trewin, A.; Bacsa, J.; Slawin, A. M. Z.; Steiner, A.; Cooper, A. I. *Nat. Mater.* **2009**, *8*, 973−978.

13. Zhang, G.; Presly, O.; White, F.; Oppel, I. M.; Mastalerz, M. *Angew. Chem. Int. Ed.* **2014**, *53*, 1516−1520.

14. Leonhardt, E. J.; Van Raden, J. M.; Miller, D. J.; Zakharov, L. N.; Alemán, B. J.; Jasti, R. *Nano Lett.* **2018**, *18*, 7991−7997.

15. Van Raden, J. M.; Leonhardt, E. J.; Zakharov, L. N.; Pérez-Guardiola, A.; Pérez-Jiménez, A. J.; Marshall, C. R.; Brozek, C. K.; Sancho-García, J.-C.; Jasti, R. *J. Org. Chem.* **2020**, *85*, 129−141.

16. Kayahara, E.; Sun, L.; Onishi, H.; Suzuki, K.; Fukushima, T.; Sawada, A.; Kaji, H.; Yamago, S. *J. Am. Chem. Soc.* **2017**, *139*, 18480−18483.

17. Cui, S.; Zhuang, G.; Wang, J.; Huang, Q.; Wang, S.; Du, P. *Org. Chem. Front.* **2019**, *6*, 1885−1890.

18. Patel, V. K.; Kayahara, E.; Yamago, S. *Chem. Eur. J.* **2015**, *21*, 5742−5749.

19. Elbert, S. M.; Regenauer, N. I.; Schindler, D.; Zhang, W.-S.; Rominger, F.; Schröder, R. R.; Mastalerz, M. *Chem. Eur. J.* **2018**, *24*, 11438−11443.

20. Van Raden, J. M.; Louie, S.; Zakharov, L. N.; Jasti, R. *J. Am. Chem. Soc.* **2017**, *139*, 2936−2939.

21. Vidal, Á. V.; López, C. S.; Faza, O. N. *Phys. Chem. Chem. Phys.* **2018**, *20*, 8607−8615.

22. White, B. M.; Zhao, Y.; Kawashima, T. E.; Branchaud, B. P.; Pluth, M. D.; Jasti, R. *ACS Cent. Sci.* **2018**, *4*, 1173−1178.

23. Kunyane, P.; Sonopo, M. S.; Selepe, M. A. *J. Nat. Prod.* **2019**, *82*, 3074−3082.

24. Lovell, T. C.; Colwell, C. E.; Zakharov, L. N.; Jasti, R. *Chem. Sci.* **2019**, *10*, 3786−3790.